Exploring Models of Electroweak Symmetry Breaking at the LHC and Beyond

Dissertation
zur Erlangung des Doktorgrades
an der Fakultät für Mathematik, Informatik und Naturwissenschaften
im Fachbereich Physik
der Universität Hamburg

vorgelegt von
Jonas Wittbrodt

Hamburg, 2019

Gutachter/innen der Dissertation:	Prof. Dr. Georg Weiglein Prof. Dr. Géraldine Servant
Zusammensetzung der Prüfungskommission:	Prof. Dr. Georg Weiglein Prof. Dr. Géraldine Servant Prof. Dr. Günter Sigl Prof. Dr. Peter Schleper Dr. Kai Schmidt-Hoberg
Vorsizender der Prüfungskomission:	Prof. Dr. Günter Sigl
Datum der Disputation:	28.10.19
Vorsitzender des Fach-Promotionsausschusses Physik:	Prof. Dr. Günter Sigl
Leiter des Fachbereichs Physik:	Prof. Dr. Wolfgang Hansen
Dekan der Fakultät MIN:	Prof. Dr. Heinrich Graener

Abstract

We explore different scenarios of electroweak symmetry breaking by studying the phenomenology of several models that extend the scalar sector of the Standard Model (SM). We investigate resonant multiscalar production in a singlet extension of the SM. The resulting benchmark scenarios illustrate many previously unstudied signatures of Higgs-to-Higgs decays that could serve as discovery channels for additional scalars. While many properties of the 125 GeV Higgs boson (h_{125}) are precisely measured, it could nevertheless be a CP-mixed state with a sizeable CP-odd admixture. We investigate this possibility in the CP-violating two-Higgs-doublet model (2HDM) and discuss the impact of bounds from fermionic electric dipole moments. We find that maximally CP-violating Yukawa couplings of h_{125} are compatible with current measurements. The Higgs sector could also contain CP violation that is confined to a dark sector. In the minimal model that allows this possibility, we find that the CP violation is in principle observable through loop-induced anomalous triple gauge couplings. However, the CP-violating form factor and the resulting asymmetries are strongly suppressed, making them challenging to observe even for maximally CP-violating scenarios. In many beyond the SM (BSM) models with extended scalar sectors — for example in this dark sector model — the scalar potential is so complicated that its vacuum structure can only be studied numerically. We present a novel approach to vacuum stability constraints that aims at an efficient and reliable evaluation for use in large parameter scans of BSM models. We study the vacuum structure of the next-to 2HDM (N2HDM) — an extension of the 2HDM by a real scalar singlet. We show analytically that — in contrast to the 2HDM — the electroweak vacuum of the N2HDM is not necessarily stable against charge- or CP-breaking vacua. Using our numerical approach, we study the phenomenological consequences of the intricate N2HDM vacuum structure and find a direct constraint from vacuum stability on the predictions for the decay of h_{125} into two photons. We finally derive vacuum stability constraints on benchmark scenarios in the minimal supersymmetric extension of the SM. We validate our approach against results in the literature and find good agreement. In particular, we show that the better numerical stability of our approach can lead to more reliable results in a fraction of the runtime of alternative methods. The phenomenological studies carried out in this thesis aim to contribute to a better understanding of electroweak symmetry breaking and facilitate the exploration of models with extended scalar sectors using future experimental results.

Zusammenfassung

In dieser Arbeit werden unterschiedliche Szenarien für die elektroschwache Symmetriebrechung untersucht. Dazu werden Modelle betrachtet, in denen der Skalarsektor des Standardmodells (SM) um zusätzliche Felder erweitert wird. In einer Erweiterung des SM um skalare Singletfelder wird die resonante Produktion von mehreren Skalaren analysiert. Die daraus resultierenden Beispielszenarien veranschaulichen viele bisher ungeprüfte Signaturen mit Higgs-nach-Higgs-Zerfällen, die zur Entdeckung zusätzlicher Skalare beitragen könnten. Obwohl viele Eigenschaften des 125 GeV Higgs-Bosons (h_{125}) bereits präzise gemessen sind, könnte es sich bei h_{125} dennoch um einen CP-Mischzustand mit erheblicher Beimischung einer pseudoskalaren Komponente handeln. Im Kontext des CP-verletzenden zwei Higgs Doublet Modells (2HDM) wird diese Möglichkeit sowie die Auswirkungen von Obergrenzen an elektrische Dipolmomente von Fermionen diskutiert. Die Yukawa-Kopplungen von h_{125} können im 2HDM maximal CP-verletzend sein, ohne dass sich Widersprüche zu aktuellen Messungen zeigen. Der Higgs-Sektor könnte auch CP-Verletzung enthalten, die auf einen dunklen Sektor beschränkt ist. In dem minimalen Modell, das dieses Szenario ermöglicht, kann die CP-Verletzung prinzipiell durch anomale Triple-Eich-Kopplungen beobachtet werden. Der CP-verletzende Formfaktor dieser Kopplungen sowie die daraus resultierenden Asymmetrien sind jedoch selbst bei maximaler CP-Verletzung so klein, dass es schwierig sein wird, CP-verletzende Effekte zu beobachten. In diesem und vielen anderen Modellen ist der Skalarsektor so kompliziert, dass dessen Vakuumstruktur nur numerisch untersucht werden kann. Mit einem neuartigen Ansatz können Einschränkungen aus der Vakuumstabilität auf effiziente und zuverlässige Weise bestimmt werden, sodass sie auch für den Einsatz in großen Parameterscans von BSM-Modellen zur Verfügung stehen. Diese Methode wird, in Kombination mit einer analytischen Untersuchung, auf das N2HDM angewandt, in welchem das 2HDM um ein reelles Singletfeld erweitert wird. Im Gegensatz zum 2HDM gibt es im N2HDM Parameterbereiche, in denen das elektroschwache Vakuum instabil gegenüber Ladungs- oder CP-brechenden Minima ist. Bei der Untersuchung der vollständigen Vakuumstruktur des N2HDM mit unserer numerischen Methode ergeben sich direkte Einschränkungen aus der Vakuumstabilität an die Modellvorhersage für die Zerfallsrate des h_{125} in zwei Photonen. Schließlich werden Einschränkungen aus der Vakuumstabilität in einigen Beispielszenarien der minimalen supersymmetrischen Erweiterung des SM bestimmt und für einen Vergleich unserer Methode zu Ergebnissen in der Literatur genutzt. Dabei zeigt sich eine gute Übereinstimmung und, dass die bessere numerische Stabilität unseres Ansatzes zu verlässlicheren Ergebnissen bei deutlich reduzierter Laufzeit führen kann. Die phänomenologischen Studien, die in dieser Arbeit durchgeführt werden, haben das Ziel, zu einem besseren Verständnis der elektroschwachen Symmetriebrechung beizutragen und die Erforschung von Modellen mit erweiterten Skalarsektoren mithilfe kommender experimenteller Resultate zu erleichtern.

List of Publications

This thesis is based on the following publications:

[1] D. Fontes, M. Mühlleitner, J. C. Romão, R. Santos, J. P. Silva and J. Wittbrodt, 'The C2HDM revisited', JHEP **02** (2018) 073, 1711.09419

[2] D. Azevedo, P. M. Ferreira, M. M. Mühlleitner, S. Patel, R. Santos and J. Wittbrodt, 'CP in the dark', JHEP **11** (2018) 091, 1807.10322

[3] W. G. Hollik, G. Weiglein and J. Wittbrodt, 'Impact of Vacuum Stability Constraints on the Phenomenology of Supersymmetric Models', JHEP **03** (2019) 109, 1812.04644

[4] P. M. Ferreira, R. Santos, M. Mühlleitner, G. Weiglein and J. Wittbrodt, 'Vacuum Instabilities in the N2HDM', (2019), 1905.10234

[5] T. Robens, T. Stefaniak and J. Wittbrodt, 'Two-real-scalar-singlet extension of the SM: LHC phenomenology and benchmark scenarios', (2019), 1908.08554

The following additional publications were completed during the time of the thesis, but will not be discussed in detail in this manuscript:

[6] P. Basler, M. Krause, M. Mühlleitner, J. Wittbrodt and A. Wlotzka, 'Strong First Order Electroweak Phase Transition in the CP-Conserving 2HDM Revisited', JHEP **02** (2017) 121, 1612.04086

[7] M. Mühlleitner, M. O. P. Sampaio, R. Santos and J. Wittbrodt, 'The N2HDM under Theoretical and Experimental Scrutiny', JHEP **03** (2017) 094, 1612.01309

[8] P. Basler, M. Mühlleitner and J. Wittbrodt, 'The CP-Violating 2HDM in Light of a Strong First Order Electroweak Phase Transition and Implications for Higgs Pair Production', JHEP **03** (2018) 061, 1711.04097

[9] M. Mühlleitner, M. O. P. Sampaio, R. Santos and J. Wittbrodt, 'Phenomenological Comparison of Models with Extended Higgs Sectors', JHEP **08** (2017) 132, 1703.07750

[10] P. M. Ferreira, S. Liebler and J. Wittbrodt, '$pp \to A \to Zh$ and the wrong-sign limit of the two-Higgs-doublet model', Phys. Rev. **D97** (2018) 055008, 1711.00024

[11] I. Engeln, M. Mühlleitner and J. Wittbrodt, 'N2HDECAY: Higgs Boson Decays in the Different Phases of the N2HDM', Comput. Phys. Commun. **234** (2018) 256, 1805.00966

[12] D. Azevedo, P. M. Ferreira, M. M. Mühlleitner, R. Santos and J. Wittbrodt, 'Models with Extended Higgs Sectors at Future e^+e^- Colliders', Phys. Rev. **D99** (2019) 055013, 1808.00755

Some of the results of this thesis contributed to the following CERN report:

[13] J. de Blas et al., 'The CLIC Potential for New Physics', (2018), 1812.02093

List of Acronyms

2HDM	two-Higgs-doublet model
BR	branching ratio
BSM	beyond the SM
C2HDM	CP-violating 2HDM
CCB	charge or colour breaking
CMB	cosmic microwave background
DM	dark matter
EDM	electric dipole moment
EFT	effective field theory
EW	electroweak
EWSB	electroweak symmetry breaking
FCNC	flavour changing neutral current
ggF	gluon fusion
h_{125}	the 125 GeV Higgs boson
h_{SM}	SM-like Higgs boson
IDM	inert-doublet model
LHC	Large Hadron Collider
MDM	most dangerous minimum
MFV	minimal flavour violation
MSSM	minimal supersymmetric extension of the SM
N2HDM	next-to 2HDM
NFC	natural flavour conservation
NMSSM	next-to-minimal supersymmetric extension of the SM
NP	new physics
PHC	polynomial homotopy continuation
QCD	quantum chromodynamics
QED	quantum electrodynamics
QFT	quantum field theory
R2HDM	real (CP-conserving) 2HDM
RGE	renormalisation group equation
SM	Standard Model of particle physics
STXS	simplified template cross sections
SUSY	supersymmetry
TRSM	two-real-singlet model
vev	vacuum expectation value
WIMP	weakly interacting massive particle

Contents

1 Introduction

In 2012 the ATLAS and CMS collaborations at the Large Hadron Collider (LHC) discovered a new scalar boson with a mass of about 125 GeV [14, 15]. The existence of a scalar Higgs boson had been predicted almost 50 years before [16–18], and it was certain that the LHC would either discover a Higgs boson or observe substantial deviations from the Standard Model (SM). Within the current uncertainties, the properties of the discovered particle were found to be in good agreement with the Higgs boson predicted in the SM [19]. At the same time, the properties of the observed Higgs boson also fit the predictions of many alternative theories of electroweak symmetry breaking (EWSB).

While it is well known that the SM is not a complete theory of nature — as it does not include gravitational interactions and cannot account for most of the energy density of the universe — there is no prediction for the energy scale at which these issues have to be addressed. Alternative models of EWSB, however, typically feature new particles with masses around the electroweak (EW) scale in reach of current experiments. Searching for these beyond the SM (BSM) particles is one facet of distinguishing different models of EWSB. The phenomenological exploration of the signatures such BSM theories could produce provides crucial input to the experimental search for new physics (NP).

The dynamics of EWSB can also be probed experimentally by studying the 125 GeV Higgs boson (h_{125}). Through the Brout-Englert-Higgs mechanism [16–18] all fermions and gauge bosons acquire masses and related couplings to the Higgs boson when the Higgs vacuum expectation value (vev) spontaneously breaks the EW symmetry. Precision measurements of these couplings are essential to test whether EWSB proceeds as predicted in the SM. Observing deviations from the SM expectations would be a clear indication of NP and might hint that there is not a single Higgs boson, but an extended Higgs sector with multiple scalars.

Even within the constrained framework of renormalisable and gauge-invariant quantum field theory (QFT), there is an infinite number of possible BSM models. In the past, theoretically appealing theories such as supersymmetry (SUSY) have been a focus of phenomenological studies. In the absence of any experimental results pointing to such a specific model, it is useful to explore BSM models that cover a wide range of possible experimental signatures. Phenomenological studies of the new particles or modified couplings predicted in these models can initiate experimental investigations. The experimental results, together with theoretical consistency constraints on the model parameter space, can then be used to judge whether such a model is a viable theory of EWSB.

In this work, we focus on the broad category of BSM models with extended scalar sectors. These models add scalar particles to the SM that may mix and interact with the SM Higgs boson. As a result, they both modify the predicted couplings of h_{125} and allow direct searches for the additional neutral and potentially charged scalars predicted by the model.

Additional scalar fields also modify the scalar potential that governs EWSB. This may lead to scenarios where the scalar potential has multiple local minima in addition to the EW minimum that results in the correct EWSB. If the EW vacuum is not the global minimum of the scalar potential, the universe could obtain an energetically favourable state through vacuum decay [20, 21]. While not inconsistent from a theoretical point of view, such a decay would lead to a vacuum bubble that expands through the universe. The requirement that a theory does not predict a lifetime of the EW vacuum shorter than the age of the universe can provide an important constraint — especially on models with large BSM scalar sectors.

Directly probing the structure of the scalar sector is possible by measuring couplings between multiple scalars. In the SM, the Higgs self couplings are so small that they are challenging to observe even at the high luminosity LHC [22]. BSM models can feature considerably larger couplings that may be probed more easily. Of particular interest are processes of resonant multiscalar production, where a resonantly produced heavy scalar decays into two or more lighter scalars. Observing these processes could provide substantial insight into the structure of the scalar sector. These processes are also the most promising discovery channels for additional scalars that dominantly decay into other scalars.

Extended scalar sectors may also introduce new sources of CP violation to the theory. If the parameters of the scalar potential or the vacuum state lead to a mixing of CP-eigenstates with different CP-quantum numbers, the resulting scalar mass eigenstates will have CP-violating interactions. While it is known that h_{125} is not a pure CP-odd state [23, 24], it could be a CP-mixed state with a substantial CP-odd admixture without violating current constraints. However, models with CP-violating Yukawa couplings face strong constraints from bounds on fermionic electric dipole moments (EDMs). If the CP violation does not enter the Yukawa sector, loop-induced anomalous gauge couplings may reveal the CP-nature of the Higgs sector.

Supersymmetric theories are far more elaborate than pure extensions of the SM Higgs sector. However, they share numerous features with the simpler models as they also add many scalar fields to the SM. It is particularly interesting to study vacuum decay in supersymmetric theories. Due to the many degrees of freedom in the scalar sector, the constraints from vacuum stability can become extremely important in some regions of parameter space. These constraints can be complementary to experimental results in probing supersymmetric models.

Structure of this Thesis

In the remainder of this chapter, we introduce the SM of particle physics and discuss some of the open questions that cannot be addressed within the SM.

In chapter 2, we present the guiding principles in constructing BSM models with extended scalar sectors and discuss theoretical and experimental constraints applied to the models considered in this work. At the end of chapter 2, we introduce the basic features of the two-Higgs-doublet model (2HDM) and the minimal supersymmetric extension of the SM (MSSM) — two BSM models that we will refer to throughout this work.

Chapter 3 describes our numerical approach to vacuum stability in models with extended scalar sectors based on our ref. [3]. We discuss how to calculate the lifetime of the EW vacuum in models with complicated scalar sectors, and obtain vacuum stability constraints with the efficiency and stability required for BSM parameter scans. We also discuss unbounded scalar potentials, which form a special case among the scalar potentials with unstable EW vacua.

Chapter 4 presents phenomenological results in the two-real-singlet model (TRSM) that we obtained in ref. [5]. We discuss current constraints on the model from measurements of h_{125} and searches for additional Higgs bosons and present benchmark scenarios for resonant multiscalar production that feature signatures that are not currently investigated at the LHC.

CP violation in the Higgs sector is the topic of chapter 5, which contains results from our refs. [2, 25]. We first discuss the phenomenology of a CP-mixed h_{125} in the CP-violating 2HDM (C2HDM). We show that h_{125} can have maximally CP-violating Yukawa couplings to some fermions and discuss the impact of EDM constraints on this conclusion. The second part of chapter 5 introduces a model with a minimal CP-violating dark sector where the CP violation can only be probed through anomalous gauge couplings.

In chapter 6, we study the vacuum structure of the next-to 2HDM (N2HDM), an extension of the SM by both a second Higgs doublet and a real scalar singlet. Based on our ref. [4], we systematically categorise the different phases of the models and establish analytical relations between the depths of different kinds of vacua. In particular, we show that an EW vacuum in the N2HDM is not necessarily safe against vacuum decay into deeper CP or charge breaking minima. We illustrate the phenomenological relevance of this analysis by using our approach of chapter 3 to study the vacuum structure of a large sample of phenomenologically viable parameter points.

Chapter 7 contains a detailed application of our vacuum stability results from chapter 3 to the MSSM. We have published this discussion in ref. [3]. We obtain vacuum stability constraints on recently proposed MSSM benchmark scenarios for Higgs physics [26], and use these results to validate our approach against existing results and methods in the literature.

We conclude in chapter 8.

1.1 The Standard Model of Particle Physics

The SM of particle physics is a quantum field theoretical description of the elementary particles observed in nature, and their interactions mediated by the electroweak force [27–31] and strong force [32–36]. Gravitational interactions are not included in the SM. In the following, we give a short overview of the SM that is loosely based on refs. [37–39].

The SM is the most general renormalisable QFT with a field content corresponding to the observed particles that is invariant under the gauge symmetry

$$\mathrm{SU}(3)_c \otimes \mathrm{SU}(2)_L \otimes \mathrm{U}(1)_Y \,. \tag{1.1}$$

$\mathrm{SU}(3)_c$ is the gauge group of quantum chromodynamics (QCD) operating on fields with colour charge, while $\mathrm{SU}(2)_L \otimes \mathrm{U}(1)_Y$ is the EW gauge group operating on left chiral fields and fields carrying hypercharge (Y).[1] The field content of the SM consists of fermions (spin 1/2), gauge bosons (spin 1), and a scalar boson (spin 0). There is one gauge field corresponding to each of the above gauge symmetries: the gluon field G^a_μ of QCD, the $\mathrm{SU}(2)_L$ gauge field W^a_μ and the $\mathrm{U}(1)_Y$ gauge field B_μ, where a is the index of the gauge representation. The SM includes two categories of fermion fields: the quark fields, which are triplets under $\mathrm{SU}(3)_c$, and leptons, which carry no colour charge. All of the SM fermions are Dirac fermions with two chiralities, left- and right-handed. The left-handed fields are doublets under $\mathrm{SU}(2)_L$, and the right-handed fields are singlets. The SM treats neutrinos — which are known to be massive — as massless particles and does not introduce right-handed neutrinos. However, the neutrino masses are constrained to be so small that treating them as massless particles is sufficient for our purposes. Table 1.1 shows this structure of the fermionic fields. Finally, fermions come in three generations with identical quantum numbers but different masses.

1.1.1 Kinetic Terms and Gauge Invariance

In a generic QFT, the kinetic terms of a fermion ψ, a gauge boson A^a_μ, and a scalar ϕ are determined by Poincaré symmetry to be

$$\mathcal{L}_{\text{kin}} = \psi i \not{\partial} \bar{\psi} - \frac{1}{4} F^a_{\mu\nu} F^{a\,\mu\nu} + (\partial_\mu \phi)^\dagger (\partial^\mu \phi) \,, \tag{1.2}$$

where $\bar{\psi} = \psi^\dagger \gamma^0$ and $\not{\partial} = \gamma_\mu \partial^\mu$. The field strength tensor $F^a_{\mu\nu}$ for a gauge field is given by

$$F^a_{\mu\nu} = \partial_\mu A^a_\nu - \partial_\nu A^a_\mu + g f^{abc} A^b_\mu A^c_\nu \,, \tag{1.3}$$

where g is the gauge coupling, and f^{abc} are the structure constants of the corresponding gauge group. In order for the eq. (1.2) to be invariant under a gauge symmetry is has to

[1] There are different conventions for the hypercharge. We use the convention where the electric charge is $Q = I_3 + Y$, where I_3 is the third component of the $\mathrm{SU}(2)_L$ isospin. The value of Y is then the average electric charge of an $\mathrm{SU}(2)_L$ multiplet.

Table 1.1: One generation of chiral fermions in the SM.

	quarks			leptons	
$\mathrm{SU}(2)_L$	$Q_L = \begin{pmatrix} u_L \\ d_L \end{pmatrix}$	u_R	d_R	$L_L = \begin{pmatrix} \nu_L \\ e_L \end{pmatrix}$	e_R
colour	triplet	triplet	triplet	singlet	singlet
Y	$1/6$	$2/3$	$-1/3$	$-1/2$	-1

respect the corresponding gauge transformations. In infinitesimal form these are given by

$$\psi \to \left(1 + \sum i\,\alpha^a t^a\right)\psi\,, \tag{1.4}$$

$$A^a_\mu \to A^a_\mu + \frac{1}{g}\partial_\mu \alpha^a + f^{abc} A^b_\mu \alpha^c\,, \tag{1.5}$$

$$\phi \to \left(1 + \sum i\,\alpha^a t^a\right)\phi\,, \tag{1.6}$$

where the sum runs over the different gauge groups and their generators t^a and structure constants f^{abc} carry indices of the gauge representation. The transformations are parametrised by α which in general depends on the spacetime. In the special case where $\partial^\mu \alpha = 0$ the corresponding transformations are called *global*. To restore gauge invariance with respect to the SM gauge groups the derivatives ∂_μ in the fermionic and scalar kinetic terms need to be replaced by covariant derivatives

$$D_\mu \coloneqq \partial_\mu - i\,g_s \frac{\lambda_a}{2} G^a_\mu - i\,g_2 \frac{\sigma^a}{2} W^a_\mu - i\,g_1 \frac{Y}{2} B_\mu\,. \tag{1.7}$$

The g_s, g_2, and g_1 are the coupling constants, and G^a_μ, W^a_μ, and B_μ are the corresponding gauge fields. The generators of the gauge groups are expressed through the Gell-Mann matrices λ_a, the Pauli matrices σ_a, and the hypercharge Y. In the SM eq. (1.2) therefore becomes

$$\mathcal{L}_{\text{kin}} = \sum_{\text{fermions}} \psi i \not{D} \bar{\psi} - \frac{1}{4}\left(G^a_{\mu\nu} G^{a\mu\nu} + W^a_{\mu\nu} W^{a\mu\nu} + B_{\mu\nu} B^{\mu\nu}\right) + (D_\mu \Phi)^\dagger (D^\mu \Phi)\,, \tag{1.8}$$

While all kinetic terms are gauge invariant by the use of covariant derivatives, the same is not possible for all the mass terms we might want to write, *e.g.*

$$\mathcal{L}_{\text{mass}} \supset \begin{cases} -m\psi\bar{\psi}\,, & \text{for a fermion } \psi \\ +m^2 A_\mu A^\mu\,, & \text{for a gauge boson } A_\mu \\ -m^2|\phi|^2\,, & \text{for a scalar boson } \phi\,. \end{cases} \tag{1.9}$$

The fermion and gauge boson mass terms are forbidden by the gauge symmetry of the standard model, only the scalar mass term is allowed. Therefore, all fermions and gauge bosons of the SM would be massless (up to quantum effects) which is in clear contradiction to observations.

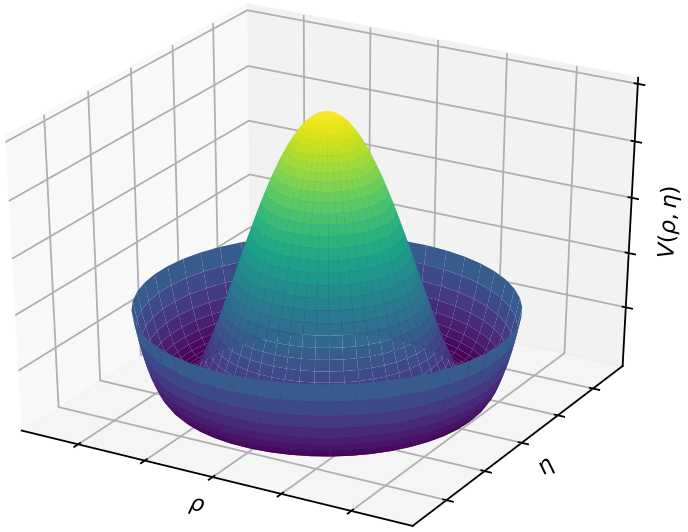

Figure 1.1: A sketch of the scalar potential of the SM, eq. (1.14), as a function of the neutral components ρ and η of the Higgs field. The potential rises monotonically for larger values of $\rho^2 + \eta^2$.

1.1.2 The BEH Mechanism and Electroweak Symmetry Breaking

The BEH mechanism [16–18] solves this issue through spontaneous EWSB. In the SM, a single scalar field

$$\Phi = \begin{pmatrix} \phi^+ \\ \frac{1}{\sqrt{2}}(\rho + i\,\eta) \end{pmatrix} \tag{1.10}$$

that is a colour singlet, $\mathrm{SU}(2)_L$-doublet with $Y = 1/2$ is introduced into the Lagrangian

$$\mathcal{L}_{\text{Higgs}} = (D^\mu \Phi)^\dagger (D_\mu \Phi) - V(\Phi) + \mathcal{L}_{\text{Yukawa}}\,. \tag{1.11}$$

The numerical prefactors in eq. (1.10) are chosen such that both the charged field ϕ^+ and the neutral fields ρ and η have *canonically normalised* kinetic terms. For a real scalar field ρ this convention requires the kinetic and mass terms to have the form

$$\mathcal{L} \supset \frac{1}{2}(\partial^\mu \rho)(\partial_\mu \rho) - \frac{1}{2} m^2 \rho^2\,. \tag{1.12}$$

Complex scalar fields — such as ϕ^+ — are conventionally written as

$$\phi^+ \to \frac{\mathrm{Re}(\phi^+) + i\,\mathrm{Im}(\phi^+)}{\sqrt{2}} \tag{1.13}$$

and their real and imaginary parts are normalised according to eq. (1.12).

For the SM case of a single Higgs doublet Φ, the most general gauge-invariant scalar potential $V(\Phi)$ in a renormalisable QFT is

$$V(\Phi) = -\mu^2 \Phi^\dagger \Phi + \lambda (\Phi^\dagger \Phi)^2 \,. \tag{1.14}$$

If $\mu^2, \lambda > 0$ this potential has a minimum not at the origin but for a finite value of the Higgs field Φ. In fig. 1.1 the shape of the potential is shown as a function of the neutral components of the Higgs field. In the vacuum state, Φ will take the energetically favourable value in this minimum and thus acquire a vev

$$\langle \Phi \rangle = \frac{1}{\sqrt{2}} \begin{pmatrix} 0 \\ v \end{pmatrix} \,, \tag{1.15}$$

with

$$|v|^2 = \frac{\mu^2}{2\lambda} \,. \tag{1.16}$$

The vev v is a classical background field with a globally uniform value. Choosing this vev to lie in the real, neutral component of Φ *spontaneously breaks* EW symmetry by selecting one specific point out of an orbit of physically equivalent vacua related by global transformations under the SM gauge groups. We expand the Higgs field around the vev as

$$\Phi = \begin{pmatrix} \phi^+ \\ \frac{1}{\sqrt{2}} (v + \rho + i\eta) \end{pmatrix} \,. \tag{1.17}$$

Since we can, without loss of generality, choose the vev to lie in the neutral component, the residual $U(1)_{\mathrm{EM}}$ symmetry of quantum electrodynamics (QED) is left intact.

If the EW symmetries were purely global, the theory would — according to the Goldstone theorem [40–42] — contain three massless Nambu-Goldstone bosons after the expansion of eq. (1.17). However, since the symmetries are gauged, the would-be Nambu-Goldstone bosons are related to the EW gauge bosons. In particular, the remaining freedom to perform local $\mathrm{SU}(2)_L \otimes \mathrm{U}(1)_Y$ transformations can be used to transform these bosons into longitudinal components of the gauge fields, thus giving masses to the gauge bosons. This gauge is called the unitary gauge and results in bosonic mass terms of the form

$$\mathcal{L}_{\mathrm{bosons}} \supset \frac{v^2}{8} \left[g_2^2 (W_\mu^1)^2 + g_2^2 (W_\mu^2)^2 + (g_1 B_\mu - g_2 W_\mu^3)^2 \right] - \lambda v^2 \rho^2 \,. \tag{1.18}$$

After mass diagonalisation this yields the physical gauge bosons

$$W_\mu^\pm = \frac{W_\mu^1 \mp W_\mu^2}{\sqrt{2}} \,, \tag{1.19}$$

$$Z_\mu = \frac{g_2 W_\mu^3 - g_1 B_\mu}{\sqrt{g_1^2 + g_2^2}} = \cos\theta_{\mathrm{W}} W_\mu^3 - \sin\theta_{\mathrm{W}} B_\mu \,, \tag{1.20}$$

$$A_\mu = \frac{g_1 W_\mu^3 + g_2 B_\mu}{\sqrt{g_1^2 + g_2^2}} = \sin\theta_{\mathrm{W}} W_\mu^3 + \cos\theta_{\mathrm{W}} B_\mu \,, \tag{1.21}$$

with the weak mixing angle θ_{W} defined through

$$\cos\theta_{\mathrm{W}} = \frac{g_2}{\sqrt{g_1^2 + g_2^2}}\,. \tag{1.22}$$

The corresponding masses are

$$m_W = g_2\frac{v}{2}\,, \quad m_Z = \sqrt{g_1^2 + g_2^2}\frac{v}{2}\,, \tag{1.23}$$

the photon field A^μ is massless, and the Higgs boson $h = \rho$ has a mass of

$$m_h = \sqrt{2\lambda v^2} = \sqrt{2\mu^2}\,. \tag{1.24}$$

The mass of the $W^\pm$ can also be expressed through the Fermi constant, which is the effective interaction strength of the weak interaction in the low energy Fermi theory. They are related at lowest order as $m_W^2 = \sqrt{2}g_2^2/8G_F$ leading to

$$v = \left(\sqrt{2}G_F\right)^{-\frac{1}{2}} \approx 246\,\mathrm{GeV}\,. \tag{1.25}$$

The Higgs mass m_h is a free parameter of the SM. The parameters of the scalar potential, λ and μ, can be expressed through v and m_h via eqs. (1.16) and (1.24).

The fermions interact with the Higgs field through the Yukawa couplings. In unitary gauge, these are given by

$$\mathcal{L}_{\mathrm{Yukawa}} = -\sum_{\mathrm{f}} y_f \psi_L^f \bar{\psi}_R^f \frac{v+h}{\sqrt{2}} \tag{1.26}$$

and yield fermion masses of

$$m_f = \frac{v}{\sqrt{2}} y_f\,, \tag{1.27}$$

where y_f is the corresponding Yukawa coupling. Note that in the SM the Yukawa couplings (which are in general a matrix) are diagonalised simultaneously with the fermion masses. Therefore, there are no tree-level flavour changing neutral currents in the SM. Starting from a manifestly gauge invariant Lagrangian, eq. (1.11), the BEH mechanism thus generated the required mass terms of the form eq. (1.9) for all the massive particles of the SM.

Since it is the combination $v + h$ that leads to the gauge boson and fermion mass terms of the SM the couplings of the Higgs boson h to fermions and gauge bosons are directly linked to their masses. The Feynman rules for these vertices are

$$g_{hff} = -i\frac{m_f}{v}\,, \quad g_{hVV} = 2i\frac{M_V^2}{v}\,, \quad g_{hhVV} = \frac{g_{hVV}}{v}\,. \tag{1.28}$$

The scalar potential eq. (1.14) additionally leads to triple and quartic Higgs self-couplings with Feynman rules

$$g_{hhh} = -3i\frac{m_h^2}{v}\,, \quad g_{hhhh} = \frac{g_{hhh}}{v}\,. \tag{1.29}$$

1.2 Open Questions in the SM

While the SM agrees very well with a large number of experimental observations, there are many indications that there must be physics beyond the SM. We have already mentioned neutrino masses and gravity that are not part of the SM. In this section, we will give short overviews of some of the open questions of particle physics that cannot be addressed within the SM.

1.2.1 Dark Matter

The existence of a gravitationally interacting but invisible kind of matter — called dark matter (DM) — was first postulated by Zwicky [43, 44]. Astrophysical evidence for DM has since been established *e.g.* in rotation curves of galaxies [45, 46], galaxy cluster mergers [47], and through precision measurements of the cosmic microwave background (CMB) [48]. The following short overview of the subject is based on refs. [39, 49].

The most recent CMB measurements by the Planck collaboration [48] obtain a dark matter density Ω_c normalised to the total energy density of the universe of

$$\Omega_c h^2 = 0.120 \pm 0.001\,, \tag{1.30}$$

where h is the reduced Hubble parameter. Within current constraints, DM is allowed to interact with SM particles with couplings comparable to the weak interaction. This makes the inclusion of DM candidates an interesting extension of the SM.[2] Any particle that is electrically neutral, a singlet of $\mathrm{SU}(3)_c$, and stable on cosmological time scales is a candidate for DM. In this work, we consider only weakly interacting massive particle (WIMP) dark matter candidates will. These have masses around the EW scale and interact with the SM with comparable strength to the weak interaction. WIMPs can be produced in the early universe as thermal relics, and their density is naturally rather close to the observed DM density — this coincidence is called the WIMP-miracle.

There are ongoing experimental efforts in the search for DM particles. Most of the WIMP searches rely on scattering processes between two DM particles χ and two SM particles s through a vertex

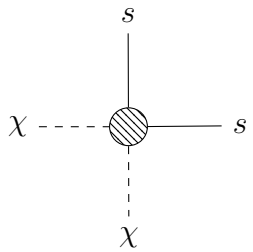

(1.31)

[2] There are also non-particle DM candidates such as primordial black holes.

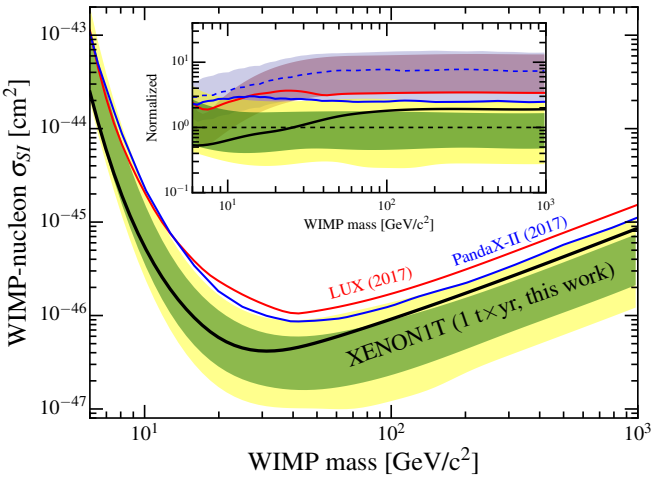

Figure 1.2: Bound on the spin-independent dark matter nucleon scattering cross section at 90 % confidence level as a function of the DM mass. Result by the XENON1T experiment from [50]. The blue and red curves indicate previous bounds by different experiments and the inset shows a normalisation of the plot the expected XENON1T limit.

where the content of the blob depends on the specific dark matter model. The annihilation of two χ into two s can be looked for in cosmic rays and is called indirect detection. Pair production of dark matter particles can be studied at colliders through searches for initial state radiation plus missing energy — called mono-X searches, where $\mathrm{X} \in \{j, h, \gamma, \ldots\}$ depending on the radiated particle. The third possibility — scattering a dark matter particle off a SM particle — is called direct detection. Direct detection experiments typically look for scattering of DM against heavy nucleons, where Xenon is currently the most prominent scattering medium for WIMPs.

Direct detection experiments currently provide the strongest bounds for WIMPs. These constraints are also straightforward to apply as they put a bound on the DM nucleon scattering cross section which can be calculated in many models using public tools like `MicrOMEGAs` [51–57]. The currently strongest direct detection bound by the XENON1T experiment on the spin-independent scattering cross section is shown in fig. 1.2.

1.2.2 Baryogenesis

The matter-antimatter asymmetry in the universe can be estimated from the baryon to photon ratio η by assuming that all CMB photons are the result of thermal annihilations of baryons

$$\left.\frac{N_b - N_{\bar{b}}}{N_b + N_{\bar{b}}}\right|_{T \gtrsim 1\,\mathrm{GeV}} \approx \eta = \left.\frac{N_b}{N_\gamma}\right|_{\text{today}} \sim 6 \times 10^{-10}\,. \tag{1.32}$$

The numerical value is obtained from CMB measurements [48]. Without a theory of baryogenesis that leads to a matter-antimatter asymmetry, no matter is expected to remain after thermal annihilations.

Explaining this ratio requires a theory of baryogenesis in which the three Sakharov criteria [58] — baryon number violation, C and CP violation, and departure from thermal equilibrium — are fulfilled in the early universe. Two classes of baryogenesis have been studied in detail. In leptogenesis [59, 60], the baryon asymmetry is generated through CP-violating scattering processes involving heavy neutrinos. In electroweak baryogenesis [61–64], the baryon asymmetry is generated during a strong first-order EW phase transition. Leptogenesis can be realised at a high scale with little observable consequences. However, electroweak baryogenesis requires new physics at the EW scale, making it an interesting possibility to consider when studying BSM models with extended Higgs sectors.

In the SM, a first-order EW phase transition would require $m_h \lesssim 60\,\text{GeV}$ [65, 66] which does not match the observed mass of h_{125}. However, in models with extended Higgs sectors a strong first-order EW phase transition can be realised (see *e.g.* refs. [6, 8, 67–69] for applications to the two-Higgs-doublet model). Such a phase transition will progress through an expanding vacuum bubble which is out of thermal equilibrium and satisfies the third Sakharov criterion. During the phase transition, baryon number violating EW sphaleron processes [70, 71] will occur and satisfy the first Sakharov criterion. If the BSM model also introduces new sources of CP violation — to satisfy the second criterion — this can generate a baryon asymmetry of the required size [72, 73].

1.2.3 Vacuum Stability in the SM

At tree-level, the scalar potential of the SM, eq. (1.14), has exactly one minimum — up to physically equivalent minima related by gauge transformations. However, when extrapolating the model to high scales this behaviour can change as a consequence of the running of the quartic Higgs coupling λ [74–92]. Based on current theoretical predictions and the experimental inputs of the top-quark mass, Higgs boson mass, and the strong coupling constant the EW vacuum of the SM is no longer the global minimum of the scalar potential for energy scales $\gtrsim 10^{10}\,\text{GeV}$.

If the EW vacuum is not the global minimum of the scalar potential, the vacuum may decay through a tunnelling process into a minimum where the Higgs vev takes an energetically favourable value. The lifetime of such a tunnelling process was first calculated in [20, 21] with the most recent calculations for the SM finding lifetimes around $\sim 10^{139}\,\text{yr}$ [90].

This lifetime is enormous compared to the age of the universe. The EW vacuum of the SM is thus metastable at these energy scales — it is not the global minimum, but with a lifetime large enough to be viable. This result is very sensitive to parametric uncertainties from the top-quark mass, the Higgs mass, and the strong coupling constant as shown in fig. 1.3. Within the 3σ bands for these uncertainties, the current observations are still

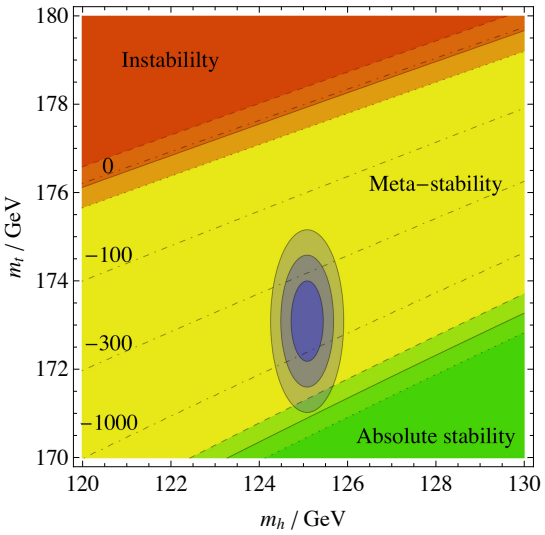

Figure 1.3: Stability of the SM in the plane of the top-quark and Higgs masses, from ref. [92]. The blue ellipses give the 1σ, 2σ, and 3σ regions around the currently measured values. The labelled dashed lines approximately indicate the $\log_{10}$ of the ratio between the lifetime of the EW vacuum and the age of the universe.

compatible with the SM being absolutely stable, *i.e.* the EW vacuum being the global minimum of the scalar potential up to the Planck scale. On the other hand, a short-lived instability of the SM is incompatible with current measurements. Note that this analysis is performed at such high energy scales that threshold corrections from a Planck-scale theory of quantum gravity may impact the result [88, 93].

Vacuum stability is, therefore, not a critical issue of the SM. From an observational point of view, metastability is perfectly acceptable. However, these conclusions only hold if there is no NP at all below the Planck scale. In BSM theories that introduce NP at lower scales, the vacuum stability behaviour may be completely different.

2 Constraints on Models with Extended Higgs Sectors

This chapter first reviews the guiding principles used to extend the SM scalar sector. Subsequently, we present and discuss the constraints from theoretical consistency and experimental observations that we impose on the resulting models of physics BSM. We also aim to provide some simple understanding regarding the expected impact of the individual constraints. This chapter is inspired by refs. [38, 94].

2.1 Guiding Principles in Extending the SM

In order to address some of the issues of the SM discussed in section 1.2 or to explore the possible phenomenology at current and future colliders, it is of interest to study BSM models. There is a multitude of possible directions to extend the SM in. Most approaches add additional particle content of some kind to the SM — this may be additional gauge bosons of an enlarged gauge group, fermions, or additional scalars. We focus on the effects of extending the Higgs sector by adding new scalar fields that couple to the Higgs doublet of the SM. In this section, we will present some of the considerations necessary when extending the SM.

Renormalisability

When categorising extensions of the SM, the first distinction is between renormalisable models and effective field theorys (EFTs). In an EFT (*e.g.* the SMEFT [95]) heavy particles are integrated out leading to non-renormalisable higher-dimensional operators of light fields. EFTs are agnostic regarding the details of the additional particles making them a very generic approach to studying extensions of the SM. However, for practical reasons, it is usually necessary to make additional symmetry assumptions (*e.g.* regarding flavour symmetries, see section 2.1) to reduce the number of operators under consideration. The main issue with EFTs is their limited range of validity. The EFT is only a valid description of the underlying theory if the scale of the new particles — set by the ratio of their masses and couplings — is sufficiently large compared to the energy at which the theory is probed.

Phenomenological studies of new particles with masses around the electroweak (EW) scale at present colliders require a renormalisable model of these new particles. Such a model is constructed by adding renormalisable terms involving the new fields to the Lagrangian.[1] Renormalisable terms are those that do not involve prefactors of negative mass dimensions — or equivalently have operators of mass dimension no higher than four.

For the theory to be renormalisable, all terms that respect the imposed symmetries must be added to the Lagrangian. Otherwise, higher-order corrections will induce the corresponding operators and eventually lead to divergencies. If these operators are not present in the Lagrangian, there are no counterterms to cancel these divergencies rendering the theory non-renormalisable. Soft breaking terms may be added up to some fixed operator mass dimension $d \leq 3$ without spoiling renormalisability [96].

Gauge Invariance

The gauge structure of the SM is well established and any BSM model should have a gauge structure that is equivalent to the SM or larger (*i.e.* contains the SM gauge groups as subgroups, *e.g.* in grand unified theories [97–99]). For pure extensions of the Higgs sector — without additional gauge symmetries — all additional scalars need to be grouped into complete representations of $\mathrm{SU}(3)_c \otimes \mathrm{SU}(2)_L \otimes \mathrm{U}(1)_Y$, and the whole Lagrangian has to be invariant under the gauge transformations eqs. (1.4) to (1.6). This constrains the interactions of scalars to gauge bosons to originate entirely from the covariant derivatives of the scalar kinetic terms. The doublet nature of the left-handed SM fermions also constrains possible scalar-fermion interactions.

One consequence of gauge invariance is the requirement to reproduce the correct electroweak symmetry breaking (EWSB). This includes both breaking $\mathrm{SU}(2)_L \times \mathrm{U}(1)_Y$ in a way that gives masses to the W and Z bosons and preserving the $U(1)_{\mathrm{EM}}$ symmetry and thus the conservation of electric charge. In particular, only electrically neutral scalar fields may acquire a vacuum expectation value (vev).

The ρ-Parameter and Custodial Symmetry

The ρ-Parameter [100, 101] was originally defined as an observable to measure the relative strength of neutral and charged current processes in neutrino scattering experiments. Its current experimental value is obtained from a fit to EW precision measurements and given by [39]

$$\rho = 1.000\,39 \pm 0.000\,19\,. \tag{2.1}$$

[1] It is possible to extend the SM by both additional field content and higher-dimensional operators. However, this approach has no strong motivation until new particles have been experimentally established.

In the SM its theoretical value at lowest order is

$$\rho = \frac{m_W^2}{m_Z^2 \cos\theta_{\mathrm{W}}} \,. \tag{2.2}$$

Using the relations eqs. (1.22) and (1.23), this is identical to unity. This is the result of the accidental custodial symmetry of the SM. The Higgs potential eq. (1.14) preserves an accidental global $\mathrm{SU}(2)_L \otimes SU(2)_{\mathrm{R}}$ symmetry. The Higgs vev breaks this down to its diagonal subgroup — the $SU(2)_{\mathrm{diag}}$ custodial symmetry. The remainder of the Lagrangian approximately preserves this symmetry. It is broken by the $\mathrm{U}(1)_Y$ gauge interaction and by the difference in Yukawa couplings between up- and down-type quarks. However, one consequence of this symmetry is that in the limit $g_1 \to 0$ the masses of $W^\pm$ and Z would be equal in accordance with eq. (2.2).

When extending the SM the custodial symmetry — being an accidental symmetry — can easily be completely removed. In generic gauge-invariant and renormalisable extensions the ρ-Parameter at tree-level becomes [39]

$$\rho = \frac{\sum \left(t(t+1) - Y^2\right) v^2}{\sum 2Y^2 v^2} \,, \tag{2.3}$$

where the sum runs over all scalar multiplets and their corresponding weak isospin t, hypercharge Y and neutral vev v. Without relying on cancellations between different multiplets the simplest representations where this is equal to unity are

$$(t, Y) = \begin{cases} (\frac{1}{2}, \frac{1}{2}) & \text{doublet, like in the SM,} \\ (3, 2) & \text{septet,} \\ (\frac{25}{2}, \frac{15}{2}) & \text{26-plet.} \end{cases} \tag{2.4}$$

It is also trivially fulfilled for $\mathrm{SU}(2)_L$ singlets with $Y = 0$ which do not contribute to the ρ-Parameter at all. Out of these multiplets that naturally fulfil $\rho = 1$ at lowest order the singlet and doublet extensions are by far the most studied[2] and all of the models treated in this work only add singlets and/or doublets to the SM.

Additional scalars only contribute to the tree-level value of the ρ-Parameter if they acquire a vev. Therefore, arbitrary scalar multiplets can be added to the SM provided they have vanishing vevs. This possibility is mainly interesting in the context of certain dark matter models where additional scalars without a vev are required (see *e.g.* ref. [104]). Additionally, it is possible to add different multiplets provided that their vevs are sufficiently small, and the predicted value of ρ still agrees with the observed one. In particular, it is possible to impose an (approximate or exact) $\mathrm{SU}(2)_L \otimes SU(2)_{\mathrm{R}}$ symmetry on the extended Higgs sector. In this case, the custodial symmetry will remain after EWSB just like in the SM. Georgi-Machacek [105] or left-right-symmetric models [106–108] which include scalar triplets take this approach.

[2] Recently minimal septet extensions have also been subject to phenomenological studies [102, 103].

Higher-order corrections to the ρ-Parameter provide an important constraint on BSM models, even if $\rho = 1$ at tree-level. These will be discussed in section 2.4.1. Finally, the considered multiplets directly relate to the maximal electric charge a scalar can have. Standard doublets can only contain singly charged scalars, triplets contain double charged, and septets with $\rho = 1$ allow charges of up to five.

Flavour Changing Neutral Currents

One prominent feature of the SM is the absence of tree-level flavour changing neutral currents (FCNCs). This is not due to some flavour symmetry of the SM but rather an accidental consequence of $\mathrm{SU}(2)_L \otimes \mathrm{U}(1)_Y$ gauge invariance. Processes mediated by FCNCs are loop-induced processes in the SM, and many of them have been observed at colliders. Due to their loop-induced nature, the rates for these processes are typically tiny and therefore very sensitive to BSM contributions.

Consider a generic BSM model that adds at least a second scalar doublet Φ_2 to the SM. The quark Yukawa Lagrangian becomes

$$-\mathcal{L}_\mathrm{Y} \supset \bar{Q}'_L(X_{d1}\Phi_1 + X_{d2}\Phi_2)d'_R + \bar{Q}'_L(X_{u1}\Phi_1^c + X_{u2}\Phi_2^c)u'_R \tag{2.5}$$

with generic flavour space matrices X. The quark fields denoted with the prime are the gauge eigenstates. After electroweak symmetry breaking this leads to quarks mass matrices ($q \in \{u, d\}$)

$$M_q \propto (v_1 X_{q1} + v_2 X_{q2}) \tag{2.6}$$

which — for general X — cannot be diagonalised simultaneously with the Yukawa interactions. This will lead to FCNC interactions mediated by some of the physical neutral Higgs bosons. The lepton sector can be treated equivalently.

Several approaches have been developed to ensure that such BSM contributions to FCNC observables remain small [109]. In natural flavour conservation (NFC) the absence of FCNCs is ensured by requiring each fermion multiplet to couple to exactly one scalar multiplet. For the Yukawa Lagrangian eq. (2.5) this would correspond to either $X_{q1} = 0$ or $X_{q2} = 0$ for each $q \in \{u, d\}$. In this case, Yukawa interactions and quark masses are simultaneously diagonalised, and tree-level FCNCs are absent. The NFC condition can be easily enforced by imposing discrete or continuous symmetries on the Higgs and Yukawa sectors. The resulting absence of FCNCs in NFC is related to an accidental flavour symmetry in analogy to SM.

The hypothesis of minimal flavour violation (MFV) is a more general framework postulating that the accidental flavour symmetry of the SM is only broken by terms proportional to SM Yukawa couplings. As such, the X matrices of eq. (2.5) are given by

$$X_{q1} = c_{q1} Y_q\,, \quad X_{q2} = c_{q2} Y_q\,, \tag{2.7}$$

where Y_q are the SM Yukawa matrices, and c are numerical prefactors. This can be realised by explicitly imposing an appropriate flavour symmetry.

Table 2.1: Fermionic $\mathbb{Z}_2$ charge assignments (first three columns) and the resulting coupling structure (last two columns) of the four Yukawa types of 2HDM-like models with a $\mathbb{Z}_2$ symmetry. The coupling structure is denoted by the Higgs doublet that has Yukawa couplings to the respective kind of fermion. The up-type quarks always couple to Φ_2 with the charge assignment given in eq. (2.9).

	d_R	L	l_R	d-type	leptons
type I	$-$	$+$	$-$	Φ_2	Φ_2
type II	$+$	$+$	$+$	Φ_1	Φ_1
lepton-specific	$-$	$+$	$+$	Φ_2	Φ_1
flipped	$+$	$+$	$-$	Φ_1	Φ_2

Since we are mostly interested in scalar phenomenology, we only consider models with NFC, which offers a simple way to avoid tree-level FCNCs. In many models, it is appealing to impose discrete symmetries on the scalar potential to reduce the number of free parameters. These symmetries can often be extended to the Yukawa sector in order to realise NFC.

The most frequently used NFC symmetry leads to the four Yukawa types of the two-Higgs-doublet model (2HDM) and similar models. In a theory with two $\mathrm{SU}(2)_L$ doublets Φ_1 and Φ_2 a (possibly softly broken) $\mathbb{Z}_2$ symmetry on the scalar potential

$$\Phi_1 \to \Phi_1\,, \quad \Phi_2 \to -\Phi_2 \tag{2.8}$$

can be used to realise NFC. Without loss of generality, it can be assumed that up-type quarks only couple to Φ_2 — *i.e.* $X_{u2} = 0$. The corresponding $\mathbb{Z}_2$ charge assignment is

$$Q_L \to Q_L\,, \quad u_R \to -u_R\,. \tag{2.9}$$

This leaves four possible cases for coupling the down-type quarks and leptons to the Higgs doublets. The corresponding charge assignments and resulting coupling structures are given in table 2.1. Type I and type II are the most frequently studied Yukawa types. In type I models, all fermions couple to Φ_2 resulting in a fermion-universal rescaling of the Yukawa couplings for each Higgs boson. In type II up-type quarks couple to Φ_2 while down-type quarks and leptons couple to Φ_1. The resulting coupling structure is equivalent to that obtained in supersymmetric theories such as the minimal supersymmetric extension of the SM (MSSM) (see section 2.5.2 and section 7.1).

Summary

As model building guidelines, we choose to respect renormalisability, gauge invariance, $\rho = 1$ at tree-level, and NFC to prevent tree-level FCNCs. The class of BSM models fulfilling these prerequisites includes all theories with a scalar potential of at most quartic terms that are composed of $\mathrm{SU}(2)_L$ singlets and doublets in a gauge-invariant way. The

Yukawa terms have the same form as in the SM where only one scalar doublet couples to each kind of fermions to preserve NFC. The kinetic terms for all additional scalars are given by the covariant derivatives that also induce the appropriately gauge-invariant scalar-gauge couplings. Adding fermions in a renormalisable and gauge-invariant way is also possible.

This class of models covers all pure extensions of the Higgs sector (*e.g.* the 2HDM [110], next-to 2HDM (N2HDM) [7], or singlet extensions [111]) as well as supersymmetric models (*e.g.* the MSSM [112] or the next-to-minimal supersymmetric extension of the SM (NMSSM) [113, 114]) that introduce many scalars and some additional fermions. However, simply following these guidelines does not ensure that the resulting models agree with observations. In general, there will be only some part of their parameter space that is phenomenologically viable. In order to find this region of parameter space, we need to impose additional constraints coming from theoretical self-consistency or experimental results. The rest of the chapter is dedicated to the discussion of these constraints.

2.2 Unitarity

Unitarity of scattering processes in the limit of very high energies was one of the guiding principles in establishing the $\mathrm{SU}(2)_L$ gauge structure and the Higgs mechanism of the SM [115–120]. There are intricate links between renormalisability, gauge invariance, and unitarity in model building (see *e.g.* ref. [119]). It is even possible to derive EW theory by postulating only unitarity and renormalisability and obtain the $\mathrm{SU}(2)_L$ gauge structure as an accidental consequence [121].

In order for a theory to be well defined its S-matrix has to be unitary,

$$SS^\dagger = 1\,. \tag{2.10}$$

Violating this condition would imply violations of probability conservation, *i.e.* the probability for $X \to$ anything scattering processes (where X is any fixed initial state) could become larger than unity. If eq. (2.10) is violated in perturbation theory this implies that the perturbative expansion is not valid as the theory is strongly coupled. Unitarity constraints can easily be derived from the optical theorem

$$\sigma = \frac{1}{s}\mathrm{Im}(\mathcal{M}_{\theta=0})\,, \tag{2.11}$$

which follows from eq. (2.10). It relates the total cross section at a center of mass energy s to the imaginary part of the matrix element $\mathcal{M}_{\theta=0}$ for forward scattering. In the partial wave decomposition the scatter matrix element $\mathcal{M}$ can be decomposed into partial wave amplitudes a_J of wave number J as

$$\mathcal{M}(s,\theta) = 16\pi \sum_J (2J+1) a_J(s) P_J(\cos\theta)\,, \tag{2.12}$$

where P_J are Legendre polynomials, and θ is the scattering angle. In case of two particle scattering the differential cross section can be expressed through $\mathcal{M}$ as

$$\frac{\mathrm{d}\sigma}{\mathrm{d}\Omega} = \frac{1}{64\pi^2 s}|\mathcal{M}|^2 \,. \tag{2.13}$$

Combining eqs. (2.12) and (2.13) and using the orthogonality of the Legendre polynomials to perform the angular integral yields the total cross section for $2 \to 2$ scattering expressed through the partial wave amplitudes

$$\sigma = \frac{16\pi}{s} \sum_J (2J+1)|a_J|^2 \,. \tag{2.14}$$

Applying the optical theorem (2.11) to this cross section then yields the unitarity bound

$$|a_J|^2 = \mathrm{Im}(a_J) \quad \forall J \,. \tag{2.15}$$

Since the a_J are in general matrices, this should be interpreted as a bound on their eigenvalues a_J^i. Furthermore, the unitarity bound eq. (2.15) is only saturated for purely elastic scattering. The resulting unitarity constraint on the a_J^i for partially inelastic scattering is

$$|a_J^i|^2 \leq \mathrm{Im}(a_J^i) \quad \forall J \,. \tag{2.16}$$

This bound is displayed in fig. 2.1. It can be easily shown — or seen from fig. 2.1 — that this in particular implies

$$|\mathrm{Re}(a_J^i)| \leq \frac{1}{2} \,. \tag{2.17}$$

The above discussion holds at the level of the S-matrix for which all perturbative calculations can only be an approximation. In particular, a_J^i will always be real at the tree-level and therefore necessarily lie outside the unitarity circle for non-trivial scattering processes. Loop corrections are expected to move the a_J^i back into the circle. However, for perturbation theory to be valid the loop corrections to $\mathrm{Re}(a_J)$ must be small compared to the tree-level contribution, while $\mathrm{Im}(a_J)$ is loop-induced, and higher-order contributions may be large without invalidating perturbation theory (see *e.g.* the discussion in ref. [122]). Therefore, a leading-order estimate of the unitarity bound in perturbation theory — called perturbative unitarity — can be obtained by applying eq. (2.17) to the tree-level scattering amplitude a_J^{tree}.

The High Energy Limit and LQT Bounds

In order to use eq. (2.17), it is necessary to calculate and diagonalise the relevant part of a_J in the model of interest. This is most straight forward in the high energy limit $s \to \infty$, where the condition can be split into two parts.

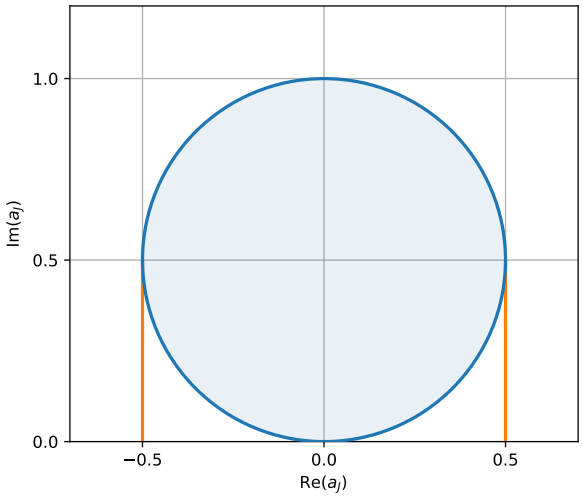

Figure 2.1: The unitarity constraint, eq. (2.15), in the complex plane of a partial wave amplitude a_J. All a_J for all unitary scattering process lie inside or — for purely elastic scattering — on the blue circle. The orange lines indicate the projection to the real axis of eq. (2.17)

Since eq. (2.17) states that the eigenvalues of the scattering matrix are bounded by a constant, necessarily

$$\lim_{s\to\infty}(a_J^i) \overset{!}{\to} \text{constant}\,. \tag{2.18}$$

Therefore, no element of the scattering matrix may grow with s in the high energy limit. It has been shown that all renormalisable spontaneously broken gauge theories — so in particular all extensions of the SM Higgs sector — have this correct scaling behaviour of the scattering matrix [119].

The second part involves calculating $\lim_{s\to\infty}(a_J^i)$ and verifying eq. (2.17) explicitly. This condition was first used by Lee, Quigg and Thacker [120] to put an upper bound of $m_h \lesssim 1\,\text{TeV}$ on the Higgs mass of the SM. Their approach is known as LQT bound and is the simplest method to apply unitarity constraints to BSM models (*e.g.* in the 2HDM [122–124], N2HDM [7], or in singlet extensions [5, 125]).

The scattering processes that are potentially relevant for unitarity are those that are not of typical electroweak strength $\sim \alpha_{\text{em}}$ at all energies. This leaves scattering among all the Higgs bosons and the longitudinal gauge bosons $W_L^\pm$ and Z_L.[3] In the high energy limit, this is equivalent to scattering among Higgs and Goldstone bosons by the Goldstone equivalence theorem [117, 119, 120]. All pure scalar scattering processes involving a propagator are suppressed by $1/s$ in the high energy limit. Therefore, including only contact interactions in the derivation of a_J is a good approximation in which a_J is independent of the energy. As a result, perturbative unitarity of $2 \to 2$ scalar scattering

[3] We do not consider processes involving top quarks which may also be relevant due to their large Yukawa couplings [126–128].

processes can be used to constrain the contact interactions between Higgs and Goldstone bosons — the quartic Higgs couplings.

There is no angular dependence in $2 \to 2$ scattering through contact interactions of scalars such that the only contributing mode is a_0. We can use eq. (2.12) for $J = 0$ to rewrite eq. (2.17) into

$$\left|\mathcal{M}^i_{2\to2}\right| \leq 8\pi\,, \tag{2.19}$$

where $\mathcal{M}^i$ are the eigenvalues of the scattering matrix elements.

In models with extended Higgs sectors, the matrix $\mathcal{M}_{2\to2}$ in the mass basis can be too complicated for an analytic diagonalisation even with these approximations. However, since basis transformations are unitary transformations, the eigenvalues of $\mathcal{M}_{2\to2}$ are independent of the basis [122], and the most convenient basis — usually the gauge basis — can be used for the calculation.

With an appropriately normalised set of two scalar states

$$|AB\rangle = \frac{1}{\sqrt{1+\delta_{AB}}} AB\,, \tag{2.20}$$

where A and B run over all the scalar states of the model, $\mathcal{M}_{2\to2}$ can be derived directly from the scalar potential through

$$\langle AB|\mathcal{M}|CD\rangle = \frac{1}{\sqrt{(1+\delta_{AB})(1+\delta_{CD})}} \frac{\partial^4 V}{\partial A \partial B \partial C \partial D}\,. \tag{2.21}$$

The resulting matrix is typically a block matrix according to the symmetries of the scalar sector, *i.e.* there are blocks for each possible value of the conserved charges. This allows most if not all of the eigenvalues to be calculated analytically while only small remaining submatrices require numerical diagonalisation. The perturbative unitarity bound can then be obtained by applying eq. (2.19).

Impact of Perturbative Unitarity Constraints

From eqs. (2.19) and (2.21) it is clear that perturbative unitarity puts upper bounds on some combinations of the dimensionless quartic couplings of the scalar potential. If the masses of the scalar particles are purely given by the quartic couplings and the vev, *e.g.* in the SM, perturbative unitarity constraints directly translate to upper bounds on the scalar masses. In the presence of other constraints, this is often true even in models with explicit mass scales (*e.g.* m_{12}^2 in the 2HDM).

A constraint similar to perturbative unitarity is the so called perturbativity constraint which is usually given as

$$|\lambda_i| < 4\pi\,, \tag{2.22}$$

where λ_i are the quartic scalar couplings of the scalar potential. This is motivated by the loop factors $\propto (4\pi)^{-n}$ that suppress n-loop diagrams. If eq. (2.22) was violated, the loop

contributions could become larger than the tree-level and thus invalidate perturbation theory. However, eq. (2.22) is no firm bound. For example, it depends on arbitrary choices of prefactor and basis when defining the λ_i. We prefer to use perturbative unitarity constraints since they provide better-defined and often equivalent or stronger constraints than perturbativity while being neither hard to derive nor numerically complicated.

Beyond High Energy LQT Bounds

Improvements over the LQT bounds have been proposed by weakening either the tree-level or the high energy approximation. One of the most straightforward approaches is to apply the LQT perturbative unitarity bounds not to the tree-level parameters of the scalar potential but instead to their renormalisation group equation (RGE) improved values [129] (see *e.g.* ref. [130] for a recent application to the 2HDM).

Recently, numerical studies of unitarity constraints beyond the high energy limit have been performed in BSM models [131–133]. In this case Feynman diagrams with propagators are no longer neglected, leading to unitarity constraints on triple Higgs couplings. In this case, eq. (2.17) is applied for the value of s, where it gives the strongest constraint. This necessitates a scan of s and a careful treatment of the poles that may appear as propagators go on-shell. This approach can provide substantially stronger constraints in some regions of the parameter space.

These approaches provide interesting ways to improve upon the LQT perturbative unitarity bounds. It may be useful to account for possible strengthened unitarity constraints through higher-order or finite-s effects already at the tree level. One possibility is replacing the 8π in eq. (2.19) with a smaller value leading to more stringent LQT bounds on the tree-level parameters. Since smaller tree-level parameters tend to lead to even smaller loop effects, this can reduce the impact of RGE running. In theories without explicit trilinear couplings in the Higgs potential, this will also reduce the finite s contributions to a_0. It can,therefore, be a worthwhile approach in models with a large number of free parameters that are hard to sample efficiently, while accommodating interesting phenomenology even with this stronger cut.

2.3 Other Theoretical Constraints

Stability of the EW vacuum is an essential source of additional constraints. It is discussed separately in the dedicated chapter 3.

Another possible source of theoretical constraints are Landau poles — divergences in the running couplings — that may appear when using RGE running to study physics at different scales. This signals a breakdown of perturbation theory. Requiring the absence of Landau poles up to a given energy scale leads to constraints on the parameter space.

We do not apply these constraints in this work as we only consider models at fixed energy scales.

2.4 Experimental Constraints

In addition to the constraints from theoretical consistency, we also need to impose agreement with experimental observations and the limits from experimental searches for new particles or new production and decay modes. In this section, we will give a short overview of the different kinds of experimental constraints we use. We aim to apply all experimental constraints at the 2σ level consistently.

2.4.1 Electroweak Precision Constraints

In section 2.1 we introduced the ρ-Parameter. We discussed the resulting model building constraints on scalar $\mathrm{SU}(2)_L$ representations that can be added to the SM while retaining the correct value of the $\rho = 1$ at tree-level.

However, higher-order effects will always contribute to the ρ-Parameter and will differ between BSM models even if only scalar singlets and doublets — which give the correct tree-level value — are added to the SM. The oblique parameters S, T, and U were introduced by Peskin and Takeuchi [134] as a framework to study one-loop contributions of BSM physics to EW precision observables relative to the SM. As long as BSM effects only contribute through gauge boson self energies — which holds in all of the models considered in this work — these variables parametrise the W mass m_W as well as several Z-pole observables. In particular

$$T \propto \rho - 1 \tag{2.23}$$

directly parametrises the deviation of the ρ parameter from its tree-level value of one.

The experimental values for the oblique parameters can be extracted from a global fit to EW precision measurements. We use the fit results from ref. [135]

$$S = 0.04 \pm 0.11\,, \quad T = 0.09 \pm 0.14\,, \quad U = -0.02 \pm 0.11\,. \tag{2.24}$$

More technical information on the fitting procedure can be found in ref. [136]. Since the parameters are defined relative to the SM reference values of $m_{h_{\mathrm{SM}}} = 125\,\mathrm{GeV}$ and $m_t = 172.5\,\mathrm{GeV}$ are assumed [135].

Predictions for the oblique parameters have been calculated in a wide class of BSM models with extended scalar sectors encompassing any number of added $\mathrm{SU}(2)_L$ doublets, $Y = 0$ singlets, and $Y = 1$ singlets [137, 138]. We use these results to obtain the theory predictions for the oblique parameters and compare these to the fit results of eq. (2.24). Including the correlation matrix given in ref. [135] we obtain a χ^2 value and apply a cut

of $\chi^2 < 7.81$ corresponding to a 2σ limit in the three-dimensional space of S, T, and U.

The parametrisation of BSM effects through the oblique parameters is only valid as long as the new particles are sufficiently heavy that they cannot go on-shell in the loops of the self-energy diagrams. This allows individual BSM particles to be lighter than the gauge boson masses as long as BSM decays of $W^\pm$ and Z are kinematically forbidden. Extensions to the S, T, and U framework have been proposed to capture subleading effects in the s/m^2_{BSM} expansion by including observables that are probed at a higher center of mass energy $s > m^2_W, m^2_Z$. These three additional parameters are called V, W, and X [139].

AnEW precision observable that cannot be parametrised through the oblique parameters is the $g-2$ of the muon. There is a long-standing discrepancy between its measured value and the SM prediction [39]. It is possible to address this discrepancy in some of the models studied in this work such as the 2HDM [140] and the MSSM [141]. However, there can be significant tension between the regions of parameter space favoured by the muon $g-2$ and the regions favoured by other constraints. The measurement of the muon $g-2$ is so precise, that model predictions including higher-order effects are essential to match the experimental precision. For simplicity, we do not impose constraints from the muon $g-2$ in this work.

Impact of EW Precision Constraints

The constraints from oblique parameter directly constrain the possible mass spectra of theories. In models with additional doublets, the T parameter puts a very stringent upper bound on the mass difference between the charged scalars and the corresponding closest-in-mass neutral scalars. The S parameter constrains large mass differences between scalar states that are considerably mixed. However, its impact on phenomenology is less pronounced compared to the T parameter. The U parameter is only rarely relevant. However, since the fit results for the three parameters are strongly correlated, including S and even U can lead to substantially stronger constraints. Since the oblique parameters are inherently related to EW gauge symmetries, they are small in pure singlet extensions where they are often not competitive with other constraints.

2.4.2 Constraints from Flavour Physics

Even in models that do not introduce tree-level FCNCs (see section 2.1) BSM particles may still contribute to the loop-induced FCNC processes. Additionally, charged BSM scalars may contribute at tree-level to charged current interactions in the flavour sector. Precise measurements for many of these processes are available and can be used to constrain BSM models. These observables are mainly sensitive to charged Higgs effects

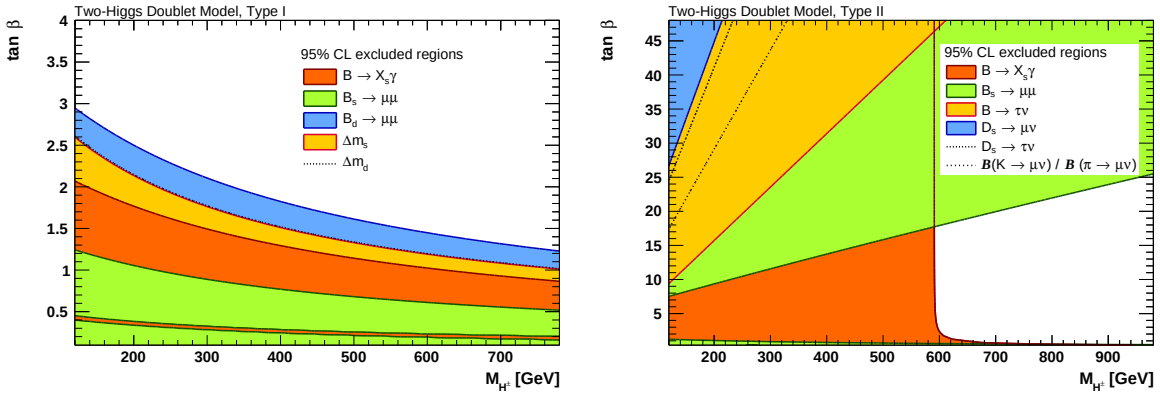

(a) Type I (b) Type II

Figure 2.2: Constraints from flavour physics in the 2HDM in the plane of the charged Higgs mass $m_{H^\pm}$ and the parameter $\tan\beta$ for a Yukawa sector of type I (a) and type II (b). Figure taken from ref. [135].

which can both mediate tree-level charged current processes and contribute to loop-induced FCNCs. With these assumptions, we expect precision flavour observables to mainly put constraints on the charged Higgs boson mass and its couplings to fermions.

A fit to flavour observables within the 2HDM was performed in ref. [135]. Figure 2.2 shows the resulting limits in the plane of the charged Higgs mass $m_{H^\pm}$ and the parameter $\tan\beta$ which governs the Yukawa couplings of the charged Higgs boson. Figure 2.2 shows the results for the two most commonly studied Yukawa types (see section 2.1). These results generalise to all models where one additional $\mathrm{SU}(2)_L$ scalar doublet is added to the SM and the appropriate Yukawa type is realised — irrespective of the number of additional singlets. The Yukawa couplings of the charged Higgs boson are given by [110]

$$\mathcal{L}_{\text{Yukawa}} \supset -\frac{\sqrt{2}V_{ud}}{v}\bar{u}\left(m_u\xi^u P_L + m_d\xi^d P_R\right)dH^+ - \frac{\sqrt{2}m_l}{v}\xi^l\bar{\nu}_L l_R H^+ - \text{H.c.}\,, \tag{2.25}$$

where V_{ud} is the CKM matrix, $m_{u,d,l}$ are the quark masses, $v^2 = v_1^2 + v_2^2$ is the Higgs vev, and $P_{L,R}$ are projection operators for left- and right-handed fermions. The factors ξ depend on the Yukawa type and $\tan\beta = v_2/v_1$[4] as given in table 2.2.

Flavour constraints on flavour conserving models mainly arise from precision B-physics measurements. The most important of these are the FCNC process $B \to X_s\gamma$ [142] with theory-predictions from refs. [143, 144] and the leptonic decays $B_s \to \mu^+\mu^-$ and $B_d \to \mu^+\mu^-$ [145, 146] with theory predictions from refs. [147–149]. The neutral Higgs bosons contribute to the $B \to \mu^+\mu^-$ observables at NLO. However, their contribution was found to be subdominant compared to the charged Higgs boson and was marginalised to obtain limits independent of the neutral Higgs masses [135].

[4] In general 2HDMs $\tan\beta$ cannot be defined without relying on an arbitrary basis choice. However, in the 2HDM with a $\mathbb{Z}_2$ symmetry that ensures NFC $\tan\beta$ can be uniquely defined in the basis where the $\mathbb{Z}_2$ symmetry is manifest.

Table 2.2: Scaling factors of the charged Higgs boson Yukawa couplings in the different Yukawa types of 2HDM-like models as a function of the parameter β.

	ξ^u	ξ^d	ξ^l
type I	$\cot\beta$	$-\cot\beta$	$-\cot\beta$
type II	$\cot\beta$	$\tan\beta$	$\tan\beta$
lepton-specific	$\cot\beta$	$-\cot\beta$	$\tan\beta$
flipped	$\cot\beta$	$\tan\beta$	$-\cot\beta$

Recently, anomalies in some flavour observables reported by the BaBar, Belle, CMS, and LHCb experiments have received considerable attention (for a recent review see ref. [150] and references therein). None of the models considered in this work are designed to reproduce those anomalies, and we will not comment on them any further.

Impact of Flavor Constraints

Since the flavour constraints are available as fit results in planes of a physical mass and an easily interpretable coupling parameter, they relate very clearly to phenomenology. The most important effect in the context of this work is the lower bound of $m_{H^\pm} \gtrsim 600\,\text{GeV}$ which can be derived from $B \to X_s\gamma$ irrespective of $\tan\beta$ in NFC realisations where up- and down-type quarks couple to different Higgs doublets (see fig. 2.2b). In type II Yukawa sectors the constraints from $B_s \to \mu^+\mu^-$ also lead to an upper limit on $\tan\beta$. Additionally, flavour constraints impose a lower bound on the parameter $\tan\beta$ (with a value depending on the Yukawa type) which rules out substantially enhanced top Yukawa couplings in 2HDM-like models.

2.4.3 Electric Dipole Moments and CP violation

In models that introduce additional sources of CP violation to the scalar sector the fermionic electric dipole moments (EDMs) provide important constraints. These CP-violating quantities are expected to be very small within the SM where they only appear at the multi-loop level (*e.g.* for the electron EDM the leading SM contribution is of four-loop order [151, 152]).[5] Their smallness in the SM makes EDMs very sensitive to new physics contributions.

The most precise measurement of an EDM is that of the electron by the ACME collaboration [156]:

$$d_e < 1.1 \times 10^{-29}\, e\,\text{cm} \tag{2.26}$$

at 95 % confidence level, where e is the electric charge of the electron. Theoretical predictions have been calculated in many models (*e.g.* in the CP-violating 2HDM [157]).

[5] This is only true if the strong CP-problem is resolved, *e.g.* by the Pecci-Quinn mechanism [153–155].

Precise limits on the neutron EDM have also been obtained [158]. However, due to the composite nature of the neutron, it is considerably more complex to obtain a precise theoretical prediction for this quantity. Different approaches exist [159, 160] but their results can differ by orders of magnitude depending on the used parametrisation of non-perturbative effects.

Impact of EDM Constraints

The upper bound on the electron EDM severely constrains CP violation in the Yukawa sectors. However, cancellations between different diagrams and (potentially) several Higgs bosons can lead to a small electron EDM even for large CP-violating phases. In this case, the EDM constraints instead impose complicated correlations between Higgs masses and couplings to ensure these cancellations. The inclusion of several EDM observables can then forbid these cancellations and lead to substantially stronger constraints [161, 162]. Note that CP-violating Higgs sectors only induce EDMs if they lead to CP-violating Yukawa couplings in the mass basis. If there are no couplings between the CP-violating sector and the SM fermions all EDMs vanish.

2.4.4 Searches for Additional Higgs Bosons

A crucial constraint when studying BSM models with extended Higgs sectors are the limits from direct collider searches for additional scalars. The ATLAS and CMS experiments at the LHC as well as the experiments at the Tevatron and LEP colliders have searched for additional BSM particles in a large variety of decay channels. It is imperative in phenomenological studies to make sure that the signature or phenomenology under consideration it not already excluded by one of these searches. However, due to the large number of experimental results, it is necessary to ensure a correct statistical interpretation.[6]

For this reason the code `HiggsBounds` [163–168] has been developed. The code takes the theory predictions for all Higgs production processes and decay rates of the model and checks whether the considered parameter point is excluded. It uses the narrow width approximation to assemble the supplied production cross sections and branching ratios into signal rates with corresponding experimental limits.

The experimental results are supplied as expected and observed limits at 2σ or 95 % confidence level as a function of one or more model parameters — typically the masses of the involved scalars. Figure 2.3 shows a limit by the ATLAS collaboration on a heavy Higgs decaying into $\tau\tau$. This is a comparatively simple, fairly model-independent result depending only on the mass of the heavy Higgs boson. When considering multiple limits, the naive approach of applying all limits simultaneously leads to an overestimated total

[6] Also, it would be very time consuming and error-prone to apply the limits individually.

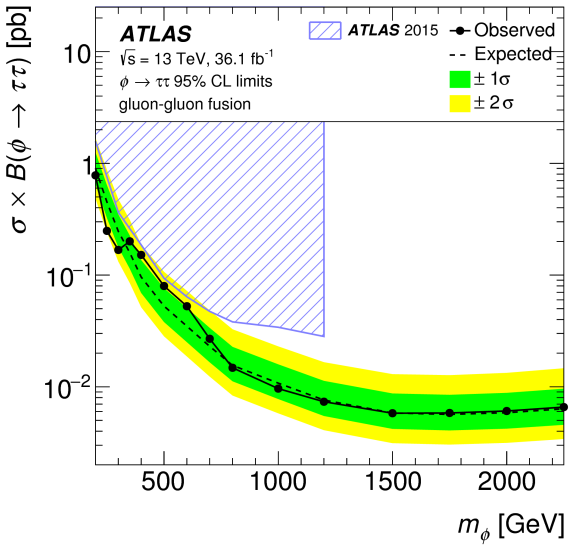

Figure 2.3: Exemplary result of a search for an additional Higgs boson ϕ of mass m_ϕ. Limit at 95 % confidence level on its production cross section through $gg \to \phi$ times its branching ratio into $\tau\tau$. Result by the ATLAS collaboration from ref. [169].

limit that is considerably stronger than a properly combined limit at 95 % confidence level.[7] For this reason, `HiggsBounds` uses the expected limits (dashed line and coloured confidence intervals in fig. 2.3) to select the most sensitive experimental search for each Higgs boson of the model. Only for these searches are the observed limits (solid line of fig. 2.3) then applied. This leads to an approximate combined 2σ limit from searches for additional Higgs bosons.

Impact of Constraints from Higgs Searches

The constraints derived from Higgs searches immediately impact the phenomenology of additional Higgs bosons by limiting their allowed production times decay rate as a function of their mass.

2.4.5 Properties of the Observed Higgs Boson

Any BSM model needs to reproduce the properties of the observed Higgs boson. The tool `HiggsSignals` [170–173] has been developed to compare the model predictions to the Higgs measurements. The code interfaces with `HiggsBounds` to use the same input

[7] For example, when applying 20 limits at 95 % confidence level one of them is statistically expected to show a significant fluctuation which could lead to an erroneous exclusion of the parameter point. For more applied limits this becomes ever more likely.

data. It then calculates a χ^2 value quantifying the agreement between model predictions and observations for each parameter point.

`HiggsSignals` includes a large number of LHC results from the ATLAS and CMS experiments. It combines mass measurements and rate measurements for all currently observed processes. For the results at 7 TeV and 8 TeV the experimental collaborations have released combined results for the mass [174] and signal rates [19] of the observed Higgs boson. The newest included 13 TeV results are given in the simplified template cross sections (STXS) [175] framework by the ATLAS [176] and CMS [177–186] collaborations based on up to $\sim 137\,\text{fb}^{-1}$ of data collected at the 13 TeV LHC. From these experimental results, `HiggsSignals` calculates χ^2 values, which can be combined to check the agreement of the model prediction with the Higgs measurements.

There are different ways to interpret the χ^2 value returned by `HiggsSignals`. In our parameter scans, we use a profiled likelihood ratio test with the SM as the alternative hypothesis. In practice, we calculate the likelihood ratio test statistic in the gaussian approximation as

$$\Delta\chi^2 = \chi^2_{\text{Model}} - \chi^2_{\text{SM}}\,, \tag{2.27}$$

where both χ^2_{Model} and χ^2_{SM} are obtained from `HiggsSignals`. We use this test statistic — instead of *e.g.* constructing a goodness-of-fit test using $\chi^2_{\text{Model}}/\text{d.o.f.}$ — as it allows a much easier statistical interpretation. Additionally, all effects related to the number of experimental observables cancel in the normalisation such that $\Delta\chi^2$ directly compares the model to the SM.

The resulting $\Delta\chi^2$ approximately describes the best-fit region of the model parameter space. The upper bound χ^2_{crit} to impose on $\Delta\chi^2$ depends on the desired confidence level and on the number ν of degrees of freedom. As stated above, we always aim to impose 2σ constraints in the gaussian limit and thus $\Delta\chi^2 < \chi^2_{\text{crit}}(2\sigma, \nu)$. When presenting results where all but n model parameters and all nuisance parameters are profiled over, the set of allowed parameter points are those with $\Delta\chi^2 < \chi^2_{\text{crit}}(2\sigma, n)$. We choose $n = 2$, which is appropriate for presenting results as scatter plots and in benchmark planes. This leads to the criterion

$$\Delta\chi^2 < 6.18\,, \tag{2.28}$$

which corresponds to the region allowed at 2σ under the assumption of gaussian errors.

Impact of Constraints from Higgs Measurements

So far, no significant deviation from the SM has been observed in the properties of the discovered Higgs boson. Therefore, imposing agreement with these observations forces most models to have one scalar that behaves similarly to the SM Higgs boson. In many models, this is an alignment limit — where the couplings of one scalar to SM particles become SM-like. Deviations from such a limit — while certainly not excluded — are strongly constrained by the Higgs measurements.

Note that this behaviour changes when there is more than one Higgs boson around 125 GeV. If these scalars cannot be distinguished due to limited mass resolution they can all contribute to the observed Higgs signal. This case allows for larger deviations from the alignment limit compared to what is possible for a single the 125 GeV Higgs boson (h_{125}). For simplicity, we mostly focus on the case of only one Higgs boson around 125 GeV.

2.5 Basic Models Beyond the SM

In this section we will give short overviews on two classes of BSM extensions. We will first discuss the consequences of having two instead of only one scalar $\mathrm{SU}(2)_L$ doublet and then introduce supersymmetry.

2.5.1 Models with Two Higgs Doublets

The 2HDM [187] extends the SM Higgs sector by a second $\mathrm{SU}(2)_L$ scalar doublet (see *e.g.* ref. [110] for a detailed review). The most general renormalisable and gauge invariant potential of two $\mathrm{SU}(2)_L$ doublets Φ_1 and Φ_2 is

$$\begin{aligned} V = {} & m_{11}^2 \Phi_1^\dagger \Phi_1 + m_{22}^2 \Phi_2^\dagger \Phi_2 - \left(m_{12}^2 \, \Phi_1^\dagger \Phi_2 + \mathrm{H.c.} \right) \\ & + \frac{\lambda_1}{2} (\Phi_1^\dagger \Phi_1)^2 + \frac{\lambda_2}{2} (\Phi_2^\dagger \Phi_2)^2 + \lambda_3 (\Phi_1^\dagger \Phi_1)(\Phi_2^\dagger \Phi_2) + \lambda_4 (\Phi_1^\dagger \Phi_2)(\Phi_2^\dagger \Phi_1) \\ & + \left[\frac{\lambda_5}{2} (\Phi_1^\dagger \Phi_2)^2 + \lambda_6 (\Phi_1^\dagger \Phi_1)(\Phi_1^\dagger \Phi_2) + \lambda_7 (\Phi_1^\dagger \Phi_2)(\Phi_2^\dagger \Phi_2) + \mathrm{H.c.} \right] . \end{aligned} \tag{2.29}$$

The parameters m_{12}^2 and $\lambda_{5,6,7}$ can in general be complex and may lead to CP violation. During EW symmetry breaking the two scalar doublets acquire (in general complex) vevs v_1 and v_2 that have to fulfil

$$|v_1|^2 + |v_2|^2 = v^2 \approx (246\,\mathrm{GeV})^2 \tag{2.30}$$

to reproduce the correct gauge boson masses. The parameter $\tan\beta$ — that already appeared in section 2.4.2 — is defined through

$$\tan\beta \equiv \frac{v_2}{v_1} \, . \tag{2.31}$$

However, the values of v_1, v_2, and $\tan\beta$ depend on the basis chosen for Φ_1 and Φ_2 and are not invariant under a basis transformation

$$\begin{pmatrix} \Phi_1 \\ \Phi_2 \end{pmatrix} \to S \begin{pmatrix} \Phi_1 \\ \Phi_2 \end{pmatrix} \tag{2.32}$$

that redefines the two doublets through a unitary 2×2 matrix S. The parameter $\tan\beta$ is therefore not useful when studying the most general potential, eq. (2.29).

The terms involving λ_6 and λ_7 will induce FCNCs for any possible coupling of Φ_1 and Φ_2 to the fermion sector. For this reason it is appealing to impose a softly broken $\mathbb{Z}_2$ symmetry,

$$\Phi_1 \to \Phi_1\,, \quad \Phi_2 \to -\Phi_2\,, \tag{2.33}$$

on the scalar potential of the 2HDM. This symmetry forces $\lambda_6 = \lambda_7 = 0$ resulting in the scalar potential

$$\begin{aligned} V = {} & m_{11}^2|\Phi_1|^2 + m_{22}^2|\Phi_2|^2 - \left(m_{12}^2\,\Phi_1^\dagger\Phi_2 + \text{H.c.}\right) \\ & + \frac{\lambda_1}{2}(\Phi_1^\dagger\Phi_1)^2 + \frac{\lambda_2}{2}(\Phi_2^\dagger\Phi_2)^2 + \lambda_3(\Phi_1^\dagger\Phi_1)(\Phi_2^\dagger\Phi_2) \\ & + \lambda_4(\Phi_1^\dagger\Phi_2)(\Phi_2^\dagger\Phi_1) + \left[\frac{\lambda_5}{2}(\Phi_1^\dagger\Phi_2)^2 + \text{H.c.}\right]. \end{aligned} \tag{2.34}$$

In this scalar potential, the basis where the $\mathbb{Z}_2$ symmetry is manifest is special and $\tan\beta$ can be uniquely defined in this basis. Extending this symmetry to the Yukawa sector to realise NFC as described in section 2.1 leads to the four 2HDM Yukawa types of table 2.1.

After electroweak symmetry breaking three of the eight degrees of freedom in the two doublets become the would-be Goldstone bosons that get absorbed by the EW gauge bosons. These would-be Goldstone bosons are separated from the physical degrees of freedom through a rotation into the so-called Higgs basis through eq. (2.32) with

$$S = \begin{pmatrix} \cos\beta & \sin\beta \\ -\sin\beta & \cos\beta \end{pmatrix}. \tag{2.35}$$

This rotation diagonalises the charged Higgs sector leading to a pair of charged Higgs boson mass eigenstates $H^\pm$. The mixing between the neutral scalar degrees of freedom depends on the pattern of EWSB and if CP violation occurs in the Higgs sector. In the most commonly considered case — eq. (2.34) with $v_1, v_2 \neq 0$ and imposing CP-conservation — the neutral mass eigenstates of the model are two CP-even scalars h and H, and a CP-odd scalar A. We call this case the real (CP-conserving) 2HDM (R2HDM).

2.5.2 Supersymmetry

A popular symmetry to impose on BSM models is supersymmetry (SUSY). It introduces a fundamental symmetry between fermionic and bosonic fields. As such it predicts a bosonic (fermionic) superpartner for every fermion (boson) of the SM. The bosonic superpartners are called sfermions — *e.g.* the stop $\tilde{t}$— and an "-ino" is appended to the names of the fermionic superpartners — *e.g.* the gluino $\tilde{g}$.

The MSSM [188–190] is probably the most studied BSM model overall. For a more complete introduction to supersymmetry and the MSSM see ref. [112] on which the overview presented in this section is based.

SUSY requires an extended Higgs sector that contains at least two $\mathrm{SU}(2)_L$ Higgs doublets. They are conventionally called Φ_u and Φ_d as one of them couples to up-type quarks and the other one to down-type quarks and leptons similar to a type II 2HDM. Just like in a 2HDM, these acquire vevs v_u and v_d during EWSB which have to fulfil

$$v_u^2 + v_d^2 = v^2 \approx (246\,\mathrm{GeV})^2 \tag{2.36}$$

and the parameter $\tan\beta$ is defined through[8]

$$\tan\beta \equiv \frac{v_u}{v_d}\,. \tag{2.37}$$

At tree-level the MSSM Higgs sector conserves CP and thus contains two neutral CP-even scalars h and H with $m_h < m_H$, a CP-odd scalar A, and a pair of charged Higgs bosons $H^\pm$ just like the R2HDM. SUSY imposes strong symmetry requirements on the scalar potential. In particular, the quartic Higgs couplings are given in terms of the $\mathrm{U}(1)_Y$ and $\mathrm{SU}(2)_L$ gauge couplings, and the Higgs boson masses are related to the gauge boson masses. The tree-level Higgs sector of the MSSM is fully parametrised through m_Z, m_W, $\tan\beta$ and either m_A or $m_{H^\pm}$. In contrast to all the non-supersymmetric models discussed in this work, the neutral CP-even Higgs masses cannot be chosen as free parameters of the MSSM.

At tree-level in the MSSM the relation

$$m_h \leq m_Z |\cos(2\beta)| \leq m_Z \tag{2.38}$$

holds. This mass range was already excluded at LEP for a SM-like Higgs boson [191] and cannot fit the mass of h_{125}. However, loop corrections to m_h can make it substantially heavier and allow the MSSM to fit observations. At the same time, they make m_h dependent on many of the other parameters of the theory leading to considerable complexity in determining the phenomenologically viable regions of parameter space. See *e.g.* ref. [192] for a recent review on Higgs-mass calculations in the MSSM. In the case $H = h_{125}$ the Higgs mass at tree-level can reproduce the observed value. However, this scenario requires A and $H^\pm$ to be rather light and faces strong constraints from searches for additional Higgs bosons, see *e.g.* refs. [193–196].

[8] The basis invariance of the 2HDM is broken by SUSY such that $\tan\beta$ can be uniquely defined.

3 Vacuum Stability

This chapter discusses vacuum stability and the resulting constraints on BSM models. We present in detail the method to obtain vacuum stability constraints that was developed within this thesis. We have published large parts of this discussion in ref. [3].

3.1 Vacua in Extended Scalar Sectors

In section 1.2.3 we discussed vacuum stability when extrapolating the SM to very high energies. In BSM models with additional scalar fields constraints from vacuum stability can already become relevant at tree-level and for fixed scale. While this shares a name with the SM analysis the method and the encountered issues are very different. The SM discussion relies on high precision to run parameters over many orders of magnitude in energy, while for the resulting potential the tunnelling calculation is of the simplest possible form. In BSM scalar extensions, on the other hand, the analysis is confined to the electroweak (EW) scale but the multidimensional scalar potential can be much more complicated with potentially many different coexisting vacua. The main issue is to efficiently find all minima of the multifield scalar potential, to identify the vacua relevant for vacuum decay, and to calculate the decay rates of the possible decays to obtain a vacuum stability constraint.[1]

The vacuum state of a (quantum) field is a minimum of the potential energy. This potential energy is given by the (effective) potential $V(\phi)$ which describes the potential energy density as a function of the scalar fields[2] in the theory. Formally, the effective potential is defined for *classical* field values ϕ_{cl} that minimise the effective action. For our purpose and at lowest order, the field theoretical potential and the effective potential are the same when replacing field operators ϕ by classical commuting field values ϕ_{cl} and defining the effective potential $V(\phi = \phi_{\text{cl}})$ as a function of $\phi \equiv \phi_{\text{cl}}$ [199].

[1] Another related but separate issue is vacuum decay at finite temperature [197]. It is best studied in the context EW baryogenesis (see section 1.2.2) but can also be used to obtain vacuum stability constraints [198]. Vacuum stability constraints at zero temperature — which we exclusively consider — and at finite temperature are complementary as they stem from very different cosmic time scales. Constraints derived at finite temperature necessarily rely on additional assumptions about the cosmological history of the universe.

[2] Only scalar fields can acquire classical background field values as fermionic or higher spin background fields would break Lorentz invariance.

Consider the most general renormalisable scalar potential of n real scalar fields ϕ_a with $a \in \{1, \ldots, n\}$ at tree-level

$$V(\vec{\phi}) = \lambda_{abcd}\phi_a\phi_b\phi_c\phi_d + A_{abc}\phi_a\phi_b\phi_c + m^2_{ab}\phi_a\phi_b + t_a\phi_a + c\,, \tag{3.1}$$

where the sum over repeated indices is implied. The totally symmetric coefficient tensors λ_{abcd}, A_{abc}, m^2_{ab} and t_a as well as the constant c contain all possible real coefficients with non-negative mass dimension. Any scalar potential can be expanded into this form by splitting all complex fields and coefficients into their real and imaginary parts and appropriately symmetrising the coefficient tensors.

This potential has up to 3^n complex stationary points. Since we have defined the ϕ^a to be real only the real stationary points are of interest to us. We select a (local) minimum out of these stationary points to be the initial vacuum $\vec{\phi}_v$ which — by construction — fulfils

$$\left.\frac{\partial V}{\partial \phi_a}\right|_{\vec{\phi}=\vec{\phi}_v} = 0\,, \tag{3.2}$$

and the mass matrix

$$M_{ab} = \left.\frac{\partial^2 V}{\partial\phi_a\partial\phi_b}\right|_{\vec{\phi}=\vec{\phi}_v} \tag{3.3}$$

is positive definite. After expanding eq. (3.1) around the vacuum as $\vec{\phi} = \vec{\phi}_v + \vec{\varphi}$, with $\vec{\varphi} = (\varphi_1, \ldots, \varphi_n)^{\mathrm{T}}$, we obtain

$$V(\vec{\varphi}) = \lambda'_{abcd}\varphi_a\varphi_b\varphi_c\varphi_d + A'_{abc}\varphi_a\varphi_b\varphi_c + m'^2_{ab}\varphi_a\varphi_b\,, \tag{3.4}$$

where t'_a vanishes due to eq. (3.2), and we have normalised the potential energy at $\vec{\varphi} = 0$ to zero. For particle physics applications this normalisation is irrelevant but it could be related to a non-vanishing cosmological constant [200].

We rewrite the field-space vector as $\vec{\varphi} \to \varphi\hat{\varphi}$ with a unit vector $\hat{\varphi}$ and its absolute value $\varphi = \sqrt{\varphi_1^2 + \cdots + \varphi_n^2}$ and obtain

$$V(\varphi, \hat{\varphi}) = \lambda(\hat{\varphi})\varphi^4 - A(\hat{\varphi})\varphi^3 + m^2(\hat{\varphi})\varphi^2\,, \tag{3.5}$$

where all the dependence on the normalised direction in field space $\hat{\varphi}$ has been absorbed into the coefficients $\lambda(\hat{\varphi})$, $A(\hat{\varphi})$ and $m^2(\hat{\varphi})$. For convenience, we allow φ to take negative values which corresponds to the absolute value in the opposite direction $-\hat{\varphi}$. Since we constructed this potential to have a minimum at $\varphi = 0$ the condition $m^2(\hat{\varphi}) > 0$ has to be satisfied for all $\hat{\varphi}$. We can use the symmetry

$$\hat{\varphi} \to -\hat{\varphi}\,, \quad A \to -A \tag{3.6}$$

to set $A > 0$ without loss of generality. Finally, for the potential to be bounded from below $\lambda(\hat{\varphi}) > 0$ is necessary for all $\hat{\varphi}$.

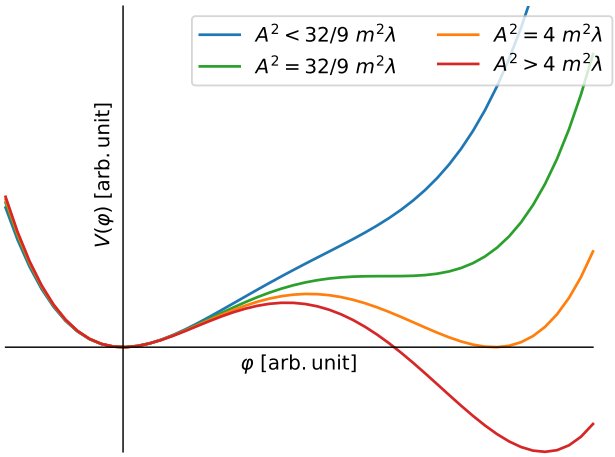

Figure 3.1: Behaviour of the generic quartic potential as given in eq. (3.5) for different relations between the coefficients $A(\hat{\varphi})$, $m^2(\hat{\varphi})$ and $\lambda(\hat{\varphi})$ as indicated in the legend for arbitrary units on both axes. Figure from our ref. [3].

Figure 3.1 shows the possible shapes of the potential in eq. (3.5). Since it is a quartic polynomial in one variable it can have at most two minima, one of which we have chosen to lie at the origin. The second minimum exists if

$$(A(\hat{\varphi}))^2 > \frac{32}{9} m^2(\hat{\varphi})\lambda(\hat{\varphi}) \tag{3.7}$$

and is deeper than the minimum at the origin if

$$(A(\hat{\varphi}))^2 > 4m^2(\hat{\varphi})\lambda(\hat{\varphi})\,. \tag{3.8}$$

This implies that large cubic terms A compared to the mass parameters and self-couplings are potentially dangerous for the stability of the initial vacuum at the origin. We call the directions $\hat{\varphi}$ fulfilling eq. (3.8) *deep directions*.

3.1.1 Calculation of the Bounce Action

The semi-classical tunnelling and first quantum corrections in a theory of one scalar field were calculated in refs. [20, 21]. It was found that the decay rate Γ of a metastable vacuum state per (spatial) volume V_S is given by the exponential decay law

$$\frac{\Gamma}{V_S} = Ke^{-B}\,, \tag{3.9}$$

where K is a dimensionful parameter that will be specified below, and B denotes the bounce action which gives the dominant contribution to Γ. The $O(4)$-symmetric bounce [201] $\phi_B(\rho)$ is the solution of the Euclidean equation of motion

$$\frac{\mathrm{d}^2\phi}{\mathrm{d}\rho^2} + \frac{3}{\phi}\frac{\mathrm{d}\phi}{\mathrm{d}\rho} = \frac{\partial U}{\partial \phi} \tag{3.10}$$

with the boundary conditions

$$\phi(\infty) = \phi_v\,, \quad \left.\frac{\mathrm{d}\phi}{\mathrm{d}\rho}\right|_{\rho=0} = 0\,. \tag{3.11}$$

U is the Euclidean scalar potential, ρ is the radius in Euclidean space,s and ϕ_v is the location of the metastable minimum. The bounce action B is the stationary point of the Euclidean action given by the integral

$$B = 2\pi^2 \int_0^\infty \rho^3 \mathrm{d}\rho \left[\frac{1}{2}\left(\frac{\mathrm{d}}{\mathrm{d}\rho}\phi_B(\rho)\right)^2 + U(\phi_B(\rho))\right]\,. \tag{3.12}$$

In the one field case, eqs. (3.10) and (3.12) can be solved numerically by the undershoot/overshoot method (see *e.g.* ref. [202] for a detailed explanation of the method). While all of the above equations generalise trivially to the multi-field case $\phi \to \vec{\phi}$, the determination of B becomes considerably more involved. In order to judge the stability of the EW vacuum we need to obtain the minimal bounce action for tunnelling into a deeper point in the scalar potential. There exist methods for solving eq. (3.10) numerically in multiple field dimensions [203–213] using optimisation, discretisation, path-deformation or multiple shooting. For our purposes a fast evaluation of the bounce action is more important than an extremely precise result (see section 3.3.2). For this reason, we approximate the path of the bounce by the straight line in a given deep direction.

Figure 3.2 illustrates this approximation. While the green path solves eq. (3.10) we instead use the bounce action calculated along the straight, blue path. The potential along this straight path is a simple quartic polynomial as given by eq. (3.5). For this form of the potential a semi-analytic result exists for the bounce action [214]

$$B = \frac{\pi^2}{3\lambda}(2-\delta)^{-3}\left(13.832\,\delta - 10.819\,\delta^2 + 2.0765\,\delta^3\right) \tag{3.13}$$

with

$$\delta = \frac{8\lambda m^2}{A^2}\,. \tag{3.14}$$

The expression in brackets was obtained in ref. [214] by fitting a cubic polynomial in δ to the numerical result. The coefficients do not depend on any model parameters, and the polynomial approximation agrees with the numerical result within a 0.004 absolute tolerance for all values of δ. We use this formula to calculate B for all deep directions

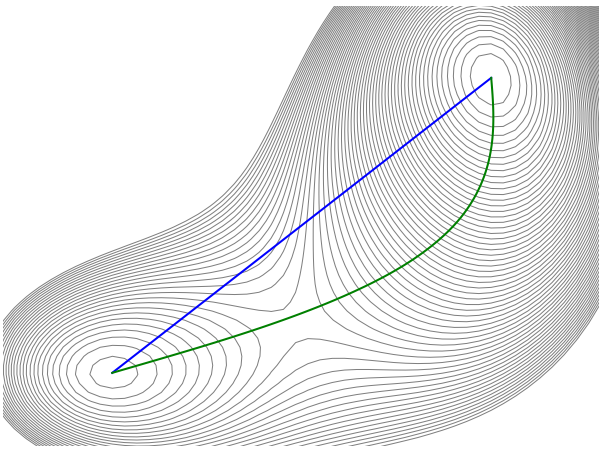

Figure 3.2: Straight path (blue) and correct bounce path (green) connecting two minima in a two-dimensional scalar potential. Sketch from ref. [211].

from the initial vacuum. The deep direction with the smallest bounce action is the dominant decay path.

The value of B is not invariant under rescaling of the field φ of eq. (3.5)

$$\varphi \to n\varphi \Rightarrow \lambda \to n^4\lambda\,,\ A \to n^3 A\,,\ m^2 \to n^2 m^2\,,\ \delta \to \delta \tag{3.15}$$

$$\Rightarrow B \to n^{-4} B\,. \tag{3.16}$$

This dependence on the field normalisation arises from the equation of motion, where eq. (3.10) only applies to fields with canonically normalised kinetic terms. A consistent expansion of the form of eq. (3.5) therefore requires all real field components φ_i to have canonically normalised kinetic terms. If $|\hat{\varphi}| = 1$ this ensures that φ is appropriately normalised. It is crucial to ensure that the parametrisation of the scalar potential fulfils this requirement.

3.1.2 Lifetime, Metastability, and Instability

The vacuum decay rate eq. (3.9) also depends on the quantity K. The value of K is both challenging to calculate and a subdominant effect towards the tunnelling rate as it does not enter in the exponent. Since it is a dimensionful parameter, $[K] = \mathrm{GeV}^4$, it can be estimated from a typical scale $\mathcal{M}$ of the theory as

$$K = \mathcal{M}^4\,. \tag{3.17}$$

Comparing the vacuum decay time τ_{decay} to the age of the universe t_{uni} [48] yields [90]

$$\frac{\tau_{\mathrm{decay}}}{t_{\mathrm{uni}}} = \left(\frac{\Gamma}{V_S}\right)^{-\frac{1}{4}} \frac{1}{t_{\mathrm{uni}}} = \frac{1}{t_{\mathrm{uni}}\mathcal{M}} e^{B/4}\,. \tag{3.18}$$

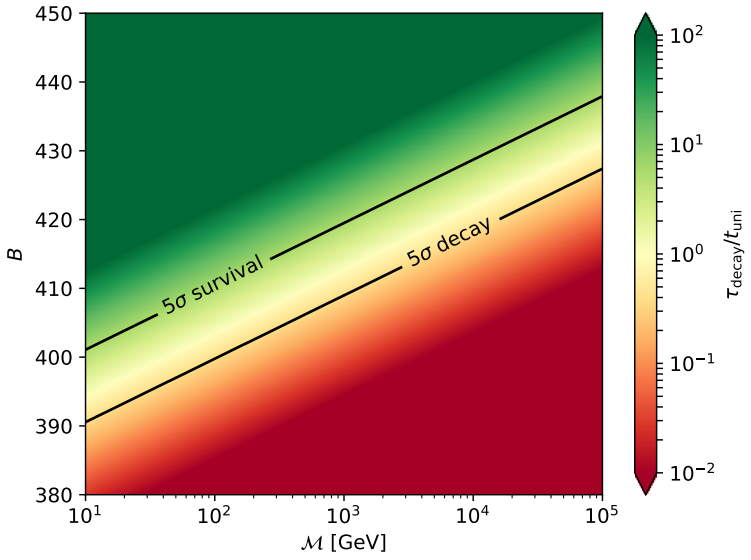

Figure 3.3: The instantaneous lifetime of the metastable vacuum τ_{decay} relative to the age of the universe t_{uni} (as defined in eq. (3.18)) is given in the plane of the scale $\mathcal{M}$ and the bounce action B. The contour lines denote a 5σ probability for decay and survival, respectively.

Figure 3.3 shows the relative lifetime $\tau_{\text{decay}}/t_{\text{uni}}$ as a function of B and $\mathcal{M}$. As expected, the threshold of instability where $\tau_{\text{decay}} \sim t_{\text{uni}}$ is highly sensitive to B and only mildly sensitive to $\mathcal{M}$.

Note that properly defining τ_{decay} is non-trivial. Here we use a definition for an *instantaneous* decay time corresponding to the typical lifetime of unit volume in space. Another possibility would be to define the decay time for the whole universe

$$\tau_{\text{decay, alt}} = \left(\frac{\Gamma}{V_S} V_S\right)^{-1} \approx \left(\frac{\Gamma}{V_S} H_0^3\right)^{-1}, \tag{3.19}$$

which is numerically similar but assumes a static universe of fixed size. This ambiguity is resolved for the survival probability P given by

$$P = \exp\left(-\frac{\Gamma}{V_S}\tilde{V}_{\text{light-cone}}\right) = \exp\left(-\mathcal{M}^4 \tilde{V}_{\text{light-cone}} e^{-B}\right), \tag{3.20}$$

where the (spacetime) volume of the past light-cone is $\tilde{V}_{\text{light-cone}} \sim 0.15/H_0^4$ [83], and H_0 is the current value of the Hubble parameter [48]. The contours corresponding to a $5\,\sigma$ expected decay or a $5\,\sigma$ expected survival of the vacuum during the evolution of the universe are also show in fig. 3.3.

The points in the green region of fig. 3.3 are definitely long-lived — *i.e.* have a survival probability extremely close to one — while the red points are definitely short-lived

— having a survival probability extremely close to zero. Varying the scale $\mathcal{M}$ over a generous range from 10 GeV to 100 TeV shifts the border between metastability and instability by less than 10% in B. We consider points where $B > 440$ as long-lived and points where $B < 390$ as short-lived. We treat the intermediate range $390 < B < 440$ as an uncertainty on the stability threshold from the unknown $\mathcal{M}$.

3.1.3 Beyond Leading Order Calculations of the Decay Rate

The calculation presented here is a leading order computation of the decay rate.[3] This includes the estimation of K on dimensional grounds as K is formally a higher order effect in the $\hbar$ expansion [93].

The calculation could be improved in several directions. The easiest improvement would be to perform the calculation not at a fixed input scale but to use a scale where the higher order corrections to the decay rate are minimised. In the SM this is typically used with NNLO matching and three loop beta functions to reach the highest possible precision for the input parameters [87]. In models with only one scalar degree of freedom in the vacuum stability calculation (*e.g.* the SM) this scale has been shown to be the μ_X for which [93]

$$\beta_\lambda(\mu_X) = 0\,, \tag{3.21}$$

where $\beta_\lambda(\mu)$ is the beta function of the quartic self coupling corresponding to the scalar degree of freedom. This condition is hard to generalise to the multi-field case. One possibility would be to choose the scale where

$$\beta_{\lambda(\hat{\varphi})}(\mu_X) = 0 \tag{3.22}$$

using the beta function for $\lambda(\hat{\varphi})$ corresponding to the deep direction under consideration. However, this would explicitly rely on the straight path approximation. We instead choose to neglect the scale dependence of the parameters, which is justified as long as all vacua are approximately at the EW scale.

Full NLO calculations of the decay rate have recently been performed in the SM [90–92]. The NLO correction to the decay rate is obtained by evaluating the prefactor K instead of estimating it. There are different approaches to handle the calculation of the required functional determinants, and we refer to refs. [90, 91] for the details of the calculation. Note that, in these approaches, the NLO contributions to the decay rate exclusively involve the prefactor K. Corrections to the shape of the bounce and thus to the bounce action only enter at NNLO. It is currently unknown how to generalise these methods to multi-field cases.

One method that could be used as an attempt to take into account NLO contributions to decay rates in BSM models is to numerically find bounce solutions in the loop corrected

[3] In addition, we use the straight path approximation of the bounce, which is a further approximation on top of the perturbative expansion.

effective potential. This is the approach taken in the public code `Vevacious` [198, 215] using the one-loop Coleman–Weinberg potential. However, it has been argued that it is in general insufficient to use the loop-corrected effective potential to calculate vacuum decay rates [93] as this only captures part of the NLO contributions. This happens because the effective action is a perturbative expansion both in powers of $\hbar$ and the momentum transfer, where the effective potential corresponds to the zeroth order term of the momentum expansion. While the full one-loop effective action could in principle be used to calculate NLO corrections to the decay rate, truncating the momentum expansion does not result in a consistent perturbative approximation. Therefore, higher momentum terms of the full one-loop effective action contain contributions to the bounce action comparable to those from the effective potential. Since it seems unfeasible to calculate even the leading higher momentum terms of the effective action in general BSM models it appears questionable whether using the one-loop effective potential for decay rate calculations systematically improves upon the LO result.[4]

3.2 Boundedness — Existence of a Global Minimum

If a scalar potential is not bounded from below it tends to $-\infty$ as the fields tend to ∞ for some directions in field space. In terms of eq. (3.5) these directions in fieldspace are those $\hat{\varphi}$ for which $\lambda(\hat{\varphi}) < 0$ since as $\varphi \gg A(\hat{\varphi}), m(\hat{\varphi})$

$$V(\varphi, \hat{\varphi}) \to \lambda(\hat{\varphi})\varphi^4 \,, \tag{3.23}$$

which is clearly unbounded from below if λ is negative for any $\hat{\varphi}$. If $\lambda(\hat{\varphi}) > 0$ for all $\hat{\varphi}$ the scalar potential is called bounded from below *in the strong sense*. If directions exist where $\lambda(\hat{\varphi}) = 0$ the potential may still be bounded if $A(\hat{\varphi}) = 0$ and $m^2(\hat{\varphi}) > 0$ for these directions.[5] This boundedness *in the weak sense* can lead to constraints on the cubic and quadratic coefficients. We do not include this possibility in our models and require boundedness *in the strong sense* constraining only $\lambda(\hat{\varphi})$.

Tunnelling from any — necessarily local — minimum into an unbounded direction is always possible. Usually, this process involves large field values such that the structure of the scalar potential around the initial vacuum can be neglected as a first approximation, and it is sufficient to study eq. (3.23). The initial state is the local *maximum* at $\varphi = 0$. For small $|\lambda|$ corresponding to a flat region around $\varphi = 0$ this state will dominantly decay through tunnelling even though classical rolling is possible [217]. Equation (3.23) with $\lambda < 0$ is one of the few scalar potentials for which analytic solutions for the bounce ϕ_B and the bounce action

$$B = \frac{8\pi^2}{3|\lambda|} \tag{3.24}$$

[4] This is in contrast to tests for absolute stability, where finding the global minimum of the effective potential is a method that is superior to a leading-order analysis [84, 216].

[5] The trilinear term $A(\hat{\varphi})$ has to vanish in this case because it would make either $\varphi \to \infty$ ($A(\hat{\varphi}) > 0$) or $\varphi \to -\infty$ ($A(\hat{\varphi}) < 0$) unbounded.

exist [217]. Using this result and the discussion of section 3.1.2 we impose $B > 440$ as a condition for metastability and obtain

$$-\frac{\pi^2}{165} \approx -0.06 < \lambda(\hat{\varphi})\,. \tag{3.25}$$

This means that the EW vacuum would still be metastable if eq. (3.25) is fulfilled for all unbounded directions $\hat{\varphi}$.

In most cases, the phenomenological difference between requiring $\lambda(\hat{\varphi}) > -0.06$ and $\lambda(\hat{\varphi}) > 0$ is negligible.[6] Therefore, we do not allow metastability when considering boundedness of the scalar potential. In our notation, the question of boundedness is thus reduced to establishing $\lambda(\hat{\varphi}) > 0$ for all $\hat{\varphi}$. Finding closed form analytic solutions to this condition is a technically difficult endeavour, and such conditions have only been found for rather simple or highly symmetric scalar potentials (*e.g.* the two-Higgs-doublet model (2HDM) [219, 220], the N2HDM [221], and several pure singlet extensions [125, 222, 223]).

In more complicated scalar potentials the algorithmic approaches often do not lead to closed form analytic solutions and have to be evaluated numerically. In this case it may be more efficient to employ a fully numerical approach — *e.g.* by minimising $\lambda(\hat{\varphi})$ — and checking that the minimal value is positive (see *e.g.* ref. [224]). A recent overview over the different methods and their applications can be found in ref. [225].

Effect of Boundedness Constraints

Boundedness places constraints on the coefficients of the scalar potential. In the case of boundedness *in the strong sense* — as discussed above — only the quartic coefficients are constrained. The clearest consequence of enforcing boundedness is that the coefficients of ϕ_a^4 terms must be positive as otherwise the ϕ_a direction would be unbounded. A combination of boundedness and unitarity constraints (see section 2.2) can often be used to derive absolute upper and lower bounds on some of the quartic coefficients of the scalar potential (see section 5.2.1 for an example).

3.3 Stability of the EW Vacuum

In unbounded scalar potentials the most severe instabilities appear at arbitrarily large field values. We will now assume that the potential is bounded from below and turn towards vacuum decay between different minima at finite field values. In this case φ is of similar size as the dimensionful parameters of eq. (3.5), and the full scalar potential

[6] Additionally, it can be argued that it would be highly unlikely in most inflationary models for the universe to end up in a local minimum while unbounded directions are present [218].

is relevant. Calculating decay rates will establish three categories of stability in our analysis.

- *Absolute stability:* the EW vacuum is the global minimum of the scalar potential, no tunnelling is possible.
- *Long-lived metastability:* the EW vacuum is a local minimum, but tunnelling into all deeper minima is long-lived with $B > 440$.
- *Short-lived instability:* the EW vacuum is a local minimum, and tunnelling into at least one deeper minimum is short-lived with $B < 390$.

We use the definitions of long-lived and short-lived vacuum decay as well as the uncertainty band in between, $390 < B < 440$, as defined in section 3.1.2.

3.3.1 Additional Minima of the Scalar Potential

As mentioned above, the most general scalar potential of n scalar fields, eq. (3.1), has up to 3^n isolated complex stationary points. However, if the scalar potential — or its first derivative — is invariant under any continuous global symmetries none of these stationary points will be isolated and instead span multidimensional surfaces in field space related by these symmetries. While all points on such a surface are physically equivalent vacua it is nevertheless crucial to isolate the stationary points in order to reduce the complexity of the minimisation problem and to allow for better numerical convergence.

In BSM theories with the SM gauge groups at the very least the $\mathrm{SU}(2)_L$ and $\mathrm{U}(1)_Y$ gauge symmetries give rise to corresponding global continuous symmetries of the scalar potential.[7] These symmetries can be used to remove up to four degrees of freedom. Through a global $\mathrm{SU}(2)_L$ transformation one of the doublets of the theory can be brought into the form

$$\Phi = \begin{pmatrix} \phi^+ \\ \phi^0 \end{pmatrix} \xrightarrow{\mathrm{SU}(2)_L} \begin{pmatrix} 0 \\ \mathrm{Re}(\phi'^0) \end{pmatrix} . \tag{3.26}$$

The $\mathrm{Re}(\phi'^0)$ indicates that this component is made real as a result of the transformation and thus three degrees of freedom have been removed. If this leaves any complex Y-charged degrees of freedom in the theory (*e.g.* in models with a second $\mathrm{SU}(2)_L$ doublet) the global $\mathrm{U}(1)_Y$ symmetry can be used to render one Y-charged degree of freedom real, *e.g.*

$$\Phi = \begin{pmatrix} \phi^+ \\ \phi^0 \end{pmatrix} \xrightarrow{\mathrm{U}(1)_Y} \begin{pmatrix} \mathrm{Re}(\phi'^+) \\ \phi'^0 \end{pmatrix} \tag{3.27}$$

for a $Y = 1$ doublet. If the model under consideration has additional continuous BSM symmetries — either gauged or global — even more degrees of freedom can be removed.

[7] Since we treat all fields as classical background fields, only global transformations are relevant and we fo not need to distinguish between gauged and non-gauged continuous symmetries.

This reduces the number of degrees of freedom that have to be considered in the numerical solution and prevents convergence problems for non-isolated solutions.

We use the numerical method of polynomial homotopy continuation (PHC) (see ref. [226] for a physics based introduction or *e.g.* ref. [227] for technical details) to find all solutions of eq. (3.2). PHC efficiently finds all isolated and complex solutions of systems of polynomial equations. Since — as all ϕ_a are real by definition — only real solutions are of interest to us, the main source of missed or erroneously included stationary points lies in judging whether a solution is real or complex. This can be ameliorated by a careful preconditioning of the system of equations [227]. Another subtlety is that PHC only finds point-like, isolated solutions. If any continuous symmetries are left in the model the stationary points cannot be found by the algorithm. For this reason it is essential to remove all continuous symmetries as described above.

Finally, stationary points of the scalar potential always come in sets of physically equivalent stationary points related by any remaining discrete symmetries of eq. (3.2).[8] In particular, in general multiple degenerate vacua with the correct pattern of EW symmetry breaking exist that are related by some discrete symmetry $\mathcal{S}$. We need to pick one of these to be the EW vacuum which is possible without loss of generality. The EW vacuum then spontaneously breaks $\mathcal{S}$. As a result, other sets of stationary points related by $\mathcal{S}$ are no longer equivalent regarding vacuum stability constraints and the tunnelling time into these minima can be different [3, 228].

In the presence of many local and global minima the tunnelling from the EW vacuum to the global minimum of the scalar potential may not provide the most stringent constraint. Therefore, we calculate the decay rates into all deep directions and select the most dangerous minimum (MDM) as the deeper minimum with the largest decay rate. This is often, but not always, the deeper minimum which is closest in field space to the EW vacuum.

3.3.2 Parameter Scans and Vacuum Stability Calculations

Typical BSM parameter scans consider millions of different parameter points which places strong requirements on evaluation time and reliability of any numerical method to evaluate vacuum stability constraints.

The first trade-off between speed and precision is in the calculation of the bounce action described in section 3.1.1. Using one of the available sophisticated solvers [211–213] may take a lot of runtime and could encounter numerical problems. As described above, we instead approximate the tunnelling path with a straight line in field space and use the semi-analytic solution eq. (3.13) [214]. A comparison between such simple approximations and the multiple-shooting method of ref. [212] has been performed in ref. [229] where

[8] This includes both explicitly imposed discrete symmetries and accidental discrete remainders of the removed continuous symmetries.

agreement within $\mathcal{O}(10\%)$ for polynomial potentials has been found. The approximation according to eq. (3.13) is evaluated instantaneously while the available solvers typically take between a few seconds and several minutes per tunnelling calculation.

This approximation, as well as the discussion at the beginning of chapter 3, relies on the potential being a quartic polynomial — which is only true at tree-level. This is sufficient to obtain a LO calculation of the decay rate when estimating the prefactor K on dimensional grounds. As discussed in section 3.1.3 there is currently no method available to calculate the NLO decay rate in models with multiple scalar degrees of freedom. For this reason we stick to the LO calculation instead of using the Coleman–Weinberg potential to obtain a partial NLO result for the decay rate which may or may not be more accurate than the LO result. This also allows us to employ the very concise formulation presented in this section and considerably increases the speed and numerical stability of our calculation.

The tunnelling time with respect to the age of the universe as given in eq. (3.18) depends exponentially on the value of the bounce action B. For any given parameter point, small uncertainties on B are therefore amplified to large uncertainties on the tunnelling time. While this makes precise predictions for the lifetime of individual parameter points very challenging, it is less problematic for constraining the parameter space of BSM models since the bounce action B is also very sensitive to the values of the model parameters. Therefore, a small shift in parameter space typically leads to a change in the bounce action substantially larger than the uncertainties described above. For this reason the resulting constraints on the model parameter space depend only mildly on the precise way B is calculated. This dependence can be estimated from the width of the uncertainty band $390 < B < 440$ (see section 3.1.2) in parameter space.

Impact of EW-Scale Vacuum Stability Constraints

The constraints obtained in this way depend on all parameters of the scalar potential and are obtained fully numerically in most models. Based on eq. (3.8) it can be argued that if the trilinear coefficients for some directions are substantially larger than the quadratic coefficients, vacuum stability constraints are expected to be relevant.

4 Singlet Extensions and Higgs-to-Higgs Decays

In this chapter we study the collider phenomenology of a singlet extension of the SM in detail. In particular, we focus on novel signatures in resonant multiscalar production for which we provide benchmark scenarios. The results in this chapter have been published in our ref. [5].

4.1 Pure Singlet Extensions of the SM

Extensions of the SM by scalar singlets are among the simplest possible BSM models. According to the criteria established in section 2.1, the most general extension of the SM by n real scalar singlet fields ϕ_i ($i \in [1, \ldots, n]$) has a scalar potential of the form

$$\begin{aligned} V(\phi_i, \Phi) = & \, a_i\phi_i + m_{ij}\phi_i\phi_j + T_{ijk}\phi_i\phi_j\phi_k + \lambda_{ijkl}\phi_i\phi_j\phi_k\phi_l \\ & + T_{iHH}\phi_i(\Phi^\dagger\Phi) + \lambda_{ijHH}\phi_i\phi_j(\Phi^\dagger\Phi) \\ & + V_{\text{SM}}(\Phi)\,, \end{aligned} \tag{4.1}$$

with real coefficient tensors and $V(\Phi)_{\text{SM}}$ of eq. (1.14). An extension by complex singlets can always be brought into this form by expanding fields and coefficients into real and imaginary parts. Since the ϕ_i are pure gauge singlets they have trivial kinetic terms that do not induce any gauge interactions. Additionally, it is not possible to write down gauge invariant and renormalisable interactions between a scalar singlet and any of the SM fermions. The singlets will therefore only interact with the SM Higgs boson through the couplings of the scalar potential and — if they acquire a vacuum expectation value (vev) — mix with the SM Higgs boson and inherit some of its gauge and Yukawa couplings.

This is also the reason why there is no physical difference between a parametrisation in terms of n complex or $2n$ real scalar singlet fields. Naively, one would expect that imaginary parts of complex scalar fields are CP-odd, and mixing them with the real parts or the SM Higgs boson would lead to CP violation. However, since the singlets have no gauge or Yukawa couplings it is always possible to find a CP-transformation under which all of them are CP-even [94, 230]. Thus any pure singlet extension of the SM is a theory of only CP-even scalars.[1]

[1] This is no longer true in the presence of additional doublets (*e.g.* in the 2HDMS [231–233] or the NMSSM [113, 114]) or vector-like fermions which couple to the singlets [234, 235].

Singlet extensions of the SM have been subject to detailed phenomenological studies before. This includes both extensions by a single real singlet [236–240] (see refs. [241–245] for recent phenomenological studies) and by a complex singlet or two real singlets [9, 111, 125, 246–251]. The models are also interesting in the context of scalar singlet dark matter [252–260] and a strong first-order electroweak phase transition [256, 258, 260–264]. We will focus on a specific extension of the SM by two real singlets that has not been previously considered in the literature.

Experimentally, singlet extensions can be explored in two complementary ways at the LHC. First, precisely measuring the signal rates of the 125 GeV Higgs boson (h_{125}) probes the structure of the doublet-singlet mixing, as well as possible new decay modes of h_{125} to new light scalar states. Second, direct searches for new scalars may reveal the existence of mostly singlet-like Higgs bosons. The discovery prospects for direct searches depend on the singlet-doublet mixing and the mass of the new scalars (both governing the production rates), and on the decay pattern of the produced scalar state. In general, decays directly to SM particle final states as well as to two lighter scalar states ("Higgs-to-Higgs decays") are possible. While some of the former decays are already searched for by the LHC experiments, current searches for Higgs-to-Higgs decays focus almost exclusively on the signatures $h_S \to h_{125}h_{125}$ (where h_S denotes a new Higgs state with mass above 250 GeV) [265–276], or $h_{125} \to h_S h_S$ (with the h_S mass below 62.5 GeV) [277–283]. The model considered in the following, however, features also Higgs decays to unidentical scalar bosons ("asymmetric decays"), Higgs decays involving only non-SM-like Higgs bosons, as well as the possibility of successive Higgs-to-Higgs cascade decays. All of these decay signatures have not been experimentally explored in detail.[2] We will discuss them in detail in this chapter and show that they lead to novel collider signatures with sizeable signal rates that are experimentally interesting for the analysis of Run-II data as well as the upcoming LHC runs. We provide six dedicated two-dimensional benchmark scenarios, each highlighting a different Higgs-to-Higgs decay signature that has not been probed experimentally so far. We strongly encourage the experimental collaborations to investigate these novel signatures using current and future collider data.

4.2 The TRSM

The two-real-singlet model (TRSM) adds two real singlet degrees of freedom to the SM. These are written as two real singlet fields S and X. In order to reduce the number of free parameters two discrete $\mathbb{Z}_2$ symmetries

$$\mathbb{Z}_2{}^S : \quad S \to -S\,, \tag{4.2}$$

$$\mathbb{Z}_2{}^X : \quad X \to -X \tag{4.3}$$

$$\tag{4.4}$$

[2] A first search result for a symmetric Higgs-to-Higgs decay involving only non-SM Higgs states has been presented by ATLAS in the $W^+W^-W^+W^-$ final state [266].

are introduced. The most general renormalisable scalar potential invariant under the ${\mathbb{Z}_2}^S \otimes {\mathbb{Z}_2}^X$ symmetry is

$$\begin{aligned} V = &\mu_\Phi^2 \Phi^\dagger\Phi + \lambda_\Phi (\Phi^\dagger\Phi)^2 + \mu_S^2 S^2 + \lambda_S S^4 + \mu_X^2 X^2 + \lambda_X X^2 \\ &+ \lambda_{\Phi S}\Phi^\dagger\Phi S^2 + \lambda_{\Phi X}\Phi^\dagger\Phi X^2 + \lambda_{XS} S^2 X^2 \,. \end{aligned} \tag{4.5}$$

All coefficients in eq. (4.5) are real resulting in a total of nine model parameters. A translation of these coefficients to the parameters of the complex scalar singlet parametrisation is given in the appendix of ref. [5].

Depending on the vevs acquired by the scalars different *phases* of the model can be realised. We decompose the fields (in unitary gauge) as

$$\Phi = \begin{pmatrix} 0 \\ \frac{\phi_h + v}{\sqrt{2}} \end{pmatrix}, \quad S = \frac{\phi_S + v_S}{\sqrt{2}}, \quad X = \frac{\phi_X + v_X}{\sqrt{2}} \tag{4.6}$$

leading to the tadpole equations

$$-v\mu_\Phi^2 = v^3\lambda_\Phi + \frac{v v_S^2}{2}\lambda_{\Phi S} + \frac{v v_X^2}{2}\lambda_{\Phi X} \tag{4.7}$$

$$-v_S\mu_S^2 = v_S^3\lambda_S + \frac{v^2 v_S}{2}\lambda_{\Phi S} + \frac{v_S v_X^2}{2}\lambda_{SX} \tag{4.8}$$

$$-v_X\mu_X^2 = v_X^3\lambda_X + \frac{v^2 v_X}{2}\lambda_{\Phi X} + \frac{v_S^2 v_X}{2}\lambda_{SX} \,. \tag{4.9}$$

These have solutions for any values of v, v_S, v_X. However, in order to achieve electroweak symmetry breaking (EWSB) $v = v_{\text{SM}} \approx 246\,\text{GeV}$ is required. If $v_S, v_X \neq 0$ the $\mathbb{Z}_2$ symmetries are spontaneously broken, and the fields $\phi_{h,S,X}$ mix into three physical scalar states. This is called the *broken phase*.

If $v_X = 0$ the field ϕ_X does not mix with $\phi_{h,S}$, does not acquire any couplings to SM fermions and gauge bosons, and is stabilised by the ${\mathbb{Z}_2}^X$ symmetry.[3] This makes it a candidate particle for dark matter (DM). The phenomenology of the two other scalar states is very similar to the real singlet extension [241–245]. If both singlet vevs vanish, ϕ_h is the SM Higgs boson, and the two singlets both form separate dark sectors stabilised by their respective $\mathbb{Z}_2$ symmetries. In this case collider phenomenology is (at tree-level) only impacted by possible invisible decays of h_{125} to the DM particles.

In this chapter we focus on the broken phase featuring to the most interesting collider phenomenology. The mass eigenstates $h_{1,2,3}$ are related to the fields $\phi_{h,S,X}$ through the 3×3 orthogonal mixing matrix R

$$\begin{pmatrix} h_1 \\ h_2 \\ h_3 \end{pmatrix} = R \begin{pmatrix} \phi_h \\ \phi_S \\ \phi_X \end{pmatrix} . \tag{4.10}$$

[3] The case of $v_S = 0$ is equivalent by renaming $S \leftrightarrow X$.

We assume the mass eigenstates to be ordered by their masses

$$M_1 \leq M_2 \leq M_3 \tag{4.11}$$

and parametrise the mixing matrix R by three mixing angles θ_{hS}, θ_{hX}, θ_{SX}. Using the short-hand notations

$$s_1 \equiv \sin\theta_{hS}\,, \quad s_2 \equiv \sin\theta_{hX}\,, \quad s_3 \equiv \sin\theta_{SX}\,, \quad c_1 \equiv \cos\theta_{hS}\,, \ \ldots \tag{4.12}$$

it is given by

$$R = \begin{pmatrix} c_1c_2 & -s_1c_2 & -s_2 \\ s_1c_3 - c_1s_2s_3 & c_1c_3 + s_1s_2s_3 & -c_2s_3 \\ c_1s_2c_3 + s_1s_3 & c_1s_3 - s_1s_2c_3 & c_2c_3 \end{pmatrix}. \tag{4.13}$$

The angles θ can be chosen to lie in

$$-\frac{\pi}{2} < \theta_{hS}, \theta_{hX}, \theta_{SX} < \frac{\pi}{2} \tag{4.14}$$

without loss of generality. In the TRSM it is possible to express the nine parameters of the scalar potential through the three physical Higgs masses, the three mixing angles, and the three vevs. These relations are given by

$$\begin{aligned} \lambda_\Phi &= \frac{1}{2v^2} m_i^2 R_{i1}^2\,, & \lambda_S &= \frac{1}{2v_S^2} m_i^2 R_{i2}^2\,, & \lambda_X &= \frac{1}{2v_X^2} m_i^2 R_{i3}^2\,, \\ \lambda_{\Phi S} &= \frac{1}{vv_S} m_i^2 R_{i1}R_{i2}\,, & \lambda_{\Phi X} &= \frac{1}{vv_X} m_i^2 R_{i1}R_{i3}\,, & \lambda_{SX} &= \frac{1}{v_Sv_X} m_i^2 R_{i2}R_{i3}\,, \end{aligned} \tag{4.15}$$

where a sum over i is implied. Fixing one of the Higgs masses to the mass of the observed Higgs boson, $M_a \simeq 125\,\text{GeV}$, and setting v to its SM value leaves seven free input parameters of the TRSM:

$$M_b\,,\ M_c\,,\ \theta_{hS}\,,\ \theta_{hX}\,,\ \theta_{SX}\,,\ v_S\,,\ v_X\,, \tag{4.16}$$

with $a \neq b \neq c \in \{1,2,3\}$.

This is an important practical difference between the TRSM and another well-studied extension of the SM by two real singlet degrees of freedom, the CxSM [125, 249]. The CxSM is expressed in terms of a complex singlet with a softly broken $U(1)$ symmetry of the singlet phase imposed on the scalar potential. This more stringent symmetry leaves only seven model parameters such that one of the physical scalar masses and one of the singlet vevs are dependent parameters. In contrast, the TRSM is consistent for *any* combination of masses, mixing angles, and vevs. Therefore, it can cover the full kinematic phase space of Higgs-to-Higgs decay signatures for all parameters except the two non-h_{125} Higgs masses fixed. This property allows us to define two-dimensional benchmark scenarios in section 4.5.

As in all pure singlet extensions the couplings of the scalar boson h_a ($a \in \{1,2,3\}$) to *all* SM fermions and gauge bosons are given by the SM value rescaled by

$$\kappa_a = R_{a1}\,. \tag{4.17}$$

The scaling factor κ_a denotes the doublet admixture of the mass eigenstate h_a. Due to the orthogonality of the mixing matrix these obey the important sum rule

$$\sum_{a=1}^{3} \kappa_a^2 = 1\,. \tag{4.18}$$

4.2.1 Collider Phenomenology

The triple Higgs couplings are of special phenomenological interest in the TRSM. Using eq. (4.15) they can be expressed directly through the input parameters of eq. (4.16). The coupling $\tilde{\lambda}_{abb}$ of $h_a h_b h_b$ is defined through

$$V \supset \frac{h_a h_b^2}{2} \left(\sum_j \frac{R_{aj}\, R_{bj}^2}{v_j} \right) \left(M_a^2 + 2M_b^2 \right) \equiv \frac{1}{2} \tilde{\lambda}_{abb} h_a h_b^2\,. \tag{4.19}$$

Similarly, the coupling of three different scalars is given by

$$V \supset h_a h_b h_c \left(\sum_j \frac{R_{aj} R_{bj} R_{cj}}{v_j} \right) \left(\sum_i M_i^2 \right) \equiv \tilde{\lambda}_{abc} h_a h_b h_c\,, \tag{4.20}$$

and the triple Higgs self coupling $\tilde{\lambda}_{aaa}$ is defined through

$$V \supset \frac{h_a^3}{2} \left(\sum_j \frac{R_{aj}^3}{v_j} \right) M_a^2 \equiv \frac{1}{3!} \tilde{\lambda}_{aaa} h_a^3\,. \tag{4.21}$$

With these definitions the tree-level partial decay width of a scalar h_a into two scalars h_b and h_c (where $b = c$ is allowed) is then given by

$$\Gamma_{a\to bc} = \frac{\tilde{\lambda}_{abc}^2}{16\pi M_a^3} \sqrt{\lambda(M_a^2, M_b^2, M_c^2)} \frac{1}{1+\delta_{bc}} \Theta(M_a - M_b - M_c)\,, \tag{4.22}$$

with

$$\lambda(x_1, x_2, x_3) \equiv \sum_i x_i^2 - \sum_{i,j\neq i} x_i x_j\,. \tag{4.23}$$

With this information, the phenomenology of a TRSM Higgs boson h_a can be fully obtained from the predictions for a SM-like Higgs boson (h_{SM}) of the same mass. Throughout this work we employ the narrow width approximation to factorise production cross sections and branching ratios (BRs).

Production cross sections for h_a can be obtained from the corresponding h_{SM} cross section by simply rescaling

$$\sigma(h_a) = \kappa_a^2 \cdot \sigma(h_{\mathrm{SM}})|_{M_a}\,. \tag{4.24}$$

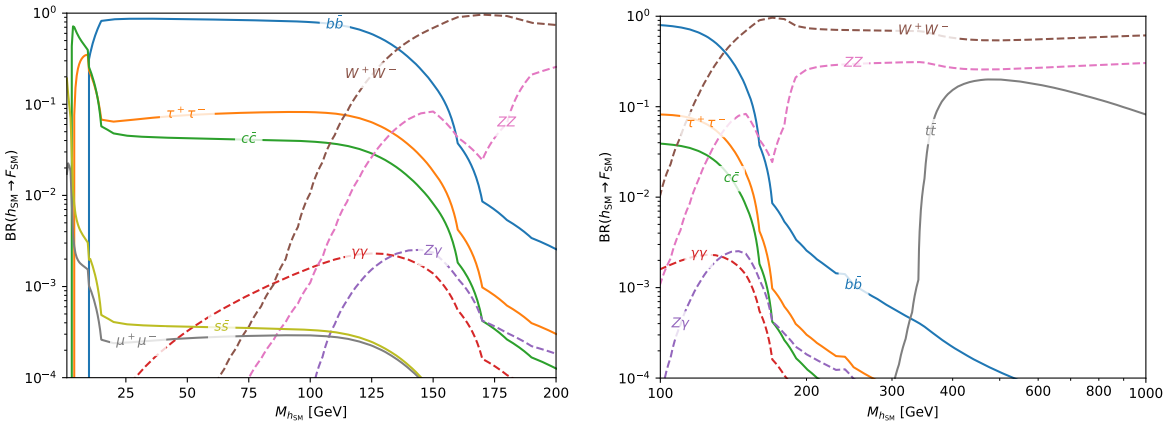

Figure 4.1: Branching ratios of a SM-like Higgs boson h_{SM} into SM final states F_{SM} as a function of its mass, $M_{h_{\mathrm{SM}}}$, from 1 GeV to 1 TeV, in the low mass region (left panel) and high mass region (right panel). The numerical values are taken from ref. [175], see text for further details.

Since κ_a rescales all couplings of h_a to SM fermions and gauge bosons, eq. (4.24) is exact up to electroweak (EW) corrections involving multi-Higgs vertices. In particular, this holds to all orders in QCD.

The scaling factor κ_a also universally rescales the partial widths of h_a into SM particles which leads to a rescaling of the h_{SM} total width as

$$\Gamma(h_a \to \mathrm{SM}) = \kappa_a^2 \cdot \Gamma_{\mathrm{tot}}(h_{\mathrm{SM}})|_{M_a} \ . \tag{4.25}$$

Note that this alone can never change the BRs of h_a into SM particles. Using the results of eq. (4.22) we can obtain the BRs of $h_a \to h_b h_c$:

$$\mathrm{BR}(h_a \to h_b h_c) = \frac{\Gamma_{a\to bc}}{\kappa_a^2\, \Gamma_{\mathrm{tot}}(h_{\mathrm{SM}}) + \sum_{xy} \Gamma_{a\to xy}} \, . \tag{4.26}$$

Denoting the sum of these new physics (NP) decay rates to multiscalar final states as

$$\mathrm{BR}(h_a \to \mathrm{NP}) \equiv \sum_{b,c} \mathrm{BR}(h_a \to h_b h_c) \, , \tag{4.27}$$

the BRs of h_a into any final state F_{SM} composed entirely of SM fermions and gauge bosons are given by

$$\mathrm{BR}(h_a \to F_{\mathrm{SM}}) = \big(1 - \mathrm{BR}(h_a \to \mathrm{NP})\big)\, \mathrm{BR}(h_{\mathrm{SM}} \to F_{\mathrm{SM}}) \, . \tag{4.28}$$

One important special case is that in the absence of BSM decay modes — which is always the case for the lightest Higgs bosons h_1 — h_a has BRs identical to an h_{SM} of the same mass.

Figure 4.1 shows the BRs of a h_{SM} as a function of its mass. As long as $\mathrm{BR}(h_a \to \mathrm{NP}) = 0$ — *i.e.* if no Higgs-to-Higgs decays are possible — the scalar h_a has exactly the BRs shown in fig. 4.1. The numerical values are taken from [175], based on state-of-the-art evaluations using `HDECAY` [284–286] and `Profecy4F` [287–289].

4.3 Constraints and Parameter Scan

In order to assess the phenomenologically viable regions of the parameter space we apply all relevant theoretical and experimental constraints described in chapter 2.

Unitarity constraints were discussed in detail in section 2.2. In the TRSM we have derived perturbative unitarity bounds in the high energy limit by requiring the eigenvalues M^i of the scatter matrix M defined through eq. (2.21) to fulfil

$$|M_i| < 8\pi\,. \tag{4.29}$$

The resulting constraints on the parameters of the scalar potential are

$$|\lambda_\Phi| < 4\pi \tag{4.30}$$
$$|\lambda_{\Phi S}|\,,\ |\lambda_{\Phi X}|\,,\ |\lambda_{SX}| < 8\pi \tag{4.31}$$
$$|a_1|,\ |a_2|,\ |a_3| < 16\pi \tag{4.32}$$

where $a_{1,2,3}$ are the three real roots of the cubic polynomial

$$\begin{aligned} &x^3 + x^2(-12\lambda_\Phi - 6\lambda_S - 6\lambda_X) \\ &+ x\left(72\lambda_\Phi(\lambda_S+\lambda_X) - 4(\lambda_{\Phi S}^2 + \lambda_{\Phi X}^2) + 36\lambda_S\lambda_X - \lambda_{SX}^2\right) \\ &+ 12\lambda_\Phi\lambda_{SX}^2 + 24\lambda_{\Phi S}^2\lambda_X + 24\lambda_{\Phi X}^2\lambda_S - 8\lambda_{\Phi S}\lambda_{\Phi X}\lambda_{SX} - 432\lambda_\Phi\lambda_S\lambda_X\,. \end{aligned} \tag{4.33}$$

Closed form conditions for boundedness (see section 3.2) of the scalar potential, eq. (4.5), have been derived in [222, 223]. In our notation they read

$$\begin{aligned} \lambda_\Phi, \lambda_S, \lambda_X &> 0\,, \\ \overline{\lambda}_{\Phi S} \equiv \lambda_{\Phi S} + 2\sqrt{\lambda_\Phi\lambda_S} &> 0\,, \\ \overline{\lambda}_{\Phi X} \equiv \lambda_{\Phi X} + 2\sqrt{\lambda_\Phi\lambda_X} &> 0\,, \\ \overline{\lambda}_{SX} \equiv \lambda_{SX} + 2\sqrt{\lambda_S\lambda_X} &> 0\,, \\ \sqrt{\lambda_S}\lambda_{\Phi X} + \sqrt{\lambda_X}\lambda_{\Phi S} + \sqrt{\lambda_\Phi}\lambda_{SX} + \sqrt{\lambda_\Phi\lambda_S\lambda_X} + \sqrt{\overline{\lambda}_{\Phi S}\overline{\lambda}_{\Phi X}\overline{\lambda}_{SX}} &> 0\,. \end{aligned} \tag{4.34}$$

It has been proven [250] that a vacuum of the form of eq. (4.6) with $v, v_S, v_X \neq 0$ is always the global minimum of the scalar potential at tree-level. Therefore, no additional constraints from vacuum decay need to be considered.

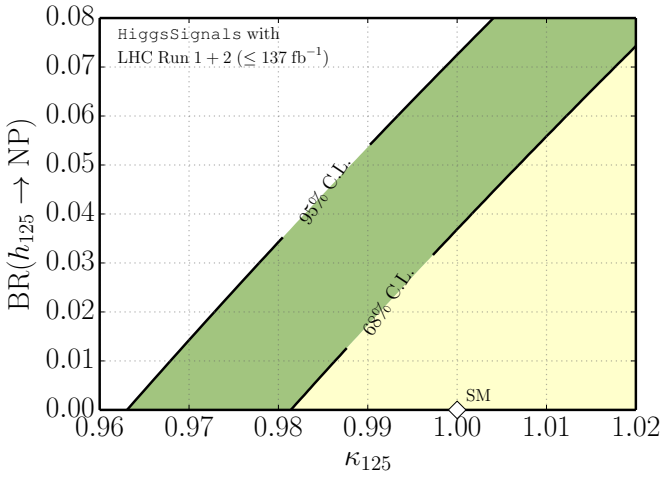

Figure 4.2: Constraints from Higgs measurements on the parameters κ_{125} and BR($h_{125} \to$ NP) as obtained from `HiggsSignals`-2.3.0. The green and yellow regions are allowed at 95 % and 68 % confidence level, respectively.

We use the oblique parameters S, T and U descried in section 2.4.1 to parametrise constraints from EW precision measurements. The results of refs. [137, 138] are applicable to the TRSM to obtain model predictions for S, T and U which are compared to the fit results of [135]. Flavour constraints are not relevant as the singlets neither change the Yukawa sector. We use `HiggsBounds`-5.4.0 [163–168] to check for agreement with the bounds from searches for additional Higgs bosons (see section 2.4.4).

Important constraints on the model parameter space arise from the signal rate measurements of the h_{125}. We use `HiggsSignals`-2.3.0 [170–173] to test for agreement with the observations at the 2σ level as described in section 2.4.5, *i.e.* we require $\Delta\chi^2 < 6.18$. These constraints are especially relevant in singlet extensions as there are effectively only two BSM parameters that enter the phenomenology of h_{125} — its coupling scaling factor κ_{125} and its BR($h_{125} \to$ NP) into new particles (see section 4.2.1). A complication may arise in case that two or even all three scalar bosons have a mass around 125 GeV. `HiggsSignals` then automatically takes into account a possible superposition of their signals in the test against the Higgs rate measurements, see ref. [171] for details.

Assuming that only one scalar boson is responsible for the observed signal at 125 GeV, we show the constraints from Higgs signal rate measurements in the two-dimensional parameter plane κ_{125}–BR($h_{125} \to$ NP) in fig. 4.2.[4] If no BSM decay modes of h_{125} exist, a lower bound on $\kappa_{125} > 0.963$ at 95 % confidence level is obtained. For the other limiting case of exactly SM-like couplings, $\kappa_{125} = 1$, we find a limit of BR($h_{125} \to$ NP) < 7.3 %. The 2σ limit between these two limiting cases approximately follows a linear slope. The

[4]The expected sensitivity of Higgs rate measurements at the high-luminosity (HL)-LHC in this parameter plane has been presented in section 6 of ref. [22].

region $\kappa > 1$ is only included for completeness in fig. 4.2 but cannot be realised in the TRSM, see eq. (4.18).

4.3.1 Parameter Scan

Based on these constraints we performed a large scan of the TRSM parameter space using an updated private version of the code `ScannerS` [7, 125, 249, 290], including all of the constraints described in the previous section. Note that bounds from signal strength measurements are evaluated with `HiggsSignals` for each point individually. This guarantees that the possibility that two or even all three Higgs bosons may have masses close to 125 GeV and therefore contribute to the observed h_{125} signal is correctly accounted for.

We parametrise the model via the input parameters given in eq. (4.16). For the numerical results presented in section 4.4 we sample the parameter space by independently drawing from uniform distributions for each parameter. We allow for the non-h_{125} Higgs masses and the singlet vevs to lie within

$$1\,\text{GeV} \leq M_b, M_c, v_X, v_S \leq 1\,\text{TeV} \tag{4.35}$$

and vary the mixing angles throughout their allowed range, eq. (4.14). In the parameter scan, we only keep parameter points that pass all constraints. For the benchmark scenarios in section 4.5, we instead fix all parameters apart from the non-h_{125} scalar masses, and scan the two-dimensional parameter space in a grid within the defined parameter ranges.

For the reference h_{SM} production cross sections and BRs, we use the predictions from refs. [175, 291]. The h_{SM} production cross sections and total width are rescaled according to eqs. (4.24) and (4.25) and combined with leading-order decay widths for the Higgs-to-Higgs decays from eq. (4.22). For the h_{125} production rates, we use the results of the N^{3}LO calculation in the gluon fusion (ggF) channel [292]. This calculation uses an effective description of the top-induced contributions. For scalar bosons with masses $M_a \neq 125\,\text{GeV}$ we instead employ results from the NNLO+NNLL calculation [291] that accounts for top-quark mass induced effects up to NLO. Indeed, we find that the predictions of these calculations differ sizeably for masses $M \gtrsim 2m_t$, for instance

$$\left.\frac{\sigma_{\text{NNLO+NNLL}}}{\sigma_{\text{N3LO}}}\right|_{M=400\,\text{GeV}} \sim 3\,. \tag{4.36}$$

In the following discussion of collider signatures we assume the production of a single scalar state via the dominant ggF process. In some cases, it might be worthwhile to investigate the subdominant Higgs production processes of vector boson fusion or Higgs-Strahlung, $pp \to V\phi$ ($V = W^\pm, Z$), as these give additional trigger options and may help to reduce the background. We leave the detailed exploration of the prospects for various production modes to future studies.

4.4 Implications of Collider Searches

The additional scalar bosons $h_a \neq h_{125}$ can decay directly to SM particles. The branching ratios of the various SM particle final states (F_{SM}) are obtained according to eq. (4.28), and their relative rates (*i.e.* the ratios of branching ratios for different F_{SM} decay modes) are identical to the corresponding SM predictions for h_{SM} with mass M_a. The rate for $h_a \to F_{\mathrm{SM}}$ signal processes normalised to the corresponding SM prediction can be expressed as

$$\frac{\sigma(pp \to h_a(+X)) \times \mathrm{BR}(h_a \to F_{\mathrm{SM}})}{\sigma_{\mathrm{SM}}(pp \to h_{\mathrm{SM}}(+X)) \times \mathrm{BR}(h_{\mathrm{SM}} \to F_{\mathrm{SM}})} = \kappa_a^2 \cdot (1 - \mathrm{BR}(h_a \to \mathrm{NP})) \ . \tag{4.37}$$

This quantity is shown in fig. 4.3 as a function of M_a in the low mass region (left) and high mass region (right) for the sampled parameter points that pass all relevant constraints (see section 4.3). For M_a roughly between 12 and 85 GeV LEP searches for $e^+e^- \to h_a Z \to b\bar{b}Z$ [293] lead to an upper limit on the possible signal rate, as shown by the red lines in fig. 4.3 (left). The whole parameter region shown in this plot could be probed at a future ILC [294]. At larger mass values $\gtrsim 190\,\mathrm{GeV}$, the upper limit originates from LHC searches for $pp \to h_a \to W^+W^-$ and ZZ. The latest ATLAS [295] and CMS [296] limits are overlaid as green and orange lines, respectively, in fig. 4.3 (right). For very large mass values $\gtrsim 700\,\mathrm{GeV}$ direct LHC searches are not yet sensitive to probe the parameter space. In addition, we include in fig. 4.3 the upper limit inferred indirectly via the sum rule, eq. (4.18), from the rate measurements of h_{125}. These lead to an upper limit of $\kappa_a^2 \leq 7.3\,\%$ (see section 2.4), except in the mass region around 125 GeV where h_a potentially contributes to the observed Higgs signal.

The model allows for resonant scalar pair-production at the LHC, or, in other words, the direct production of a single scalar h_a followed by the "symmetric" or "asymmetric" decay into identical or different scalar states, respectively. Specifically,

$$pp \to h_a\ (+X) \to h_b h_b\ (+X), \tag{4.38}$$
$$pp \to h_3\ (+X) \to h_1 h_2\ (+X), \tag{4.39}$$

where, in the symmetric case, eq. (4.38), $a = 2$, $b = 1$ or $a = 3$, $b \in \{1, 2\}$, and X denotes not further defined objects that may be produced in association with the scalar state (e.g., jets, vector bosons, etc.). The h_{125} can be either of the three scalar states h_a ($a \in \{1, 2, 3\}$).

Processes of the symmetric type, eq. (4.38), leading to pair production of h_{125} are already being investigated, see *e.g.* refs. [265–276] for recent LHC Run-II searches. Figure 4.4 (left) shows the 13 TeV LHC cross section for the resonant scalar pair production process $pp \to h_a \to h_{125}h_{125}$ ($a \in \{2, 3\}$) as a function of the M_a. Overlaid are the most recent experimental limits on this process from the ATLAS [276] and CMS [273] collaborations. Figure 4.4 (left) illustrates that experimental searches in this channel are beginning to directly constrain the TRSM for resonance masses between around 380 GeV and 550 GeV.

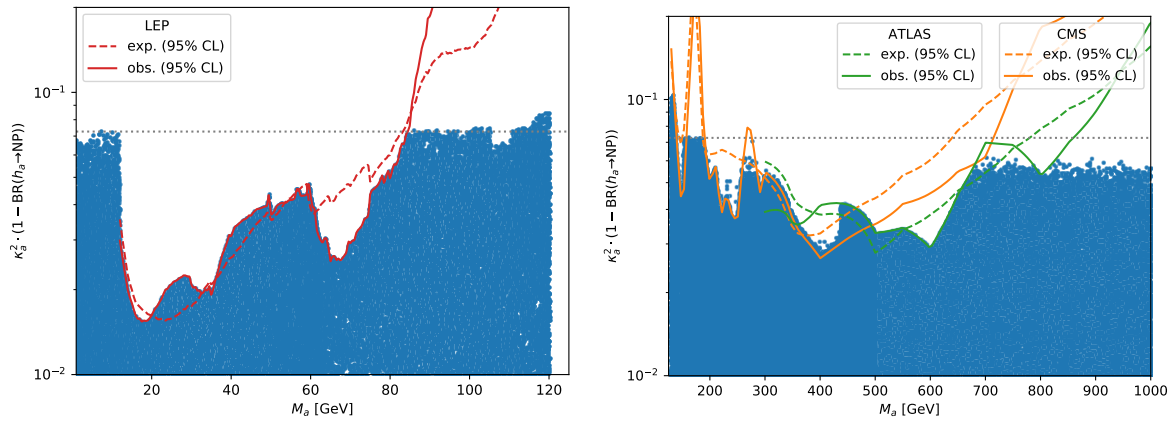

Figure 4.3: SM-normalised signal strength for an additional Higgs boson decaying to SM particle final states as a function of its mass, M_a, for all parameter points passing all relevant constraints. In the low mass region (left panel) we include the observed and expected limit from LEP searches in the $ee \to h_a Z \to b\bar{b}Z$ channel [293]. In the high mass region (right) the ATLAS [295] and CMS [296] observed and expected limits from the latest $pp \to h_a \to ZZ/WW$ searches are displayed. The dotted grey line indicates the indirect limit on κ^2 from Higgs rate measurements.

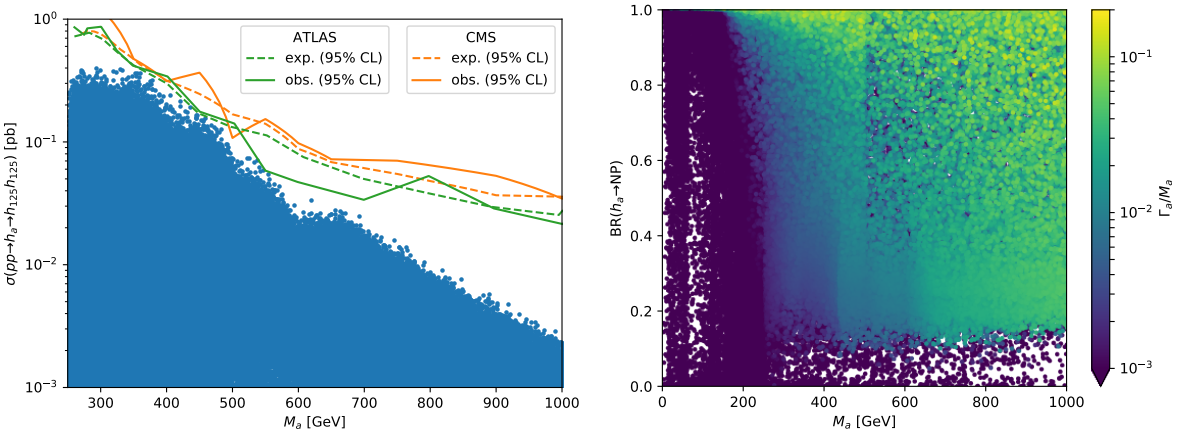

Figure 4.4: *Left panel:* Cross section for the process $pp \to h_a \to h_{125}h_{125}$ at the 13 TeV LHC as a function of the h_a mass, M_a, for all parameter points passing all relevant constraints. The current expected and observed upper limits on this process from ATLAS [276] and CMS [273] are overlaid.
Right panel: Total width over mass, Γ_a/M_a in the plane of M_a and the decay rate $\mathrm{BR}(h_a \to \mathrm{NP})$. Parameter points with larger Γ_a/M_a are plotted on top.

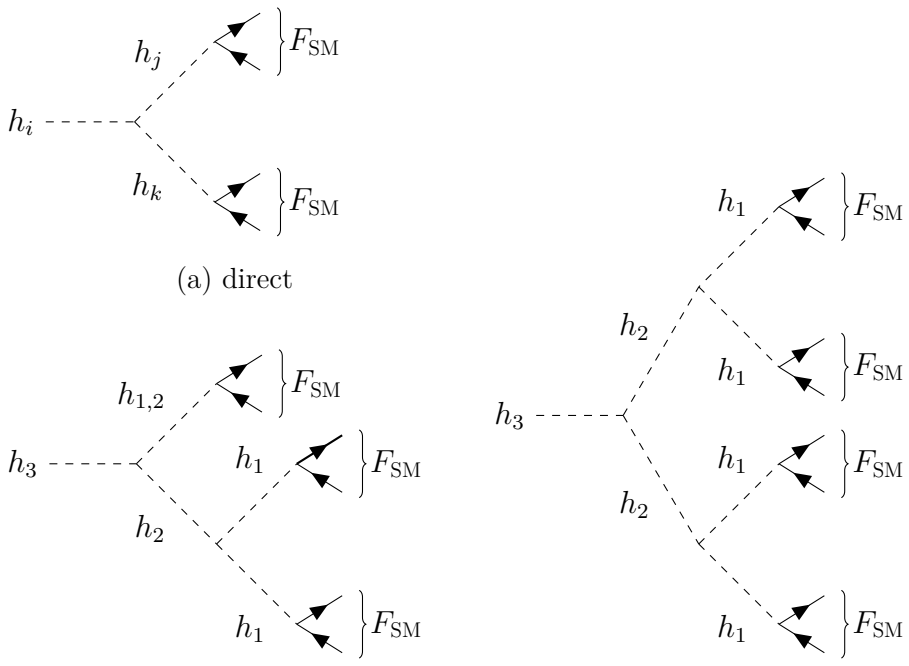

(a) direct

(b) single cascade

(c) double cascade

Figure 4.5: Possible Higgs-to-Higgs decay signatures involving three neutral (mass ordered) scalars h_i ($i \in \{1,2,3\}$): (a) $h_i \to h_j h_k$ (with $i > j,k$) with successive decay of h_j and h_k to SM particles; (b) $h_3 \to h_2 h_k$ (with $k \in \{1,2\}$) with successive decay $h_2 \to h_1 h_1$ and h_k as well as all h_1 decaying to SM particles; (c) $h_3 \to h_2 h_2 \to h_1 h_1 h_1 h_1$ and all h_1 decaying to SM particles.

In contrast, LHC searches [277–283] for the inverted signature of single-production of h_{125} which then decays into a pair of light h_a ($a \in \{1,2\}$) are not yet sensitive, as the indirect constraint from Higgs signal rates on the possible new decay modes, $\mathrm{BR}(h_{125} \to \mathrm{NP}) \leq 7.3\%$ (see fig. 4.2), are much stronger than the direct limits from these searches. Currently, the strongest limit from $h_{125} \to h_a h_a$ searches is obtained in the $b\bar{b}\tau^+\tau^-$ final state [278] at $M_a \simeq 35\,\mathrm{GeV}$, amounting to around $\mathrm{BR}(h_{125} \to h_a h_a) \leq 25\,\%$ (assuming h_a to decay exclusively to SM particles) in the TRSM. Both of these processes are under active experimental investigation and we expect the sensitivity to improve in the future.

Figure 4.4 (right) shows the ratio of the total width over the mass, Γ_a/M_a, in the plane of M_a and the sum of the h_a decays to scalar states, $\mathrm{BR}(h_a \to \mathrm{NP})$. Parameter points with larger values of Γ_a/M_a overlay parameter points with smaller values. We can clearly see that parameter points with larger Γ_a/M_a only appear for sizeable decay rates to scalar states. However, overall, Γ_a/M_a never exceeds values greater than around 18 % in the considered mass range up to 1 TeV. In the discussion of the benchmark scenarios below we will comment on cases where $\Gamma_a/M_a \gtrsim 1\,\%$.

We will now turn to the more exotic signatures resulting from eqs. (4.38) and (4.39) that

are not yet under active investigation. Following the processes in eqs. (4.38) and (4.39), the two produced scalar states may decay directly to SM particles. Alternatively, an h_2 final state particle may decay into the two lightest scalars, $h_2 \to h_1 h_1$. This can lead to interesting cascade decays resulting in three or four scalar states that eventually decay to SM particles. The possible decay patterns within our model are depicted in a generic form in fig. 4.5. Here and in the following we denote final states from Higgs decays composed of SM particles (*i.e.* gauge bosons or fermions) generically as $F_{\rm SM}$, unless otherwise specified. For the more complicated final states we will use $F^n_{\rm SM}$ to denote an n-particle SM final state, where we count the SM particles before their decay (*i.e.* $W^\pm$, Z, and t are counted as one particle). We find that all possible Higgs-to-Higgs decay signatures, fig. 4.5, can appear at sizeable rates in the allowed TRSM parameter space. In the next section we therefore present six two-dimensional benchmark scenarios that highlight these signatures, and are tailored to initiate dedicated experimental studies and facilitate the design of corresponding searches.

4.5 Benchmark Scenarios

In this section we define six benchmark scenarios in order to motivate and enable dedicated experimental studies of Higgs-to-Higgs decay signatures. Each scenario focusses on one (or more) novel signatures and features a (close-to) maximal signal yield that can be expected within the model while obeying the constraints described in section 4.3. The benchmark scenarios are defined as two-dimensional planes where all model parameters except for the two non-h_{125} scalar masses are fixed. A brief overview of the benchmark scenarios is given in table 4.1. For each benchmark scenario, **BP1**–**BP6**, it specifies the Higgs state h_a that is identified with h_{125}, the target Higgs-to-Higgs decay signature, as well as the possibilities of phenomenologically relevant[5] successive Higgs decays, potentially leading to single or double cascade decay signatures (see fig. 4.5).

We employ a factorised approach relying on the narrow width approximation. For each benchmark scenario we will show both the $\mathrm{BR}(h_a \to h_b h_c)$ $(a, b, c \in \{1, 2, 3\},\ a \neq b, c)$ and the cross section

$$\sigma(pp \to h_a \to h_b h_c) = \kappa_a^2\, \sigma(gg \to h_{\rm SM})|_{M_a} \cdot \mathrm{BR}(h_a \to h_b h_c)\,. \tag{4.40}$$

In all scenarios where either $b = c$ or $h_{b,c} \equiv h_{125}$ there is only one unknown BSM mass in the final state $h_b h_c$. In this case we will employ a further factorisation where we present the decay rate of $h_b h_c \to F_{\rm SM}$ as a function of the remaining mass parameter. For this decay rate, we use the short-hand notation

$$\mathrm{BR}(h_b h_c \to F_{\rm SM}) \equiv c \cdot \sum_{F^i_{\rm SM}+F^j_{\rm SM}=F_{\rm SM}} \mathrm{BR}(h_b \to F^i_{\rm SM})\mathrm{BR}(h_c \to F^j_{\rm SM})\,, \tag{4.41}$$

[5]For instance, in **BP2**, the successive decay $h_2 \to h_1 h_1$ could in principle occur for the case that $M_1 < 62.5\,\mathrm{GeV}$, however, Higgs signal rate measurements strongly constrain the possible BR and we do not consider this possibility further.

Table 4.1: Overview of the benchmark scenarios: The second column denotes the Higgs mass eigenstate that we identify with h_{125}, the third column names the targeted decay mode of the resonantly produced Higgs state, and the fourth column lists possible, relevant cascade decays of the resulting Higgs states.

	h_{125}	target signature	possible cascade decays
BP1	h_3	$h_{125} \to h_1 h_2$	$h_2 \to h_1 h_1$ if $M_2 > 2M_1$
BP2	h_2	$h_3 \to h_1 h_{125}$	—
BP3	h_1	$h_3 \to h_{125} h_2$	$h_2 \to h_{125} h_{125}$ if $M_2 > 250\,\text{GeV}$
BP4	h_3	$h_2 \to h_1 h_1$	—
BP5	h_2	$h_3 \to h_1 h_1$	—
BP6	h_1	$h_3 \to h_2 h_2$	$h_2 \to h_{125} h_{125}$ if $M_2 > 250\,\text{GeV}$

where c is the appropriate combinatorial factor. The full cross section into a given SM final state can be obtained by

$$\sigma(pp \to h_a \to h_b h_c \to F_{\text{SM}}) = \sigma(pp \to h_a \to h_b h_c) \cdot \text{BR}(h_b h_c \to F_{\text{SM}})\,, \tag{4.42}$$

where potential cascades, fig. 4.5, are included in the $\text{BR}(h_b h_c \to F_{\text{SM}})$ for F^6_{SM} and F^8_{SM}.

The model parameters for the selected benchmark scenarios as well as the coupling scale factors κ_a are given in table 4.2. All cross section values given in the following refer to production of the initial scalar through ggF at the 13 TeV LHC. All of the benchmark scenarios presented in the following are exemplary for the corresponding signature within the TRSM. Similar signatures are possible with different parameter choices and may also appear in different models. As such, the regions of parameter space that are excluded in a benchmark scenario should under no circumstances discourage experimental searches for the corresponding signatures.

4.5.1 BP1 — $h_{125} \to h_1 h_2$

In the first benchmark scenario, **BP1**, we identify the heaviest scalar state h_3 with h_{125}, and focus on the asymmetric decay $h_{125} \to h_1 h_2$. The parameter values (see table 4.2a) are chosen such that the couplings of h_3 to SM particles are nearly identical to the SM predictions, $\kappa_3 \simeq 1$. At the same time, the parameter choice maximizes — within the experimentally allowed range — the branching ratio $\text{BR}(h_{125} \to h_1 h_2)$, which is shown in fig. 4.6 (top left) as a function of M_1 and M_2. In fig. 4.6 (top right) we show the corresponding cross section for inclusive production via ggF. We find that the BR for $h_3 \to h_1 h_2$ reaches up to $7 - 8\,\%$ which translates into a signal cross section of around 3 pb. These maximal branching ratios are reached in the intermediate mass range for h_2, $M_2 \sim 60 - 80\,\text{GeV}$. This feature is caused by the proportionality of the triple Higgs couplings to the masses (see eq. (4.20)). Therefore, although phase space

Table 4.2: Input parameter values (a) and coupling scale factors κ_a (b) for the six benchmark planes. The doublet vev is set to $v \approx 246\,\text{GeV}$ and the mass indicated by h_{125} is set to 125.09 GeV for all BPs.

(a) Input parameters

	M_1 GeV	M_2 GeV	M_3 GeV	θ_{hS}	θ_{hX}	θ_{SX}	v_S GeV	v_X GeV
BP1	1 – 62	1 – 124	h_{125}	1.435	−0.908	−1.456	630	700
BP2	1 – 124	h_{125}	126 – 500	1.352	1.175	−0.407	120	890
BP3	h_{125}	126 – 500	255 – 650	−0.129	0.226	−0.899	140	100
BP4	1 – 62	1 – 124	h_{125}	−1.284	1.309	−1.519	990	310
BP5	1 – 124	h_{125}	126 – 500	−1.498	0.251	0.271	50	720
BP6	h_{125}	126 – 500	255 – 1000	0.207	0.146	0.782	220	150

(b) Coupling scale factors

	κ_1	κ_2	κ_3
BP1	0.083	0.007	−0.997
BP2	0.084	0.976	−0.203
BP3	0.966	0.094	0.239
BP4	0.073	0.223	0.972
BP5	0.070	−0.966	−0.250
BP6	0.968	0.045	0.246

opens up significantly for light decay products, the branching ratios become smaller for $M_2 < 40\,\text{GeV}$. In the hatched region in fig. 4.6 the decay rate slightly exceeds the 2σ upper limit inferred from the LHC Higgs rate measurements (using `HiggsSignals`). For very lows masses, $M_{1,2} \lesssim 5\,\text{GeV}$, the scenario is also constrained by boundedness. We stress again that this excluded area is dependent on our parameter choices and strongly encourage experimental searches to cover the whole mass range.

Due to the sum rule, eq. (4.18), the couplings $\kappa_{1,2}$ have to be very close to zero in order to achieve $\kappa_3 \sim 1$. This means that the couplings of h_1 and h_2 to SM particles are strongly suppressed. As a result, if the decay channel $h_2 \to h_1 h_1$ is kinematically open, $M_2 > 2M_1$, it is the dominant decay mode leading to a significant rate for the $h_1 h_1 h_1$ final state. In **BP1** we find that $\text{BR}(h_2 \to h_1 h_1) \simeq 100\,\%$ in this kinematic regime (*i.e.* above the red line in fig. 4.6) with a very sharp transition at the threshold. If in addition $M_1 \gtrsim 10\,\text{GeV}$ the h_1 decays dominantly into $b\bar{b}$ leading to a sizeable rate for the $b\bar{b}b\bar{b}b\bar{b}$ final state as shown in fig. 4.6 (bottom right).

If the $h_2 \to h_1 h_1$ decay is kinematically closed, $M_2 < 2M_1$, both scalars h_1 and h_2

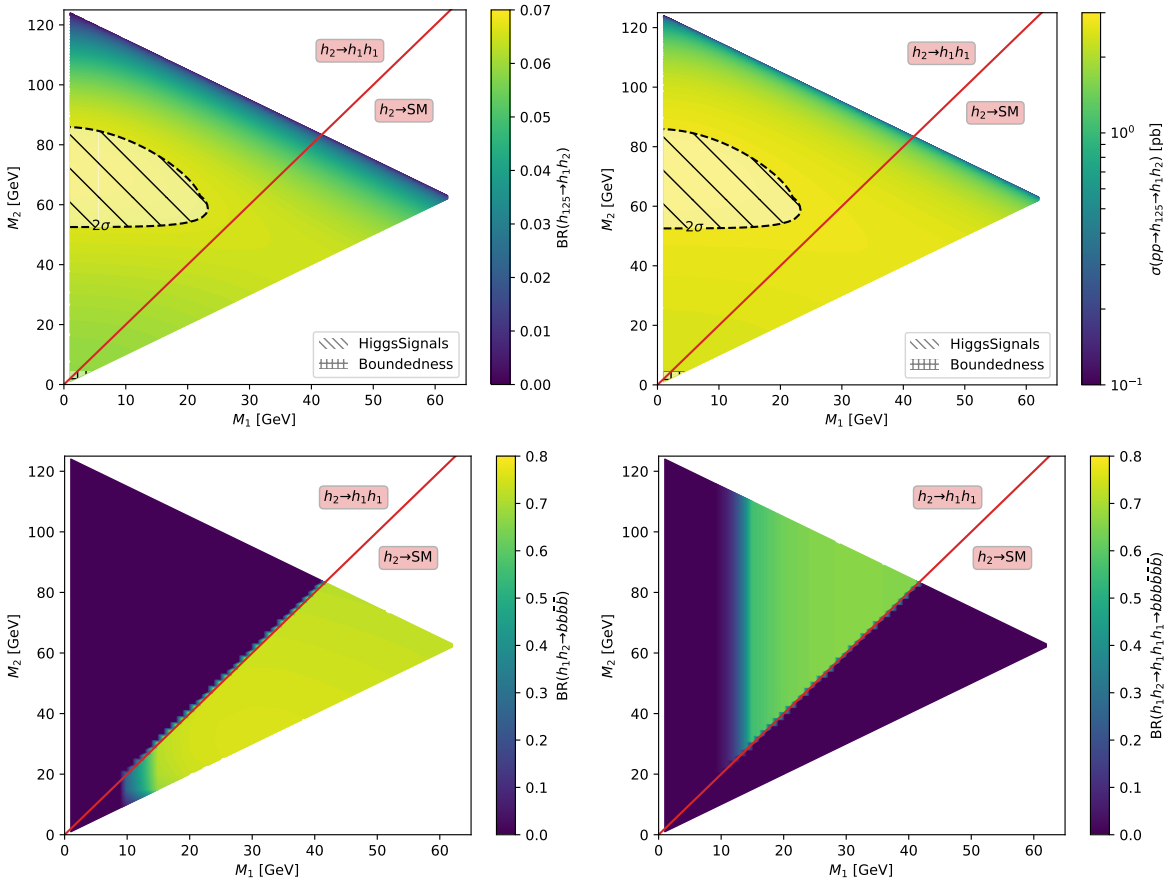

Figure 4.6: Benchmark plane **BP1** for the decay signature $h_{125} \to h_1 h_2$ with $h_{125} \equiv h_3$, defined in the (M_1, M_2) plane. The colour code shows $\mathrm{BR}(h_{125} \to h_1 h_2)$ (top left panel) and the 13 TeV-LHC cross section for $pp \to h_{125} \to h_1 h_2$ (top right panel). The red line separates the region $M_2 > 2M_1$, where $\mathrm{BR}(h_2 \to h_1 h_1) \approx 100\%$, from the region $M_2 < 2M_1$, where $\mathrm{BR}(h_2 \to F_{\mathrm{SM}}) \approx 100\%$. The decay rates of $h_1 h_2$ into $b\bar{b}b\bar{b}$ and — through a $h_2 \to h_1 h_1$ cascade — $b\bar{b}b\bar{b}b\bar{b}$ final states are shown in the bottom left and right panels, respectively.

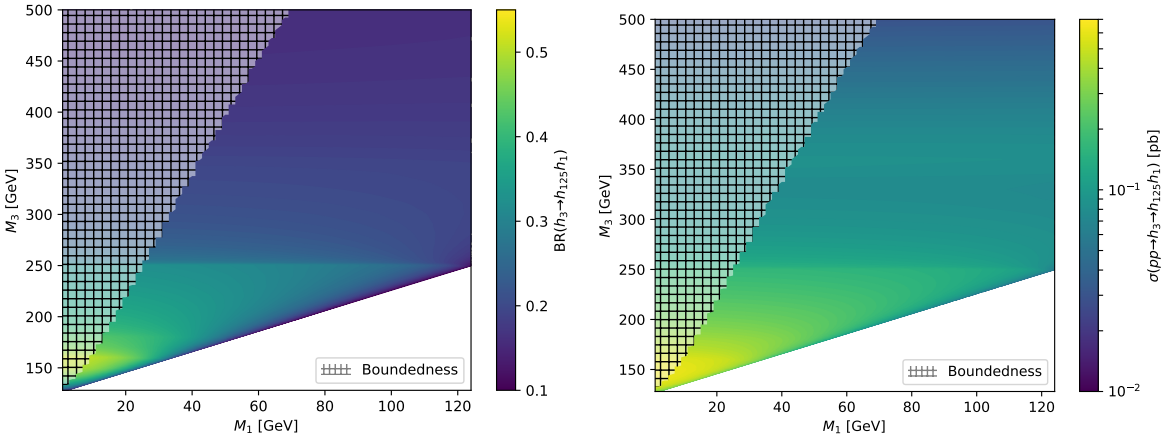

Figure 4.7: Benchmark plane **BP2** for the decay signature $h_3 \to h_1 h_{125}$ with $h_{125} \equiv h_2$, defined in the (M_1, M_3) plane. The colour code shows $\mathrm{BR}(h_3 \to h_1 h_{125})$ (left panel) and the cross section for $pp \to h_3 \to h_1 h_{125}$ (right panel).

decay directly to SM particles, with BRs identical to a SM-like Higgs boson with the corresponding mass (see fig. 4.1). Therefore, for masses $M_1, M_2 \gtrsim 10\,\mathrm{GeV}$, the $b\bar{b}b\bar{b}$ final state dominates, as shown in fig. 4.6 (bottom left), while at smaller masses, combinations with τ-leptons and eventually final states containing charm quarks, muons, and photons become relevant.

4.5.2 BP2 — $h_3 \to h_1 h_{125}$

In the second benchmark scenario, **BP2**, we identify $h_{125} \equiv h_2$ and consider the production of h_3 followed by the asymmetric decay $h_3 \to h_1 h_{125}$. The scenario is defined in the (M_1, M_3) parameter plane, and the remaining parameters are fixed to the values given in table 4.2a. The mixing angles are chosen such that the production rate of h_3 is maximised, while the h_2 properties remain consistent with the measured Higgs signal rates. This results in a h_3 production rate of roughly 4% of the production cross section for a h_{SM} at the same mass.

The phenomenology of **BP2** is illustrated by fig. 4.7. The $\mathrm{BR}(h_3 \to h_1 h_2)$ shown in fig. 4.7 (left) mostly stays above 20 % for $M_3 \lesssim 350\,\mathrm{GeV}$, reaching maximal values of around $50 - 55\,\%$ in the low mass region, $M_3 \sim 150 - 170\,\mathrm{GeV}$. In this region, the corresponding cross section in fig. 4.7 (right) is about 0.6 pb. It remains above 50 fb as long as $M_3 \lesssim 450\,\mathrm{GeV}$. The shaded region in fig. 4.7 is excluded by boundedness of the scalar potential. Again, this constraint depends strongly on the values of the model parameters and should not discourage experimental efforts to perform model-independent searches in this mass range. The total width of h_3 can reach maximal values of $\Gamma_3/M_3 \sim 1.1\,\%$ in this benchmark scenario for $M_3 \gtrsim 480\,\mathrm{GeV}$.

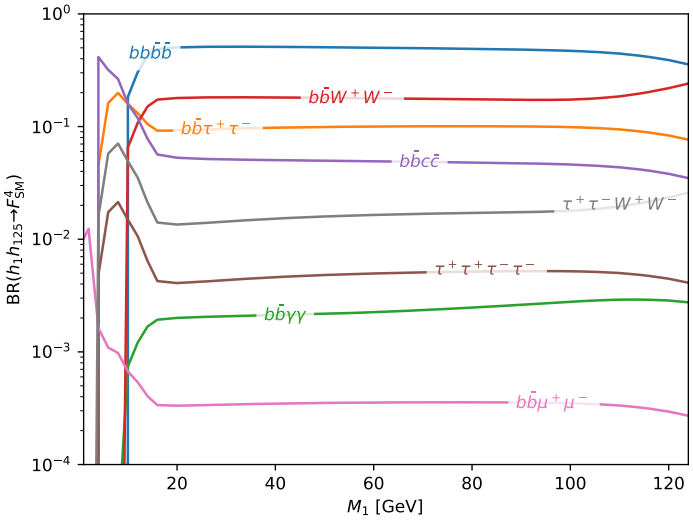

Figure 4.8: Decay rates of $h_1 h_2$ into selected SM final states as a function of M_1 in **BP2**.

The decay rates of $h_1 h_{125}$ into SM final states are shown in fig. 4.8 for **BP2** as a function of M_1. In most of the mass range, the $b\bar{b}b\bar{b}$ final state dominates, followed by $b\bar{b}W^+W^-$ and $b\bar{b}\tau^+\tau^-$ final states. The cascade decay $h_{125} \equiv h_2 \to h_1 h_1$ is in principle possible if kinematically allowed and in compliance with the observed h_{125} properties. However, we chose κ_2^2 small in order to maximize κ_3^2 within the experimental constraints. From fig. 4.2 we see that, at the corresponding value of κ_2, $\mathrm{BR}(h_{125} \to \mathrm{NP})$ must not exceed 2.5 %. In **BP2** this decay rate is always below 1 ‰.

Besides the asymmetric decay $h_3 \to h_1 h_2$ the symmetric decays $h_3 \to h_1 h_1$ and $h_3 \to h_2 h_2$ are also present in this scenario. The $\mathrm{BR}(h_3 \to h_1 h_1)$ is $\gtrsim 25\,\%$ in the mass range $M_3 \lesssim 250\,\mathrm{GeV}$. The decay mode $h_3 \to h_2 h_2$ only becomes kinematically open for $M_3 \gtrsim 2M_2 = 250\,\mathrm{GeV}$, and reaches BRs up to $\sim 28\,\%$. Although these rates are not negligible in **BP2**, we shall define dedicated benchmark scenarios **BP5** and **BP6** below, where these decay modes clearly dominate.

4.5.3 BP3 — $h_3 \to h_{125} h_2$

In benchmark scenario **BP3** we identify $h_{125} \equiv h_1$ and consider the production of h_3 followed by the asymmetric decay $h_3 \to h_{125} h_2$. Similar to the **BP2** scenario the mixing angles are chosen to maximize $\kappa_3^2 \simeq 5.7\,\%$ and $\mathrm{BR}(h_3 \to h_1 h_2)$. The benchmark plane corresponding to the parameters given in table 4.2a is shown in fig. 4.9.

The $\mathrm{BR}(h_3 \to h_{125} h_2)$ shown in fig. 4.9 (left) is $\gtrsim 35\,\%$ throughout the benchmark plane except for the region very close to threshold. It reaches values around 50 % in the parameter region $M_3 \lesssim 2M_2$. The signal cross section, $\sigma(pp \to h_3 \to h_1 h_2)$ shown in fig. 4.9 (right), reaches up to 0.3 pb while $M_3 \lesssim 500\,\mathrm{GeV}$. At large values of $M_3 \gtrsim 500 - 600\,\mathrm{GeV}$ the parameter space is partly constrained by perturbative

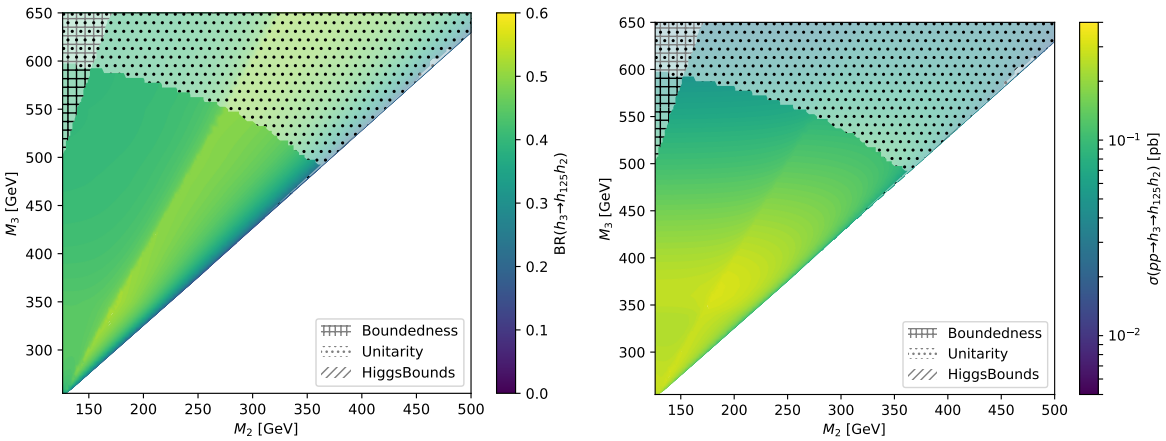

Figure 4.9: Benchmark plane **BP3** for the decay signature $h_3 \to h_{125}h_2$ with $h_{125} \equiv h_1$, defined in the (M_2, M_3) plane. The colour code shows $\mathrm{BR}(h_3 \to h_{125}h_2)$ (left panel) and the cross section for $pp \to h_3 \to h_{125}h_2$ (right panel). The shaded regions are excluded by boundedness from below, perturbative unitarity, and searches for heavy scalar resonances in diboson final states [295, 296].

unitarity, and if simultaneously $M_1 \lesssim 150\,\mathrm{GeV}$ the potential can become unbounded from below, as indicated by the shaded regions. Very close to its kinematic threshold, $M_3 \sim M_1 + 125\,\mathrm{GeV}$, the decay $h_3 \to h_{125}h_1$ is strongly suppressed. In this case, constraints can be derived from current LHC searches for heavy resonances, in particular for the process $pp \to h_3 \to ZZ$ [295, 296]. The total width of h_3 is maximal for the largest allowed values of M_3 and reaches $\Gamma_3/M_3 \sim 4\,\%$ for $M_3 \gtrsim 600\,\mathrm{GeV}$.

If $M_2 < 250\,\mathrm{GeV}$, BSM decay modes of h_2 are forbidden and its BRs are identical to an h_{SM} of the same mass (see fig. 4.1). In this region the dominant final states of $h_{125}h_2 \to F_{\mathrm{SM}}$ involve b-quarks and heavy gauge bosons as shown in fig. 4.10. As soon as $M_2 > 250\,\mathrm{GeV}$ the decay $h_2 \to h_{125}h_{125}$ becomes dominant, quickly reaching BRs of $\sim 70\,\%$. Above threshold this BR remains largely independent of M_2. The decay rates of the resulting $h_{125}h_{125}h_{125}$ into the most important six particle SM final states, F^6_{SM}, are given in table 4.3. The first row lists the direct decay rates of $h_{125}h_{125}h_{125}$ while the second row includes the factor $\mathrm{BR}(h_2 \to h_{125}h_{125}) \approx 68\,\%$, which is an approximation averaged over the mass region $260\,\mathrm{GeV} < M_2 < 500\,\mathrm{GeV}$. The resulting values can thus be compared directly to decay rates of the four particle F^4_{SM} in fig. 4.10. For instance, rates for $b\bar{b}b\bar{b}b\bar{b}$, $b\bar{b}b\bar{b}W^+W^-$ and $b\bar{b}W^+W^-$ final states are of comparable size for $M_2 \gtrsim 270\,\mathrm{GeV}$.

In **BP3**, the competing symmetric decay $h_3 \to h_2h_2$ reaches BRs of $\sim 20\,\%$ if kinematically allowed. Otherwise the decay $h_3 \to h_{125}h_{125}$ reaches similar values (and becomes dominant in the threshold region, $M_3 \sim M_1 + M_2$).

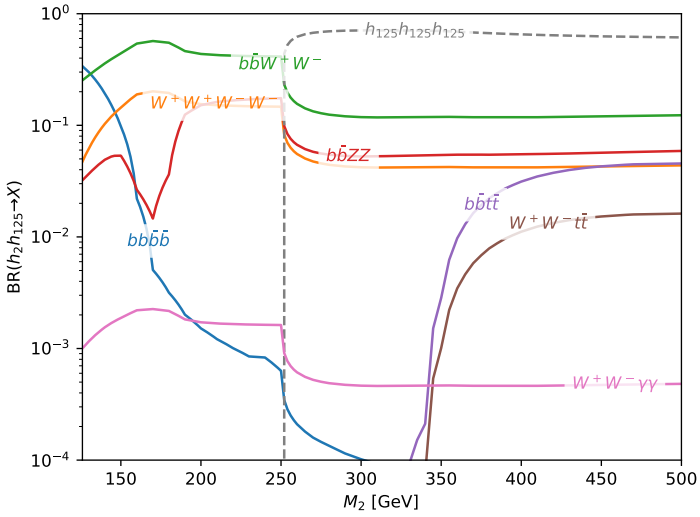

Figure 4.10: Branching ratios of the $h_{125}h_2$ state as a function of M_2 for **BP3**. Included are a selection of the decay modes into SM particles as well as the cascade decay to $h_{125}h_{125}h_{125}$.

Table 4.3: Decay rates of $h_{125}h_{125}h_{125} \to F^6_{\text{SM}}$ in **BP3**. The second row gives the corresponding rates originating from h_2h_{125}, assuming $\text{BR}(h_2 \to h_{125}h_{125}) \approx 68\,\%$.

$\text{BR}(X \to F^6_{\text{SM}})$ in %	$6b$	$4b2W$	$2b4W$	$4b2\tau$	$4b2Z$	$4b2\gamma$
$h_{125}h_{125}h_{125}$	20	22	7.8	6.6	2.8	0.24
h_2h_{125}	14	15	5.3	4.5	1.9	0.16

4.5.4 BP4 — $h_2 \to h_1h_1$ with $h_{125} \equiv h_3$

We now turn to the symmetric Higgs-to-Higgs decay signatures. In benchmark scenario **BP4** we identify $h_{125} \equiv h_3$ and focus on the production of h_2 followed by its decay $h_2 \to h_1h_1$. In order to avoid constraints from the Higgs rate measurements on the possible decays $h_{125} \to h_ah_b$ $(a, b \in \{1, 2\})$, the relevant couplings must be tuned to rather small values while keeping κ_2^2 relatively large to ensure sizeable direct production of h_2. The parameter choices for **BP4** are listed in table 4.2.

Figure 4.11 shows the collider phenomenology of **BP4**. The branching ratio $\text{BR}(h_2 \to h_1h_1)$ is larger than 40 % throughout the allowed parameter plane, as shown in fig. 4.11 (left). For $M_2 \gtrsim 40\,\text{GeV}$ it is by far the dominant decay mode of h_2 with a BR of more than 90 %. As the produced scalar boson is light, the cross sections shown in fig. 4.11 (right) are enhanced by the large ggF cross section for light scalars. Even though h_2 is only produced with a rate of about $\kappa_2^2 \sim 5\%$ of the h_{SM} cross section at the same mass we still obtain cross sections of $\mathcal{O}(100\,\text{pb})$ in the low mass region $M_2 \lesssim 20\,\text{GeV}$. However, this parameter region is partly constrained by LEP searches for $e^+e^- \to Zh_2 \to Z(b\bar{b})$ [293]. For $M_2 \geq 20\,\text{GeV}$ this limit becomes insensitive as $\text{BR}(h_2 \to h_1h_1)$ increases when the

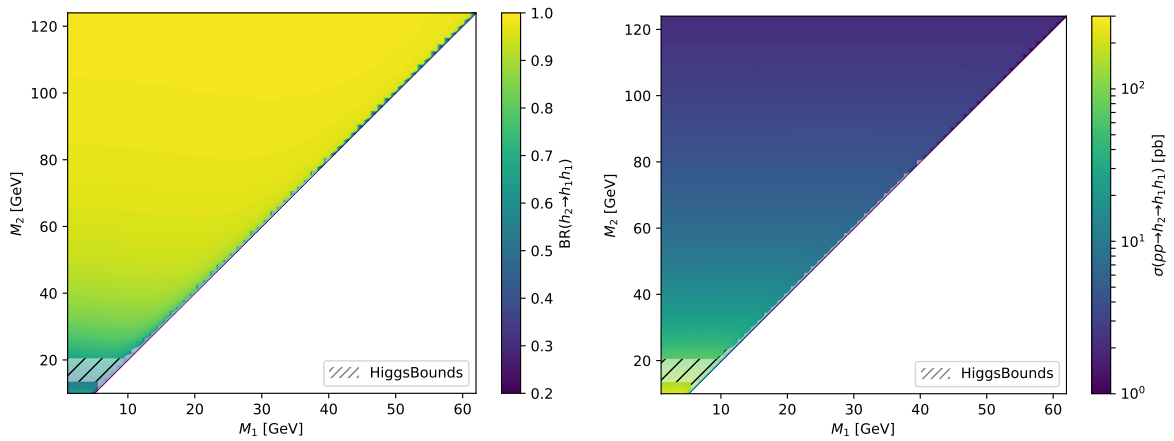

Figure 4.11: Benchmark plane **BP4** for the decay signature $h_2 \to h_1 h_1$ with $h_{125} \equiv h_3$, defined in the (M_1, M_2) plane. The colour code shows $\mathrm{BR}(h_2 \to h_1 h_1)$ (left panel) and the cross section for $pp \to h_2 \to h_1 h_1$ (right panel). The shaded region is excluded by LEP searches for $e^+e^- \to Zh_2 \to Z(b\bar{b})$ [293].

corresponding coupling is no longer suppressed by small Higgs masses (see section 4.2.1). The cross section in this region can still reach 60 pb. However, the signature remains experimentally challenging as the decay products for these low M_1 will be very soft.

The rates for the decay modes of $h_1 h_1$ into SM particles are shown in fig. 4.12. For $M_1 \gtrsim 10\,\mathrm{GeV}$ the decay into $b\bar{b}b\bar{b}$ is dominant followed by $b\bar{b}\tau^+\tau^-$. For even lighter M_1 the predominant decay is into charm quarks.

4.5.5 BP5 — $h_3 \to h_1 h_1$ with $h_{125} \equiv h_2$

In the benchmark plane **BP5** we identify $h_{125} \equiv h_2$ and consider the production of the heavier scalar h_3 followed by its symmetric decay to the lightest scalar, $h_3 \to h_1 h_1$. In our parameter scan of the TRSM (see section 4.3.1) we found that parameter points exhibiting a sizeable $pp \to h_3 \to h_1 h_1$ rate also tend to be strongly constrained by the Higgs signal strength measurements if $2M_1 < 125\,\mathrm{GeV}$. In addition, if kinematically accessible, the decay modes $h_3 \to h_{125}h_{125}$ and/or $h_3 \to h_1 h_{125}$ tend to dominate over the decay $h_3 \to h_1 h_1$. In order to define a suitable benchmark scenario for the $pp \to h_3 \to h_1 h_1$ process it is therefore necessary that all triple Higgs couplings except for $\tilde{\lambda}_{113}$ are small while not overly suppressing κ_3. The chosen parameter values of **BP5** are given in table 4.2.

The phenomenology of **BP5** is shown in fig. 4.13. Throughout the parameter plane $\mathrm{BR}(h_3 \to h_1 h_1)$ — shown in fig. 4.13 (left) — exceeds 85 % and approaches 100 % for low values of M_3. The heavy scalar h_3 is produced at a rate of around $\kappa_3^2 \approx 6\,\%$ of the corresponding prediction for h_{SM}. Figure 4.13 (right) shows the resulting signal cross sections of $\mathcal{O}(0.1 - 1\,\mathrm{pb})$ with maximal values around 3 pb for light $M_3 \lesssim 150\,\mathrm{GeV}$. The

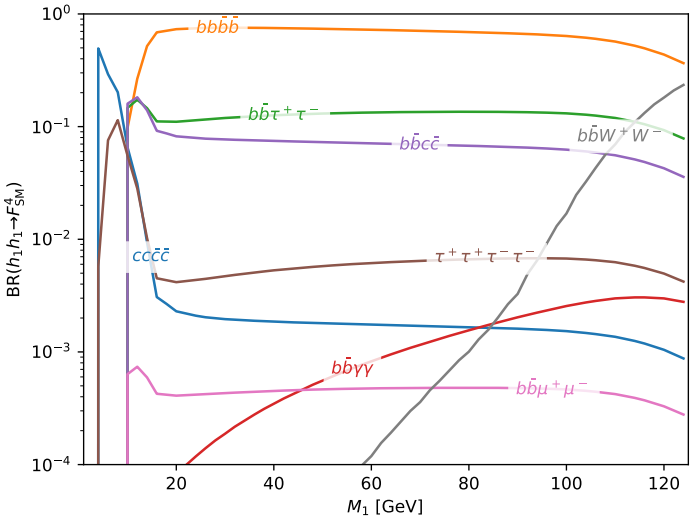

Figure 4.12: Decay rates of $h_1h_1 \to F^4_{\mathrm{SM}}$ in **BP4** and **BP5** for selected SM decay modes as a function of M_1.

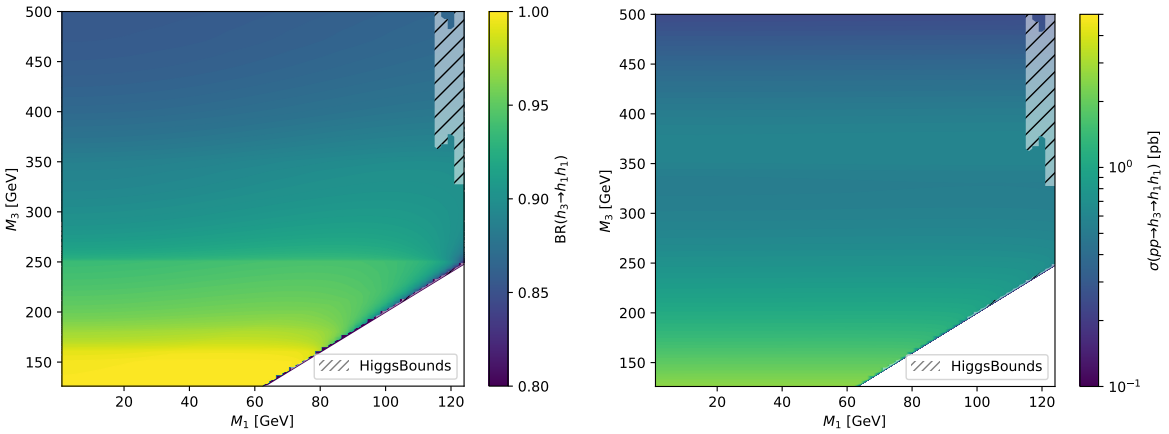

Figure 4.13: Benchmark plane **BP5** for the decay signature $h_3 \to h_1h_1$ with $h_{125} \equiv h_2$, defined in the (M_1, M_3) plane. The colour code shows $\mathrm{BR}(h_3 \to h_1h_1)$ (a) and the cross section for $pp \to h_3 \to h_1h_1$ (b). The shaded region is excluded by searches for resonant double Higgs production [270, 273] via `HiggsBounds`.

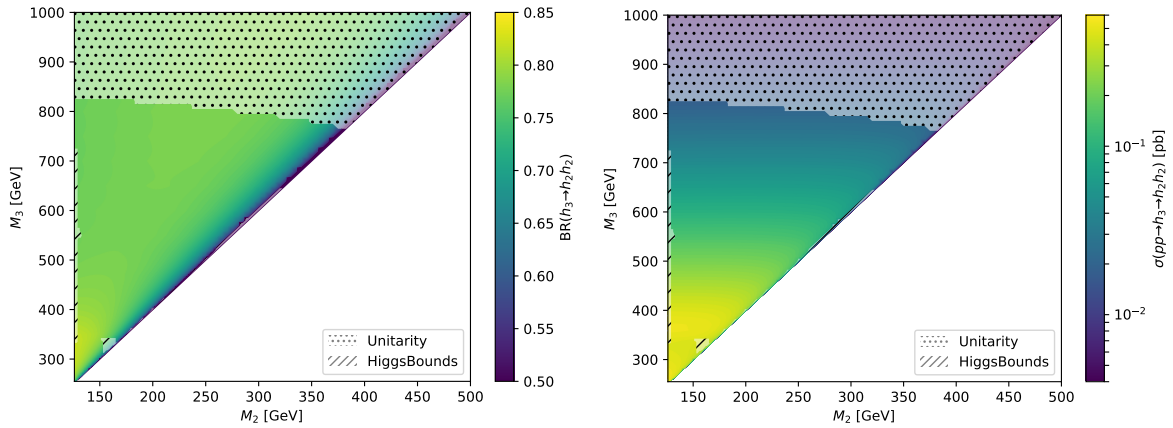

Figure 4.14: Benchmark plane **BP6** for the decay signature $h_3 \to h_2 h_2$ with $h_{125} \equiv h_1$, defined in the (M_2, M_3) plane. The colour code shows $\mathrm{BR}(h_3 \to h_2 h_2)$ (left panel) and the cross section for $pp \to h_3 \to h_2 h_2$ (right panel). The shaded region at large M_3 is excluded by perturbative unitarity. The shaded region at $M_2 \sim 125\,\mathrm{GeV}$ is excluded by searches for resonant double Higgs production [273], and the shaded parameter region around $M_2 \simeq 160\,\mathrm{GeV}$, $M_3 \simeq 330\,\mathrm{GeV}$ by an ATLAS search for $h_3 \to h_2 h_2 \to W^+W^-W^+W^-$ [266] via `HiggsBounds`.

parameter region at $M_1 \gtrsim 120\,\mathrm{GeV}$ and $M_3 \gtrsim 350\,\mathrm{GeV}$ is constrained by LHC Higgs searches for resonant double Higgs production [270, 273]. These are applied under the assumption that h_1 cannot be experimentally distinguished from $h_{125} \equiv h_2$ if they are close in mass and thus contributes to the predicted signal rate for this process.

The decay rates of $h_1 h_1 \to F^4_{\mathrm{SM}}$ can again be found in fig. 4.12. They are identical to those discussed for **BP4** since the BRs of h_1 are always identical to those of h_{SM} at the same mass (see section 4.2.1). However, now the scenario extends to M_1 values up to 125 GeV, and with increasing M_1 the final state $b\bar{b}W^+W^-$ becomes sizeable. In contrast to **BP4**, the two h_1 may be boosted if $M_3 \gg 2M_1$, leading to collimated h_1 decay products. This may provide an additional experimental handle by enabling the use of jet-substructure techniques and reducing combinatorial background. Boosted decay products may also lead to an increased trigger sensitivity.

4.5.6 BP6 — $h_3 \to h_2 h_2$ with $h_{125} \equiv h_1$

In benchmark plane **BP6** we identify $h_{125} \equiv h_1$ and consider the production of the heaviest scalar h_3 followed by its symmetric decay $h_3 \to h_2 h_2$. This constrains the mass range for h_3 to values $M_3 > 250\,\mathrm{GeV}$. In combination with the suppression of κ_3 due to the sum rule, eq. (4.18), the resulting production cross sections are rather low. The input parameters for **BP6** are listed in table 4.2.

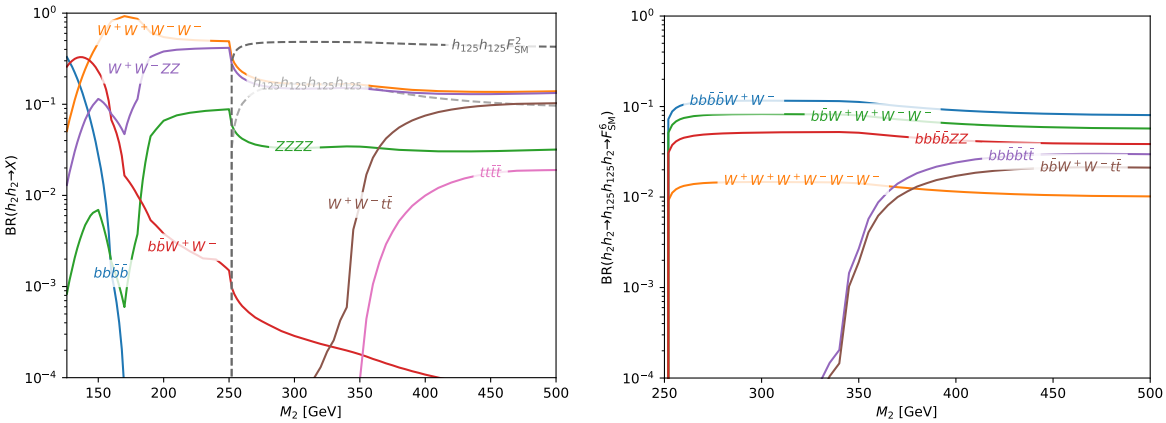

Figure 4.15: Branching ratios of the h_2h_2 state of **BP6**. The left panel contains a selection of final states from direct decays of $h_2 \to F_{\text{SM}}$ and (inclusive) decays involving $h_2 \to h_{125}h_{125}$ (both single and double cascade). The right panel shows the most important six particle SM final states, F^6_{SM}, that originate from a single cascade $h_2h_2 \to h_{125}h_{125}F_{\text{SM}}$.

Figure 4.14 shows the resulting (M_2, M_3) parameter plane. The decay channel $h_3 \to h_2h_2$ — shown in fig. 4.14 (left) — is the dominant decay mode of h_3 over the entire accessible parameter range with a BR $\gtrsim 75\,\%$ except close to the kinematic threshold. The heavy scalar h_3 is produced with about $\kappa_3^2 = 6\,\%$ of the corresponding h_{SM} rate. The resulting cross section in fig. 4.14 (right) reaches $\sim 0.5\,\text{pb}$ in the low mass range, $M_3 \lesssim 400\,\text{GeV}$, where h_2 decays directly to SM particles. The cross sections in the mass range $M_3 \gtrsim 600\,\text{GeV}$, which is interesting for cascade decays, can reach up to 100 fb for $pp \to h_3 \to h_2h_2$. In **BP6** the total width of h_3 can reach up to $\Gamma_3/M_3 \sim 14\,\%$ without violating the perturbative unitarity constraint. Therefore, it may be important to include finite width effects in experimental analyses of this scenario.

The shaded region at large masses, $M_3 \gtrsim 800\,\text{GeV}$, indicates that the parameter region is in conflict with perturbative unitarity. Additionally, experimental searches [273] are beginning to probe the region $M_2 \sim 125\,\text{GeV}$. Similar to the discussion of **BP5**, this is a limit on $h_3 \to h_{125}h_{125}$ which is sensitive under the assumption that h_2 and $h_1 \equiv h_{125}$ cannot be experimentally distinguished from each other if they are close in mass. Moreover, a first ATLAS search for the signature $pp \to h_3 \to h_2h_2 \to W^+W^-W^+W^-$ [266] constrains a small region around $M_2 \simeq 160\,\text{GeV}$, $M_3 \simeq 330\,\text{GeV}$, as shown in fig. 4.14. We expect this analysis to sensitively probe the **BP6** scenario in the future provided that the currently considered mass range is extended. The ATLAS search only considers h_3 masses up to the $t\bar{t}$ threshold, $M_3 \leq 340\,\text{GeV}$. However, in our scenario the $W^+W^-W^+W^-$ final state remains the dominant SM final state of h_3 even beyond the $t\bar{t}$ threshold.

Figure 4.15 shows the decay rates of $h_2h_2 \to F_{\text{SM}}$ in **BP6**. At low $M_2 < 250\,\text{GeV}$ only $h_2 \to F_{\text{SM}}$ decays are kinematically allowed. As shown in fig. 4.15 (left), the dominant final state is $W^+W^-W^+W^-$ followed by $b\bar{b}W^+W^-$ at low masses and W^+W^-ZZ at

Table 4.4: Rates for some decay modes of $h_{125}h_{125}h_{125}h_{125} \to F^8_{\rm SM}$ in **BP6**. The second row includes a factor of $\mathrm{BR}(h_2h_2 \to h_{125}h_{125}h_{125}h_{125}) \approx 14\,\%$.

$\mathrm{BR}(X \to F^8_{\rm SM})$ in %	$6b2W$	$8b$	$4b4W$	$6b2\tau$	$4b2W2Z$	$6b2Z$	$6b2\gamma$
$h_{125}h_{125}h_{125}h_{125}$	17.0	12.0	9.2	5.2	2.3	2.2	0.19
h_2h_2	2.5	1.7	1.3	0.75	0.33	0.31	0.027

larger mass values.

For $M_2 \gtrsim 250\,\mathrm{GeV}$ all three classes of decay chains from fig. 4.5 can occur in **BP6**: direct decays of $h_2h_2 \to F^4_{\rm SM}$, single cascade decays $h_2h_2 \to h_{125}h_{125}h_2 \to F^6_{\rm SM}$, and double cascade decays $h_2h_2 \to h_{125}h_{125}h_{125}h_{125} \to F^8_{\rm SM}$, where the latter leads to a spectacular final state composed of four h_{125}. The rates for direct decays of $h_2h_2 \to F^4_{\rm SM}$ are given in fig. 4.15 (left). The dominant final states of this class are $W^+W^-W^+W^-$ and W^+W^-ZZ, with $W^+W^-t\bar{t}$ becoming comparable at high M_2. Figure 4.15 (left) also shows the "inclusive" branching ratio for the single cascade $h_{125}h_{125}F_{\rm SM}$ (summed over all possible $h_2 \to F_{\rm SM}$) and the double cascade decay rate to the $h_{125}h_{125}h_{125}h_{125}$ final state.

The decay rates of h_2h_2 into various six-particle SM final states via the single cascade decay are shown in the right panel of fig. 4.15. The most important decay modes involve b quarks and W bosons and — due to combinatorial enhancement — have decay rates comparable to the four-particle final states. The decay $h_2h_2 \to h_{125}h_{125}h_2 \to b\bar{b}b\bar{b}W^+W^-$ is the third most likely decay mode of h_2h_2 for $250\,\mathrm{GeV} < M_2 < 350\,\mathrm{GeV}$.

The decay rates of $h_{125}h_{125}h_{125}h_{125} \to F^8_{\rm SM}$ following a double cascade decay are independent of the model parameters. They are given in table 4.4. Since the double cascade decay indicated in fig. 4.15 (left) is almost independent of M_2 we include in the second row of table 4.4 an approximate rate for the decay of h_2h_2 into an eight-particle SM final state through the double cascade. For this we use the averaged $\mathrm{BR}(h_2h_2 \to h_{125}h_{125}h_{125}h_{125}) = 14.5\,\%$ evaluated in the mass range $260\,\mathrm{GeV} < M_2 < 500\,\mathrm{GeV}$. The most important eight-particle final states are all combinations of decays into b quarks and W bosons — the most likely decay products of h_{125}. Due to combinatorial factors their overall branching fractions are, again, in some cases comparable to the four- and six-particle final states. For example, the $b\bar{b}b\bar{b}b\bar{b}W^+W^-$ final state has rates similar to the $ZZZZ$ final state for masses $M_3 \sim 300 - 350\,\mathrm{GeV}$.

4.6 Conclusions

In this chapter, we have presented the collider phenomenology of a simple extension of the SM Higgs sector — the TRSM — where two real scalar singlet fields are added to the particle content. We have imposed a discrete $\mathbb{Z}_2$ symmetry for each scalar singlet field that is spontaneously broken by the the vevs. Consequently, all scalar fields mix with

each other, leading to three neutral CP-even Higgs mass eigenstates h_a ($a = 1, 2, 3$). Any of these states can be identified with the h_{125} observed at the LHC. We have discussed current collider constraints on the model in detail and have illustrated the impact of the most constraining searches for additional Higgs bosons on the TRSM parameter space.

The model leads to an interesting collider phenomenology for searches for the additional Higgs states. Following the single production of one of the Higgs states, h_a, this state can either decay directly to SM particles, or it can decay into two lighter Higgs states, $h_a \to h_b h_c$, where the lighter states can either be identical ("symmetric" Higgs-to-Higgs decays with $b = c = 1, 2$), or different ("asymmetric" Higgs-to-Higgs decays with $b = 1$, $c = 2$). Successive decays of the second-lightest Higgs state to the lightest Higgs state, $h_2 \to h_1 h_1$ may be possible if kinematically allowed. This leads to interesting Higgs-to-Higgs cascade decay signatures, in particular, $h_3 \to h_{1,2} h_2 \to h_{1,2} h_1 h_1$ ("single cascade") and $h_3 \to h_2 h_2 \to h_1 h_1 h_1 h_1$ ("double cascade"), as shown in fig. 4.5. We find that rates for all these possible Higgs-to-Higgs decays can in general be sizeable, easily dominating the direct decay modes to SM particles.

Many of these Higgs-to-Higgs decay signatures have not been investigated experimentally to date. We have therefore presented six two-dimensional benchmark scenarios to facilitate the design of dedicated experimental searches. Each scenario is defined such that one of the novel signatures has a nearly-maximal signal rate, while still obeying all theoretical and experimental constraints on the model. Moreover, as the model can be parametrised conveniently in terms of the relevant physical parameters, *i.e.* the three Higgs masses, three mixing angles (governing the Higgs coupling strengths to SM particles) and the three vevs, the benchmark scenarios can cover the entire kinematical phase space for the decay signatures, thus rendering them as ideal references for experimental searches.

For each benchmark scenario, we discussed in detail the rates of the relevant decays, as well as the expected cross sections in the TRSM at the 13 TeV LHC. We furthermore provided an overview of the most relevant SM particle final states, as a function of the relevant mass parameters. This should provide a first step for experimental analyses to estimate the discovery potential of corresponding searches. We expect that some of the presented signatures can already be probed sensitively at the LHC with the data of $\sim 150\,\text{fb}^{-1}$ per experiment collected during Run-II.

It should be kept in mind that the Higgs-to-Higgs decay signatures (and potentially also the cascade decays) discussed here can generically appear also in other BSM models that feature three (or more) Higgs states. In that case, however, the Higgs coupling properties do not necessarily agree with those of the TRSM. This may result in different production rates of the resonantly-produced Higgs state, as well as different decay rates, in particular concerning the Higgs decays to SM particles. It is therefore important that future experimental searches present their results as limits — or ideally measurements — of the approximately model-independent signal rate, as a function of the relevant kinematical quantities (Higgs masses and, possibly, total widths). Furthermore, Higgs-to-Higgs decays to possible SM particle final states that are not dominant in the TRSM

may still be worthwhile to probe experimentally, as the anticipated rates may be different in other models.

The exploration of the scalar sector — leading to a better understanding of the mechanism of electroweak symmetry breaking — is one of the most important scientific goals of the LHC programme. This endeavour requires an open-minded and unbiased view on the potential collider signatures of new scalars. Our discussion of the TRSM and the presented benchmark scenarios demonstrate that there is a plethora of currently unexplored collider signatures involving Higgs-to-Higgs decays, and we hope that this work will initiate and facilitate the design of corresponding LHC searches in the near future.

In the next chapter, we turn to BSM models that introduce new sources of CP violation into the scalar sector. The CP-violating 2HDM discussed there also features three neutral Higgs bosons that mix with each other and can produce Higgs-to-Higgs decay signatures — similar to those discussed in this chapter — which we have studied in ref. [1]. However, in the next chapter we will instead focus on the consequences of CP-violating extended Higgs sectors for measurements of h_{125} couplings and CP-violating observables.

5 CP Violation in Visible and Invisible Higgs Sectors

In this chapter, we discuss the phenomenology of two minimal models with CP-violating scalar sectors — one where CP violation is strongly constrained and one where it is hidden in a dark sector. We have published the results in the first section in ref. [1] and those discussed in the second section in ref. [2].

5.1 CP Violation in the 2HDM

We have introduced the two-Higgs-doublet model (2HDM) in section 2.5.1. In this section we study the phenomenology of the CP-violating 2HDM with a focus on the possibilities for a CP-odd admixture to the 125 GeV Higgs boson (h_{125}). The 2HDM scalar potential with a softly broken $\mathbb{Z}_2$ symmetry, $\Phi_2 \to -\Phi_2$, is given by

$$\begin{aligned} V = {} & m_{11}^2|\Phi_1|^2 + m_{22}^2|\Phi_2|^2 - \left(m_{12}^2\,\Phi_1^\dagger\Phi_2 + \text{H.c.}\right) \\ & + \frac{\lambda_1}{2}(\Phi_1^\dagger\Phi_1)^2 + \frac{\lambda_2}{2}(\Phi_2^\dagger\Phi_2)^2 + \lambda_3(\Phi_1^\dagger\Phi_1)(\Phi_2^\dagger\Phi_2) \\ & + \lambda_4(\Phi_1^\dagger\Phi_2)(\Phi_2^\dagger\Phi_1) + \left[\frac{\lambda_5}{2}(\Phi_1^\dagger\Phi_2)^2 + \text{H.c.}\right]. \end{aligned} \tag{5.1}$$

As discussed in section 2.5.1, this $\mathbb{Z}_2$ symmetry is extended to the Yukawa sector in order to realise natural flavour conservation (NFC) leading to the four Yukawa types (see section 2.1). All couplings except for m_{12}^2 and λ_5 are required to be real by hermiticity of the Lagrangian. This scalar potential has six real and two complex parameters for a total of ten real parameters. This softly broken $\mathbb{Z}_2$ symmetric 2HDM is the minimal scalar extension of the SM that allows for CP violation.

Expanding each of the doublets Φ_i ($i = 1, 2$) around the (in general complex) vacuum expectation values (vevs) v_1 and v_2 in terms of the complex charged fields (ϕ_i^+) and the real neutral fields (ρ_i and η_i) yields

$$\Phi_1 = \begin{pmatrix} \phi_1^+ \\ \frac{v_1+\rho_1+i\eta_1}{\sqrt{2}} \end{pmatrix}, \quad \Phi_2 = \begin{pmatrix} \phi_2^+ \\ \frac{v_2+\rho_2+i\eta_2}{\sqrt{2}} \end{pmatrix}. \tag{5.2}$$

The corresponding stationarity conditions, eq. (3.2), for the potential are

$$\mathrm{Re}(m_{12}^2)v_2 = m_{11}^2 v_1 + \frac{\lambda_1}{2}v_1^3 + \frac{\lambda_{345}}{2}v_1 v_2^2\,, \tag{5.3}$$

$$\mathrm{Re}(m_{12}^2)v_1 = m_{22}^2 v_2 + \frac{\lambda_2}{2}v_2^3 + \frac{\lambda_{345}}{2}v_1^2 v_2\,, \tag{5.4}$$

$$2\mathrm{Im}(m_{12}^2) = v_1 v_2 \mathrm{Im}(\lambda_5)\,, \tag{5.5}$$

with

$$\lambda_{345} \equiv \lambda_3 + \lambda_4 + \mathrm{Re}(\lambda_5)\,. \tag{5.6}$$

We define the phases $\phi(m_{12}^2)$ and $\phi(\lambda_5)$ of the complex parameters as

$$m_{12}^2 = |m_{12}^2| e^{i\,\phi(m_{12}^2)}\,, \qquad \lambda_5 = |\lambda_5| e^{i\,\phi(\lambda_5)}\,. \tag{5.7}$$

It is always possible to absorb any phase of v_1 and v_2 into these phases of the parameters through a field redefinition. Assuming v_1 and v_2 to be real the condition [297]

$$\phi(\lambda_5) \neq 2\phi(m_{12}^2) \tag{5.8}$$

ensures that the two phases cannot be removed simultaneously and CP violation in the Higgs sector occurs. We call the region of parameter space where the inequality, eq. (5.8), is satisfied the CP-violating 2HDM (C2HDM) (see *e.g.* refs. [1, 25, 297–300]). If $\phi(\lambda_5) = 2\phi(m_{12}^2)$ for real v_1 and v_2 the model can be expressed as a real (CP-conserving) 2HDM (R2HDM) through a rephasing of the $\mathrm{SU}(2)_L$ doublets.

It is useful to introduce the Higgs basis $\{\mathcal{H}_1, \mathcal{H}_2\}$ through the field rotation

$$\begin{pmatrix}\mathcal{H}_1\\ \mathcal{H}_2\end{pmatrix} = \begin{pmatrix}\cos\beta & \sin\beta\\ -\sin\beta & \cos\beta\end{pmatrix}\begin{pmatrix}\Phi_1\\ \Phi_2\end{pmatrix} \tag{5.9}$$

with $\tan\beta = v_2/v_2$, to separate the would-be goldstone bosons from the physical degrees of freedom. The resulting doublets in the Higgs basis are given by

$$\mathcal{H}_1 = \begin{pmatrix} G^\pm \\ \frac{1}{\sqrt{2}}(v + H^0 + iG^0)\end{pmatrix}\,, \quad \mathcal{H}_2 = \begin{pmatrix} H^\pm \\ \frac{1}{\sqrt{2}}(R_2 + iI_2)\end{pmatrix}\,. \tag{5.10}$$

The electroweak (EW) vev $v = \sqrt{v_1^2 + v_2^2} \approx 246\,\mathrm{GeV}$ along with the Goldstone bosons $G^\pm$ and G^0 is now separated into $\mathcal{H}_1$, while the charged Higgs mass eigenstates $H^\pm$ are in $\mathcal{H}_2$. The neutral Higgs mass eigenstates H_i $(i = 1, 2, 3)$ can then obtained from the three neutral fields ρ_1, ρ_2 and I_2 via the rotation

$$\begin{pmatrix}H_1\\ H_2\\ H_3\end{pmatrix} = R\begin{pmatrix}\rho_1\\ \rho_2\\ I_2\end{pmatrix} \tag{5.11}$$

which diagonalises their 3×3 mass matrix $\mathcal{M}^2$ through

$$R\mathcal{M}^2 R^T = \mathrm{diag}(m_{H_1}^2, m_{H_2}^2, m_{H_3}^2)\,. \tag{5.12}$$

We parametrise the orthogonal mixing matrix R through three mixing angles $\alpha_{1,2,3}$ as[1]

$$R = \begin{pmatrix} c_1c_2 & s_1c_2 & s_2 \\ -(c_1s_2s_3 + s_1c_3) & c_1c_3 - s_1s_2s_3 & c_2s_3 \\ -c_1s_2c_3 + s_1s_3 & -(c_1s_3 + s_1s_2c_3) & c_2c_3 \end{pmatrix}, \tag{5.13}$$

with $s_i = \sin\alpha_i$ and $c_i = \cos\alpha_i$ $(i = 1, 2, 3)$. Without loss of generality, these angles can be chosen to lie in the range

$$-\frac{\pi}{2} \leq \alpha_{1,2,3} < \frac{\pi}{2}. \tag{5.14}$$

The Higgs mass eigenstates resulting from these diagonalisation are by definition ordered as

$$m_{H_1} \leq m_{H_2} \leq m_{H_3}. \tag{5.15}$$

Out of the ten real parameters of eq. (5.1) one is removed by the relation eq. (5.5). We express the remaining nine parameters through

$$m_{H_a}, \quad m_{H_b}, \quad m_{H^\pm}, \quad v = \sqrt{v_1^2 + v_2^2}, \quad \tan\beta, \quad \alpha_1, \quad \alpha_2, \quad \alpha_3, \quad \mathrm{Re}(m_{12}^2), \tag{5.16}$$

using eqs. (5.3), (5.4) and (5.12). In this parametrisation the mass of the third scalar — m_{H_c} where $a, b, c \in \{1, 2, 3\}$ with $a \neq b \neq c$ — is not independent but given through the other two scalar masses and the mixing matrix R as

$$m_{H_c}^2 = \frac{m_{H_a}^2 R_{a3}(R_{a2}\tan\beta - R_{a1}) + m_{H_b}^2 R_{b3}(R_{b2}\tan\beta - R_{b1})}{R_{c3}(R_{c1} - R_{c2}\tan\beta)}, \tag{5.17}$$

where no summation over repeated indices is implied.

Since both doublets have direct gauge couplings and can also couple to fermions, the C2HDM has a considerably more complicated coupling structure compared to the pure singlet extension discussed in chapter 4. The Higgs couplings to massive gauge bosons $V \in \{W, Z\}$ are

$$c(H_iVV) g_{h_{\mathrm{SM}}VV}, \tag{5.18}$$

where $g_{h_{\mathrm{SM}}VV}$ is the corresponding coupling of a SM-like Higgs boson (h_{SM}) of the same mass. The effective coupling is given by

$$c(H_iVV) = \cos\beta R_{i1} + \sin\beta R_{i2}. \tag{5.19}$$

Note that this coupling is identical to the one in the R2HDM. The CP violation in the C2HDM occurs through mixing between CP-even states — with standard gauge couplings — and CP-odd states — with no gauge couplings at all. Therefore, the gauge couplings of the H_i are simply the gauge coupling of the CP-even admixture to H_i. CP-violating anomalous gauge couplings for the H_i are only generated at the loop level and are usually too small to be currently observed.[2]

[1] This convention relates to the one used in eq. (4.13) through $\theta_{hS} = -\alpha_1$, $\theta_{hX} = -\alpha_2$, $\theta_{SX} = -\alpha_3$.

[2] We will discuss anomalous triple gauge couplings in more detail in the next section where they turn out to be the only possibility to observe CP violation.

Table 5.1: Effective Yukawa couplings of the Higgs bosons H_i in the C2HDM. The expressions correspond to $c^e(H_iff) + ic^o(H_iff)\gamma_5$ from eq. (5.20).

	u-type	d-type	leptons
Type I	$\frac{R_{i2}}{s_\beta} - i\frac{R_{i3}}{t_\beta}\gamma_5$	$\frac{R_{i2}}{s_\beta} + i\frac{R_{i3}}{t_\beta}\gamma_5$	$\frac{R_{i2}}{s_\beta} + i\frac{R_{i3}}{t_\beta}\gamma_5$
Type II	$\frac{R_{i2}}{s_\beta} - i\frac{R_{i3}}{t_\beta}\gamma_5$	$\frac{R_{i1}}{c_\beta} - it_\beta R_{i3}\gamma_5$	$\frac{R_{i1}}{c_\beta} - it_\beta R_{i3}\gamma_5$
Lepton-Specific	$\frac{R_{i2}}{s_\beta} - i\frac{R_{i3}}{t_\beta}\gamma_5$	$\frac{R_{i2}}{s_\beta} + i\frac{R_{i3}}{t_\beta}\gamma_5$	$\frac{R_{i1}}{c_\beta} - it_\beta R_{i3}\gamma_5$
Flipped	$\frac{R_{i2}}{s_\beta} - i\frac{R_{i3}}{t_\beta}\gamma_5$	$\frac{R_{i1}}{c_\beta} - it_\beta R_{i3}\gamma_5$	$\frac{R_{i2}}{s_\beta} + i\frac{R_{i3}}{t_\beta}\gamma_5$

The Yukawa couplings depend on the Yukawa type that is realised to ensure NFC. The Yukawa Lagrangian in the mass basis has the form

$$\mathcal{L}_Y \supset -\frac{m_f}{v}\bar{\psi}_f \left[c^e(H_iff) + ic^o(H_iff)\gamma_5\right]\psi_f H_i\,, \tag{5.20}$$

where ψ_f denotes a SM fermion of mass m_f. The effective fermion coupling contains a CP-even and a CP-odd part with coefficients $c^e(H_iff)$ and $c^o(H_iff)$. The expressions for these coefficient in the four Yukawa types can be found in table 5.1. These Yukawa couplings are clearly CP-violating if $c^e, c^o \neq 0$. They are the source of most of the CP-violating phenomenology in the C2HDM — for example by inducing non-vanishing fermionic electric dipole moments (EDMs). There have also been proposals to probe the CP-nature of the top-quark [301–304] or τ [305–309] Yukawa coupling directly at the LHC or a future collider. However, no experimental results are available at this point. The remaining Higgs couplings in the C2HDM can be found in the appendix of ref. [1].

5.1.1 Constraints and Parameter Scan

In order to obtain a sample of phenomenologically viable parameter points we performed a parameter scan of the C2HDM taking into account all of the applicable constraints from chapter 2.

Closed-form conditions for boundedness from below [219] and perturbative unitarity [122, 310, 311] in the 2HDM are well known and take the same form in the CP-violating and CP-conserving case. In order to completely avoid the possibility of an unstable EW vacuum we employed the discriminant obtained in ref. [312] to ensure that the EW vacuum is the global minimum of the model.

We require agreement with EW precision measurements at the 2σ level using the oblique parameters S, T and U as discussed in section 2.4.1 using the results of the EW fit presented in ref. [135] and the model predictions from refs. [137, 138]. The addition of CP violation in the C2HDM does not impact the charged sector of the 2HDM. Therefore the flavour constraints in the charged Higgs mass and $\tan\beta$ plane [135] that were discussed in section 2.4.2 are immediately applicable to the C2HDM. In the C2HDM the constraint

on the CP-violating EDM of the electron is highly relevant. The main contribution in the C2HDM comes from the so-called Barr-Zee type two-loop diagrams [157]. We require the resulting model prediction to agree with the upper limit obtained by the ACME collaboration [313]. This is an older bound than discussed in section 2.4.3 reflecting the experimental status at the time this analysis was performed. We will comment on the impact of the updated constraint below.

We employ `HiggsBounds`-4.3.1 [163, 164, 166] to check for 2σ compatibility with searches for additional scalars (see section 2.4.4). The CP-violating coupling structure can lead to large deviations from the SM-like behaviour of h_{125}. For simplicity, we exclude parameter points for which more than one scalar contributes to h_{125} by forcing the other scalar masses to be outside the mass window $m_{h_{125}} \pm 5\,\text{GeV}$. We obtain branching ratios and decay widths of all Higgs bosons with the `C2HDM_HDECAY` code [1]. The single Higgs boson production cross sections via gluon fusion (ggF) are calculated with `SusHi` [314, 315] at NNLO QCD. As the neutral scalars have no definite CP, we approximate the prediction for the CP-mixed state by summing the CP-odd and the CP-even contributions incoherently. That is, the signal strength of the fermionic single Higgs production modes, μ_F, is in our analysis given by

$$\mu_F \approx \frac{\sigma^{\text{even}}_{\text{C2HDM}}(gg \to H_i) + \sigma^{\text{odd}}_{\text{C2HDM}}(gg \to H_i)}{\sigma^{\text{even}}_{\text{SM}}(gg \to H_i)}\,, \tag{5.21}$$

where we have not written the small b-quark fusion cross section for simplicity. The production modes involving gauge bosons define the signal strength μ_V. Since there is no coupling of the CP-odd components to gauge bosons this is simply given by

$$\mu_V = c^2(H_i VV)\,, \tag{5.22}$$

which is correct up to NLO in QCD. The effective couplings are defined in eq. (5.18).

We ensure compatibility with the measurements of the h_{125} by requiring 2σ agreement of all signal strengths with the results of ref. [19]. That is, the observables

$$\frac{\mu_F}{\mu_V}\,, \quad \mu_{\gamma\gamma}\,, \quad \mu_{ZZ}\,, \quad \mu_{WW}\,, \quad \mu_{\tau\tau}\,, \quad \mu_{bb}\,, \tag{5.23}$$

with μ_{xx} defined as

$$\mu_{xx} = \mu_F \frac{\text{BR}(h_{125} \to xx)}{\text{BR}(h_{\text{SM}} \to xx)} \tag{5.24}$$

are within 2σ of the fitted experimental values. We use this method for simplicity. Note that performing a fit to up-to-date Higgs data using `HiggsSignals` is likely to give a stronger bound than this approach. All of the above constraints have been implemented in the code `ScannerS` [7, 125, 249, 290] that we use to perform parameter scans in the C2HDM.

The constraints from Higgs searches and measurements discussed above only include results from the 7 and 8 TeV runs of the LHC. At the time of this analysis, these were

Table 5.2: Input parameter ranges for the C2HDM parameter scan. One of the neutral Higgs masses m_{H_a} ($a, b, c \in \{1, 2, 3\}$ with $a \neq b \neq c$) is fixed to the measured value of 125.09 GeV. The three mixing angles $\alpha_{1,2,3}$ are scanned through their whole allowed range.

	m_{H_b} GeV	$m_{H^\pm}$ GeV	$\tan\beta$	$\mathrm{Re}(m_{12}^2)$ GeV^2
min	30	80	0.8	10^{-3}
max	1500	1500	20	5×10^5

still the most relevant constraints. We have verified that the phenomenology discussed in the following is still qualitatively possible even with up to date constraints (using `HiggsBounds` 5.4.0 and `HiggsSignals` 2.3.0) and will comment on their impact below.

Using `ScannerS`, we generate phenomenologically viable parameter points in all four Yukawa types in the parameter ranges given in table 5.2. We fix one of the neutral scalar masses to

$$m_{H_a} = 125.09\,\mathrm{GeV}\,, \tag{5.25}$$

randomly generate a second mass m_{H_b} within the range given in table 5.2, and require the third mass m_{H_c} calculated according to eq. (5.17) to lie within the same mass range as m_{H_b}. We also fix the EW vev v to its SM value, eq. (1.25). All parameter points shown in the following are results of this parameter scan and fulfil all of the mentioned constraints (unless otherwise noted).

5.1.2 A CP-Mixed h_{125}

In this section we study the phenomenological consequences of CP violation in the scalar sector. In particular, we want to study the CP nature of h_{125}, encoded in the couplings $c_f^e \equiv c^e(h_{125}ff)$ and $c_f^o \equiv c^o(h_{125}ff)$ of eq. (5.20). We know that h_{125} must have some CP-even content because of its observed couplings to ZZ and W^+W^-. However, in a theory with CP violation in the scalar sector (such as the C2HDM), h_{125} could have a mixed CP nature. This possibility can be probed in the couplings to fermions in a variety of ways. Two scenarios are of special interest to us:

- $c_f^o \sim c_{f'}^e \sim 0$: In this case h_{125} couples as a pure scalar to f and as a pure pseudoscalar to f'. This indicates maximal CP violation *between two* Yukawa couplings of h_{125}.

- $|c_f^e| \sim |c_f^o|$: The Yukawa coupling to one kind of fermion has CP-even and CP-odd components of similar size. This indicates maximal CP violation *in one* Yukawa coupling of h_{125}.

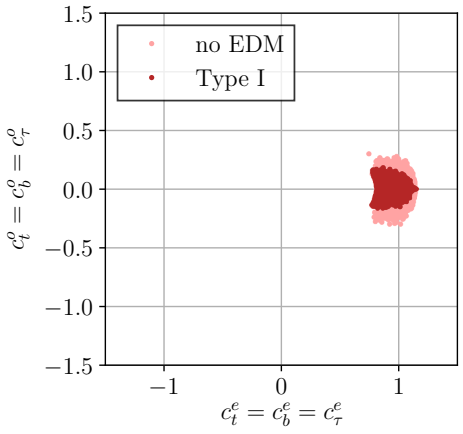

Figure 5.1: Effective CP-even and CP-odd Yukawa couplings of h_{125} in the C2HDM type I. The dark points (plotted on top) fulfil all constraints while the light points fulfil all except for the EDM constraints. Figure from our ref. [1].

We stress that maximal CP violation in the Yukawa couplings does not necessarily mean that the h_{125} has a large pseudoscalar admixture of the CP-odd component I_2 defined as

$$\Psi_{h_{125}} = \left(R_{h_{125}3}\right)^2 . \tag{5.26}$$

In ref. [9] we found that this quantity is constrained by Higgs measurements to $\Psi_{h_{125}} \lesssim 20\,\%$, which holds for all parameter points considered here. However, the enhancement of c_b^o and/or c_τ^o with $\tan\beta$ depending on the Yukawa type (see table 5.1) can lead to large c^o even for moderate values of $R_{h_{125}3}$.

For most inclusive observables the incoherent sum of CP-even and CP-odd contributions leads to a factorisation of the Yukawa couplings at leading order such that the observable is only sensitive to

$$c_f^2 = \left(c_f^e\right)^2 + \left(c_f^o\right)^2 . \tag{5.27}$$

This is not the case for the loop induced processes of Higgs production through ggF and the decay of h_{125} to $\gamma\gamma$ where the CP-even and CP-odd contributions enter with very different form factors. For this reason, even inclusive Higgs measurements can be used to constrain the CP nature of the h_{125} Yukawa couplings.

Figure 5.1 shows the possible CP-even and CP-odd Yukawa couplings of h_{125} for Yukawa type I where the couplings to all kinds of fermions are equal. We see that in type I c^e and c^o are strongly constrained to be close to the SM-like point $c^e = 1$ and $c^o = 0$. The Higgs measurements constrain these parameters to the region populated by the light points while the EDM constraints strengthen the constraint even more. As shown previously [290, 316], fig. 5.1 again demonstrates that the wrong-sign regime $c_b^e < 0$ cannot be realised in type I because the Yukawa couplings cannot be varied independently.

In Yukawa type II, shown in fig. 5.2, the results are very different. The left panel of fig. 5.2 shows c^e and c^o for the bottom quarks and tau leptons. The Higgs data alone

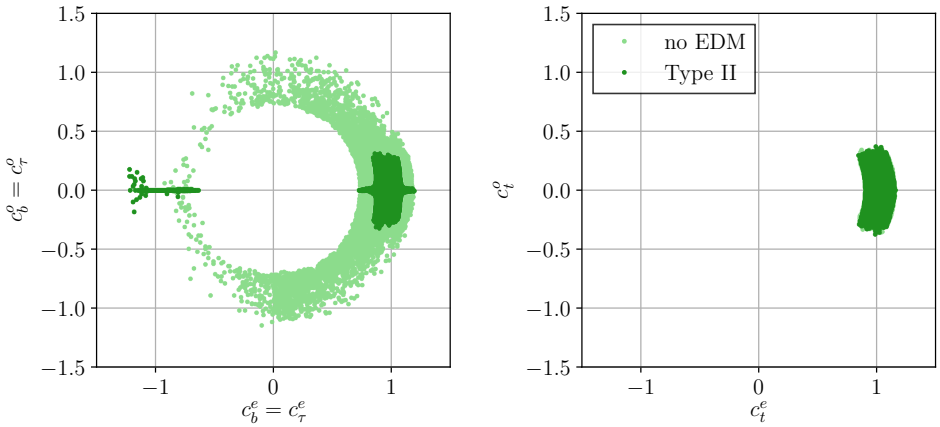

Figure 5.2: Effective CP-even and CP-odd Yukawa couplings of h_{125} in the C2HDM type II. The couplings to down-type quarks and leptons are shown on the left and the coupling to up-type quarks on the right. The dark points (plotted on top) fulfil all constraints while the light points fulfil all except for the EDM constraints. Figure as published in ref. [1].

(*i.e.* without the EDM constraint) still allows for vanishing scalar couplings to down-type quarks $c_b^e = 0$ as discussed in ref. [299]. The wrong-sign regime ($c_b^e < 0$) is possible in the type II C2HDM but faces stronger constraints than the correct sign regime from measurements of $h_{125} \to \gamma\gamma$ [290, 316] resulting in the sparser light points for $c_b^e < 0$. The inclusion of the EDM constraints, however, clearly forces $|c_b^o| \ll |c_b^e|$.[3]

The couplings to top quarks shown in fig. 5.2 (right) are constrained to $(c_t^e)^2 + (c_t^o)^2 \sim 1$ and $|c_t^e| \gg |c_t^o|$. This is similar to the behaviour observed in type I though the allowed region in type II is somewhat larger. The reason for the very different behaviour of the c_t compared to the $c_{b,\tau}$ in type II is that the top coupling is the dominant Yukawa coupling in both ggF and $h_{125} \to \gamma\gamma$, which, as discussed above, are the two main inclusive observables that are sensitive to the CP nature of the Yukawa couplings. The right plot of fig. 5.2 also shows that the EDM constraint has no discernible effect on the allowed coupling to up-type quarks.

The situation is even more striking in the other two Yukawa types. Figure 5.3 (left) displays the lepton Yukawa couplings for the lepton-specific model with and without the EDM constraints. These can still be mostly or even entirely CP-odd, despite the EDM constraints. Similarly, in the flipped model shown in fig. 5.3 (right) the bottom quark can couple to h_{125} in a fully CP-odd fashion or with comparable CP-even and CP-odd couplings even after applying the EDM constraints. In both cases, the up-type Yukawa couplings (which are equal to the down-type coupling in the lepton-specific and the lepton coupling in the flipped case) are constrained to lie close to the fully CP-even

[3] In ref. [1] we found that $c_b^o \sim 1$ remains possible if $h_{125} \equiv H_2$. However, we have been unable to verify this possibility when considering updated constraints from Higgs measurements.

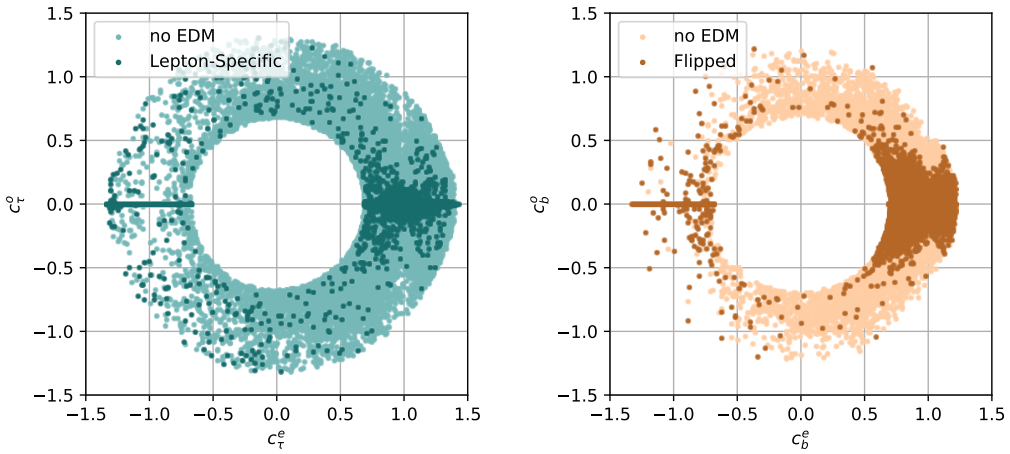

Figure 5.3: Effective CP-even and CP-odd Yukawa couplings of h_{125} in the lepton-specific and flipped C2HDM. The left plot shows the lepton Yukawa couplings in the lepton-specific C2HDM while the right plot shows the down-type Yukawa couplings for a flipped Yukawa sector. The dark points (plotted on top) fulfil all constraints while the light points fulfil all except for the EDM constraint. Figures as published in ref. [1].

SM value. Therefore, both scenarios for maximally CP-violating Yukawa couplings can be realised in lepton-specific and flipped C2HDM.

Comparing figs. 5.2 and 5.3, the constraints from Higgs measurements on c_τ in the lepton-specific and on c_b in the flipped Yukawa type are weaker than in type II. As can be seen from tab. 15 of ref. [19] the measurements of $\mu_{\tau\tau}$ and μ_{bb} are both not very precise, but have very different central values. This results in a considerably stronger constraint in type II, where $c_b = c_\tau$. Additionally, for lepton-specific Yukawa couplings, the wrong-sign regime $c_\tau < 0$ is less constrained than the wrong sign regime af a flipped Yukawa sector, $c_b < 0$. As discussed for type II, the wrong sign limit is mainly constrained by the contribution of the wrong-sign fermion to the $h_{125} \to \gamma\gamma$ decay. Since $m_\tau < m_b$, this effect is more pronounced for a wrong-sign c_b^e than for a wrong sign c_τ^e.

As we have seen from the previous discussion, there are undoubtedly strong constraints on CP violation in the Yukawa sector. However, it is still possible to realise scenarios where h_{125} has maximally CP-violating couplings to heavy fermions. This possibility remains even though in a simplified model of a single h_{125} with global Yukawa modifiers c^e and c^o the electron EDM constraint alone forces $c^o \lesssim 0.01$ [317]. We can understand this difference by studying the model prediction for the electron EDM d_e in more detail.

As mentioned above, the main contribution to electric dipole moments in the C2HDM comes from the so-called Barr-Zee type two-loop diagrams [157] shown in fig. 5.4. At the two loop level the blobs in the first diagram can contain fermions, W bosons and charged Higgs bosons. We call the resulting contributions to the EDM of the electron $d_e(f\bar{f})$, $d_e(W^\pm W^\mp)$, and $d_e(H^\pm H^\mp)$ respectively. The second diagram contains a complicated

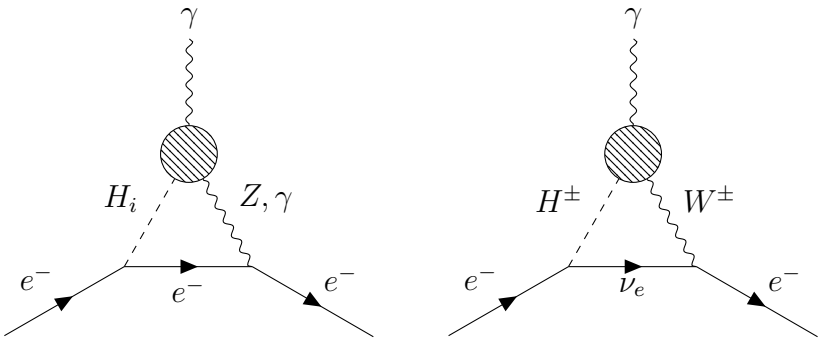

Figure 5.4: Barr-Zee type Feynman diagrams contributing to the EDM of the electron in the C2HDM.

effective vertex (see the appendix of ref. [157]) and we call its contribution $d_e(H^\pm W^\mp)$. The EDM is defined at the diagram level and given by the direct sum

$$d_e = d_e(f\bar{f}) + d_e(W^\pm W^\mp) + d_e(H^\pm H^\mp) + d_e(H^\pm W^\mp)\,. \tag{5.28}$$

Within these individual contributions, there is always a sum over the three Higgs bosons H_i and in case of $d_e(f\bar{f})$ also a sum over the relevant fermions where we include t and b quarks as well as τ leptons. There may be cancellations between different contributions, cancellations between different H_i, and cancellations between different kinds of fermions. For example, the dominant top contribution to $d_e(f\bar{f})$ is schematically given by

$$d_e(t\bar{t}) \propto \sum_i c^e(H_i ee)\, c^o(H_i tt)\, \mathcal{I}_1 + c^o(H_i ee)\, c^e(H_i tt)\, \mathcal{I}_2\,, \tag{5.29}$$

where the form factors $\mathcal{I}_{1,2}$ are of comparable size. From table 5.1 we see that in type I and flipped Yukawa sectors there is always a relative sign between these two terms which naturally leads to a cancellation.

In fig. 5.5 we show individual contributions to the EDM of the electron. For each C2HDM type, we have grouped the contributions to d_e according to their relative sign. For example, in Type II the contributions of the W-loops (y-axis) and the sum of the contributions of the fermion loops, charged Higgs loops and $d_e(H^\pm W^\mp)$ (x-axis) tend to have opposite signs. The grey shaded region represents the parameter space excluded by the EDM constraint [313]

$$d_e < 8.7 \times 10^{-29}\, e\,\mathrm{cm}\,, \tag{5.30}$$

and the colour code indicates the value of the phase $\phi(\lambda_5)$ projected into $[0, \pi/2]$. The first notable difference between the Yukawa types is that the maximum values of the contributions with opposite signs are around two orders of magnitude smaller in type I and flipped models than in type II and lepton-specific models. The reason for this behaviour is the natural cancellation in eq. (5.29) for type I and flipped Yukawa sectors. As a result, EDM constraints on type I and flipped models are considerably less severe.

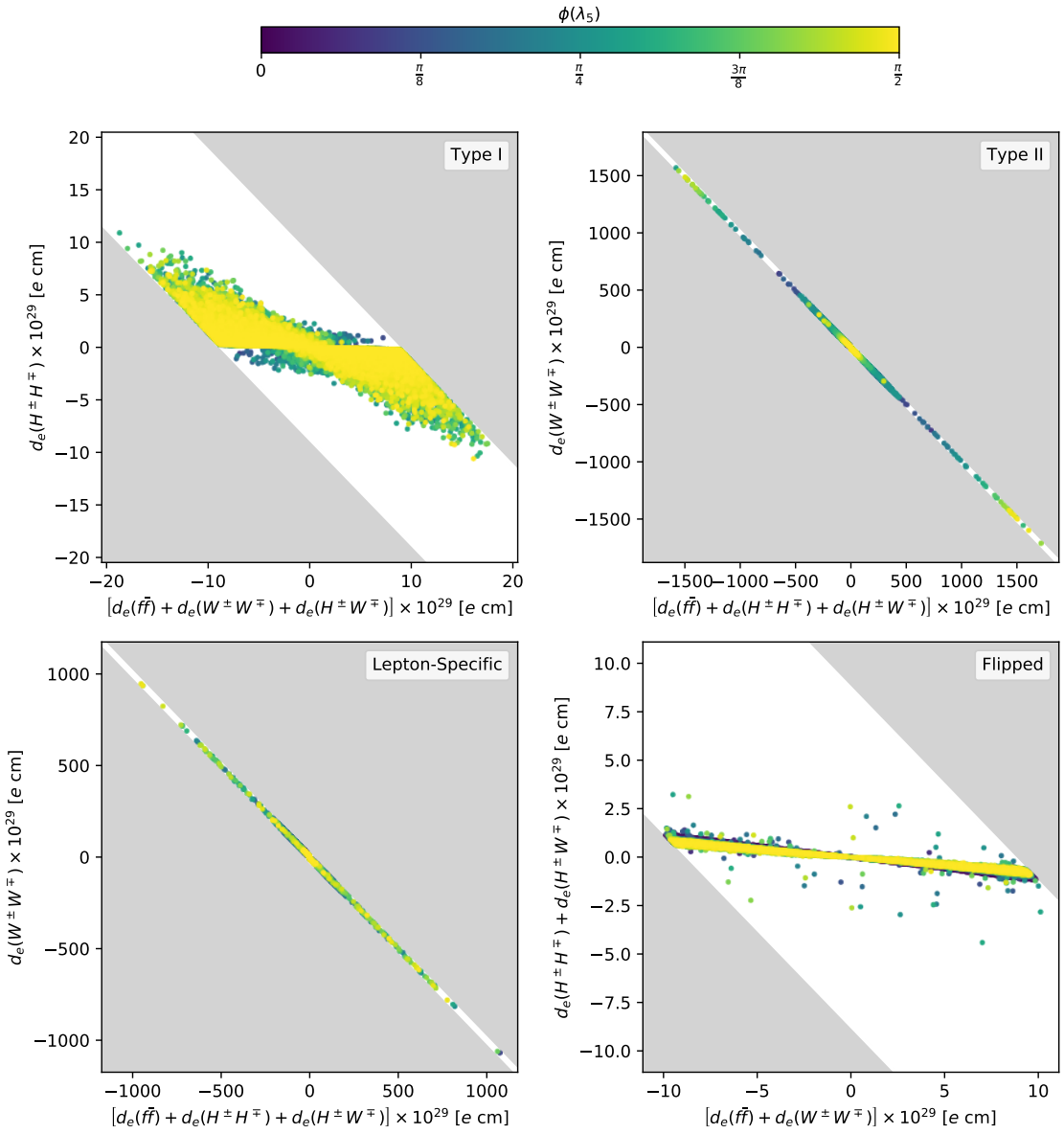

Figure 5.5: Contributions to the electron EDM d_e grouped according to their relative sign in the four different Yukawa types. In each plot, the model prediction for d_e is obtained as the sum of the x and y values for each point. The colour code indicates the phase $\phi(\lambda_5)$ projected into $[0, \pi/2]$. They grey regions are excluded by the EDM constraint. Figure as published in ref. [1].

In Type II large values of $\phi(\lambda_5)$ can be found in regions where either the EDM contributions are tiny — which requires cancellation between different H_i — or rely on substantial cancellations between different contributions. The cancellations between different scalars require them to have similar masses [161, 318] in which case they are related to the orthogonality of the mixing matrix R [25]. However, since flavour constraints in type II demand $m_{H^\pm} \gtrsim 600\,\text{GeV}$ (see section 2.4.2, specifically fig. 2.2) and the T parameter forces one H_i to be close in mass to $H^\pm$ (see section 2.4.1), these cancellations typically require that one of the neutral scalars — H_i if $m_{H_j} \sim m_{H_k}$ $(i \neq j \neq k \in \{1,2,3\})$ — is almost purely CP-even. Lepton specific models behave similarly, however, since all Higgs bosons can be light (see fig. 2.2), cancellations between different H_i can happen more naturally than in type II.

5.1.3 Summary

In this section, we have discussed the minimal model with a CP-violating scalar sector, the C2HDM. In particular, we have focussed on the possibility of CP-violating Yukawa couplings of h_{125}. We have shown that in lepton-specific and flipped Yukawa sectors, it is still possible for h_{125} to couple like a pure scalar to some fermions and like a pseudoscalar to others. It is also possible for the CP-even and CP-odd Yukawa couplings to a single kind of fermion to be of similar size. In Yukawa type II this behaviour would have been allowed by Higgs measurements but is excluded by the bound on the EDM of the electron while in type I — where the effective couplings to all fermions are equal — inclusive Higgs measurements alone force h_{125} to have SM-like, CP-even Yukawa couplings.

Overall, we have found that the large CP-violating Yukawa couplings are possible without violating the constraints from the electron EDM. We have also investigated the different impact of this constraint in the Yukawa types. The results have shown that — regardless of the Yukawa type — it is possible to remain in agreement with the electron EDM bound even for a maximal CP-violating phase $\phi(\lambda_5)$. However, this requires cancellations between different contributions to the EDM.

The constraints used in the parameters scan of the C2HDM have since become stronger with experimental progress. We have verified that all of the conclusions presented here qualitatively hold even for updated constraints. In particular, since fulfilling the EDM bound relies on large cancellations the impact of the updated electron EDM bounds [156] on the phenomenology of the C2HDM is surprisingly small. However, including other EDM measurements, like the limit on the neutron EDM [158] could have an important impact on the model as the necessary cancellations to satisfy both bounds may be in conflict with each other [152, 162].

5.2 CP Violation in a Dark Sector

After discussing the phenomenology of a CP-admixture to h_{125} in the previous section, we now turn to a very different model with a CP-violating Higgs sector. In this model — a variant of the next-to 2HDM (N2HDM) [7, 319] — CP violation occurs exclusively in a dark sector.

We consider an extension of the 2HDM by an additional real scalar singlet field Φ_S. We extend the $\mathbb{Z}_2$ symmetry of the 2HDM to include the singlet field as

$$\Phi_1 \to \Phi_1\,, \quad \Phi_2 \to -\Phi_2\,, \quad \Phi_S \to -\Phi_S\,, \tag{5.31}$$

and — in contrast to the 2HDM scalar potentials of eqs. (2.29), (2.34) and (5.1) — require this symmetry to be unbroken in the scalar potential. The resulting most general scalar potential is

$$\begin{aligned} V = {} & m_{11}^2|\Phi_1|^2 + m_{22}^2|\Phi_2|^2 + \Big[A\,\Phi_1^\dagger\Phi_2\Phi_S + \text{H.c.}\Big] \\ & + \frac{\lambda_1}{2}(\Phi_1^\dagger\Phi_1)^2 + \frac{\lambda_2}{2}(\Phi_2^\dagger\Phi_2)^2 + \lambda_3(\Phi_1^\dagger\Phi_1)(\Phi_2^\dagger\Phi_2) \\ & + \lambda_4(\Phi_1^\dagger\Phi_2)(\Phi_2^\dagger\Phi_1) + \left[\frac{\lambda_5}{2}(\Phi_1^\dagger\Phi_2)^2 + \text{H.c.}\right] \\ & + \frac{1}{2}m_S^2\Phi_S^2 + \frac{1}{8}\lambda_6\Phi_S^4 + \frac{1}{2}\lambda_7|\Phi_1|^2\Phi_S^2 + \frac{1}{2}\lambda_8|\Phi_2|^2\Phi_S^2\,, \end{aligned} \tag{5.32}$$

where all parameters except for λ_5 and the trilinear parameter A are required to be real by hermiticity. We consider all fermions to be uncharged under the $\mathbb{Z}_2$ symmetry which forbids all couplings of Φ_2 to fermions. Therefore, only Φ_1 can couple to SM fermions which ensures NFC. Since only Φ_1 has Yukawa interactions, it must have a vev to give mass to all SM fermions. This forces the Yukawa sector to be identical to the one of the SM with Φ_1 playing the role of the SM Higgs doublet. The $\mathbb{Z}_2$ symmetry eliminates many of the possible terms in the potential but still allows λ_5 and A to *a priori* take complex values. However, we can absorb one of the phases through a basis transformation. We choose, without loss of generality, λ_5 to be real and keep A complex. Therefore, the model contains a total of thirteen real parameters.

The trilinear term involving A is not invariant under the CP transformation[4]

$$\Phi_1(t,\vec{x}) \to \Phi_1^*(t,-\vec{x})\,, \quad \Phi_2(t,\vec{x}) \to \Phi_2^*(t,-\vec{x})\,, \quad \Phi_S(t,\vec{x}) \to \Phi_S(t,-\vec{x})\,. \tag{5.33}$$

The breaking of this specific CP-symmetry does not yet prove that the model is indeed CP-violating. A model is CP-conserving as long as it is invariant under any generalised CP transformation even if irreducible complex coefficients exist in its scalar potential [320]. Instead of trying to prove the existence of CP violation formally, we will construct an observable that is known to be CP-violating and show that it has a non-vanishing value

[4]Notice that the CP transformation of the singlet field is trivial as discussed in section 4.1.

within the model. As long as the vacuum preserves CP, this proves that the model is explicitly CP-violating.

We choose the simplest possible vacuum where only Φ_1 acquires a neutral vev

$$\langle \Phi_1 \rangle = \frac{1}{\sqrt{2}} \begin{pmatrix} 0 \\ v \end{pmatrix} \tag{5.34}$$

of the same form as in the SM. This vacuum clearly preserves both CP and the $\mathbb{Z}_2$ symmetry eq. (5.31). The stationarity conditions, eq. (3.2), for eq. (5.32) imply that this vacuum exists as long as

$$m_{11}^2 + \frac{1}{2}\lambda_1 v^2 = 0\,. \tag{5.35}$$

Since all fermion and gauge boson masses are necessarily generated by Φ_1, its vev has to take the same value as in the SM, eq. (1.25). At this vacuum, the doublets are expanded as

$$\Phi_1 = \begin{pmatrix} G^+ \\ \frac{1}{\sqrt{2}}(v + h + i\,G^0) \end{pmatrix}\,, \quad \Phi_2 = \begin{pmatrix} H^+ \\ \frac{1}{\sqrt{2}}(\rho + i\,\eta) \end{pmatrix}\,, \tag{5.36}$$

where — just like in the Higgs basis eq. (5.10) — the goldstone bosons G^+ and G^0 are components of Φ_1. However, in contrast to the C2HDM any mixing between the field h and ρ, η and Φ_S is forbidden by the unbroken $\mathbb{Z}_2$ symmetry, and h will therefore obtain couplings to SM gauge bosons and fermions that are identical to h_{SM}. Its mass is given by

$$m_h = \lambda_1 v^2 \tag{5.37}$$

which we fix to 125 GeV.

The charged Higgs component of Φ_2 is a charged Higgs mass eigenstate with a mass of

$$m_{H^\pm}^2 = m_{22}^2 + \frac{\lambda_3}{2} v^2\,. \tag{5.38}$$

In the basis (ρ, η, Φ_S) the mass matrix of the remaining neutral states is given by

$$M_N^2 = \begin{pmatrix} m_{22}^2 + \frac{1}{2}\lambda_{34-5} v^2 & 0 & -\mathrm{Im}(A) v \\ 0 & m_{22}^2 + \frac{1}{2}\lambda_{345} v^2 & \mathrm{Re}(A) v \\ -\mathrm{Im}(A) v & \mathrm{Re}(A) v & m_S^2 + \frac{1}{2}\lambda_7 v^2 \end{pmatrix}\,, \tag{5.39}$$

where $\lambda_{345} = \lambda_3 + \lambda_4 + \lambda_5$ and $\lambda_{34-5} = \lambda_3 + \lambda_4 - \lambda_5$. These fields mix into three BSM neutral scalar states H_1, H_2, and H_3. We use the parametrisation of eq. (5.13) for the 3×3 mixing matrix R that diagonalises M_N^2 and assume the masses of these three scalar states to be ordered as

$$m_{H_1} \leq m_{H_2} \leq m_{H_3}\,. \tag{5.40}$$

The thirteen real parameters of the scalar potential can be expressed through a more convenient set of input parameters. Using eq. (5.35) and eq. (5.37) we express m_{11}^2 and λ_1 through v and m_h. We use eq. (5.38) to express λ_3 as a function of $m_{H^\pm}$ and m_{22}^2.

We can then use the diagonalisation of M_N to express λ_4, λ_5, λ_7 as well as $\mathrm{Re}(A)$ and $\mathrm{Im}(A)$ through the three mixing angles $\alpha_{1,2,3}$ and the three Higgs masses $m_{H_{1,2,3}}$. This leads to one condition on the Higgs masses and the mixing matrix

$$\sum_i m_{H_i}^2 R_{i1} R_{i2} = 0 \tag{5.41}$$

that can be used to express one of the masses through the other ones. We fix

$$m_h = 125\,\mathrm{GeV}\,, \quad v \approx 246\,\mathrm{GeV}\,, \tag{5.42}$$

and the remaining eleven input parameters (with $a, b \in \{1,2,3\}$ and $a \neq b$) are

$$m_{H^\pm}\,, \quad m_{H_a}\,, \quad m_{H_b}\,, \quad \alpha_1\,, \quad \alpha_2\,, \quad \alpha_3\,, \quad m_{22}^2\,, \quad m_S^2\,, \quad \lambda_2\,, \quad \lambda_6\,, \quad \lambda_8\,. \tag{5.43}$$

Both the scalar potential and the vacuum preserve the $\mathbb{Z}_2$ symmetry eq. (5.31). As a result, the physical eigenstates emerging from Φ_2 and Φ_S — $H^\pm$ and $H_{1,2,3}$ — carry a conserved *dark charge* of -1 that is preserved in all interactions to all orders. We will refer to these four states as dark particles. On the other hand all SM particles and h have a *dark charge* of $+1$. As a consequence, dark particles can only be produced in pairs while their decays must always produce at least one other dark particle. In particular, the lightest of these dark particles is stable and a candidate particle for dark matter (DM) (see section 1.2.1).

This feature of the model is similar to the inert version of the 2HDM, the so-called inert-doublet model (IDM) [219, 321–323] (recently studied in *e.g.* refs. [245, 324, 325]). The main difference between our model and the IDM is the mixing between the three states ρ, η and Φ_S in our model whereas ρ and η would be mass eigenstates in the IDM (and Φ_S would be absent). The mass matrix, eq. (5.39), clearly shows that this mixing is a direct consequence of the trilinear parameter A. However, regarding the phenomenology of the dark-charged scalar, this model is equivalent to the IDM.

5.2.1 Constraints and Parameter Scan

In order to study the phenomenology of the model we created a sample of phenomenologically viable parameter points by implementing the model and its constraints in a private updated version of `ScannerS` [7, 125, 249, 290].

As discussed in sections 2.2 and 3.2, constraints on the parameters of the scalar potential can be obtained from perturbative unitarity and boundedness from below. These constraints only depend on the quartic terms of the scalar potential, which are identical between the N2HDM and our model. Therefore, the known constraints from the N2HDM on perturbative unitarity in the high energy limit [7] and boundedness from below [221] are applicable. These will be discussed in more detail when we study the N2HDM in section 6.3.1.

Table 5.3: Input parameter ranges for the parameter scan of the CP-violating dark sector model. The three mixing angles $\alpha_{1,2,3}$ are scanned through their whole allowed range and $a \neq b \in \{1, 2, 3\}$.

	$m_{H_{a,b}}$, $m_{H^\pm}$ GeV	λ_2	λ_6	λ_8	m_{22}^2, m_S^2 GeV^2
min	70	0	0	-26	10^{-3}
max	1000	9	17	26	10^6

We use the approach of chapter 3 to numerically check for vacuum stability constraints in the model. As discussed in section 3.1.2, parameter points with a bounce action $B < 390$ for tunnelling to the most dangerous minimum (MDM) are short lived and excluded by the vacuum stability constraint. For simplicity, we do not include the uncertainty region $390 < B < 440$ and use this very conservative constraint where only parameter points with a survival probability $\ll 5 \times 10^{-7}$ through the age of the universe are excluded.

Since by construction all tree-level interactions and vertices of h are identical to h_{SM} and the interactions of the dark particles are limited by their dark charge, many of the experimental constraints discussed in section 2.4 are trivially fulfilled in the model. An exception are the EW precision constraints through the oblique parameters S, T, and U discussed in section 2.4.1. We calculate model predictions using refs. [137, 138] and compare to the limits from ref. [135]. Since the charged Higgs boson $H^\pm$ does not couple to fermions, the flavour constraints from section 2.1 do not constrain the model. Since none of the CP-mixed scalars couple to fermions they also cannot induce EDMs even though the model is CP-violating.

One possibility to constrain the model through Higgs measurements would be in invisible decays of h_{125} [326, 327]. For simplicity, we require $2m_{H_1} > m_h$ such that this decay is kinematically forbidden and the bounds are trivially satisfied. The only remaining h_{125} observable that can be used to constrain the model is the decay $h \to \gamma\gamma$.[5] This decay is sensitive to a BSM coupling of h — the coupling of h to a pair of charged Higgs bosons $H^\pm$ which is allowed by the dark $\mathbb{Z}_2$ symmetry. The effect is identical to the IDM, and we may use [328]

$$\Gamma(h \to \gamma\gamma) = \frac{G_F \alpha^2 m_h^3}{128\sqrt{2}\pi^3} \left| \sum_{f=t,b} 3Q_f^2 A_{1/2}\left(\frac{4m_f^2}{m_h^2}\right) + A_1\left(\frac{4m_W^2}{m_h^2}\right) + \frac{\lambda_3 v^2}{2m_{H^\pm}^2} A_0\left(\frac{4m_{H^\pm}^2}{m_h^2}\right) \right|^2 \tag{5.44}$$

to calculate the decay width in our model.[6] The sum runs over the relevant heavy quarks (of electric charge Q_f), and A_0, $A_{1/2}$ and A_1 are known form factors [329, 330]. The

[5] The decay $h \to Z\gamma$ could also but has not yet been observed.

[6] The corresponding diagrams are shown in eq. (6.65).

third term contains the contribution of the charged Higgs and depends on the $hH^{\pm}H^{\mp}$ coupling $\propto \lambda_3$. Since the partial width of h_{SM} into $\gamma\gamma$ is tiny compared to the decay widths into $b\bar{b}$ or WW, we can neglect the effect of the charged Higgs contribution to $h \to \gamma\gamma$ in the total width and the remaining branching ratios. However, the charged Higgs contribution can substantially modify the $\mathrm{BR}(h \to \gamma\gamma)$. We compare the model prediction to a recent measurement of $pp \to h_{125} \to \gamma\gamma$ [331] to obtain a constraint.

Finally, since the model contains a dark-matter candidate, it must fulfil some dark-matter specific constraints. A rather trivial one is that dark matter must not be charged which requires

$$m_{H_1} < m_{H^{\pm}} \,. \tag{5.45}$$

Additionally, the relic density (see section 1.2.1) of H_1 must not exceed the observed DM density, and H_1 as a DM candidate must not be ruled out by existing DM searches. We use the code `MicrOMEGAs` [51–57] to calculate the relic density Ω_c and the spin independent scattering cross section between dark matter and nucleons. We then require Ω_c to be at most 2σ larger than the observed dark matter density [48]

$$\left(\Omega_c h^2\right)_{\mathrm{DM}} = 0.120 \pm 0.001 \,. \tag{5.46}$$

The spin independent dark matter scattering cross section as a function of the DM mass is constrained by direct detection experiments (see section 1.2.1). We use the strongest available bound from XENON1T [50, 332]. Since H_1 is a typical weakly interacting massive particle (WIMP) where direct detection is known to give the strongest bounds, we neglect constraints from indirect detection and searches for DM pair production at colliders.

Using these constraints, we perform a random scan using the input parameter ranges given in table 5.3. The mass of one of the neutral dark scalars is determined through eq. (5.41), but is required to lie in the same interval as the other masses. The lower bound on the masses ensures that decays of $h \to H_1 H_1$ or $h \to H^{\pm}H^{\pm}$ are always forbidden. The ranges for λ_2, λ_6 and λ_8 are chosen to cover the whole parameter space possible without violating boundedness or perturbative unitarity.

Before examining CP violation, we first discuss the impact of the $h \to \gamma\gamma$ signal strength observable on the model. Figure 5.6 shows the value of the observable

$$\mu_{\gamma\gamma} = \frac{\sigma(pp \to h_{125})}{\sigma(pp \to h_{\mathrm{SM}})} \frac{\mathrm{BR}(h_{125} \to \gamma\gamma)}{\mathrm{BR}(h_{\mathrm{SM}} \to \gamma\gamma)} \tag{5.47}$$

$$\approx \frac{\Gamma(h_{125} \to \gamma\gamma)}{\Gamma(h_{\mathrm{SM}} \to \gamma\gamma)} \,. \tag{5.48}$$

The second line holds since the production cross section of h_{125} is identical to h_{SM}, and we have neglected the impact of the modified decay width into $\gamma\gamma$, eq. (5.44), on the total width. For low charged Higgs masses $m_{H^{\pm}}$ large deviations of $\mu_{\gamma\gamma}$ from one can appear. If $\mu_{\gamma\gamma}$ is reduced — which happens for large negative values of λ_3 — the model is constrained by the measurement [331]. The upper limit obtained from the measurement

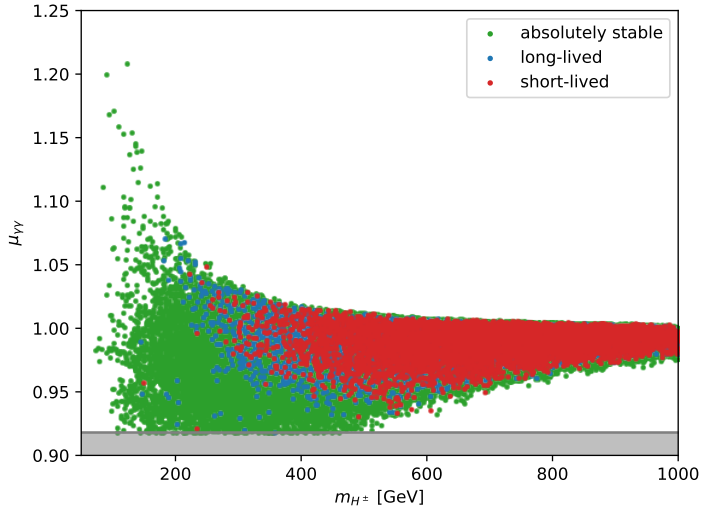

Figure 5.6: The observable $\mu_{\gamma\gamma}$ as a function of the charged Higgs mass $m_{H^\pm}$. The grey region is excluded at 95 % confidence level by the results of ref. [331]. The corresponding upper bound is outside of the range of the plot. The colour code indicates the stability of the EW vacuum distinguishing between absolutely stable (green), long-lived (blue), and short-lived (red). The more unstable points are plotted on top, green points exist throughout the parameter range.

is outside the range of the plot and does not constrain our model, which can reach values of at most $\mu_{\gamma\gamma} \sim 1.2$. This constraint directly impacts λ_3, which governs the coupling of hH^+H^-, leading to a lower limit of about $\lambda_3 > -1.03$ while the maximal value of 8.89 is only constrained by perturbative unitarity.

Figure 5.6 also shows the impact of the vacuum stability constraints through the colour code. The absolutely stable (green) and long-lived (blue) points feature sufficiently stable EW vacua, while the short-lived (red) points are excluded by vacuum stability constraints. Parameter points with stable or long-lived EW vacua exist behind the whole red region in fig. 5.6. Therefore, vacuum stability does not directly constrain the phenomenology of this observable.

Throughout the considered mass range for H_1 in table 5.3, it is possible to saturate the observed value of the relic density Ω_c without violating limits from direct detection experiments. However, for most parameter points considered in the following, H_1 is only a subdominant contribution to Ω_c such that additional sources of DM are required.

5.2.2 Observing CP Violation in a Dark Sector

We will now construct a CP-violating observable in our model. This will both prove that CP is indeed explicitly violated, and indicate an avenue towards experimentally probing this CP violation.

Several observables could be sensitive to CP violation. Most rely on the fact that all vertices of the form Zh_ah_b for $a \neq b \in \{1,2,3\}$ exist in the model. These arise from the covariant derivative in the kinetic term of Φ_2 which includes a term involving the neutral component fields ρ and η as

$$|D_\mu \Phi_2|^2 \supset \frac{g}{2\cos\theta_W} Z_\mu \left(\eta \partial^\mu \rho - \rho \partial^\mu \eta\right) , \tag{5.49}$$

where g is the $\mathrm{SU}(2)_L$ coupling constant and θ_W is the weak mixing angle. In the mass basis, this leads to couplings of the form

$$\mathcal{L} \supset Z_\mu h_a h_b \frac{g}{2\cos\theta_W} \left(p_a^\mu - p_b^\mu\right) \left[R_{a2}R_{b1} - R_{a1}R_{b2}\right] . \tag{5.50}$$

For $a \neq b \neq c$ $(a,b,c \in \{1,2,3\})$ the expression in brackets reduces to R_{c3} by the orthogonality of R. The simultaneous existence of these vertices is a clear signal of CP violation. If all h_a were CP eigenstates — like in the R2HDM where h and H are CP-even while A is CP-odd — then the vertices ZAh and ZAH could exist but ZHh would be forbidden by CP-invariance. Since all of these vertices exist in our model the h_a cannot be eigenstates of CP. Notice that no vertices of the form Zhh_a are possible as they are forbidden by the dark $\mathbb{Z}_2$ symmetry.

In principle, observation of all three Zh_ah_b vertices — either through a decay $h_a \to Zh_b$ or a production process $Z \to h_ah_b$ — could be used to establish CP violation experimentally. However, since the h_a are dark particles and the lightest of them is stable, they are only accessible through mono-Z or mono-Higgs searches in channels like $f\bar{f} \to Z^* \to h_ah_b \to h_ah_aZ$ or $f\bar{f} \to Z^* \to h_ah_b \to h_ah_ah$. Since these final states occur in many dark matter models regardless of the CP nature of the involved particles, they are not a good probe of CP violation in the dark sector.

Instead, we study the anomalous triple gauge coupling induced by these vertices. The Lorentz structure of the ZZZ vertex [333–336] can be expressed through two form factors by assuming that two Z bosons are on-shell and neglecting fermion masses. The resulting vertex function is

$$e\Gamma^{\alpha\beta\mu}_{ZZZ} = i\,e\frac{p_1^2 - m_Z^2}{m_Z^2}\left[f_4^Z\left(p_1^\alpha g^{\mu\beta} + p_1^\beta g^{\mu\alpha}\right) + f_5^Z \epsilon^{\mu\alpha\beta\rho}(p_2 - p_3)_\rho\right] , \tag{5.51}$$

where p_1 is the momentum of the off-shell Z boson and p_2 and p_3 are the momenta of the on-shell Z bosons. The form factor f_5^Z violates C and P but conserves CP, while f_4^Z is CP-violating. In our model there is only a single one-loop diagram contributing to this form factor:

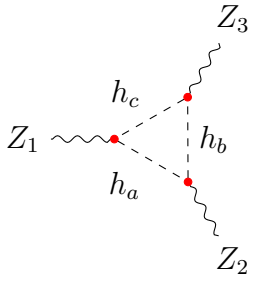

(5.52)

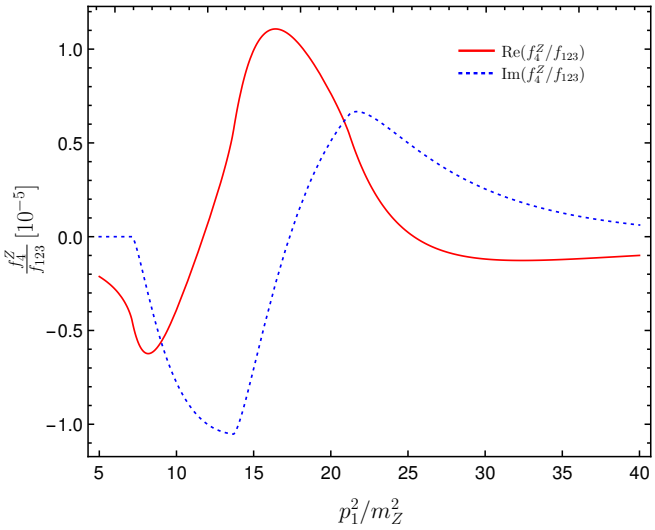

Figure 5.7: The CP-violating $f_4^Z(p_1^2)$ form factor, normalised to f_{123}, for $m_{H_1} = 80.5\,\text{GeV}$, $m_{H_2} = 162.9\,\text{GeV}$ and $m_{H_3} = 256.9\,\text{GeV}$, as a function of the squared off-shell Z boson 4-momentum p_1^2, normalised to m_Z^2. Figure from ref. [2].

In ref. [337] these form factors were studied in the C2HDM where also diagrams with internal Z bosons or neutral goldstone bosons contribute. These are absent in our model as the $h_a ZZ$ and $h_a ZG^0$ vertices are forbidden by the dark $\mathbb{Z}_2$ symmetry. We adapt the expression for f_4^Z in the C2HDM [337] to our model and find

$$f_4^Z(p_1^2) = -\frac{2\alpha}{\pi s_{2\theta_W}^3}\frac{m_Z^2}{p_1^2 - m_Z^2} f_{123} \sum_{i,j,k} \epsilon_{ijk} C_{001}(p_1^2, m_Z^2, m_Z^2, m_i^2, m_j^2, m_k^2)\,, \tag{5.53}$$

with the `LoopTools` [338] definition of the function C_{001}. The f_{123} factor denotes a normalised product of the couplings at the vertices in eq. (5.52) indicated by red dots. Using eq. (5.50) this is given by

$$f_{123} = R_{13}R_{23}R_{33} \leq \left(\frac{1}{3}\right)^{\frac{3}{2}}. \tag{5.54}$$

The upper bound is a consequence of the orthogonality of R and is saturated when all R_{i3} are equal. Notice that the third column of the mixing matrix corresponds to the admixture of Φ_S — not of the imaginary component η — into the respective mass eigenstate. This means that f_{123} is maximised if the singlet component is evenly split between the mass eigenstates.

In fig. 5.7 we show — for a typical combination of dark scalar masses ($m_{H_1} \approx 80\,\text{GeV}$, $m_{H_2} \approx 163\,\text{GeV}$ and $m_{H_3} \approx 257\,\text{GeV}$) — the evolution of f_4^Z normalised to f_{123} with p_1^2, the squared 4-momentum of the off-shell Z boson. This illustrates the highly non-linear dependence of f_4^Z on the external momentum p_a^2. Figure 5.7 can be compared to fig. 2

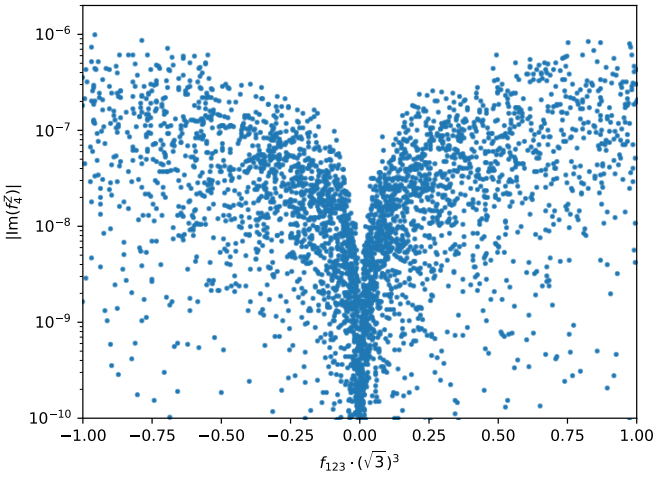

Figure 5.8: The imaginary part of f_4^Z versus the coupling f_{123} normalised to its maximum value (see eq. (5.54)) for a centre of mass energy of $p_1^2 = (450\,\mathrm{GeV})^2$.

of ref. [337], where somewhat larger magnitudes for the real and imaginary parts of f_4^Z were observed in the C2HDM.

Figure 5.8 shows the imaginary part of f_4^Z — which contributes directly to asymmetry observables — versus f_{123} that is normalised to its maximum value. We choose a value of $p_1^2 = (450\,\mathrm{GeV})^2$ corresponding to a possible collision energy at a future linear collider. Figure 5.8 illustrates that the model indeed allows maximum mixing between the neutral, dark scalars and the theoretically maximal value of f_{123} is reachable. The values of $\mathrm{Im}(f_4^Z)$ can reach values of $\mathcal{O}(10^{-6})$ for the maximum mixing scenarios. We have found that larger masses — and larger mass splittings — seem to be required for larger $|\mathrm{Im}(f_4^Z)|$. This can be understood by considering the form of the mass matrix when the mass splittings between $H_{1,2,3}$ are small. In the limiting case of three degenerate dark scalars, the mass matrix eq. (5.39) would be proportional to the identity matrix, and no mixing — and no CP violation — would occur. Therefore, regions of parameter space with small mass splittings between the dark neutral scalars tend to produce smaller values of $|\mathrm{Im}(f_4^Z)|$. This argument has been formalised in the 2HDM [337] through the use of basis invariant quantities that signal CP violation [339, 340].

Anomalous couplings, such as those responsible for a ZZZ vertex, can be probed in Z-pair production. The search for anomalous triple gauge couplings in those analyses uses an effective Lagrangian for triple neutral vertices parametrised as [333]

$$\begin{aligned}\mathcal{L}_{VZZ} = -\frac{e}{m_Z^2}\Big\{&\left[f_4^\gamma\left(\partial_\mu F^{\mu\alpha}\right) + f_4^Z\left(\partial_\mu Z^{\mu\alpha}\right)\right] Z_\beta\left(\partial^\beta Z_\alpha\right) \\ &- \left[f_5^\gamma\left(\partial^\mu F_{\mu\alpha}\right) + f_5^Z\left(\partial^\mu Z_{\mu\alpha}\right)\right]\tilde{Z}^{\alpha\beta} Z_\beta\Big\}\,,\end{aligned} \tag{5.55}$$

where γZZ vertices were also considered. In this equation, $F_{\mu\nu}$ is the electromagnetic

tensor, $Z_{\mu\nu} = \partial_\mu Z_\nu - \partial_\nu Z_\mu$, and $\tilde{Z}_{\mu\nu} = \epsilon_{\mu\nu\rho\sigma} Z^{\rho\sigma}/2$. The f_4^Z coupling above is assumed to be a constant, and as such it represents at most an approximation to the $f_4^Z(p_1^2)$ of eq. (5.53). Furthermore, the analyses take this coupling to be real, whereas it is in general — and in our model in particular — complex. With all that under consideration, the latest results from the LHC [341–344] probe the f_4^Z coupling of eq. (5.55) to order $\sim 10^{-3}$, whereas the typical magnitude of $f_4^Z(p_1^2)$ in our model (for both real and imaginary parts) is $\sim 10^{-7}$. We stress, however, that the two quantities cannot be directly compared, as they represent very different approaches to the ZZZ vertex.

An observable that might be used to probe anomalous ZZZ interactions in the future is the asymmetry A_1^{ZZ} [337, 345]. At a future linear collider with a centre of mass energy $\sqrt{s}$ the process $e^+e^- \to ZZ$ could be used to determine the cross section $\sigma_{\lambda\bar{\lambda}}$ for the production of two Z bosons of helicities λ and $\bar{\lambda}$. This can be used to construct an asymmetry

$$A_1^{ZZ} = \frac{\sigma_{+,0} - \sigma_{0,-}}{\sigma_{+,0} + \sigma_{0,-}} \propto \mathrm{Im}(f_4^Z(s))\,. \tag{5.56}$$

This asymmetry was not constrained by LEP as the helicities of pair produced Z-bosons could not be reconstructed. The direct proportionality of this asymmetry to the CP-violating form factor $\mathrm{Im}(f_4^Z)$ means that if $\mathrm{Im}(f_4^Z)$ is non-zero there is always a corresponding non-zero prediction for a CP-violating observable, the asymmetry A_1^{ZZ}. Thus we have finally proven that CP is explicitly violated in our model. However, we find this asymmetry to be at most $\sim 10^{-5}$ making it challenging to observe experimentally. We have discussed this asymmetry in more detail and have also presented an analysis of the CP-violating ZW^+W^- vertex in ref. [2].

5.2.3 Summary

In this section, we have presented another minimal model with a CP-violating Higgs sector — this time, the minimal model with a CP-violating dark scalar sector. The model adds a dark sector to the SM that is characterised by a $\mathbb{Z}_2$ symmetry and contains a $\mathrm{SU}(2)_L$ doublet and a real singlet. The lightest dark sector particle is stabilised by the $\mathbb{Z}_2$ symmetry and thus a candidate for DM. The $\mathbb{Z}_2$ symmetry allows a trilinear coupling between the two different doublets and the singlet, which introduces a CP-violating phase. The CP violation is entirely confined to the three CP-mixed dark neutral scalars and can neither enter the fermion sector nor the interactions of h_{125}.

We have discussed how to constrain such a model and found dark matter constraints and constraints on the dark-charged Higgs boson through $\mu_{\gamma\gamma}$ to be the most important. Since the CP-mixed scalars do not couple to fermions, it is highly non-trivial to observe the CP violation in the model. However, we have shown that the CP violation in this model leads to anomalous triple gauge couplings. These triple gauge couplings contain the CP-violating form factor f_4^Z, which takes non-zero values in our model.

Direct measurements of ZZ production cross sections at the LHC are being used to constrain anomalous ZZZ vertex form factors. However, these analyses assume constant and real form factors, whereas f_4^Z in our model can have a sizeable imaginary part and is highly dependent on the external momentum. Thus a direct comparison with current experimental analyses is not conclusive. We have also considered a specific asymmetry, A_1^{ZZ}, built with ZZ production cross sections, that could be probed at a future linear collider. This asymmetry observable is directly proportional to the form factor $\mathrm{Im}(f_4^Z)$. Therefore, we have constructed a CP-violating observable that takes non-zero values, which proves that CP is explicitly violated in our model. However, we found the model prediction for this asymmetry to be very small, making it challenging to observe experimentally.

5.3 Conclusions

The two CP-violating models studied in this section exhibit a completely different phenomenology. On the one hand, the C2HDM is highly constrained by Higgs measurements and bounds on EDMs. The CP violation in the model is directly accessible through the Yukawa couplings of the h_{125}, which may have sizeable CP-odd components. Within current constraints, even the possibility that h_{125} couples to some fermions as a pure pseudoscalar remains and may be probed in the future. On the other hand, for the model with a CP-violating dark sector it is challenging to establish that CP violation even occurs. Since the CP-mixed states have no couplings to fermions and the h_{125} is not one of them, the magnitude of the CP violation is unconstrained by current measurements and may only be probed through anomalous triple gauge couplings in the future.[7]

This difference is especially remarkable, considering how little difference there is between the two models from a theoretical perspective. From a symmetry point of view, the only difference is that the $\mathbb{Z}_2$ symmetry — which is broken both softly and by the vacuum in the C2HDM — remains unbroken in the dark sector model. If this were the only change, the result would be the IDM — a model where CP violation in the scalar sector is impossible [346, 347]. The addition of a simple real singlet field, which is charged under the $\mathbb{Z}_2$ symmetry, completely changes this picture. Now the model contains explicit CP violation, and the two scalar states of the IDM mix with the singlet field into three CP-mixed scalars. Even the coupling f_{123} that enters the only CP-violating anomalous triple gauge couplings turned out to be maximised if the singlet field mixes maximally into each mass eigenstate.

In the next chapter, we will discuss another example of an additional real singlet field completely changing the properties of a well known BSM model when we study the vacuum structure of the N2HDM.

[7] The presence of CP-violating Yukawa couplings is also a prerequisite for generating a matter-antimatter asymmetry through EW baryogenesis (see section 1.2.2). This is a possibility in the C2HDM (see *e.g.* refs. [67, 68, 72, 73]) but cannot be achieved in the dark sector model.

6 Vacuum Structure of the N2HDM

In this chapter, we present a detailed analysis of the vacuum structure of a BSM model and its consequences on phenomenology. We combine an analytical analysis with a numerical study based on chapter 3 to explore the phenomenological impact of the vacuum stability constraints. We demonstrate direct links between vacuum stability and collider observables. Our ref. [4] contains the results presented in this chapter.

6.1 The N2HDM

The next-to 2HDM (N2HDM) [7, 319] extends the SM by a second scalar $\mathrm{SU}(2)_L$ doublet and a real scalar singlet field Φ_S. Two $\mathbb{Z}_2$ symmetries are imposed on the scalars to reduce the number of free parameters, enable natural flavour conservation (NFC) (see section 2.1), and (potentially) allow for dark matter (DM) (see section 1.2.1). The first $\mathbb{Z}_2$ symmetry

$$\Phi_1 \to \Phi_1\,, \quad \Phi_2 \to -\Phi_2\,, \quad \Phi_S \to \Phi_2 \tag{6.1}$$

can be extended to the fermion sector leading to four distinct Yukawa types in full analogy to the two-Higgs-doublet model (2HDM) (see section 2.5.1). We allow a bilinear soft breaking term of this symmetry. The second $\mathbb{Z}_2$ symmetry

$$\Phi_{1,2} \to \Phi_{1,2}\,, \quad \Phi_S \to -\Phi_S \tag{6.2}$$

leads to a dark singlet if it remains unbroken. The most general renormalisable scalar potential with this field content and symmetry structure is

$$\begin{aligned} V = {} & m_{11}^2|\Phi_1|^2 + m_{22}^2|\Phi_2|^2 - \left(m_{12}^2\Phi_1^\dagger\Phi_2 + h.c.\right) \\ & + \frac{1}{2}\lambda_1|\Phi_1|^4 + \frac{1}{2}\lambda_2|\Phi_2|^4 + \lambda_3|\Phi_1|^2|\Phi_2|^2 + \lambda_4|\Phi_1^\dagger\Phi_2|^2 + \frac{1}{2}\left[\lambda_5\left(\Phi_1^\dagger\Phi_2\right)^2 + h.c.\right] \\ & + \frac{1}{2}m_S^2\Phi_S^2 + \frac{1}{8}\lambda_6\Phi_S^4 + \frac{1}{2}\lambda_7|\Phi_1|^2\Phi_S^2 + \frac{1}{2}\lambda_8|\Phi_2|^2\Phi_S^2\,. \end{aligned} \tag{6.3}$$

Two of the coefficients — m_{12}^2 and λ_5 — could be complex parameters and — just like in the CP-violating 2HDM (C2HDM) of section 5.1 — lead to CP violation if eq. (5.8) holds. However, we only consider the CP-conserving version of this scalar potential. Imposing the standard CP symmetry

$$\Phi_{1,2} \to \Phi_{1,2}^*\,, \quad \Phi_S \to \Phi_S \tag{6.4}$$

forces both m_{12}^2 and λ_5 to be real up to field rephasings. The model has twelve real parameters and — after mass diagonalisation — three CP-even, one CP-odd, and a pair of charged Higgs bosons.

The most general classical field configuration of the N2HDM is

$$\Phi_1 \to \frac{1}{\sqrt{2}} \begin{pmatrix} 0 \\ v_1 \end{pmatrix} , \quad \Phi_2 \to \frac{1}{\sqrt{2}} \begin{pmatrix} v_{\mathrm{CB}} \\ v_2 + i\, v_{\mathrm{CP}} \end{pmatrix} , \quad \Phi_S \to v_S \,, \tag{6.5}$$

where we have used global $\mathrm{SU}(2)_L$ and $\mathrm{U}(1)_Y$ transformations to eliminate four degrees of freedom (see section 3.3.1). Non-zero values of the vacuum expectation value (vev) v_{CP} lead to spontaneous CP violation, while a non-zero v_{CB} spontaneously breaks electric charge. The numerical prefactors have been chosen such that all of the classical fields v have canonically normalised kinetic terms. The stationarity conditions for these field configurations are

$$\frac{\partial V}{\partial v_1} = 0 = -v_2 m_{12}^2 + v_1 m_{11}^2 + \frac{1}{2} v_1 (v_1^2 \lambda_1 + v_2^2 \lambda_{345} + v_{\mathrm{CB}}^2 \lambda_3 + v_{\mathrm{CP}}^2 \lambda_{34-5} + v_S^2 \lambda_7) \,, \tag{6.6}$$

$$\frac{\partial V}{\partial v_2} = 0 = -v_1 m_{12}^2 + v_2 m_{22}^2 + \frac{1}{2} v_2 (v_1^2 \lambda_{345} + v_2^2 \lambda_2 + v_{\mathrm{CB}}^2 \lambda_2 + v_{\mathrm{CP}}^2 \lambda_2 + v_S^2 \lambda_8) \,, \tag{6.7}$$

$$\frac{\partial V}{\partial v_{\mathrm{CB}}} = 0 = v_{\mathrm{CB}} m_{22}^2 + \frac{1}{2} v_{\mathrm{CB}} (v_1^2 \lambda_3 + v_2^2 \lambda_2 + v_{\mathrm{CB}}^2 \lambda_2 + v_{\mathrm{CP}}^2 \lambda_2 + v_S^2 \lambda_8) \,, \tag{6.8}$$

$$\frac{\partial V}{\partial v_{\mathrm{CP}}} = 0 = v_{\mathrm{CP}} m_{22}^2 + \frac{1}{2} v_{\mathrm{CP}} (v_1^2 \lambda_{34-5} + v_2^2 \lambda_2 + v_{\mathrm{CB}}^2 \lambda_2 + v_{\mathrm{CP}}^2 \lambda_2 + v_S^2 \lambda_8) \,, \tag{6.9}$$

$$\frac{\partial V}{\partial v_S} = 0 = v_{\mathrm{S}} m_S^2 + \frac{1}{2} v_{\mathrm{S}} (v_1^2 \lambda_7 + v_2^2 \lambda_8 + v_{\mathrm{CB}}^2 \lambda_8 + v_{\mathrm{CP}}^2 \lambda_8 + v_S^2 \lambda_6) \,, \tag{6.10}$$

where $\lambda_{345} = \lambda_3 + \lambda_4 + \lambda_5$ and $\lambda_{34-5} = \lambda_3 + \lambda_4 - \lambda_5$. These conditions allow for many different *phases* of the model [7].[1] The two phases with the correct pattern of electroweak symmetry breaking (EWSB) are

$$\mathcal{N} : v_1, v_2 \neq 0 \,, \quad v_S, v_{\mathrm{CB}}, v_{\mathrm{CP}} = 0 \,, \tag{6.11}$$

$$\mathcal{N}s : v_1, v_2, v_S \neq 0 \,, \quad v_{\mathrm{CB}}, v_{\mathrm{CP}} = 0 \,. \tag{6.12}$$

In phase $\mathcal{N}$ the singlet $\mathbb{Z}_2$ symmetry is unbroken leading to a 2HDM-like visible sector with a dark singlet [348]. In phase $\mathcal{N}s$ all $\mathbb{Z}_2$ symmetries are broken by the vevs, and all three CP-even scalar states mix with each other [7].

Equations (6.6) to (6.10) also allow for phases where the vacuum spontaneously breaks either electric charge or CP. The charge breaking phases are

$$\mathcal{CB} : \quad v_1, v_2, v_{\mathrm{CB}} \neq 0 \,, \quad v_S, v_{\mathrm{CP}} = 0 \,, \tag{6.13}$$

$$\mathcal{CB}s : \quad v_1, v_2, v_S, v_{\mathrm{CB}} \neq 0 \,, \quad v_{\mathrm{CP}} = 0 \tag{6.14}$$

[1] Throughout this chapter and in contrast to the previous chapter, the term *phase* refers to a vacuum configuration in analogy to thermodynamics, and never to a complex model parameter.

and the CP-breaking phases are

$$\mathcal{CP}: \quad v_1, v_2, v_{\mathrm{CP}} \neq 0\,, \quad v_S, v_{\mathrm{CB}} = 0\,, \tag{6.15}$$

$$\mathcal{CP}s: \quad v_1, v_2, v_S, v_{\mathrm{CP}} \neq 0\,, \quad v_{\mathrm{CB}} = 0\,. \tag{6.16}$$

However, the stationarity conditions imply that v_{CB} and v_{CP} cannot be non-zero simultaneously. In other words, the minimisation of the potential implies that, if $v_{\mathrm{CB}} \neq 0$ then $v_{\mathrm{CP}} = 0$, and vice-versa. Another phase exists, where only the singlet $\mathbb{Z}_2$ symmetry is broken and EWSB does not occur

$$S: \quad v_S \neq 0\,, \quad v_1, v_2, v_{\mathrm{CB}}, v_{\mathrm{CP}} = 0\,. \tag{6.17}$$

The final possibility is the trivial unbroken phase where all vevs are zero.

This list does not include the phase we considered for the dark sector model in section 5.2, where only Φ_1 has a non-vanishing vev. Such a phase is forbidden in the N2HDM for $m_{12}^2 \neq 0$ as a result of eqs. (6.6) and (6.7). In the dark sector model, the exact $\mathbb{Z}_2$ symmetry eq. (5.31) forces $m_{12}^2 = 0$ and allows this phase to exist. Additionally, the following analysis relies on a decomposition of the scalar potential into field bilinears, which is impossible if trilinear terms — such as the $A\,\Phi_1^\dagger \Phi_2 \Phi_S$ term of eq. (5.32) — are present. Therefore, even though the scalar potentials of the two models — eq. (5.32) and eq. (6.3) — are very similar, the following analysis does not generalise to the dark sector model. We will discuss the phenomenological consequences of this behaviour below.

6.1.1 The Bilinear Formalism

In the 2HDM it has been shown that if a normal vacuum $\mathcal{N}$ exists any stationary point that is charge or CP breaking is necessarily a saddle point that lies above the normal minimum [220, 349–351]. Already in ref. [7] we showed through numerical counterexamples that this conclusion no longer holds in the N2HDM.

In order to substantiate this discussion with a detailed analytical analysis we make use of a bilinear formalism, similar to what has been developed for the 2HDM [220, 347, 349–360]. We define the real, five-component vector X as

$$X = \begin{pmatrix} x_1 \\ x_2 \\ x_3 \\ x_4 \\ x_5 \end{pmatrix} = \begin{pmatrix} |\Phi_1|^2 \\ |\Phi_2|^2 \\ \mathrm{Re}(\Phi_1^\dagger \Phi_2) \\ \mathrm{Im}(\Phi_1^\dagger \Phi_2) \\ \frac{1}{2}\Phi_S^2 \end{pmatrix} \tag{6.18}$$

and rewrite the scalar potential as

$$V = X^T A + \frac{1}{2} X^T B X \tag{6.19}$$

with the vector A and the symmetric matrix B given by

$$A = \begin{pmatrix} m_{11}^2 \\ m_{22}^2 \\ -2m_{12}^2 \\ 0 \\ m_S^2 \end{pmatrix}, \quad B = \begin{pmatrix} \lambda_1 & \lambda_3 & 0 & 0 & \lambda_7 \\ \lambda_3 & \lambda_2 & 0 & 0 & \lambda_8 \\ 0 & 0 & 2(\lambda_4+\lambda_5) & 0 & 0 \\ 0 & 0 & 0 & 2(\lambda_4-\lambda_5) & 0 \\ \lambda_7 & \lambda_8 & 0 & 0 & \lambda_6 \end{pmatrix}. \tag{6.20}$$

The derivative[2] of the scalar potential is given by

$$V' = \frac{\partial V}{\partial X^T} = A + BX\,. \tag{6.21}$$

At a stationary point where the fields acquire expectation values of the form eq. (6.5) the expectation value of the vector X becomes

$$\langle X \rangle = \frac{1}{2} \begin{pmatrix} v_1^2 \\ v_2^2 + v_{\mathrm{CP}}^2 + v_{\mathrm{CB}}^2 \\ v_1 v_2 \\ v_1 v_{\mathrm{CP}} \\ v_S^2 \end{pmatrix}. \tag{6.22}$$

Using the stationarity conditions

$$\left\langle \frac{\partial V}{\partial v_i} \right\rangle = \frac{\partial \langle X \rangle}{\partial v_i} \langle V' \rangle = 0 \tag{6.23}$$

with $v_i \in \{v_1, v_2, v_{\mathrm{CP}}, v_{\mathrm{CB}}\}$ as well as eq. (6.19) it can be shown that [220]

$$\langle V \rangle = \frac{1}{2} \langle X \rangle^T A = -\frac{1}{2} \langle X \rangle^T B \langle X \rangle\,. \tag{6.24}$$

In the following $\langle X \rangle$ and $\langle V' \rangle$ will be needed at each kind of stationary point. The value of $\langle X \rangle$ can be trivially deduced from eqs. (6.11) to (6.17) and (6.22). The value of $\langle V' \rangle$ can be simplified using the stationarity conditions and the eigenvalues of the mass matrices. This leads to [4]

$$\langle V' \rangle_{\mathcal{N}} = \frac{1}{v^2} \begin{pmatrix} v_2^2 m_{H^\pm}^2 \\ v_1^2 m_{H^\pm}^2 \\ -2 v_1 v_2 m_{H^\pm}^2 \\ 0 \\ v^2 m_D^2 \end{pmatrix}, \quad \langle V' \rangle_{\mathcal{N}s} = \frac{m_{H^\pm}^2}{v^2} \begin{pmatrix} {v_2}^2 \\ {v_1}^2 \\ -2 v_1 v_2 \\ 0 \\ 0 \end{pmatrix} \tag{6.25}$$

for the minima of the phases with correct EWSB. With the parameter $v^2 = v_1^2 + v_2^2$ the squared charged Higgs mass is

$$m_{H^\pm}^2 = m_{12}^2 \frac{v^2}{v_1 v_2} - \frac{1}{2}(\lambda_4 + \lambda_5) v^2\,, \tag{6.26}$$

[2] Since X is a vector of bilinears this is the first derivative in terms of X but the second derivative in terms of the fields.

and the squared dark singlet mass is given by

$$m_D^2 = m_S^2 + \frac{1}{2}\left(\lambda_7 v_1^2 + \lambda_8 v_2^2\right) . \tag{6.27}$$

The charge-breaking phases yield

$$\langle V' \rangle_{\mathcal{CB}} = \begin{pmatrix} 0 \\ 0 \\ 0 \\ 0 \\ m_{\mathcal{CB}}^2 \end{pmatrix} , \quad \langle V' \rangle_{\mathcal{CB}s} = \begin{pmatrix} 0 \\ 0 \\ 0 \\ 0 \\ 0 \end{pmatrix} , \tag{6.28}$$

where

$$m_{\mathcal{CB}}^2 = m_S^2 + \frac{1}{2}\left(\lambda_7 v_1^2 + \lambda_8 (v_2^2 + v_{\mathrm{CP}}^2)\right) \tag{6.29}$$

and the CP-breaking minima lead to

$$\langle V' \rangle_{\mathcal{CP}} = \begin{pmatrix} 0 \\ 0 \\ 0 \\ 0 \\ m_{\mathcal{CP}}^2 \end{pmatrix} , \quad \langle V' \rangle_{\mathcal{CP}s} = \begin{pmatrix} 0 \\ 0 \\ 0 \\ (\lambda_4 - \lambda_5) v_1 v_{\mathrm{CP}} \\ 0 \end{pmatrix} , \tag{6.30}$$

where

$$m_{\mathcal{CP}}^2 = m_S^2 + \frac{1}{2}\left(\lambda_7 v_1^2 + \lambda_8 (v_2^2 + v_{\mathrm{CP}}^2)\right) . \tag{6.31}$$

6.2 Stability of the EW Phases

With this information, we can study the relative depth of the different stationary points of the N2HDM. We assume that the model parameters are such that the stationarity conditions permit solutions of at least one of the phases with viable EWSB — $\mathcal{N}$ or $\mathcal{N}s$ — and another kind of stationary point. We call such a scenario *coexisting* stationary points of the corresponding phases.

If a secondary stationary point coexists with the electroweak (EW) vacuum, the secondary stationary point could be a deeper minimum and vacuum tunnelling would be possible. Therefore vacuum stability constraints as discussed in chapter 3 need to be applied in this case. The bilinear formalism allows us to establish analytically which kinds of minima can coexist in the scalar potential and lead to vacuum stability constraints.

Consider two stationary points of different phases i and j. All quantities are expectation values, and we drop the brackets for a cleaner notation. We can explicitly calculate the product $X_i^T V_j'$ but also express it through eq. (6.21) as

$$X_i^T V_j' = X_i^T (A + B X_j) = X_i^T A + X_i^T B X_j \, . \tag{6.32}$$

From eq. (6.24) we know that

$$X_i^T A = 2V_i \tag{6.33}$$

and obtain

$$X_i^T B X_j = X_i^T V_j' - 2V_i \,. \tag{6.34}$$

Since the matrix B is symmetric we obtain the same right-hand side when $i \leftrightarrow j$. Equating these leads to a formula for the depth difference of the two stationary points

$$V_i - V_j = \frac{1}{2}\left(X_i^T V_j' - X_j^T V_i'\right) \,. \tag{6.35}$$

6.2.1 Stability Against Charge and CP Breaking

We will begin by considering scenarios where a vacuum with viable EWSB coexists with a charge- or CP-breaking stationary point. In the following, we add a secondary subscript to the vacua $v_{1,2,S}$ denoting in which phase they are evaluated.

Stability of $\mathcal{N}$ Vacua Against Charge Breaking

Applying eq. (6.35) to the case of an $\mathcal{N}$ and a $\mathcal{CB}$ vacuum leads to

$$V_{\mathcal{CB}} - V_{\mathcal{N}} = \left.\frac{m_{H^\pm}^2}{4v^2}\right|_{\mathcal{N}} \left[\left(v_{2\mathcal{N}} v_{1\mathcal{CB}} - v_{1\mathcal{N}} v_{2\mathcal{CB}}\right)^2 + v_{1\mathcal{N}}^2 v_{\mathrm{CB}}^2\right] \,. \tag{6.36}$$

Both the quantity in brackets and v^2 are always positive. Therefore, if the $\mathcal{N}$ stationary point is a minimum and thus $m_{H^\pm}^2 > 0$, it will always be deeper than any $\mathcal{CB}$ stationary point and therefore stable against vacuum decay.

In the case of $\mathcal{N}$ and $\mathcal{CB}s$, the results are similar with

$$V_{\mathcal{CB}s} - V_{\mathcal{N}} = \left.\frac{m_{H^\pm}^2}{4v^2}\right|_{\mathcal{N}} \left[\left(v_{2\mathcal{N}} v_{1\mathcal{CB}s} - v_{1\mathcal{N}} v_{2\mathcal{CB}s}\right)^2 + v_{1\mathcal{N}}^2 v_{\mathrm{CB}}^2\right] + \left.\frac{m_D^2}{4}\right|_{\mathcal{N}} v_{S\mathcal{CB}s}^2 \,. \tag{6.37}$$

Again, the right-hand side is positive as long as $\mathcal{N}$ is a minimum. Therefore, a vacuum of type $\mathcal{N}$ is also stable against vacuum decay into a $\mathcal{CB}s$ stationary point.

Stability of $\mathcal{N}s$ Vacua Against Charge Breaking

The analysis for the $\mathcal{N}s$ case is analogous but leads to different conclusions. Starting with the case of an $\mathcal{N}s$ and a $\mathcal{CB}s$ stationary point we obtain

$$V_{\mathcal{CB}s} - V_{\mathcal{N}s} = \left.\frac{m_{H^\pm}^2}{4v^2}\right|_{\mathcal{N}s} \left[\left(v_{2\mathcal{N}s} v_{1\mathcal{CB}s} - v_{1\mathcal{N}s} v_{2\mathcal{CB}s}\right)^2 + v_{1\mathcal{N}s}^2 v_{\mathrm{CB}}^2\right] \,, \tag{6.38}$$

which is always positive as long as $\mathcal{N}s$ is a minimum. $\mathcal{N}s$ vacua are thus stable against vacuum decay into $\mathcal{CB}s$ stationary points.

However, the depth difference between an $\mathcal{N}s$ and a $\mathcal{CB}$ stationary point is

$$V_{\mathcal{CB}} - V_{\mathcal{N}s} = \frac{m_{H^\pm}^2}{4v^2}\bigg|_{\mathcal{N}s} \left[(v_{2\mathcal{N}s}v_{1\mathcal{CB}} - v_{1\mathcal{N}s}v_{2\mathcal{CB}})^2 + v_{1\mathcal{N}s}^2 v_{\mathrm{CB}}^2\right] - \frac{1}{4}v_{S\mathcal{N}s}^2 m_{\mathcal{CB}}^2 \,. \tag{6.39}$$

The sign of the right-hand side now cannot be established, and there is no clear relationship between the depths of the two vacua. As such, $\mathcal{N}s$ vacua can coexist with potentially deeper $\mathcal{CB}$ minima.

Stability of $\mathcal{N}$ Vacua Against CP Breaking

The analysis for the CP-breaking phases is analogous. The depth difference between an $\mathcal{N}$ and $\mathcal{CP}$ vacuum is

$$V_{\mathcal{CP}} - V_{\mathcal{N}} = \frac{m_A^2}{4v^2}\bigg|_{\mathcal{N}} \left[(v_{2\mathcal{N}}v_{1\mathcal{CP}} - v_{1\mathcal{N}}v_{2\mathcal{CP}})^2 + v_{1\mathcal{N}}^2 v_{\mathrm{CP}}^2\right] \tag{6.40}$$

and for $\mathcal{N}$ and $\mathcal{CB}s$ it is

$$V_{\mathcal{CP}s} - V_{\mathcal{N}} = \frac{m_A^2}{4v^2}\bigg|_{\mathcal{N}} \left[(v_{2\mathcal{N}}v_{1\mathcal{CP}s} - v_{1\mathcal{N}}v_{2\mathcal{CP}s})^2 + v_{1\mathcal{N}}^2 v_{\mathrm{CP}}^2\right] + \frac{m_D^2}{4}\bigg|_{\mathcal{N}} v_{S\mathcal{CP}s}^2 \,. \tag{6.41}$$

The pseudo scalar mass at $\mathcal{N}$ (and $\mathcal{N}s$) stationary points is given by

$$m_A^2 = m_{H^\pm}^2 + \frac{1}{2}(\lambda_4 - \lambda_5)v^2 \,. \tag{6.42}$$

As long as $\mathcal{N}$ is a vacuum and thus $m_A^2 > 0$, both right-hand sides are positive, and $\mathcal{N}$ is therefore stable against tunnelling into $\mathcal{CP}$ and $\mathcal{CP}s$ stationary points.

Stability of $\mathcal{N}s$ Vacua Against CP Breaking

The results for $\mathcal{N}s$ EW vacua is, again, more interesting. For an $\mathcal{N}s$ and a $\mathcal{CP}s$ stationary point we obtain

$$V_{\mathcal{CP}s} - V_{\mathcal{N}s} = \frac{m_A^2}{4v^2}\bigg|_{\mathcal{N}s} \left[(v_{2\mathcal{N}s}v_{1\mathcal{CP}s} - v_{1\mathcal{N}s}v_{2\mathcal{CP}s})^2 + v_{1\mathcal{N}s}^2 v_{\mathrm{CP}}^2\right] \,, \tag{6.43}$$

which is positive when $\mathcal{N}s$ is a minimum. Vacua of phase $\mathcal{N}s$ are thus stable against vacuum decay into $\mathcal{CP}s$ stationary points.

The depth difference between an $\mathcal{N}s$ and a $\mathcal{CP}$ stationary point is

$$V_{\mathcal{CP}} - V_{\mathcal{N}s} = \frac{m_A^2}{4v^2}\bigg|_{\mathcal{N}s} \left[(v_{2\mathcal{N}s}v_{1\mathcal{CP}} - v_{1\mathcal{N}s}v_{2\mathcal{CP}})^2 + v_{1\mathcal{N}s}^2 v_{\mathrm{CP}}^2\right] - \frac{1}{4}v_{S\mathcal{N}s}^2 m_{\mathcal{CP}}^2 \,. \tag{6.44}$$

Again, the sign of the right-hand side is not fixed and $\mathcal{N}s$ vacua can coexist with potentially deeper $\mathcal{CP}$ minima.

6.2.2 Other Coexisting Minima

Vacuum instabilities may also arise if $\mathcal{N}$, $\mathcal{N}s$, or even S minima coexist. This can happen either if minima of different phases coexist or if the stationarity conditions admit multiple stationary points of the same phase but with different depths. If an $\mathcal{N}$ and an $\mathcal{N}s$ stationary point coexist we obtain

$$V_{\mathcal{N}s} - V_{\mathcal{N}} = \frac{1}{4}\left(\left.\frac{m_{H^\pm}^2}{4v^2}\right|_{\mathcal{N}} - \left.\frac{m_{H^\pm}^2}{4v^2}\right|_{\mathcal{N}s}\right)\left(v_{1\mathcal{N}}v_{2\mathcal{N}s} - v_{1\mathcal{N}s}v_{2\mathcal{N}}\right)^2 + \frac{1}{4}m_D^2 v_{s\mathcal{N}s}^2\,. \tag{6.45}$$

for their depth difference. No definite sign can be established, and if $\mathcal{N}$ and $\mathcal{N}s$ minima coexist either of them may be deeper. Therefore, though $\mathcal{N}$ is stable against charge breaking or CP breaking minima, it is not guaranteed to be stable against a deeper $\mathcal{N}s$ vacuum. Likewise, an $\mathcal{N}s$ minimum may not only be unstable against deeper $\mathcal{CB}$ or $\mathcal{CP}$ minima but also against a deeper $\mathcal{N}$ minimum. Similarly, stability between $\mathcal{N}$ and S as well as $\mathcal{N}s$ and S minima cannot be established analytically.

The final possibility for instability of vacua of types $\mathcal{N}$ (or $\mathcal{N}s$) is that the stationarity conditions eqs. (6.6) to (6.10) yield more than one solution of a given phase. This means that *e.g.* a solution

$$\mathcal{N} \equiv \{\langle\Phi_1\rangle, \langle\Phi_2\rangle\} = \frac{1}{\sqrt{2}}\{v_1, v_2\} \tag{6.46}$$

exists as well as another one with

$$\mathcal{N}' \equiv \frac{1}{\sqrt{2}}\{v_1', v_2'\} \tag{6.47}$$

and different vevs $v_1 \neq v_1'$, $v_2 \neq v_2'$ and values of the scalar potential $V_{\mathcal{N}} \neq V_{\mathcal{N}'}$.

This possibility already arises in the 2HDM [220, 351, 355, 361, 362] — therein dubbed "panic vacua" — and it remains in the N2HDM as an avenue for instability of the $\mathcal{N}$ vacuum (and also of the $\mathcal{N}s$ one, since the minimisation equations of the potential may yield more than one solution of type $\mathcal{N}s$). We do not study this possibility analytically but include it in the numerical analysis of section 6.3.

6.2.3 Summary

The results of the previous sections show how the addition of the real singlet field to the 2HDM qualitatively changes the vacuum structure of the model. In the N2HDM normal EW-breaking minima are no longer necessarily the global minima of the model. We summarise the results we obtained in table 6.1. If a minimum of type $\mathcal{N}$ exists, it is certainly deeper than any charge or CP-breaking stationary points that the potential might have — the model guarantees the stability of $\mathcal{N}$ against CP or charge breaking. However, this does not hold for minima of type $\mathcal{N}s$. These can coexist with charge-breaking $\mathcal{CB}$ or CP-breaking $\mathcal{CP}$ minima. Additionally, there is no fixed ordering of depths between $\mathcal{N}$, $\mathcal{N}s$, and S minima.

Table 6.1: Stability of EW-breaking $\mathcal{N}$ and $\mathcal{N}s$ vacua in the N2HDM. An EW-breaking vacuum (*i.e.* a local minimum) in the given phase is necessarily deeper than all stationary points marked as "stable". For the stationary points marked with $\times$ either of the two extrema may be the deeper minimum depending on the model parameters.

EW vacuum	$\mathcal{N}$	$\mathcal{N}s$	$\mathcal{CB}$	$\mathcal{CB}s$	$\mathcal{CP}$	$\mathcal{CP}s$	S
$\mathcal{N}$	$\times$	$\times$	stable	stable	stable	stable	$\times$
$\mathcal{N}s$	$\times$	$\times$	$\times$	stable	$\times$	stable	$\times$

These results underline the curiously unique nature of the vacuum structure in the 2HDM, where the existence of a minimum of a given nature automatically implies that no minima of different types may exist. Models with a different scalar content do not share this property (this has previously been shown for singlet extensions of the SM [250] and models with more than two doublets [363]). We have shown that the mere addition of a real singlet to the 2HDM is enough to qualitatively change the vacuum structure of the model. The N2HDM preserves some of the properties of the 2HDM — wherein the $\mathcal{N}$ minimum mimics the stability behaviour of the normal minima of the 2HDM — but when $\mathcal{N}s$ minima are considered, tunnelling to deeper minima of different types become possible.

6.3 Phenomenological Impact of Vacuum Stability

We perform a numerical study to illustrate the impact of the N2HDM vacuum structure on the phenomenologically relevant regions of the parameter space. We focus on parameter points where the EW vacuum is of type $\mathcal{N}s$ since — following the analytical analysis — this is the most interesting case for vacuum stability constraints. We have studied the phenomenology of this phase — called *broken phase* — in detail in ref. [7].

The pseudoscalar and charged sector of the N2HDM are — identically to the 2HDM — diagonalised with the mixing angle β defined through

$$\tan\beta = \frac{v_2}{v_1} \tag{6.48}$$

separating the would-be Goldstone bosons from the physical pseudoscalar A with mass given in eq. (6.42) and the charged Higgs bosons $H^\pm$ with mass given by eq. (6.26). For an $\mathcal{N}s$ EW-vacuum all three neutral, CP-even scalar fields mix into three physical Higgs bosons $H_{1,2,3}$. Their 3×3 mixing matrix is parametrised as eq. (5.13) in terms of the mixing angles α_1 to α_3 that can be chosen to lie in the range

$$-\frac{\pi}{2} \leq \alpha_{1,2,3} < \frac{\pi}{2}\,. \tag{6.49}$$

The CP-even scalars are assumed to be mass-ordered such that

$$m_{H_1} < m_{H_2} < m_{H_3}\,. \tag{6.50}$$

Using the mass diagonalisation and the minimum conditions of the phase $\mathcal{N}s$ it is possible to express the twelve real parameters of the N2HDM Lagrangian through the parameters

$$\alpha_1\,,\quad \alpha_2\,,\quad \alpha_3\,,\quad \tan\beta\,,\quad v = v_1^2 + v_2^2\,,\quad v_S\,,\quad m_{H_{1,2,3}}\,,\quad m_A\,,\quad m_{H^\pm}\,,\quad m_{12}^2\,. \tag{6.51}$$

The relations between these and the parameters of eq. (6.3) can be found in the appendix of ref. [7].

6.3.1 Parameter Scan

We performed a scan of the N2HDM parameter space using an improved private version of `ScannerS` [7, 125, 249, 290]. All of the resulting parameter points fulfil the applied theoretical constraints and are compatible with the applied current experimental constraints at the 2σ level (see below). We focus on the Yukawa type I but occasionally comment on type II. The Yukawa type has no direct impact on vacuum stability at the tree-level. However, since the regions of parameter space favoured by the experimental constraints strongly depend on the Yukawa type, there will be visible differences regarding the impact of vacuum stability constraints.

The tree-level perturbative unitarity bounds in the high-energy limit as described in section 2.2 were derived in ref. [7]. Closed-form conditions for boundedness from below (see section 3.2) were first derived in ref. [221]. In our notation the parameter region allowed by boundedness is

$$\Omega_1 \cup \Omega_2 \tag{6.52}$$

with

$$\Omega_1 = \left\{ \begin{array}{l} 0 < \lambda_{1,2,6}\,; \quad 0 < \sqrt{\lambda_1\lambda_6} + \lambda_7\,; \quad 0 < \sqrt{\lambda_1\lambda_2} + \lambda_3 + D\,; \\ \qquad\qquad\qquad\quad 0 < \sqrt{\lambda_2\lambda_6} + \lambda_8\,; \quad 0 \leq \lambda_7 + \sqrt{\dfrac{\lambda_1}{\lambda_2}}\lambda_8 \end{array} \right\} \tag{6.53}$$

and

$$\Omega_2 = \left\{ \begin{array}{ll} 0 < \lambda_{1,2,6}\,; & \sqrt{\lambda_1\lambda_6} > -\lambda_7 \geq \sqrt{\dfrac{\lambda_1}{\lambda_2}}\lambda_8\,; \\ 0 \leq \lambda_2\lambda_6 - \lambda_8^2\,; & \sqrt{(\lambda_7^2 - \lambda_1\lambda_6)(\lambda_8^2 - \lambda_2\lambda_6)} > \lambda_7\lambda_8 - (D + \lambda_3)\lambda_6 \end{array} \right\} \tag{6.54}$$

depending on the discriminant

$$D = \min(\lambda_4 - |\lambda_5|, 0)\,. \tag{6.55}$$

In contrast to earlier works [7, 9], we do not impose absolute stability of the EW vacuum as a theoretical constraint since we want to study the vacuum structure in detail

Table 6.2: Input parameter ranges for the N2HDM parameter scan ($y, z \in \{1, 2, 3\}$). The three mixing angles $\alpha_{1,2,3}$ in the CP-even scalar sector vary through their whole allowed range.

	m_{H_y}, m_{H_z}, m_A GeV	$m_{H^\pm}$ GeV	$\tan\beta$	m_{12}^2 GeV^2	v_S GeV
min	30	150	0.8	10^{-3}	1
max	1500	1500	20	5×10^5	3000

and take into account that long-lived, metastable regions of the parameter space are phenomenologically viable.

We include all applicable experimental constraints described in section 2.4. We use the oblique parameters to parametrise EW precision constraints as described in section 2.4.1. The predictions for S, T and U from refs. [137, 138] are compared against the results of ref. [135]. The flavour constraints in the $m_{H^\pm}$–$\tan\beta$ plane [135] that were discussed in section 2.4.2 are directly applicable to the N2HDM. In type I the strongest constraint is obtained from $B_d \to \mu^+\mu^-$ (see fig. 2.2). We check for agreement with the collider Higgs data using `HiggsBounds`-5.3.2beta [163–167] and `HiggsSignals`-2.2.3beta [165, 170–172]. `HiggsBounds` checks for 2σ compatibility with all searches for additional scalars (see section 2.4.4). With `HiggsSignals` we employ a cut on $\Delta\chi^2 = \chi^2_{\text{N2HDM}} - \chi^2_{\text{SM}} < 6.18$ corresponding approximately to a 2σ region around the SM expectation — see section 2.4.5 for a more detailed discussion. The required model predictions for branching ratios and total widths are obtained from `N2HDECAY` [7, 11] and the hadron collider production cross sections from `SusHi` [314, 315].

We generate a sample of valid parameter points on which to study the vacuum structure and vacuum stability. One of the three CP-even, neutral Higgs masses is fixed to

$$m_{H_x} = m_{h_{125}} = 125.09\,\text{GeV}\,, \tag{6.56}$$

and the EW vev is set to its SM value

$$v \approx 246\,\text{GeV}\,. \tag{6.57}$$

Random values for the remaining input parameters are independently drawn from uniform distributions with the ranges given in table 6.2. The three mixing angles in the CP-even scalar sector vary through their whole allowed range. Note that we do not specify a mass ordering for $m_{H_{x,y,z}}$ — the 125 GeV Higgs boson (h_{125}) can be the lightest or heaviest state as well as the one in between.

For each of these parameter points, we use the method described in chapter 3 to find all minima of the tree-level scalar potential and calculate the lifetime of the EW vacuum if it is not absolutely stable. We call those vacua short-lived, where

$$B < 390 \tag{6.58}$$

Table 6.3: Percentage of phenomenologically viable points in our scan that have a second minimum in addition to an EW vacuum of type $\mathcal{N}s$. The first row contains the percentage of *coexisting* minima, the second line the ones that are *deeper* and the third line the *dangerous*, short-lived, ones. The minima of type $\mathcal{N}s'$ have vevs like those of $\mathcal{N}s$ but $v' \neq 246\,\text{GeV}$ and differ from the EW vacuum in depth.

	$\mathcal{N}s'$	$\mathcal{N}$	$\mathcal{CB}$	$\mathcal{CP}$
	prevalence in %			
exists	0.05	23.3	4.49	2.80
deep	0.0015	20.9	4.11	2.55
dangerous	0.0	6.89	1.12	0.678

holds for tunnelling to any other minimum. This is a very conservative estimate where only vacua with a survival probability P through the age of the universe

$$P \ll 1 - 5\sigma \approx 5.73 \times 10^{-7} \tag{6.59}$$

are considered short lived. We have verified that our results remain qualitatively unchanged when varying the bound in eq. (6.58) by 20%. This accounts for the uncertainties discussed in section 3.3.2.

6.3.2 Discussion

In this section, we present a numerical and phenomenological analysis of the N2HDM vacuum structure and vacuum stability based on a sample of $\sim 10^6$ phenomenologically viable parameter points generated according to section 6.3.1. We aim to investigate whether the possible coexistence of minima discussed analytically in section 6.1

- is found in a substantial region of the N2HDM parameter space that is compatible with current theoretical and experimental constraints,
- can be directly related to phenomenological observations at colliders.

Since we assume the EW vacuum to be of type $\mathcal{N}s$ the potentially dangerous minima are $\mathcal{CB}$, $\mathcal{CP}$, $\mathcal{N}$, and a second different minimum of type $\mathcal{N}s$ (see below for a discussion of minima of type S). We will distinguish three cases for these potentially dangerous vacua:

- they *coexist* with the EW vacuum,
- they are also *deeper* than the EW vacuum,
- they are additionally *dangerous*, *i.e.* tunnelling from the EW vacuum is fast as defined in eq. (6.58).

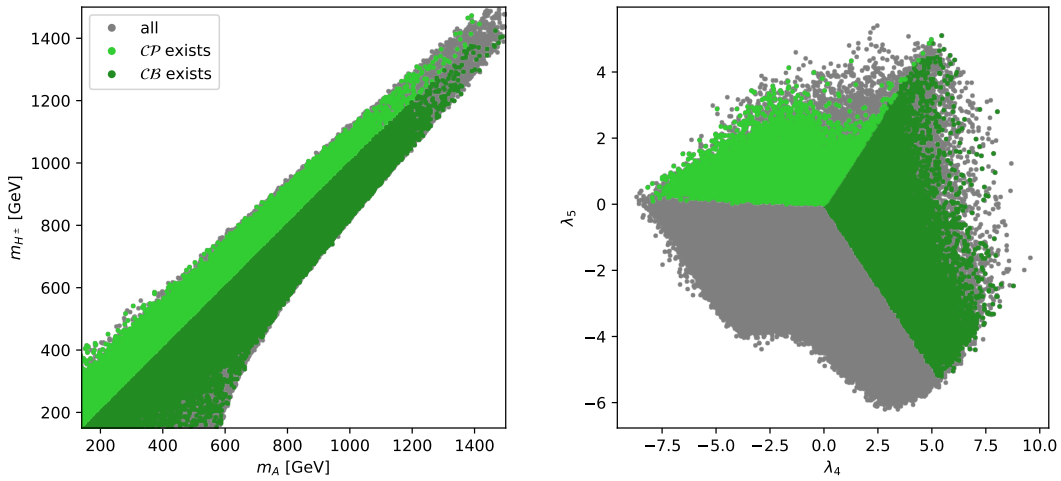

Figure 6.1: The distribution of secondary charge and CP breaking minima. The left plot shows the plane of the CP-odd Higgs mass m_A and charged Higgs mass $m_{H^\pm}$. The right plot shows the plane of the scalar potential parameters λ_4 and λ_5. In grey, we show all parameter points fulfilling the theoretical and experimental constraints. On top, we show the points where a secondary minimum of type $\mathcal{CB}$ (dark green) or $\mathcal{CP}$ (light green) exists. Figure as published in ref. [4].

Table 6.3 shows the prevalence of these cases for the different possible secondary minima in our sample. The precise numbers in table 6.3 have no physical significance as they depend on the sampling method of the parameter space. However, the displayed results clearly show that the possibilities discussed in section 6.1 remain relevant even after considering all other applicable constraints. Especially, dangerous minima of type $\mathcal{N}$ occur frequently. Table 6.3 also shows that the requirement of absolute stability would be a substantially stronger constraint on the parameter space compared to the condition that the EW vacuum should be sufficiently long-lived. Important regions of parameter space with metastable vacua could be left out if absolute stability was imposed.

The only case missing in table 6.3 that is allowed by the analytical analysis are secondary minima of type S. We have not found a single parameter point in our sample where a stationary point of type S is a minimum. This could mean that minima of type S cannot coexist with an $\mathcal{N}s$ vacuum, that all points where this is possible are ruled out by current constraints, or that these minima are exceedingly rare. Either way, this means that secondary minima of type S are of limited phenomenological interest and we will not discuss them further here.

Figure 6.1, left, shows the distribution of charge- and CP-breaking secondary minima in the plane of the pseudoscalar Higgs mass m_A and charged Higgs mass $m_{H^\pm}$ at the EW vacuum. The overall distribution of the phenomenologically viable parameter points is primarily driven by the EW precision constraints, which force the neutral Higgs bosons to be relatively close in mass to the charged Higgs boson (see section 2.4.1). Parameter

points without any secondary minima, as well as parameter points with secondary $\mathcal{N}$ minima, exist throughout the allowed region. In contrast, secondary $\mathcal{CB}$ minima only exist as long as $m_A > m_{H^\pm}$ while $\mathcal{CP}$ minima only exist when $m_{H^\pm} > m_A$. This happens because the pseudoscalar and charged masses in an $\mathcal{N}s$ minimum are such that (see eq. (6.42))

$$m_A^2 - m_{H^\pm}^2 = \frac{1}{2}(\lambda_4 - \lambda_5)v^2 \,. \tag{6.60}$$

At the same time, in a $\mathcal{CB}$ stationary point one of the eigenvalues of the scalar mass matrix is

$$m^2\big|_{\mathcal{CB}} = \frac{1}{2}(\lambda_4 - \lambda_5)[v_1^2 + v_2^2 + v_{\mathrm{CB}}^2] \tag{6.61}$$

while at the $\mathcal{CP}$ stationary point one eigenvalue is

$$m^2\big|_{\mathcal{CP}} = \frac{1}{2}(\lambda_5 - \lambda_4)[v_1^2 + v_2^2 + v_{\mathrm{CP}}^2] \,. \tag{6.62}$$

The quantities in square brackets are always positive and the squared masses are positive if the corresponding stationary points are minima. Therefore, for the $\mathcal{CB}$ stationary point to be a minimum $\lambda_4 > \lambda_5$ which requires $m_A > m_{H^\pm}$ at the $\mathcal{N}s$ vacuum. Similarly, a $\mathcal{CP}$ minimum requires $\lambda_4 < \lambda_5$ which implies $m_A < m_{H^\pm}$.

Figure 6.1, right, illustrates the same behaviour in the plane of λ_4 and λ_5. The points without secondary minima or with secondary $\mathcal{N}$ minima are again scattered throughout the allowed parameter space while the $\mathcal{CP}$ and $\mathcal{CB}$ minima can only occur in sharply defined regions. From the previous discussion $\lambda_4 = \lambda_5$ is the expected border between the regions where $\mathcal{CP}$ and $\mathcal{CB}$ can exist. However, fig. 6.1, right, shows that there is an additional region

$$\lambda_5 < 0 \wedge \lambda_4 < -\lambda_5 \tag{6.63}$$

where neither $\mathcal{CP}$ nor $\mathcal{CB}$ minima can exist. The analytical explanation for this behaviour is given in the appendix of ref. [4].

In fig. 6.2, we compare analytical and numerical results for the relative depth of $\mathcal{N}$ and $\mathcal{N}s$ vacua. The relative depth of an $\mathcal{N}s$ and $\mathcal{N}$ vacuum — as given by eq. (6.45) — is shown as a function of $\tan\beta$ at the $\mathcal{N}s$ EW vacuum. The plot only includes parameter points where a secondary $\mathcal{N}$ minimum exists and shows its depth relative to the depth of the $\mathcal{N}s$ EW vacuum. As expected, in all parameter points where $V_{\mathcal{N}s} - V_{\mathcal{N}} > 0$ the $\mathcal{N}$ minimum is classified as either deep (blue points) or dangerous (red points). The parameter points with dangerous $\mathcal{N}$ only begin to appear if $V_{\mathcal{N}s} - V_{\mathcal{N}} \gtrsim 10^7$, and their distribution shows some dependence on $\tan\beta$. For small $\tan\beta \lesssim 2$ the $\mathcal{N}$ vacuum is only unstable if the depth difference is $\gtrsim 10^9$ while for large $\tan\beta \gtrsim 12$ the majority of deep $\mathcal{N}$ vacua in our sample is dangerous.[3]

So far, we have illustrated how the analytical results of section 6.1 are reflected in the phenomenologically viable parameter space. We will now discuss the vacuum stability

[3] This is more clearly visible when reversing the plotting order of fig. 6.2 and plotting the parameter points with deep but not dangerous $\mathcal{N}$ vacua on top.

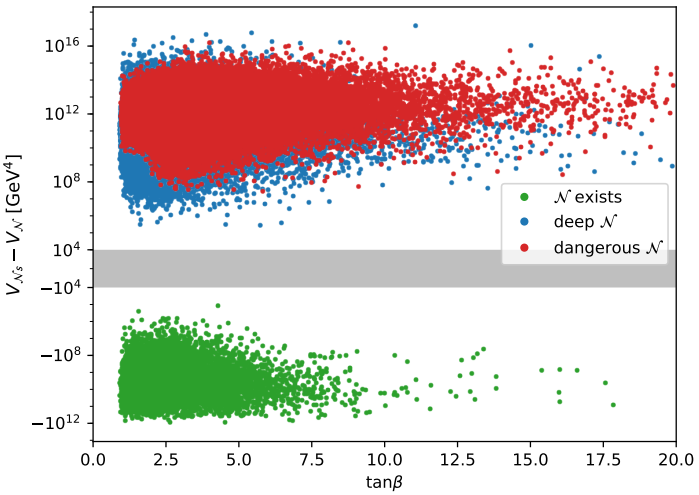

Figure 6.2: The difference in the value of the scalar potential between the EW $\mathcal{N}s$ vacuum and a secondary $\mathcal{N}$ minimum according to eq. (6.45) as a function of $\tan\beta$ at the EW vacuum. Only parameter points where a secondary $\mathcal{N}$ vacuum exists are shown. The colour code represents the results of the numerical analysis. The green parameter points have a secondary $\mathcal{N}$ minimum, but tunnelling from the EW vacuum is not possible. For the blue parameter points tunnelling is possible but slow while at the red points (plotted on top) the EW vacuum is short-lived (see eq. (6.58)). Figure as published in ref. [4].

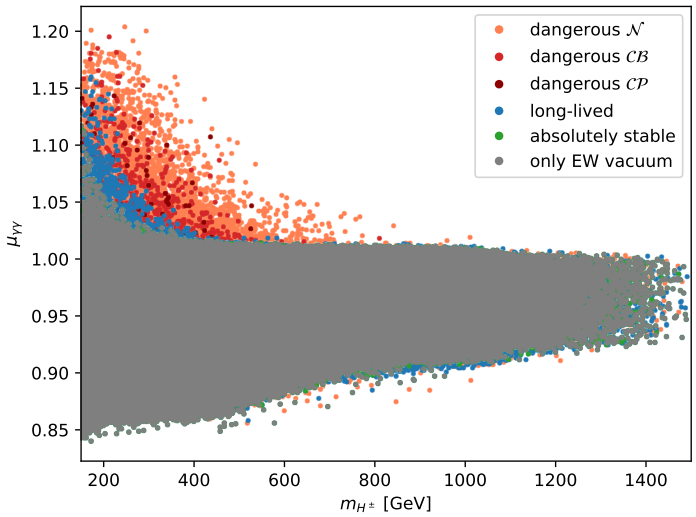

Figure 6.3: The signal strength $\mu_{\gamma\gamma}$ of $pp \to h_{125} \to \gamma\gamma$ as a function of the charged Higgs mass. The parameter points without any secondary minima (grey) are plotted on top, followed by the absolutely stable (green), and long-lived (blue) parameter points. Below these, the points with *dangerous* secondary minima are shown in different shades of red denoting the type of dangerous minimum present ($\mathcal{N}$ — light red, $\mathcal{CB}$ — red, $\mathcal{CP}$ — dark red). Figure as published in ref. [4].

constraints arising from these secondary vacua. In imposing vacuum stability constraints, we distinguish the following cases:

- parameter points where the EW vacuum is the only vacuum,
- absolutely stable parameter points where secondary minima *exist* but are never *deep*,
- long-lived parameter points where secondary vacua are *deep* but never *dangerous*,
- short-lived parameter points that have *dangerous* secondary minima.

Figure 6.3 demonstrates the phenomenological impact of vacuum stability constraints. It shows the signal strength of h_{125} in the $\gamma\gamma$ channel defined as

$$\mu_{\gamma\gamma} = \frac{\sigma(pp \to h_{125})\mathrm{BR}(h_{125} \to \gamma\gamma)}{\sigma(pp \to h_{\mathrm{SM}})\mathrm{BR}(h_{\mathrm{SM}} \to \gamma\gamma)} \tag{6.64}$$

as a function of the charged Higgs mass. The short-lived (different shades of red) parameter points are plotted below the grey points, for which no secondary minima exist. Therefore, vacuum stability excludes any region of parameter space where only the red parameter points are visible. One can see that significant parts of the parameter space corresponding to an enhanced signal strength, $\mu_{\gamma\gamma} > 1$, are excluded because they have a dangerous $\mathcal{N}$, $\mathcal{CP}$, or $\mathcal{CB}$ minimum below the EW vacuum. If, for instance, a charged

Higgs with a mass of 500 GeV is discovered, fig. 6.3 implies a bound of about $\mu_{\gamma\gamma} \lesssim 1.03$ in the N2HDM of type I. If on the other hand $m_{H^\pm}$ could be constrained to be larger than 250 GeV (*e.g.* by a 500 GeV e^+e^--collider) enhancements of $\mu_{\gamma\gamma} \gtrsim 1.1$ would be excluded in the N2HDM of type I by the vacuum stability constraint. One can also see from fig. 6.3 that imposing the constraint of an absolutely stable EW vacuum would exclude the blue points in fig. 6.3 — which indicate a long-lived EW vacuum — with possibly misleading conclusions.

The behaviour observed in fig. 6.3 stems from the BR($h_{125} \to \gamma\gamma$). The three kinds of diagrams contributing to this loop-induced decay are

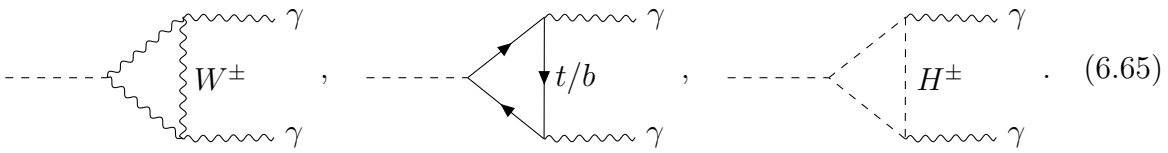

(6.65)

For h_{125} the first diagram with the $W^\pm$ loop is the dominant contribution. The second diagram involving heavy fermion loops interferes destructively with it. We have verified that vacuum stability is not sensitive to the Yukawa or gauge couplings that enter the first two diagrams. The third diagram describes the contribution of a charged Higgs boson and is sensitive to its mass $m_{H^\pm}$ and its coupling $g_{h_{125}H^+H^-}$ (defined in the appendix of ref. [7]). The mass and trilinear scalar coupling are directly related to the scalar potential and may be impacted by vacuum stability constraints. Figure 6.4 shows the impact of vacuum stability on the allowed values of the $h_{125}H^+H^-$ coupling. Dangerous vacua exclude large negative values of this coupling. Negative values, however, lead to an enhancement of $\mu_{\gamma\gamma}$ through constructive interference with the $W^\pm$ loop.[4]

The large impact of the vacuum stability constraint on $\mu_{\gamma\gamma}$ is specific to the N2HDM of type I. This is due to the fact that in type I all Yukawa couplings are rescaled by the same factor $c(h_{125}f\bar{f})$. In the approximation $\Gamma_{\text{tot}}(h_{125}) \approx \Gamma(h_{125} \to b\bar{b})$ and $\sigma(pp \to h_{125}) \approx c^2(h_{125}t\bar{t})\sigma(pp \to h_{\text{SM}})$ a cancellation

$$\mu_{\gamma\gamma} \approx c^2(h_{125}t\bar{t}) \frac{\Gamma(h_{125} \to \gamma\gamma)}{\Gamma(h_{125} \to b\bar{b})} \frac{\Gamma_{\text{tot}}(h_{\text{SM}})}{\Gamma(h_{\text{SM}} \to \gamma\gamma)} \tag{6.66}$$

$$\approx c^2(h_{125}t\bar{t}) \frac{\Gamma(h_{125} \to \gamma\gamma)}{c^2(h_{125}b\bar{b})\Gamma(h_{\text{SM}} \to \gamma\gamma)} \tag{6.67}$$

$$= \frac{\Gamma(h_{125} \to \gamma\gamma)}{\Gamma(h_{\text{SM}} \to \gamma\gamma)} \tag{6.68}$$

occurs in type I. This allows for a direct sensitivity to $\Gamma(h_{125} \to \gamma\gamma)$ and thus to $g_{h_{125}H^+H^-}$. In contrast, for Yukawa types where $c(h_{125}t\bar{t}) \neq c(h_{125}b\bar{b})$ (*e.g.* type II) the effect of vacuum stability constraints on $\mu_{\gamma\gamma}$ is no longer visible as the ratio of Yukawa couplings has a much stronger impact on the signal rate than the charged Higgs contribution to

[4] We use the coupling convention employed by `HDECAY` where there is a relative sign between the spin-zero and the spin-one form factor in the $h \to \gamma\gamma$ decay.

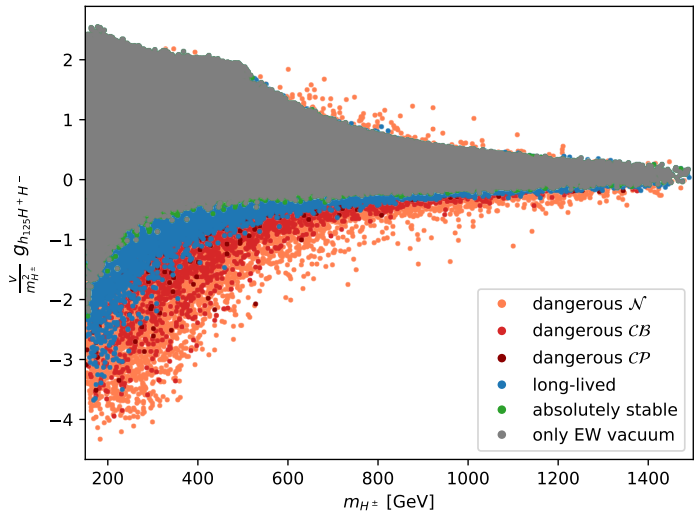

Figure 6.4: The normalised coupling $g_{h_{125}H^+H^-}$ as a function of the charged Higgs mass. Colour code as in fig. 6.3. Figure as published in ref. [4].

$\Gamma(h_{125} \to \gamma\gamma)$. It is interesting to note that although the allowed range for $\mu_{\gamma\gamma}$ is very similar in the type I 2HDM [9] and in the type I N2HDM, a measurement of $\mu_{\gamma\gamma} > 1$ for certain charged Higgs masses could exclude the N2HDM but be compatible with the 2HDM due to the different vacuum stability constraints.

This behaviour is different from what we observed for the dark sector model in section 5.2. In fig. 5.6 we showed that vacuum stability does not lead to direct constraints on $\mu_{\gamma\gamma}$ in that model. This difference may seem surprising since the scalar potential eq. (5.32) of that model is very similar to the N2HDM. However, the different symmetry structure and the different phase of the EW vacuum lead to entirely different behaviour of the vacuum stability constraints. In particular, we repeat that the analytic analysis of section 6.1 does not generalise to the dark sector model (see the discussion right before section 6.1.1).

Figure 6.5 shows vacuum stability constraints in the plane of the mass m_{H_2} of the second lightest Higgs boson (assuming here that $H_1 = h_{125}$) and the signal strength $\mu_{\tau\tau}$ of h_{125} (defined analogously to eq. (6.64)). In this case, there are hardly any regions in this projection, which can be excluded due to the existence of a dangerous secondary vacuum. There are regions where only points with a non-stable vacuum exist, which can be either dangerous or long-lived. However, in contrast to fig. 6.3, these regions are always populated by long-lived metastable vacua, so that allowed parameter points exist in these regions. Therefore, no direct bounds can be derived from the experimental measurements of $\mu_{\tau\tau}$. This is not unexpected, as $\mu_{\tau\tau}$ has no sensitivity to triple scalar couplings. Still, fig. 6.5 clearly shows the phenomenological difference between requiring an absolutely stable EW vacuum (keeping only the grey and green parameter points) and a long-lived EW vacuum (additionally keeping the blue parameter points). As

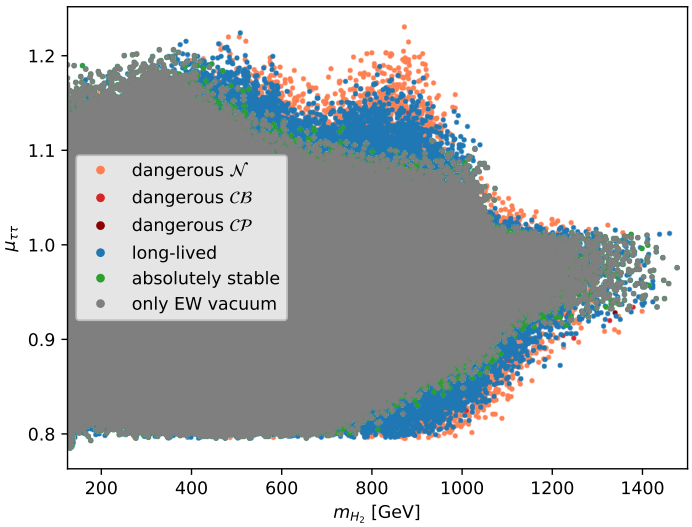

Figure 6.5: The signal strength $\mu_{\tau\tau}$ of $h_{125} \to \tau\tau$ as a function of the second lightest neutral scalar mass m_{H_2}. The parameter points without any secondary minima (grey) are plotted on top, followed by the absolutely stable (green), and long-lived (blue) parameter points. Below these, the points with *dangerous* secondary minima are shown in different shades of red denoting the type of dangerous minimum present ($\mathcal{N}$ — light red, $\mathcal{CB}$ — red, $\mathcal{CP}$ — dark red). Figure as published in ref. [4].

discussed above, enforcing absolute stability could result in misleading phenomenological conclusions.

6.4 Conclusions

In this chapter, we have presented a detailed analysis of the N2HDM vacuum structure and its phenomenological consequences. We have derived analytical expressions for the depth differences of minima of different phases. As long as the singlet field does not acquire a vev, the conclusions are identical to the 2HDM: minima of different nature — $\mathcal{N}$, $\mathcal{CB}$, $\mathcal{CP}$— never coexist [349]. However, stability of an $\mathcal{N}s$ minimum — which has a non-vanishing singlet vev — against charge and CP breaking vacua is not ensured. An $\mathcal{N}s$ vacuum is stable against $\mathcal{CB}s$ and $\mathcal{CP}s$ minima, but charge and CP-breaking minima without singlet vevs may be deeper and vacuum decay a possibility. Additionally, the more intricate vacuum structure compared to the 2HDM allows for more cases of panic vacua [220, 351, 355, 361, 362] where a second normal minimum exists below the EW vacuum. In the N2HDM, panic vacua of types $\mathcal{N}$ and $\mathcal{N}s$ can appear for EW vacua of either type. Finally, minima of type S with only a singlet VEV could, in principle, appear as panic vacua. However, we have found this case to be numerically irrelevant.

Based on this analytical analysis, we have numerically studied the impact of the intricate vacuum structure on the phenomenology of the N2HDM. We have generated a large sample of parameter points with an EW vacuum in the $\mathcal{N}s$ phase that fulfil all applicable theoretical and experimental constraints. Using this sample we have compared minima of different nature and distinguished regions of parameter space where the EW vacuum is the global minimum, where deeper minima exist but the EW vacuum is long-lived, and regions that are excluded because the EW vacuum has a short lifetime.

We have found panic vacua of type $\mathcal{N}$, as well as charge-breaking $\mathcal{CB}$, and CP-breaking $\mathcal{CP}$ minima deeper than the EW vacuum in a significant portion of the (otherwise) phenomenologically viable parameter space. We have also studied the distribution of secondary $\mathcal{CB}$ and $\mathcal{CP}$ minima and established the boundaries of the disjunct parameter regions where these minima can exist.

We have then turned towards the impact of vacuum stability constraints on collider observables and found that vacuum stability puts direct limits on the values of $\mu_{\gamma\gamma}$ reachable in the type I N2HDM. An observed value of $\mu_{\gamma\gamma}$ significantly above 1 could exclude the model on the grounds of vacuum stability alone unless the charged Higgs is very light. This is due to the sensitivity of $\mu_{\gamma\gamma}$ to the triple Higgs coupling $g_{h_{125}H^+H^-}$, which is constrained by vacuum stability. If the Yukawa sector is of type I this effect is clearly visible in $\mu_{\gamma\gamma}$ because of an approximate cancellation. For other collider observables, such as $\mu_{\tau\tau}$, large regions of parameter space exist where EW vacua are never absolutely stable, but always metastable. This illustrates the difference between enforcing absolute stability and accepting metastability. Neglecting parameter regions with a long-lived, metastable vacuum may lead to incorrect phenomenological conclusions.

In the next chapter, we will continue to study vacuum stability but with a focus on validating our approach from chapter 3. We will derive vacuum stability constraints on benchmark scenarios in the minimal supersymmetric extension of the SM (MSSM) and compare our method to results in the literature.

7 Vacuum Stability in the MSSM

In this chapter, we apply our approach to vacuum stability from chapter 3 to the MSSM. We validate our approach against existing results and present constraints from vacuum We have published the results in this chapter in ref. [3].

7.1 The Scalar Sector of the MSSM

The minimal supersymmetric extension of the SM (MSSM) [188–190] probably is the most studied BSM model overall. Due to its supersymmetric structure, it features a greatly enlarged scalar sector with very interesting vacuum-stability behaviour. In the following, we introduce the scalar sector of the MSSM and establish the notation necessary to derive the scalar potential. We refer to ref. [112] for a more detailed introduction to the model.

As discussed in section 2.5.2, the MSSM Higgs sector consists of two scalar $\mathrm{SU}(2)_L$ doublets H_u and H_d, with vacuum expectation values (vevs) v_u and v_d that define the parameter

$$\tan\beta \equiv \frac{v_u}{v_d}\,. \tag{7.1}$$

The supersymmetric part of the MSSM is described through the superpotential

$$W = \mu H_u \cdot H_d + \sum_{\text{generations}} y_u Q_L \cdot H_u \bar{u}_R + \sum_{\text{gens.}} y_d H_d \cdot Q_L \bar{d}_R + \sum_{\text{gens.}} y_l H_d \cdot L_L \bar{l}_R\,. \tag{7.2}$$

This is written in terms of the chiral $\mathrm{SU}(2)_L$ doublet Higgs superfields $H_u = (H_d^0, H_d^-)$ with $Y = -1$ and $H_d = (H_u^+, H_u^0)$ with $Y = 1$, the left-chiral superfields containing the SM quark and lepton doublets $Q_L = (u_L, d_L)$ and $L_L = (\nu_L, l_L)$, respectively, as well as the superfields containing the $\mathrm{SU}(2)_L$ singlets $\bar{u}_R$, $\bar{d}_R$ and $\bar{l}_R$. The parameters of the superpotential are the Yukawa couplings y and the parameter μ. The dot product denotes $\mathrm{SU}(2)_L$ invariant multiplication of $\mathrm{SU}(2)_L$ doublets

$$\Phi_i \cdot \Phi_j = \epsilon_{ab} \Phi_i^a \Phi_j^b\,, \tag{7.3}$$

where ϵ_{ab} is the totally antisymmetric tensor with $\epsilon_{12} = -1$. In the following expressions, we only include third-generation SM fermions and their superpartners for conciseness.

The superpotential contributes to the scalar potential through the F-terms

$$F = \sum_{\phi} |\partial_x W|^2 \,, \quad \phi \in \{h_u^0, h_u^+, h_d^0, h_d^-, \tilde{t}_L, \tilde{b}_L, \tilde{\tau}_L, \tilde{\nu}_L, \tilde{t}_R^*, \tilde{b}_R^*, \tilde{\tau}_R^*\} \,, \tag{7.4}$$

where ϕ runs over all scalar components of the superfields in eq. (7.2). The F-terms give rise to quadratic, cubic and quartic terms in the scalar potential.

Additional supersymmetric contributions to the scalar potential arise from the gauge structure of the model. These D-terms are

$$D = D_{\mathrm{U}(1)_Y} + D_{\mathrm{SU}(2)_L} + D_{\mathrm{SU}(3)_c} \,, \tag{7.5}$$

$$D_{\mathrm{U}(1)_Y} = \frac{g_1^2}{8} \left(\sum_{\phi} Y_\phi |\phi|^2 \right)^2 \,, \tag{7.6}$$

$$D_{\mathrm{SU}(2)_L} = \frac{g_2^2}{8} \sum_{\Phi_i} \sum_{\Phi_j} 2(\Phi_i^\dagger \Phi_j)(\Phi_j^\dagger \Phi_i) - (\Phi_i^\dagger \Phi_i)(\Phi_j^\dagger \Phi_j) \,, \tag{7.7}$$

$$D_{\mathrm{SU}(3)_c} = \frac{g_3^2}{6} \Big(|\tilde{t}_L|^2 - |\tilde{t}_R|^2 + |\tilde{b}_L|^2 - |\tilde{b}_R|^2 \Big)^2 \,, \tag{7.8}$$

where $\Phi_{i,j} \in \{h_u, h_d, \tilde{Q}_L, \tilde{L}_L\}$ runs over the scalar $\mathrm{SU}(2)_L$ doublets, and ϕ runs over all scalar components as defined in eq. (7.4). The different prefactor of $S_{\mathrm{SU}(3)_c}$ follows from the sum over $\mathrm{SU}(3)_c$ generators. The D terms contribute only quartic terms to the scalar potential.

7.1.1 Supersymmetry Breaking in the MSSM

In nature, supersymmetry (SUSY) has to be broken at some high scale. Otherwise, all superpartners would have identical masses, and we would surely have observed *e.g.* selectrons — the superpartners of the electron — in QED and nuclear physics experiments. Most of the theoretically appealing properties of supersymmetric models are preserved as long as the effects that break supersymmetry only lead to soft breaking terms with dimensionful coupling (see also section 2.1) at the low scale. The possible soft SUSY-breaking terms of the MSSM scalar potential are given by [364]

$$\begin{aligned} V_{\mathrm{soft}} = {} & m_{H_u}^2 h_u^\dagger h_u + m_{H_d}^2 h_d^\dagger h_d + (B_\mu h_u \cdot h_d + \mathrm{h.c.}) \\ & + m_{Q_3}^2 \tilde{Q}_L^\dagger \tilde{Q}_L + m_{L_3}^2 \tilde{L}_L^\dagger \tilde{L}_L + m_{U_3}^2 |\tilde{t}_R|^2 + m_{D_3}^2 |\tilde{b}_R|^2 + m_{E_3}^2 |\tilde{\tau}_R|^2 \\ & + \Big(y_t A_t \tilde{t}_R^* \tilde{Q}_L \cdot h_u + y_b A_b \tilde{b}_R^* h_d \cdot \tilde{Q}_L + y_\tau A_\tau \tilde{\tau}_R^* h_d \cdot \tilde{L}_L + \mathrm{h.c.} \Big) \,. \end{aligned} \tag{7.9}$$

In the most general case, all of the m^2 and A parameters in the second and third line of eq. (7.9) could be (complex) matrices in flavour space leading to more than 100 free parameters. Assumptions about the high-scale physics of supersymmetry

breaking can reduce this huge number of parameters. An alternative is to employ low-scale, phenomenological arguments leading to the so-called pMSSM models. For example, many soft SUSY-breaking parameters lead to tree-level flavour changing neutral currents (FCNCs) and are thus strongly disfavoured. The soft SUSY-breaking terms may also introduce additional sources of CP violation, which are strongly constrained by electric dipole moment (EDM) measurements (see also section 5.1).

For our analysis of vacuum stability, we impose CP-conservation and assume flavour diagonal $A_{t,b,\tau}$. This ensures flavour conservation by forbidding the flavour violating off-diagonal elements in the $A_{t,b,\tau}$. For most of the analysis, we will furthermore neglect all first and second generation sfermions, in which case all the m^2 and A parameters are real numbers. We express the soft breaking parameter B_μ through the (tree-level) mass m_A of the CP-odd Higgs boson,

$$B_\mu = m_A^2 \sin\beta \cos\beta \,. \tag{7.10}$$

At tree-level, the minimum conditions for the electroweak (EW) vacuum can also be used to express the soft Higgs masses $m_{H_u}^2$ and $m_{H_d}^2$ through v and β. The full scalar potential of the MSSM including all Higgs and third generation sfermion fields is given through eqs. (7.4), (7.5) and (7.9) as

$$V = F + D + V_{\text{soft}} \,. \tag{7.11}$$

7.1.2 Resummed Yukawa Couplings

The third generation Yukawa couplings y_t, y_b, y_τ are the largest Yukawa couplings. Their value is determined via the quark masses and the vev of the Higgs doublet coupling to them at the tree level (SUSY results in the Yukawa structure of a type II two-Higgs-doublet model (2HDM), see section 2.1):

$$y_t^{\text{tree}} = \frac{\sqrt{2} m_t}{v_u} = \frac{\sqrt{2} m_t}{v \sin\beta} \,, \tag{7.12}$$

$$y_b^{\text{tree}} = \frac{\sqrt{2} m_b}{v_d} = \frac{\sqrt{2} m_b}{v \cos\beta} \,, \tag{7.13}$$

$$y_\tau^{\text{tree}} = \frac{\sqrt{2} m_\tau}{v_d} = \frac{\sqrt{2} m_\tau}{v \cos\beta} \,. \tag{7.14}$$

We treat the quark masses as running masses at the SUSY scale

$$M_{\text{SUSY}} = \sqrt{m_{\tilde{t}_1} m_{\tilde{t}_2}} \,, \tag{7.15}$$

where $m_{\tilde{t}_{1,2}}$ are the masses of the two stop mass eigenstates. To this end we use `RunDec` [365–367] to run the $\overline{\text{MS}}$ quark masses to M_{SUSY} assuming SM running. The numerical values of the Yukawa couplings depend sensitively on $\tan\beta$ already at the tree

level. For small $\tan\beta$, the value of the bottom and τ Yukawa couplings are suppressed with respect to the top Yukawa coupling, while for large $\tan\beta$ they are enhanced. This results in $y_b^{\text{tree}} \approx y_t^{\text{tree}}$ at $\tan\beta \approx 60$ for $M_{\text{SUSY}} = 1\,\text{TeV}$.

For large $\tan\beta$, the bottom Yukawa coupling is very sensitive to SUSY loop corrections. The leading corrections can be resummed [368–371]. They effectively change the value of the bottom Yukawa coupling, and it is advantageous to include them even though the scalar potential is evaluated at the tree level. The impact of the resummed corrections on the Yukawa coupling can be included by replacing y_b^{tree} in eq. (7.13) by

$$y_b^{\text{res}} = \frac{\sqrt{2} m_b}{v_d(1+\Delta_b)}\,, \tag{7.16}$$

where Δ_b contains SUSY loop corrections. The dominant contributions arise from the gluino-sbottom and higgsino-stop loops yielding

$$\Delta_b = \Delta_b^{\tilde{g}} + \Delta_b^{\tilde{h}}\,, \tag{7.17}$$

$$\Delta_b^{\tilde{g}} = \frac{2\alpha_s}{3\pi}\mu M_3 \tan\beta\, C(m^2_{\tilde{b}_1}, m^2_{\tilde{b}_2}, M_3^2)\,, \tag{7.18}$$

$$\Delta_b^{\tilde{h}} = \frac{y_t^2}{16\pi^2}\mu A_t \tan\beta\, C(m^2_{\tilde{t}_1}, m^2_{\tilde{t}_2}, \mu^2)\,, \tag{7.19}$$

where $m_{\tilde{t}_{1,2}}$, $m_{\tilde{b}_{1,2}}$ are the masses of the tree-level $\tilde{t}$ and $\tilde{b}$ mass eigenstates, M_3 denotes the gluino mass, and μ is the higgsino mass parameter. The function $C(x,y,z)$ is given by

$$C(x,y,z) = \frac{xy\ln\frac{y}{x} + yz\ln\frac{z}{y} + xz\ln\frac{x}{z}}{(x-y)(y-z)(x-z)}\,. \tag{7.20}$$

These Δ_b corrections lead to an enhancement of y_b especially for large $\mu < 0$ and $A_t, M_3 > 0$ as both contributions are negative in this case and reduce the denominator of eq. (7.16). For $\Delta_b \to -1$ the bottom Yukawa coupling gets pushed into the non-perturbative regime. Taking eq. (7.16) into account significantly impacts vacua with $\tilde{b}$ vevs in the MSSM as will be visible in our numerical analysis below (see also ref. [372]). We furthermore take into account a similar but numerically smaller effect for the Yukawa coupling of the τ lepton, y_τ [373].

7.2 Vacuum Stability in the MSSM

Vacuum stability constraints in the MSSM have been actively studied in the literature [3, 198, 203, 218, 372, 374–397]. The so-called charge or colour breaking (CCB) vacua provide the most important vacuum stability constraints in the MSSM. These are minima where some of the charged sfermions obtain vevs, thus breaking electric charge and possibly colour. The existing results include both analytic and semi-analytic studies

of specific directions in field space as well as fully numeric approaches. The public code `Vevacious` [198, 215] can be used to check the stability of the EW vacuum including one-loop and finite temperature effects. To our knowledge, it is the only dedicated public tool that is applicable to a variety of BSM models. `Vevacious` has been applied to the MSSM in different contexts in the literature [198, 391, 392].

We apply our method described in chapter 3 to the MSSM in a numerical study of CCB vacua. We use this very well studied model to illustrate the reliability of our approach and compare to existing results. As a first step, the complex fields in eq. (7.11) must be expressed through real fields with canonically normalised kinetic terms as discussed in section 3.1.1. We expand

$$\phi \to \frac{1}{\sqrt{2}}\mathrm{Re}(\phi) + \frac{i}{\sqrt{2}}\mathrm{Im}(\phi)\,. \tag{7.21}$$

In this convention, the correct normalisation for φ from eq. (3.5) is ensured as long as $|\hat{\varphi}| = 1$. The EW vacuum in this notation is given by

$$\left\langle \mathrm{Re}(h_u^0) \right\rangle = v \sin\beta\,, \quad \left\langle \mathrm{Re}(h_d^0) \right\rangle = v \cos\beta\,, \tag{7.22}$$

where $v = \sqrt{v_u^2 + v_d^2} \approx 246\,\mathrm{GeV}$ is the EW vev.

The MSSM contains a large number of scalar fields. The total number of real, scalar, classical degrees of freedom is

$$\begin{aligned}(\overbrace{\{\tilde{l}_L, \tilde{l}_R, \tilde{\nu}_L\}}^{3} + \overbrace{\text{colour}}^{3} \times \overbrace{\tilde{u}_L, \tilde{u}_R, \tilde{d}_L, \tilde{d}_R)}^{4} \times \overbrace{\text{generations}}^{3} \times \overbrace{\text{complex}}^{2} \\ + \overbrace{\text{Higgs bosons}}^{4} = 94\,,\end{aligned} \tag{7.23}$$

where we have already used global $\mathrm{SU}(2)_L$ and $\mathrm{U}(1)_Y$ transformations to eliminate four degrees of freedom from the Higgs doublets (see section 3.3.1). It is unfeasible to vary all of these simultaneously, as the complexity of finding stationary points scales exponentially with the dimensionality of the field-space.[1] For our studies of the MSSM we combine all stationary points found by varying the three sets of fields

$$\left\{\mathrm{Re}(h_u^0), \mathrm{Re}(h_d^0), \mathrm{Re}(\tilde{t}_L), \mathrm{Re}(\tilde{t}_R), \mathrm{Re}(\tilde{b}_L), \mathrm{Re}(\tilde{b}_R)\right\}\,, \tag{7.24}$$

$$\left\{\mathrm{Re}(h_u^0), \mathrm{Re}(h_d^0), \mathrm{Re}(\tilde{t}_L), \mathrm{Re}(\tilde{t}_R), \mathrm{Re}(\tilde{\tau}_L), \mathrm{Re}(\tilde{\tau}_R)\right\}\,, \tag{7.25}$$

$$\left\{\mathrm{Re}(h_u^0), \mathrm{Re}(h_d^0), \mathrm{Re}(\tilde{b}_L), \mathrm{Re}(\tilde{b}_R), \mathrm{Re}(\tilde{\tau}_L), \mathrm{Re}(\tilde{\tau}_R)\right\}\,. \tag{7.26}$$

All sets contain the real parts of the neutral Higgs fields that participate in EW symmetry breaking. The first set additionally contains the real $\tilde{t}$ and $\tilde{b}$ fields, the second set the

[1] For example, considering the set of fields in eq. (7.24) yields ~ 10 times longer runtimes than varying the two sets of four fields $\{\mathrm{Re}(h_u^0), \mathrm{Re}(h_d^0), \mathrm{Re}(\tilde{t}_L), \mathrm{Re}(\tilde{t}_R)\}$ and $\{\mathrm{Re}(h_u^0), \mathrm{Re}(h_d^0), \mathrm{Re}(\tilde{b}_L), \mathrm{Re}(\tilde{b}_R)\}$ separately.

$\tilde{t}$ and $\tilde{\tau}$ fields and the third set the $\tilde{b}$ and $\tilde{\tau}$ fields. Therefore, this method will find all stationary points where any two kinds of third generation sfermions acquire vevs but cannot find stationary points for which $\tilde{t}$, $\tilde{b}$ and $\tilde{\tau}$ vevs are simultaneously non-zero. This is a valid approximation as the distance in field space between the EW vacuum and another minimum is expected to increase as more fields take non-zero values at this second minimum. Since the tunnelling time increases with the fieldspace distance the stationary points with many non-zero vevs tend to be less dangerous.

We initially also included field sets with $\tilde{\nu}$ vevs and vevs of the first and second generation sfermions. However, we found that they had no impact on the observed constraints and will not include them in the plots shown below. We will, however, comment on their behaviour where appropriate.

We neglect charged and CP-odd Higgs directions motivated by the absence of any dangerous CP or charge breaking vacua in the Higgs sector of the 2HDM [220, 349–351] and thus the MSSM at lowest order. As discussed in detail in chapter 6, this argument breaks down in the presence of an additional singlet. Non-vanishing sfermion vevs lead to trilinear terms in the scalar potential (see eq. (7.29) below) which may spoil these results in a similar way. To test this, we initially included field sets with charge and CP-breaking Higgs vevs in our analysis. We did not encounter any regions of parameter space where they appear and we will not comment on them further. This conclusion is specific to the MSSM. In the next-to-minimal supersymmetric extension of the SM (NMSSM), for example, the different kinds of Higgs vevs are more relevant [398]. Since the NMSSM also adds a scalar singlet to the MSSM Higgs sector, this is much in line with the discussion of chapter 6.

We ignore the imaginary parts of the sfermions as they are not expected to add new features in the absence of additional sources of CP violation. Finally, we ignore the different colours of the squarks, where it is equivalent to either assume that only one colour participates or to set all three coloured vevs to the same value with an appropriate normalisation factor. This is justified as the scalar potential is completely agnostic toward the different colours.

The resulting scalar potential of the MSSM as a function of the classical fields that appear in eqs. (7.24) to (7.26) is given by

$$V = V_2 + V_3 + V_4\,, \tag{7.27}$$

consisting of a quadratic part

$$\begin{aligned} V_2 = {} & \frac{m_{Q_3}^2}{2}\left(\mathrm{Re}(\tilde{b}_L)^2 + \mathrm{Re}(\tilde{t}_L)^2\right) + \frac{m_{U_3}^2}{2}\mathrm{Re}(\tilde{t}_R)^2 + \frac{m_{D_3}^2}{2}\mathrm{Re}(\tilde{b}_R)^2 \\ & + \frac{m_{L_3}^2}{2}\mathrm{Re}(\tilde{\tau}_L)^2 + \frac{m_{E_3}^2}{2}\mathrm{Re}(\tilde{\tau}_R)^2 - m_A^2\mathrm{Re}(h_d^0)\mathrm{Re}(h_u^0)\sin(\beta)\cos(\beta) \\ & + \frac{1}{2}\mathrm{Re}(h_d^0)^2\left(m_{H_d}^2 + \mu^2\right) + \frac{1}{2}\mathrm{Re}(h_u^0)^2\left(m_{H_u}^2 + \mu^2\right)\,, \end{aligned} \tag{7.28}$$

a cubic part

$$
\begin{aligned}
V_3 = &\frac{y_b}{\sqrt{2}}\mathrm{Re}(\tilde{b}_L)\mathrm{Re}(\tilde{b}_R)\left(A_b\mathrm{Re}(h_d^0) - \mu\mathrm{Re}(h_u^0)\right) \\
&+ \frac{y_\tau}{\sqrt{2}}\mathrm{Re}(\tilde{\tau}_L)\mathrm{Re}(\tilde{\tau}_R)\left(A_\tau\mathrm{Re}(h_d^0) - \mu\mathrm{Re}(h_u^0)\right) \\
&+ \frac{y_t}{\sqrt{2}}\mathrm{Re}(\tilde{t}_L)\mathrm{Re}(\tilde{t}_R)\left(A_t\mathrm{Re}(h_u^0) - \mu\mathrm{Re}(h_d^0)\right)\,,
\end{aligned} \tag{7.29}
$$

and a quartic part

$$
\begin{aligned}
V_4 = &\frac{g_1^2+g_2^2}{32}\left(\mathrm{Re}(h_u^0)^2 - \mathrm{Re}(h_d^0)^2\right)^2 \\
&+ \frac{g_1^2-3g_2^2+12y_t^2}{48}\mathrm{Re}(h_u^0)^2\mathrm{Re}(\tilde{t}_L)^2 + \frac{3y_t^2-g_1^2}{12}\mathrm{Re}(h_u^0)^2\mathrm{Re}(\tilde{t}_R)^2 \\
&+ \frac{g_1^2+3g_2^2}{48}\mathrm{Re}(h_u^0)^2\mathrm{Re}(\tilde{b}_L)^2 + \frac{1}{24}g_1^2\mathrm{Re}(h_u^0)^2\mathrm{Re}(\tilde{b}_R)^2 \\
&+ \frac{g_2^2-g_1^2}{16}\mathrm{Re}(h_u^0)^2\mathrm{Re}(\tilde{\tau}_L)^2 + \frac{1}{8}g_1^2\mathrm{Re}(h_u^0)^2\mathrm{Re}(\tilde{\tau}_R)^2 \\
&+ \frac{3g_2^2-g_1^2}{48}\mathrm{Re}(h_d^0)^2\mathrm{Re}(\tilde{t}_L)^2 + \frac{g_1^2}{12}\mathrm{Re}(h_d^0)^2\mathrm{Re}(\tilde{t}_R)^2 \\
&- \frac{g_1^2+3g_2^2-12y_b^2}{48}\mathrm{Re}(h_d^0)^2\mathrm{Re}(\tilde{b}_L)^2 - \frac{g_1^2-6y_b^2}{24}\mathrm{Re}(h_d^0)^2\mathrm{Re}(\tilde{b}_R)^2 \\
&+ \frac{g_1^2-g_2^2+4y_\tau^2}{16}\mathrm{Re}(h_d^0)^2\mathrm{Re}(\tilde{\tau}_L)^2 - \frac{g_1^2-2y_\tau^2}{8}\mathrm{Re}(h_d^0)^2\mathrm{Re}(\tilde{\tau}_R)^2 \\
&+ \frac{g_1^2+9g_2^2+12g_3^2}{288}\left(\mathrm{Re}(\tilde{t}_L)^2 + \mathrm{Re}(\tilde{b}_L)^2\right)^2 - \frac{g_1^2+3g_2^2}{48}\mathrm{Re}(\tilde{t}_L)^2\mathrm{Re}(\tilde{\tau}_L)^2 \\
&- \frac{g_1^2+3g_3^2-9y_t^2}{36}\mathrm{Re}(\tilde{t}_L)^2\mathrm{Re}(\tilde{t}_R)^2 + \frac{g_1^2-6g_3^2+18y_b^2}{72}\mathrm{Re}(\tilde{t}_L)^2\mathrm{Re}(\tilde{b}_R)^2 \\
&+ \frac{g_1^2}{24}\mathrm{Re}(\tilde{t}_L)^2\mathrm{Re}(\tilde{\tau}_R)^2 \\
&+ \frac{3g_2^2-g_1^2}{48}\mathrm{Re}(\tilde{b}_L)^2\mathrm{Re}(\tilde{\tau}_L)^2 - \frac{g_1^2+3g_3^2-9y_t^2}{36}\mathrm{Re}(\tilde{b}_L)^2\mathrm{Re}(\tilde{t}_R)^2 \\
&+ \frac{g_1^2-6g_3^2+18y_b^2}{72}\mathrm{Re}(\tilde{b}_L)^2\mathrm{Re}(\tilde{b}_R)^2 + \frac{g_1^2}{24}\mathrm{Re}(\tilde{b}_L)^2\mathrm{Re}(\tilde{\tau}_R)^2 \\
&+ \frac{g_1^2+g_2^2}{32}\mathrm{Re}(\tilde{\tau}_L)^4 + \frac{g_1^2}{12}\mathrm{Re}(\tilde{\tau}_L)^2\mathrm{Re}(\tilde{t}_R)^2 - \frac{g_1^2}{24}\mathrm{Re}(\tilde{\tau}_L)^2\mathrm{Re}(\tilde{b}_R)^2 \\
&- \frac{g_1^2-2y_\tau^2}{8}\mathrm{Re}(\tilde{\tau}_L)^2\mathrm{Re}(\tilde{\tau}_R)^2 \\
&+ \frac{4g_1^2+3g_3^2}{72}\mathrm{Re}(\tilde{t}_R)^4 - \frac{2g_1^2-3g_3^2}{36}\mathrm{Re}(\tilde{t}_R)^2\mathrm{Re}(\tilde{b}_R)^2 - \frac{g_1^2}{6}\mathrm{Re}(\tilde{t}_R)^2\mathrm{Re}(\tilde{\tau}_R)^2 \\
&+ \frac{g_1^2+3g_3^2}{72}\mathrm{Re}(\tilde{b}_R)^4 + \frac{g_1^2}{12}\mathrm{Re}(\tilde{b}_R)^2\mathrm{Re}(\tilde{\tau}_R)^2 + \frac{g_1^2}{8}\mathrm{Re}(\tilde{\tau}_R)^4 \\
&+ \frac{y_b y_\tau}{2}\mathrm{Re}(\tilde{b}_L)\mathrm{Re}(\tilde{\tau}_L)\mathrm{Re}(\tilde{b}_R)\mathrm{Re}(\tilde{\tau}_R)\,.
\end{aligned} \tag{7.30}
$$

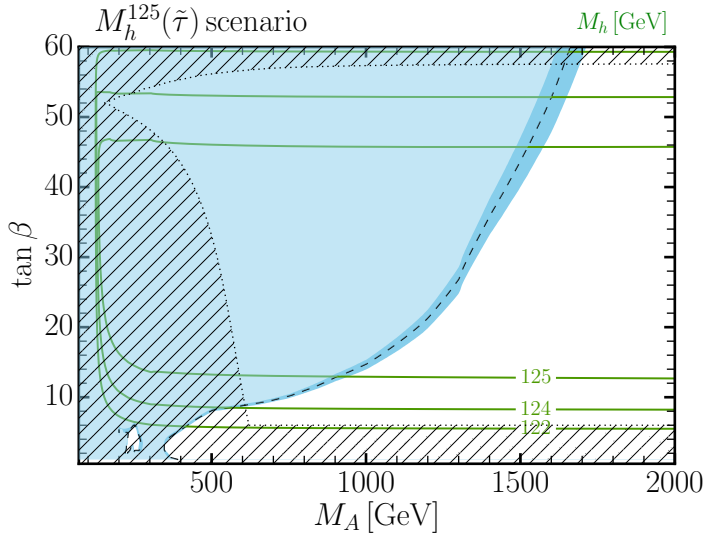

Figure 7.1: The $M_h^{125}(\tilde{\tau})$ scenario from ref. [26] in the m_A–tan β plane as an example of a MSSM benchmark scenario. The blue region is excluded by searches for additional Higgs bosons, making use of `HiggsBounds` (see section 2.4.4). The grey slashed region cannot reproduce the observed properties of the 125 GeV Higgs boson (h_{125}) and is thus excluded, making use of `HiggsSignals` (see section 2.4.5). The annotated green contours indicate the mass of the light Higgs bosons h. Figure from ref. [26].

7.3 Numerical Results

Even when only CP and flavour conserving soft breaking terms are considered, the number of free parameters in the MSSM remains high. For phenomenological studies, this is commonly reduced by assuming universality — setting some related parameters to have identical values. Depending on the assumptions, this leads to different variants of the pMSSM named according to the remaining number of free parameters — *e.g.* the pMSSM11 [141]. However, even these simplified models remain too complicated for presenting model interpretations of experimental results. For this reason benchmark planes — that fix all but two of the model parameters and are designed to highlight a particular phenomenology — have been established in the MSSM [26, 399–403].

In the following, we consider the recent benchmark scenarios from ref. [26]. Figure 7.1 shows an example of one of the benchmark scenarios we consider — the so-called $M_h^{125}(\tilde{\tau})$ scenario that features a light $\tilde{\tau}$. Unitarity and experimental constraints from Higgs physics have been included in the definition of the benchmark scenarios. Constraints from flavour physics, dark matter and EW precision observables were not imposed as they largely depend on parameters that do not strongly impact Higgs boson phenomenology.

We will apply our method for obtaining vacuum stability constraints from chapter 3 to these scenarios. We use the results to both illustrate the impact of the constraints and to

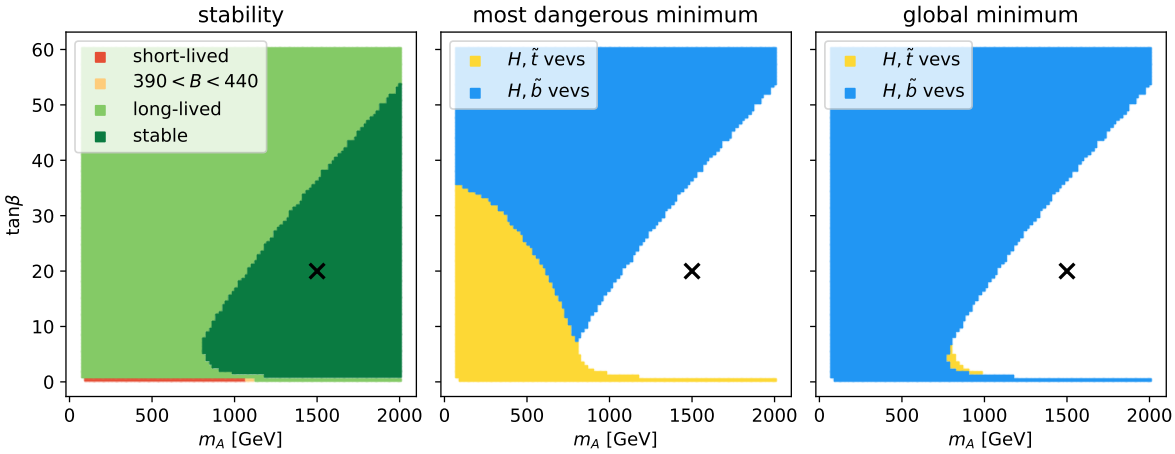

Figure 7.2: Constraints from vacuum stability in the M_h^{125} scenario defined in ref. [26]. The colour code in the left panel indicates the lifetime of the EW vacuum, while the centre and right panels illustrate which fields have non-zero vevs at the most dangerous and the global minimum, respectively. The black × marks the same point shown in fig. 7.3. Figure as published in ref. [3].

compare our method to previous approaches. As such, this application is an important validation of our approach in a well-studied model and also provides complementary information to ref. [26] through a detailed study of vacuum stability in the benchmark scenarios.

7.3.1 Vacuum Stability in the M_h^{125} Scenario

The first benchmark scenario defined in ref. [26] is the M_h^{125} scenario. It features rather heavy SUSY particles with $h_{125} \equiv h$ and can be used to present results from searches for additional Higgs bosons at the LHC. Its parameters are

$$\begin{aligned} m_{Q_3} = m_{U_3} = m_{D_3} = 1.5\,\text{TeV}\,, \quad m_{L_3} = m_{E_3} = 2\,\text{TeV}\,, \quad \mu = 1\,\text{TeV}\,, \\ X_t = A_t - \frac{\mu}{\tan\beta} = 2.8\,\text{TeV}\,, \quad A_b = A_\tau = A_t\,, \\ M_1 = M_2 = 1\,\text{TeV} \quad M_3 = 2.5\,\text{TeV}\,, \end{aligned} \tag{7.31}$$

while m_A and $\tan\beta$ are varied in order to span the considered parameter plane. The soft SUSY-breaking parameters $A_{t,b,\tau}$ vary as a function of $\tan\beta$ for fixed X_t. Note that the gaugino mass parameters $M_{1,2,3}$ only enter our analysis through the Δ_b and Δ_τ corrections. Figure 7.2 shows the vacuum stability analysis in this benchmark plane.

In the left panel of fig. 7.2, the colour code indicates the lifetime of the EW vacuum at each point in the parameter plane. In the dark green region the EW vacuum is the global minimum of the theory, and the EW vacuum is stable in this parameter region. The

light green area depicts regions where deeper minima exist, but the lifetime of the false EW vacuum is large compared to the age of the universe (see section 3.1.2). For these parameter points, the EW vacuum is metastable, and the parameter points are allowed. For points in the red region, on the other hand, the tunnelling process is fast, and they are excluded as the EW vacuum is short-lived. The small yellow region contains all points in the intermediate region discussed in section 3.1.2 where the estimated uncertainties allow no decisive conclusion on the longevity of the false vacuum. This plot of fig. 7.2 (left) shows that the requirement of vacuum stability hardly constrains the M_h^{125} benchmark plane. Only a parameter region with small values of $\tan\beta \lesssim 1$ can be excluded.

The middle panel of fig. 7.2 shows the character of the most dangerous minimum (MDM), *i.e.* it displays which fields acquire non-vanishing vevs at this vacuum. The MDM is defined as the minimum with the lowest bounce action for tunnelling from the EW vacuum. One can see that for small values of $\tan\beta$ or both moderate $\tan\beta$ and m_A the MDM is a CCB minimum with $\tilde{t}$ vevs (yellow). For larger values of $\tan\beta$ and m_A a minimum with $\tilde{b}$ vevs takes over (blue). This behaviour is expected as for higher $\tan\beta$ the couplings of the Higgs sector to d-type (s)quarks are enhanced which also increases the impact of $\tilde{b}$ vevs on our vacuum stability analysis.

The right panel of fig. 7.2 displays the character of the global minimum for the M_h^{125} benchmark plane. As noted in section 3.3.1, the MDM and the global minimum of the scalar potential can, in general, differ from each other.[2] We see that the global minimum has only $\tilde{b}$ vevs for most of the parameter space, while there is a large region where the MDM involves $\tilde{t}$ vevs.

Impact of the Trilinear Terms

We noted based on eq. (3.8) that the parameters entering the cubic terms, eq. (7.29), of the potential are expected to be especially relevant for the stability of the EW vacuum. Since m_A is related to a bilinear term in the potential, and $\tan\beta$ mostly affects the quartic Yukawa couplings, we switch to a different slice of the parameter space which is more relevant for vacuum stability studies. We start from a point in the m_A–$\tan\beta$ plane of the M_h^{125} scenario that is absolutely stable and given by

$$\tan\beta = 20\,, \quad m_A = 1.5\,\text{TeV}\,. \tag{7.32}$$

This point is indicated with a $\times$ in figs. 7.2 and 7.3. It features a Higgs mass of $m_h \approx 125\,\text{GeV}$ and is allowed by all the constraints considered in ref. [26]. Among these, a search for heavy Higgs bosons decaying into τ pairs [169, 404] (see fig. 2.3) is the most relevant constraint. In contrast to the m_A–$\tan\beta$ plane of the M_h^{125} scenario, we now vary the parameters μ and $A \equiv A_t = A_b = A_\tau$ starting from this point. These parameters

[2] Out of the minima that are deeper than the EW vacuum, the MDM is in most cases the one that is closest to the EW vacuum in field space. However, this is not always the case, see fig. 7.5 below for a counterexample.

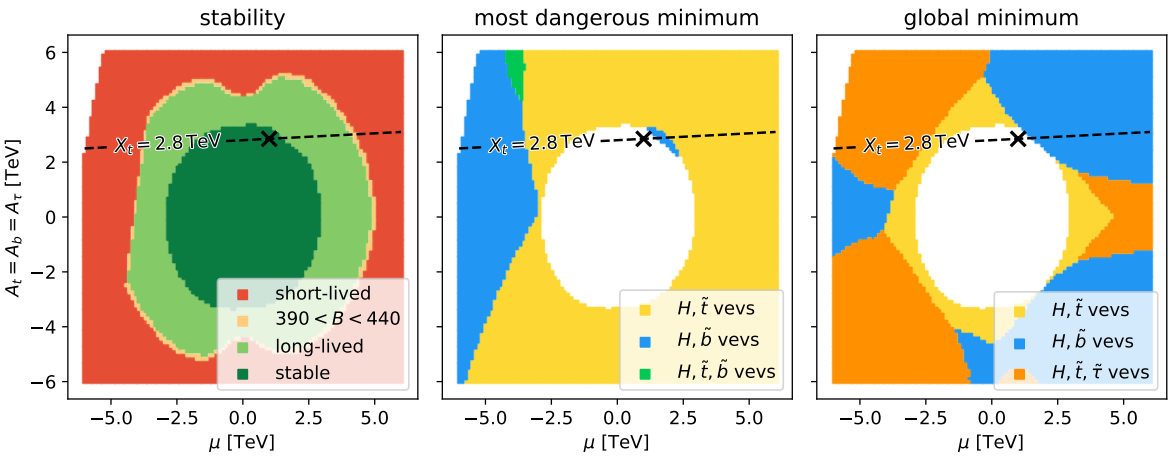

Figure 7.3: Constraints from vacuum stability in the plane of μ and A containing the selected point from the M_h^{125} benchmark scenario. The starting point in the M_h^{125} plane of fig. 7.2 with $\tan\beta = 20$ and $m_A = 1.5\,\text{TeV}$ is indicated by the black $\times$. The colour code is the same as in fig. 7.2. The dashed line corresponds to constant $X_t = 2.8\,\text{TeV}$. Figure as published in ref. [3].

appear exclusively in V_3, see eq. (7.29). Figure 7.3 shows the vacuum stability analysis in this new parameter plane.

The left panel of fig. 7.3 indicates the lifetime of the EW vacuum. The colour coding is the same as in the corresponding plot of fig. 7.2, *i.e.* red points depict short-lived configurations, while the EW vacuum for light green points is metastable, and the EW vacuum in the dark green area is stable. The thin yellow band indicates the uncertainty band of $390 < B < 440$ discussed in section 3.1.2. The EW vacuum becomes more and more unstable for larger absolute values of μ and A. For small values of these parameters, the potential is absolutely stable with a region of long-lived metastability in between. Note that also in this parameter plane the yellow uncertainty region of $390 < B < 440$ corresponds to only a thin band between long- and short-lived regions. The point marked by the $\times$ is the starting point in the M_h^{125} plane depicted in fig. 7.2. One can see that in the plane of fig. 7.3 this point is close to a region of metastability, but quite far from any dangerously short-lived parameter regions. The missing points in the top-left corner of the plot are points with tachyonic tree-level $\tilde{b}$ masses where the EW vacuum is a saddle point.

The character of the MDM, *i.e.* the fields that acquire non-zero vevs in this vacuum, is shown in the middle panel of fig. 7.3. It is dominated by yellow $\tilde{t}$ vevs in this plane, but blue $\tilde{b}$ vevs are also important for large negative values of μ. The Δ_b corrections described in section 7.1.2 are enhanced in this parameter region and have a large impact. They are also the cause of the tachyonic region for large negative μ and positive A. Between the $\tilde{t}$-vev and $\tilde{b}$-vev regime a region appears (shown in green) where $\tilde{t}$ and $\tilde{b}$ vevs occur simultaneously. The small blue region for $\mu > 0$ is visible because the more dangerous

minima with $\tilde{t}$ vevs only appear for slightly higher values of A and μ. Therefore, only the global $\tilde{b}$-vev minimum coexists with the EW vacuum in this region of parameter space.

The right panel of fig. 7.3 indicates the fields which acquire non-zero vevs at the global minimum. In this parameter plane, there are large regions with simultaneous $\tilde{t}$ and $\tilde{\tau}$ vevs at the global minimum. Through most of the plane, the fields acquiring vevs differ between the MDM and the global minimum. The green region of simultaneous $\tilde{t}$ and $\tilde{b}$ vevs, which is visible in the middle panel of fig. 7.3, does not correspond to the global minimum of the theory. This is expected as additional large quartic F and D-term contributions appear if multiple kinds of squarks take on non-zero vevs simultaneously. These are positive contributions to the scalar potential that lift these regions of field space. No such contributions appear in the case of simultaneous squark and slepton vevs which is why the orange regions of simultaneous $\tilde{t}$ and $\tilde{\tau}$ vevs are present in the right panel of fig. 7.3. Note that the quartic F and D-term contributions do not prevent the minima with mixed $\tilde{t}$ and $\tilde{b}$ vevs from being the MDM as fig. 7.3 (centre) shows. However, for the parameter plane considered here these minima featuring simultaneous $\tilde{t}$ and $\tilde{\tau}$ vevs have no impact on the stability constraints of fig. 7.3 (left).

We finally comment on the impact of additional field content — in particular, the first and second generation sfermions and the $\tilde{\nu}$ vevs — on these results. The small Yukawa couplings of these particles tend to push any additional minima to very large field values, which renders these configurations long-lived. As a consequence, the metastability bound (yellow region in fig. 7.3, left) and the character of the MDM (fig. 7.3, centre) are insensitive to those fields. On the other hand, the character of the global minimum may be significantly affected by fields with relatively small couplings to the Higgs sector. Indeed, if we were to include $\tilde{c}$ and $\tilde{s}$ vevs they would dominate the global minimum (fig. 7.3, right) through most of the parameter plane. They would even cut slightly into the edges of the stable dark green region, rendering it long-lived. Therefore, our analysis shows that neither the investigation of just the region of absolute stability nor of the character of the global minimum yields reliable bounds from vacuum stability. This is because both of these quantities sensitively depend on the considered field content, where even very weakly coupled scalar degrees of freedom can have a significant impact. Instead, the correct determination of the boundary between the short-lived and the long-lived region crucially relies on the correct identification of the MDM, which in general can be very different from the global minimum. This boundary, and accordingly the constraint on the parameter space from vacuum stability, is governed by the fields with the largest Yukawa couplings and is insensitive to effects from particles with a small coupling to the Higgs sector.

Comparison to Semi-Analytic Bounds and Existing Codes

We now compare our results shown in fig. 7.3 with results from the literature. An approximate bound for MSSM CCB instabilities including vacuum tunnelling is given

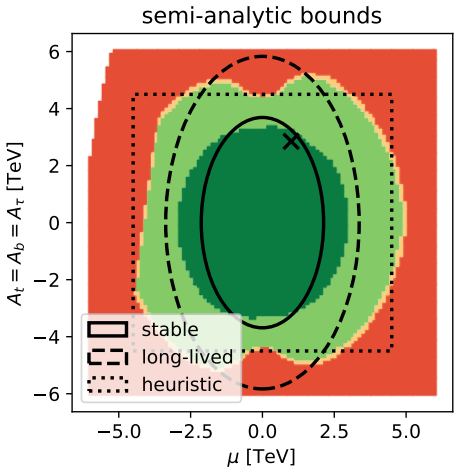

Figure 7.4: Constraints from vacuum stability in the plane of μ and A containing the selected point (black ×) from the M_h^{125} benchmark scenario. The results from fig. 7.3 are shown with superimposed contours indicating the approximate absolute and metastability bounds of eq. (7.33) and the heuristic bound of eq. (7.34). Figure as published in ref. [3].

by [203, 380]

$$A_t^2 + 3\mu^2 < (m_{\tilde{t}_R}^2 + m_{\tilde{t}_L}^2) \cdot \begin{cases} 3 & \text{stable,} \\ 7.5 & \text{long-lived.} \end{cases} \tag{7.33}$$

Furthermore, a "heuristic" bound of

$$\frac{\max(A_{\tilde{t},\tilde{b}}, \mu)}{\min(m_{Q_3,U_3})} \lesssim 3 \tag{7.34}$$

is sometimes used to judge whether a parameter point might be sufficiently long-lived (see *e.g.* the discussion in ref. [195]).

The public code `Vevacious` [198, 215] can calculate the lifetime of the EW vacuum in BSM models using the tree-level or Coleman–Weinberg one-loop potential, optionally including finite temperature effects, see *e.g.* ref. [392].

Figure 7.4 displays our results in comparison to the approximate bounds given in eqs. (7.33) and (7.34), where the contours arising from eqs. (7.33) and (7.34) are superimposed on our results. The solid black contour arising from eq. (7.33) should be compared with the edge of the dark green region where the vacuum is stable. This comparison shows significant deviations. This is in particular because the absolute stability bound from eq. (7.33) considers only the D-flat direction. The dashed black contour should be compared with the yellow region at the border between the long-lived (light green) and short-lived (red) regions and shows similar deviations. One source of these deviations is that the metastability bound in eq. (7.33) becomes less reliable for values of $m_{\tilde{t}_R}^2 + m_{\tilde{t}_L}^2 \gtrsim 1200\,\text{GeV}^2$ and large $(A_t^2 + 3\mu^2)$ (see Fig. 4 in ref. [203]). Moreover, the dependence on $\tan\beta$ [394] is

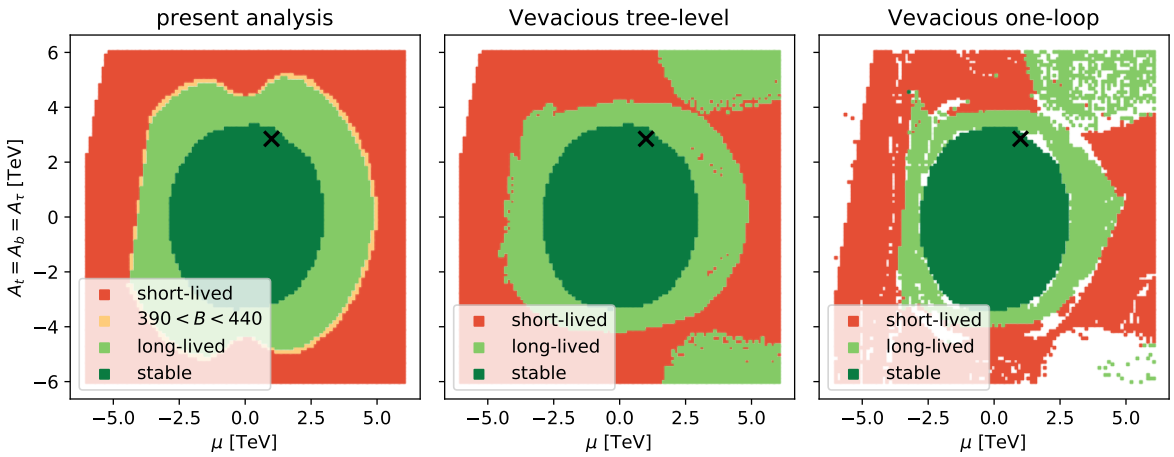

Figure 7.5: Constraints from vacuum stability in the plane of μ and A containing the selected point (black ×) from the M_h^{125} benchmark scenario. The results from fig. 7.3 are shown in the left panel. The other two plots show results of the code `Vevacious` for the tree-level (centre) and one-loop effective potential at zero temperature (right) for the same parameter plane. Figure as published in ref. [3].

not included in the approximate bound. Another reason is that only $\tilde{t}$-related parameters enter eq. (7.33), while our analysis shows that also $\tilde{b}$ vevs have important effects in this case.

The heuristic bound eq. (7.34) (dotted black contour in fig. 7.4) should also be compared to the yellow region. While there are clear differences in shape, the size of the long-lived region in our result roughly matches the heuristic bound. This can be qualitatively understood from eq. (3.8). For $\lambda \sim \mathcal{O}(1)$ this yields $A/m > 2$ as a bound for absolute stability. Therefore, $A/m > 3$ as a bound for metastability appears to be a reasonable estimate. While we only show these comparisons for one parameter plane they hold very similarly for every plane we have studied. Our comparison shows that all of these approximate bounds have deficiencies in determining the allowed parameter region, and dedicated analyses are necessary to obtain more reliable conclusions.

Next we compare our results (fig. 7.5, left) to the tree-level (fig. 7.5, centre) and one loop (right) results of `Vevacious`. In the `Vevacious` runs we have taken into account only the fields from eq. (7.24) since we found no relevant constraints from $\tilde{\tau}$ vevs in this plane. `Vevacious` by default considers tunnelling to the minimum which is closest in field space to the EW vacuum. In the newest version (`1.2.03+` [405]) one can optionally consider tunnelling to the global minimum instead. In generating fig. 7.5 we combined the results from both of these approaches by choosing the option giving the stronger bound at each individual point. One obvious difference between our results and `Vevacious` are the metastable regions that `Vevacious` finds for $\mu \sim 3\,\text{TeV}$ and $|A| \sim 5\,\text{TeV}$. In this region `Vevacious` considers the wrong minimum to be the MDM. The global minimum (with $\tilde{b}$

vevs, see fig. 7.3, right) is closest to the EW vacuum in field space. Therefore, `Vevacious` can only consider tunnelling into this minimum instead of a slightly further and shallower minimum with $\tilde{t}$ vevs, which gives the stronger constraints shown in our results. A similar issue is responsible for the edge in the `Vevacious` result around $\mu \sim -2.5\,\text{TeV}$ and $A \sim 4\,\text{TeV}$. Another visible difference is the absence in the `Vevacious` result of the bumps in the long-lived region in our result around $|\mu| \sim 2\,\text{TeV}$ and $|A| \sim 5\,\text{TeV}$. The optimisation of the bounce action by `CosmoTransitions` [211], which is used by `Vevacious`, leads to a slightly stronger and more reliable metastability bound in this region.[3] Apart from these deviations, our results are in good agreement with the tree-level results of `Vevacious`. The deviations for individual points and the rugged edges of the light green region in the `Vevacious` result are likely signs of numerical instability. This especially includes the isolated red points in the light green region, which result from numerical problems in the calculation of the tunnelling time.

The comparison with the `Vevacious` results using the Coleman–Weinberg one-loop effective potential at zero temperature (fig. 7.5, right) shows that the one-loop effects on the allowed parameter space are small for this scenario. The one-loop result from `Vevacious` clearly suffers from numerical instabilities. However, the stable region is nearly identical to the tree-level results, and the long-lived region is similarly sized as the tree-level `Vevacious` result with differences in shape. The long-lived region appearing around $A \sim 5\,\text{TeV}$ and $\mu \sim 4\,\text{TeV}$ as well as the missing region around $A \sim -5\,\text{TeV}$ and the spikes around $\mu \sim -2.5\,\text{TeV}$ are consequences of the same MDM misidentification as in the `Vevacious` tree-level result (see previous paragraph). Comparing the runtime of our code to the runtime of `Vevacious` in this parameter plane including only the field set of eq. (7.24) we find our tree-level code to be ~ 5 times faster than the tree-level and ~ 200 times faster than the one-loop `Vevacious` run.

Parameter Dependence of the Vacuum Structure and Degenerate Vacua

The dashed line in fig. 7.3 is the line where X_t has the same value as in the benchmark plane, fig. 7.2. The mass m_h of h_{125} depends dominantly on the parameters $\tan\beta$, X_t and the stop masses. We, therefore, expect the Higgs mass to stay close to 125 GeV when moving away from the point $\times$ along this line.[4] We use this as motivation to further investigate the vacuum structure along this line.

Figure 7.6 shows the depth of the stationary points of the scalar potential as a function of μ along this line. The constant depth of the EW vacuum is shown in grey while the other colours indicate the CCB stationary points. Note that not only local minima, but all stationary points including saddle points and local maxima are shown in fig. 7.6. The dashed line indicates the MDM for each value of μ.

[3] As a cross check, forcing `Vevacious` to use the direct path approximation yields the same lifetimes as our approach.

[4] We have verified using `FeynHiggs 2.14.3` [406–412] that $124\,\text{GeV} \lesssim m_h \lesssim 126\,\text{GeV}$ indeed holds along this line as long as $|\mu| \lesssim 3\,\text{TeV}$.

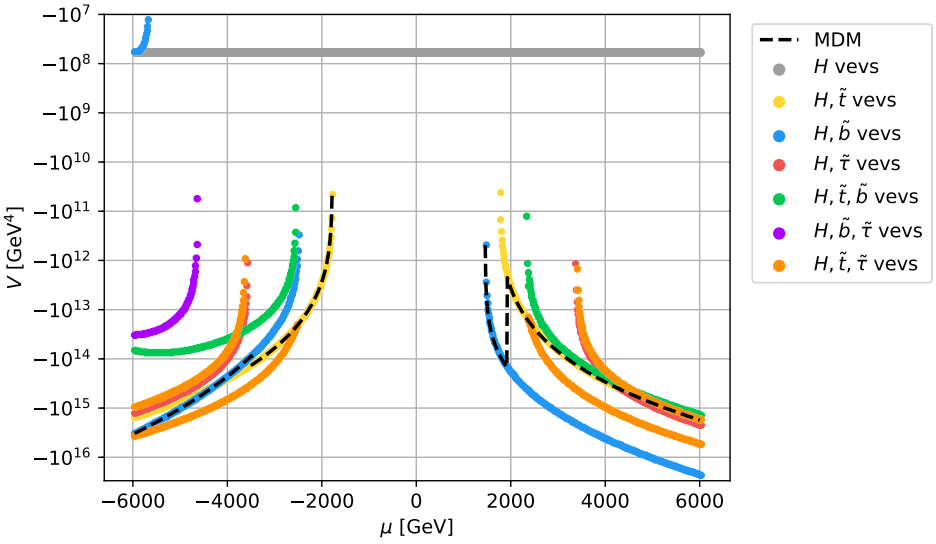

Figure 7.6: Depth of the different types of stationary points along the line of constant $X_t = 2.8\,\text{TeV}$ from fig. 7.3. The colour code indicates which fields acquire vevs at the stationary point. The dashed line indicates which of the stationary points is the MDM. The grey line is the EW vacuum. Figure as published in ref. [3].

It can be seen from fig. 7.6 that for large negative μ simultaneous $\tilde{t}$ and $\tilde{\tau}$ vevs (orange) dominate the global minimum for the considered field content until the $\tilde{\tau}$ vevs at these stationary points approach zero around $\mu = -2.2\,\text{TeV}$, and pure $\tilde{t}$ vevs take over. From $\mu \approx -1.8\,\text{TeV}$ onwards the EW vacuum is the global minimum until a CCB vacuum with $\tilde{b}$ vevs appears at $\mu \approx 1.6\,\text{TeV}$. The MDM, on the other hand, is the second deepest $\tilde{b}$-vev minimum for $\mu \lesssim -3.5\,\text{TeV}$, before switching to the $\tilde{t}$-vev minimum, followed by the window of absolute stability $\mu \in [-1.8\,\text{TeV}, 1.5\,\text{TeV}]$. For positive values of $\mu > 1.5\,\text{TeV}$ the instability first develops towards the global $\tilde{b}$-vev minimum until the $\tilde{t}$-vev minimum takes over at $\mu \approx 2\,\text{TeV}$.

In fig. 7.6 several stationary points with multiple kinds of sfermion vevs appear. Stationary points with mixed squark and slepton vevs can be deeper than the corresponding stationary points with only one type of vev (this can be seen for instance by comparing the deepest stationary point with orange $\tilde{t}$ and $\tilde{\tau}$ vevs to the ones with yellow $\tilde{t}$ vevs and red $\tilde{\tau}$ vevs). A stationary point with multiple kinds of squark vevs, however, is always higher than one with only one kind of the involved vevs. This is due to the additional positive quartic contributions to the potential for stationary points with both kinds of squark vevs.

Another feature visible in fig. 7.6 is the $\tilde{b}$-vev stationary point approaching the EW vacuum at $\mu \ll 0$ from above. In this regime the Δ_b corrections significantly enhance the bottom Yukawa coupling giving rise to a large mixing in the $\tilde{b}$ sector and a corresponding decrease of one of the $\tilde{b}$ masses. The depth of this stationary point becomes degenerate

with the EW vacuum. For even larger negative μ, one $\tilde{b}$ squark becomes tachyonic, and the EW vacuum turns into a saddle point. The plot ends before this happens (corresponding to the white region in fig. 7.3) as we require the existence of an EW vacuum.

The scalar potential eq. (7.27) has two accidental $\mathbb{Z}_2$ symmetries that illustrate the behaviour discussed in section 3.3.1. The potential is symmetric under simultaneous sign flips of the left- and right-handed sfermions of a kind

$$\mathrm{Re}(\tilde{f}_L),\, \mathrm{Re}(\tilde{f}_R) \to -\mathrm{Re}(\tilde{f}_L),\, -\mathrm{Re}(\tilde{f}_R) \quad \text{with } \tilde{f} \in \{\tilde{t}, \tilde{b}, \tilde{\tau}\} \tag{7.35}$$

and under simultaneous sign flips of all doublet components

$$\begin{aligned} &\mathrm{Re}(h_u^0),\, \mathrm{Re}(h_d^0),\, \mathrm{Re}(\tilde{t}_L),\, \mathrm{Re}(\tilde{b}_L),\, \mathrm{Re}(\tilde{\tau}_L) \\ \to \quad &-\mathrm{Re}(h_u^0),\, -\mathrm{Re}(h_d^0),\, -\mathrm{Re}(\tilde{t}_L),\, -\mathrm{Re}(\tilde{b}_L),\, -\mathrm{Re}(\tilde{\tau}_L)\,. \end{aligned} \tag{7.36}$$

This results in sets of degenerate and physically equivalent stationary points related by these symmetries.[5] Since the EW vacuum is also invariant under eq. (7.35) the tunnelling time to minima related by this symmetry is always identical. However, since the EW vacuum breaks eq. (7.36)[6] the tunnelling time into two stationary points related through this transformation can differ. In most cases, whichever of these two points is closer in field space to the EW vacuum gives the lower value for B. Note that this is not a small effect. The values of B for stationary points related by eq. (7.36) can differ by more than an order of magnitude. This effect has recently been studied for the simpler case of a 2HDM in ref. [228].

7.3.2 Vacuum Stability in the $M_h^{125}(\tilde{\tau})$ Scenario

A benchmark scenario with light $\tilde{\tau}$ has been proposed in ref. [26] under the name $M_h^{125}(\tilde{\tau})$. It is defined by

$$\begin{aligned} m_{Q_3} = m_{U_3} = m_{D_3} = 1.5\,\mathrm{TeV}\,, \quad m_{L_3} = m_{E_3} = 350\,\mathrm{GeV}\,, \quad \mu = 1\,\mathrm{TeV}\,, \\ X_t = A_t - \frac{\mu}{\tan\beta} = 2.8\,\mathrm{TeV}\,, \quad A_b = A_t\,, \quad A_\tau = 800\,\mathrm{GeV}\,, \\ M_1 = M_2 = 1\,\mathrm{TeV}\,, \quad M_3 = 2.5\,\mathrm{TeV}\,, \end{aligned} \tag{7.37}$$

and was shown in fig. 7.1 as an example.

The scenario differs from the M_h^{125} scenario of eq. (7.31) only in greatly reduced soft $\tilde{\tau}$ masses with a correspondingly reduced $A_{\tilde{\tau}}$. However, μ is not reduced and is now $\mu \sim 3m_{\tilde{\tau}}$. According to eq. (7.34) we would therefore expect vacuum stability constraints to be relevant in the $M_h^{125}(\tilde{\tau})$ benchmark plane. The authors of ref. [26] used `Vevacious` to check for vacuum instabilities in this scenario and found a short-lived region in the parameter space for large $\tan\beta$ and small m_A.

[5] Since these minima are degenerate they cannot be distinguished in fig. 7.6.

[6] We can, without loss of generality, choose the EW vacuum with $\mathrm{Re}(h_u^0)$, $\mathrm{Re}(h_d^0) > 0$.

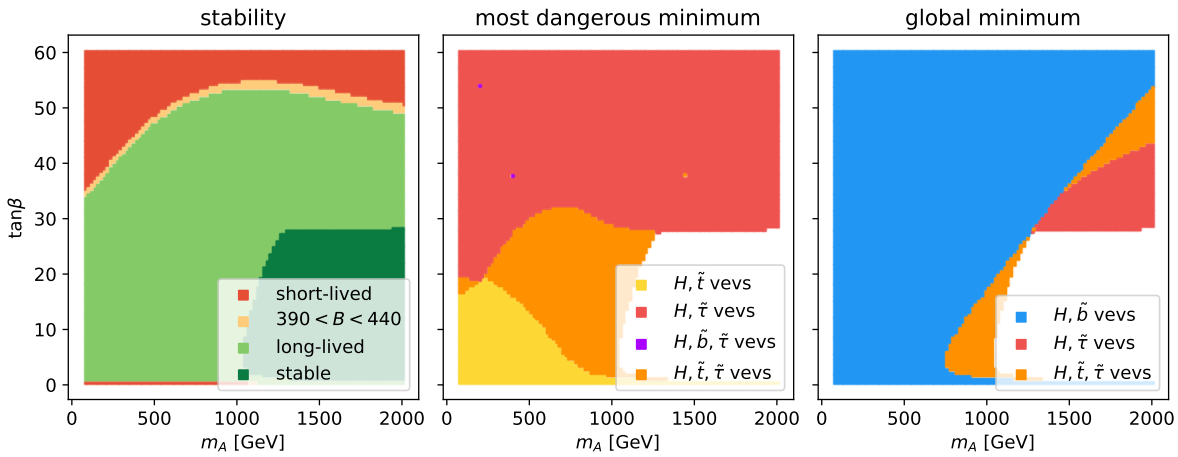

Figure 7.7: Constraints from vacuum stability in the $M_h^{125}(\tilde{\tau})$ scenario. The colour code in the left plot indicates the lifetime of the EW vacuum, while the centre and right plots illustrate which fields have non-zero vevs at the MDM and the global minimum, respectively. Figure as published in ref. [3].

Our results shown in fig. 7.7 confirm these observations. Figure 7.7 (left) shows a short-lived region for large $\tan\beta$. This region extends towards smaller values of $\tan\beta$ in the low m_A regime as noted in ref. [26] but also in the region of large m_A. Also visible is the small region of instability for $\tan\beta < 1$ noted in fig. 7.2. Comparing the red region excluded by vacuum stability to the reach of the experimental constraints as shown in fig. 7.1 shows a clear complementarity at large $\tan\beta$. While Higgs searches provide the strongest constraint at $m_A \lesssim 1.5\,\text{TeV}$, vacuum stability constraints are stronger than the constraints from Higgs searches for larger m_A.

The MDM for the instability at large $\tan\beta$ is a vacuum with $\tilde{\tau}$ vevs as can bee seen from fig. 7.7 (centre). Compared to fig. 7.2 the absolutely stable region is additionally reduced by a $\tilde{t}$-$\tilde{\tau}$-vev minimum appearing around $m_A \sim 1\,\text{TeV}$ and $\tan\beta < 30$. The minima with $\tilde{b}$ vevs, which were the MDM for large regions of the M_h^{125} scenario, are entirely replaced by minima with $\tilde{\tau}$ vevs. Only a very small purple region with simultaneous $\tilde{b}$ and $\tilde{\tau}$ vevs at the MDM exists. In fig. 7.7 (right) the global minimum with $\tilde{b}$ vevs is very similar to fig. 7.2 (right). Only at larger m_A — where the EW vacuum in the M_h^{125} scenario was absolutely stable — global minima with $\tilde{\tau}$ vevs are now present. Our results in the $M_h^{125}(\tilde{\tau})$ scenario compared to the M_h^{125} scenario illustrate that constraints from vacuum stability indeed become relevant when the cubic terms in the scalar potential become larger than the quadratic terms. Since $\mu \sim 3m_{\tilde{\tau}}$ in this scenario, a further increase of μ or a decrease of $m_{\tilde{\tau}}$ could render the $M_h^{125}(\tilde{\tau})$ scenario entirely short-lived. In the region of $\mu \sim 3m_{\tilde{\tau}}$ chosen in the $M_h^{125}(\tilde{\tau})$ scenario, the vacuum stability constraints show a significant dependence on the parameters m_A and $\tan\beta$.

7.3.3 Vacuum Stability in the M_h^{125}(alignment) Scenario

In this section, we turn to another scenario from ref. [26], the M_h^{125}(alignment) scenario, where constraints from vacuum stability turn out to have a very large impact. The scenario is defined by

$$\begin{aligned} m_{Q_3} = m_{U_3} = m_{D_3} = 2.5\,\text{TeV}\,, \quad m_{L_3} = m_{E_3} = 2\,\text{TeV}\,, \\ \mu = 7.5\,\text{TeV}\,, \quad A_t = A_b = A_\tau = 6.25\,\text{TeV}\,, \\ M_1 = 500\,\text{GeV}\,, \quad M_2 = 1\,\text{TeV}\,, \quad M_3 = 2.5\,\text{TeV}\,, \end{aligned} \tag{7.38}$$

with $m_A \in [100\,\text{GeV}, 1\,\text{TeV}]$ and $\tan\beta \in [1, 20]$. It is chosen to accommodate light additional Higgs bosons through the so-called alignment without decoupling behaviour [195, 196, 413–419]. Alignment without decoupling in the phenomenologically interesting region of relatively small $\tan\beta$ requires $\mu, A_t \gg m_{\tilde{t}}$. This requirement — according to eq. (7.34) — has already been noted to be problematic for vacuum stability in ref. [26]. Indeed we find that the EW vacuum in this scenario is short-lived through all of its parameter space. The MDM is characterised by $\tilde{t}$ vevs throughout the parameter plane, while the global minimum has $\tilde{b}$ vevs for $\tan\beta \gtrsim 5.5$ and $\tilde{t}$-$\tilde{\tau}$ vevs for smaller values of $\tan\beta$.[7]

In order to assess how far away this scenario is from a region of metastability we again select a phenomenologically interesting point in its parameter plane,

$$m_A = 500\,\text{GeV}\,, \quad \tan\beta = 6\,, \tag{7.39}$$

and vary $A = A_t = A_b = A_\tau$ and μ starting from this point. The resulting plane is shown in fig. 7.8. The colour code and the quantities shown in the sub-plots are the same as in figs. 7.2 and 7.3. In the left panel, we have superimposed the contours for the mass of the light Higgs boson calculated with `FeynHiggs 2.14.3` [406–412]. This shows that in order to obtain a long-lived scenario while keeping the correct Higgs mass one could for example change

$$\mu = 7.5\,\text{TeV} \to 4\,\text{TeV} \quad \text{and} \quad A = 6.25\,\text{TeV} \to 5\,\text{TeV}\,. \tag{7.40}$$

Other choices are possible within the theoretical uncertainty of the Higgs-mass prediction. The alignment-without-decoupling behaviour implies that h_{125} has SM-like properties. In the MSSM this behaviour arises from a cancellation between tree-level mixing contributions and higher-order corrections in the Higgs-boson mass matrix. Shifting the parameters towards the region where the vacuum is metastable like it is done in eq. (7.40) could affect these cancellations and therefore spoil the alignment properties. Indeed, with `FeynHiggs` we obtain $\sim 10\%$ enhanced couplings of h to bottom and tau pairs leading to a $\sim 10\%$ reduced $\text{BR}(h \to \gamma\gamma)$ compared to the SM for the parameter point of eq. (7.40). While the change in the couplings indicates that the cancellation that is present in the alignment without decoupling regime does not fully occur for the shifted point, this

[7] The corresponding plots are omitted as they do not add any information.

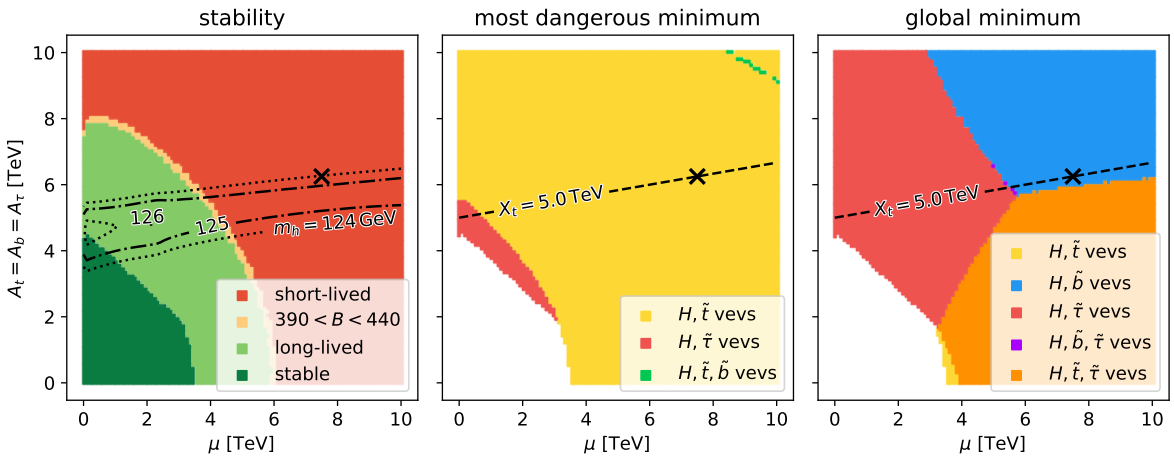

Figure 7.8: Constraints from vacuum stability in the plane of μ and A containing the selected point from the M_h^{125}(alignment) scenario marked with the black $\times$. The selected point in the m_A-tan β plane of the M_h^{125}(alignment) scenario has $\tan\beta = 6$ and $m_A = 500\,\text{GeV}$. The colour code in the left plot indicates the lifetime of the EW vacuum, while the centre and right plots illustrate which fields have non-zero vevs at the MDM and the global minimum, respectively. The contours in the left plot indicate the mass of the Higgs boson h, and the dashed line shown in the centre and right panels indicates the line of constant $X_t = 5\,\text{TeV}$. Figure as published in ref. [3].

parameter point is nevertheless still compatible with the LHC Higgs measurements within the present uncertainties [420].

In the middle panel of fig. 7.8 one can see that the MDM directions through most of the parameter space are directions with $\tilde{t}$ vevs. If the instabilities were in directions with $\tilde{b}$ or $\tilde{\tau}$ vevs, the lifetime of the EW vacuum could have been increased by increasing m_{D_3,L_3,E_3} or decreasing $A_{b,\tau}$ while keeping μ and the $\tilde{t}$ sector unchanged such that the phenomenology would not be much affected. However, our analysis shows that the parameter region associated with the alignment-without-decoupling behaviour gives rise to minima with $\tilde{t}$ vevs that render the electroweak vacuum short-lived. Accordingly, the behaviour of alignment without decoupling and the requirement of a long-lived vacuum are in some tension with each other, since adjusting m_{Q_3,U_3} and A_t to ensure vacuum stability in the stop directions would change the mass and phenomenology of the light Higgs boson h. The right plot of fig. 7.8 illustrates that the global minimum has non-vanishing $\tilde{\tau}$ vevs through significant parts of the parameter plane, while for large values of $A, \mu \gtrsim 5\,\text{TeV}$ $\tilde{b}$ vevs take over. However, the deepest minima appear to be nearly degenerate as can be seen from fig. 7.9.

The depth of the stationary points of the scalar potential along the line of constant $X_t = 5\,\text{TeV}$ (which is indicated in fig. 7.8 centre and right) is shown in fig. 7.9. It includes all stationary points in the selected field sets that are at least as deep as the EW vacuum.

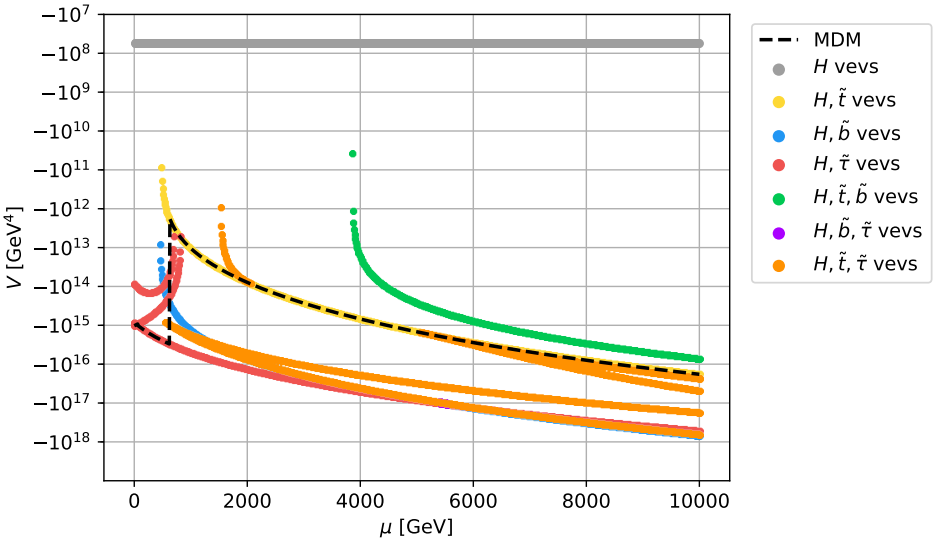

Figure 7.9: Depth of the different types of stationary points along the line of constant $X_t = 5\,\text{TeV}$ from fig. 7.8. The colour code indicates which fields have non-zero vevs at the stationary point. The dashed line indicates which of the stationary points is the MDM. The EW vacuum is shown in grey. Figure as published in ref. [3].

The EW vacuum is shown in grey, and the other colours distinguish the CCB stationary points. The plot illustrates that there is no stable region along this slice of parameter space, in accordance with fig. 7.8. As already pointed out, the MDM along this line is a minimum with $\tilde{t}$ vevs through most of the parameter range, except for the region with small values of μ where the MDM has $\tilde{\tau}$ vevs. There exist stationary points that are deeper than the MDM with $\tilde{b}$ vevs[8], $\tilde{t}$-$\tilde{\tau}$ vevs and $\tilde{\tau}$ vevs with the $\tilde{\tau}$-vev minimum being the global minimum until the $\tilde{b}$-vev minimum takes over for $\mu \gtrsim 5.5\,\text{TeV}$. These deeper minima are however very far from the EW vacuum in field space with high barriers and have no impact on the tunnelling rate. For large values of μ stationary points with both $\tilde{t}$ and $\tilde{b}$ vevs develop. In agreement with the previous discussions these stationary points are less deep than the stationary points with only one kind of squark vev. All points along this line of constant $X_t = 5\,\text{TeV}$ would be long-lived if the MDM with $\tilde{t}$ vevs was absent.

A detailed analysis of the question whether adjustments of the proposed scenarios for alignment without decoupling could bring these scenarios into better agreement with the constraints from vacuum stability while retaining their alignment properties goes beyond the scope of this work. We leave this issue for future studies.

[8]The $\tilde{b}$-vev stationary point is almost degenerate with the deepest $\tilde{t}$-$\tilde{\tau}$-vev stationary point for most of the parameter range and therefore hidden behind the orange points.

7.3.4 Vacuum Stability in the Remaining Benchmark Scenarios

The remaining (CP-conserving) benchmark scenarios from ref. [26] are either entirely stable or unstable. We will describe these results in short in this section.

The light neutralino scenario $M_h^{125}(\tilde{\chi})$ is defined through

$$\begin{aligned} m_{Q_3} = m_{U_3} = m_{D_3} = 1.5\,\text{TeV}\,, \quad m_{L_3} = m_{E_3} = 2\,\text{TeV}\,, \quad \mu = 180\,\text{GeV}\,, \\ X_t = A_t - \frac{\mu}{\tan\beta} = 2.5\,\text{TeV}\,, \quad A_b = A_\tau = A_t\,, \\ M_1 = 160\,\text{GeV}\,, \quad M_2 = 180\,\text{GeV}\,, \quad M_3 = 2.5\,\text{TeV}\,. \end{aligned} \tag{7.41}$$

The entire benchmark plane features an absolutely stable EW vacuum.[9] This is unsurprising since μ is very small and the soft sfermion masses relatively large while the A parameter is not much larger than the soft masses. The small gaugino mass parameters do not lead to instabilities as they only enter the scalar potential through the Δ_b and Δ_τ corrections.

Finally, the heavy Higgs alignment scenario M_H^{125} is defined through

$$\begin{aligned} m_{Q_3} = m_{U_3} = 750\,\text{GeV} - 2(m_{H^\pm} - 150\,\text{GeV})\,, \\ \mu = (5800\,\text{GeV} + 20(m_{H^\pm} - 150\,\text{GeV}))\, m_{Q_3}/(750\,\text{GeV})\,, \\ A_t = A_b = A_\tau = 0.65 m_{Q_3}\,, \quad m_{D_3} = m_{L_3} = m_{E_3} = 2\,\text{TeV}\,, \\ M_1 = m_{Q_3} - 75\,\text{GeV}\,, \quad M_2 = 1\,\text{TeV}\,, \quad M_3 = 2.5\,\text{TeV}\,. \end{aligned} \tag{7.42}$$

In this scenario, the heavy Higgs boson is identified with $h_{125} = H$. Since the scenario has small soft SUSY-breaking squark mass parameters and a very large μ it is unsurprising that the entire benchmark plane has a short-lived EW vacuum. Throughout the plane, the MDM has non-vanishing $\tilde{t}$ vevs while the global minimum has $\tilde{t}$-$\tilde{\tau}$ vevs.[9] Considering how constrained the region of phenomenologically viable parameter space for this scenario is (see fig. 10 of ref. [26]) we do not expect that a heavy Higgs alignment scenario with a long-lived vacuum exists in the MSSM. However, a detailed assessment of this possibility would require a dedicated study.

We have omitted the CP-violating scenario that was proposed in ref. [26] for simplicity only. Our approach is fully applicable also to models containing CP-violating phases.

7.4 Conclusions

In this chapter, we have applied our fast and efficient approach for evaluating vacuum stability constraints presented in chapter 3 to the MSSM. In order to evaluate the constraints from vacuum stability, it is in principle desirable to simultaneously take into

[9] The corresponding plots are omitted as they do not add any information.

account all possible vevs of all the scalar fields in the considered model. However, this often becomes impractical in models with large scalar sectors. Our efficient approach has allowed us to consider up to six real degrees of freedom simultaneously. We have included the possible vevs of the particles with the largest Yukawa couplings (namely $\tilde{t}$, $\tilde{b}$ and $\tilde{\tau}$) in addition to the Higgs vevs when searching for unstable directions. We have observed that this yields robust vacuum stability constraints — especially when including multiple kinds of sfermions simultaneously. However, for the studied scenarios, we would have obtained very similar vacuum stability constraints if we had considered each kind of sfermion separately as an approximation.

We have found the sfermions of the first and second generation as well as the sneutrinos to have a minor impact on vacuum stability constraints. Their small Yukawa couplings lead to additional minima at very large field values, which renders these configurations long-lived. On the other hand, the global minimum — and to some extent, the region of absolute stability — shows a significant dependence on additional field content that couples only weakly to the Higgs sector. We have also found several parameter regions where vevs of different sfermions are simultaneously non-zero at the global minimum.

As a result, our analysis shows that neither the investigation of just the region of absolute stability nor of the character of the global minimum is sufficient to obtain reliable bounds from vacuum stability. Instead, determining the boundary between short-lived and long-lived regions crucially relies on the correct identification of the MDM. This is the minimum with the shortest tunnelling time from the EW vacuum, which in general differs from the global minimum.

For the considered M_h^{125} MSSM benchmark scenario from ref. [26] we have found that the impact of vacuum stability constraints is small in the m_A–$\tan\beta$ parameter plane defining the scenario. However, a variation of the parameters μ and A around their values chosen in the benchmark scenario shows an important impact of vacuum stability constraints. In this plane, we have illustrated that the most dangerous and the global minimum are in general different. We have furthermore stressed the importance of corrections to the relation between the bottom-quark mass and the bottom Yukawa coupling in certain regions of parameter space. These Δ_b corrections can significantly enhance the value of the bottom Yukawa coupling and thus trigger $\tilde{b}$-vev instabilities.

We have also used this parameter plane to compare our results with existing studies and codes. Comparing our results to approximate analytic vacuum stability bounds, we have seen that those approximations can serve as a rough estimate of the effect of vacuum stability constraints. However, they cannot capture the complexity of a detailed numerical analysis. Furthermore, we have compared the results of our method to the public code `Vevacious`. The tree-level results of the codes show some notable differences. The most significant differences arise from the determination of the MDM. By default, `Vevacious` uses the closest minimum in field space — and optionally the global minimum. In contrast, by the use of an analytic expression for the bounce action, we can calculate all tunnelling times to deeper minima and select the one with the shortest time as the MDM. In the benchmark plane under consideration, we have found regions where the MDM is

neither the global minimum nor the minimum closest to the EW vacuum in field space. We have also seen that the impact of the more sophisticated tunnelling path calculation in `Vevacious` (using the path deformation of `CosmoTransitions`) is visible but does not substantially change the boundary between parameter regions with long- and short-lived EW vacuum. Calculating the vacuum stability bounds with `Vevacious` using the one-loop effective potential leads to results qualitatively similar to the tree-level results. The one-loop calculation showed strong indications of numerical instability in addition to the problems in the identification of the MDM. Even ignoring the latter problem, we have found the improvement by the one-loop effective potential on the vacuum stability constraints to be small given the significantly increased amount of numerical instabilities and the much longer runtime. Furthermore, as discussed in section 3.1.3, it is unclear whether the use of a loop-corrected effective potential yields a systematic improvement of vacuum stability constraints compared to a tree-level analysis. The tree-level constraints of our approach using the straight tunnelling path approximation yield numerically stable results in a fraction of the runtime of `Vevacious` and `CosmoTransitions`.

We have exemplarily studied the depths of the different stationary points along a line of $m_h \sim 125\,\text{GeV}$ through the parameter space. This has shown the typical number of stationary points appearing in an analysis of vacuum stability and illustrated the importance of the different scalar degrees of freedom. The MDM was found to coincide with the global minimum only within a small part of the parameter range. We have also discussed the impact of degenerate stationary points that are related to each other by a discrete symmetry and found that — in agreement with recent results in the literature [228] — if such a symmetry is broken by the EW vacuum the tunnelling times into the degenerate vacua can be vastly different.

In a benchmark scenario with light $\tilde{\tau}$, we have shown important constraints from vacuum stability in the m_A–$\tan\beta$ plane defining the scenario. In ref. [26] a parameter region with high $\tan\beta$ and low m_A of this benchmark plane was identified as being excluded by vacuum stability constraints. Our results provide a more detailed study of these constraints and show that the excluded region extends to high m_A.

A further scenario that we have studied in detail is a benchmark scenario in the alignment without decoupling regime. Since all parameter points in the benchmark plane yield short-lived EW vacua we have discussed what kind of shift in parameter space could lead to a long-lived vacuum while preserving the correct value of the Higgs mass. We found that this naïve approach would not obviously spoil the alignment without decouplings behaviour. The question to what extent the alignment without decoupling behaviour can be realised in phenomenologically viable scenarios including vacuum stability constraints would require a detailed study that is beyond the scope of the present work. Finally, we evaluated the vacuum stability constraints in the remaining CP-conserving benchmark scenarios of ref. [26]. We found that the $M_h^{125}(\tilde{\chi})$ scenario with light neutralinos yields absolutely stable EW vacua, while the vacua of the heavy Higgs alignment scenario M_H^{125} are entirely short-lived.

8 Summary and Conclusions

Unravelling the nature of electroweak symmetry breaking (EWSB) is one of the most important goals of current particle physics. The study of different BSM models with extended Higgs sectors in comparison with the SM provides crucial insights into the theoretical possibilities for EWSB and the related experimental signatures.

Measuring the parameters of the scalar potential that governs EWSB requires observing interactions between several Higgs bosons. Within the SM, this requires measuring the Higgs self-couplings, which are challenging to observe directly at the LHC. However, models with extended Higgs sectors also include interactions between different scalars that could be probed at the LHC and even serve as a discovery channel for additional Higgs bosons. We have explored this possibility in detail in chapter 4, where we studied the two-real-singlet model (TRSM), a simple extension of the SM by two scalar singlet fields. We have shown that the "classical" searches for new scalars, *e.g.* in $pp \to H \to W^+W^-/ZZ$ channels, probe the model. However, we have also found large regions of parameter space where constraining the model or, preferably, discovering new particles would require searches in multiscalar final states, possibly not even involving the 125 GeV Higgs boson (h_{125}). In chapter 4, we presented two-dimensional benchmark scenarios for all possible Higgs-to-Higgs decay signatures involving two different non-h_{125} scalars. These scenarios illustrate the relevance of these currently unexplored signatures and could serve to facilitate experimental studies at the LHC or future colliders.

The CP-properties of the Higgs sector are not only phenomenologically interesting, but additional sources of CP violation are also a requirement for explaining baryogenesis. At the same time, experimentally establishing the CP-nature of h_{125} beyond the fact that it is not a pure CP-odd state is very challenging. In chapter 5, we first discussed the CP-violating 2HDM (C2HDM), which is the minimal model with a CP-violating Higgs sector. It introduces a single CP-violating phase that induces a mixing between the CP-even and CP-odd states of the two-Higgs-doublet model (2HDM). We have studied the phenomenological consequences of a CP-odd admixture to h_{125} and found that large CP-violating Yukawa couplings are compatible with current measurements. In particular, we showed that the Yukawa couplings of h_{125} to down-type quarks or leptons could be maximally CP-violating with CP-even and CP-odd parts of similar size. It is also possible that some Yukawa couplings of h_{125} are CP-even and some are CP-odd. We hope that such scenarios can be studied experimentally in the future. These scenarios face strong constraints from bounds on fermionic electric dipole moments (EDMs). We discussed how the bounds from the electron EDM can be evaded through cancellations

between different contributions. It should, however, be noted that the viability of these cancellations has not been demonstrated if different EDM bounds are simultaneously considered.

In the second half of chapter 5, we introduced a model with a minimal CP-violating dark sector. The $\mathbb{Z}_2$ symmetry that makes the lightest dark sector particle a stable dark matter (DM) candidate also forbids the appearance of CP-violating Yukawa couplings. As a result, it is challenging to experimentally establish that the model is indeed CP-violating. We studied the ZZZ anomalous triple gauge coupling induced by the dark sector particles and found non-vanishing values for the CP-violating form factor f_4^Z. The imaginary part of this form factor is directly proportional to a potentially observable asymmetry, A_1^{ZZ}, which establishes that CP is violated in the model. The model prediction for both f_4^Z and A_1^{ZZ} is tiny, however, making it challenging to probe this model even at a future linear collider. The form factor f_4^Z is also being constrained at the LHC through fits to the Z-pair production process. However, these analyses assume a real and constant form factor, while the model predicts a complex and highly momentum dependent value.

In models with extended scalar sectors, the scalar potential can, in general, have multiple different minima. After EWSB, some of these additional minima could be energetically favourable compared to the electroweak (EW) vacuum. In this case, the EW vacuum would not be stable as it could decay through a tunnelling process. If this tunnelling is slow compared to the age of the universe, the EW vacuum is metastable and phenomenologically viable. A short-lived, unstable EW vacuum, however, is in contradiction to observations and parameter regions predicting such a scenario must be excluded. These vacuum stability constraints can have a significant impact on models with extended scalar sectors as scalar potentials with many degrees of freedom typically have many minima in addition to the EW vacuum. In such scalar potentials, vacuum decay is often possible at the EW scale — in contrast to the SM where the vacuum only becomes metastable at very high energy scales. We have presented a novel numerical approach to obtain vacuum stability constraints in chapter 3 that is designed to be efficient and reliable for use in parameter scans of BSM models. The method relies on the tree-level scalar potential and uses a straight path approximation to efficiently evaluate the tunnelling time into all possible minima.

In some simpler extensions of the Higgs sector, vacuum stability at the tree-level can be studied analytically. For example, the vacuum of the TRSM of chapter 4 is known to be absolutely stable [250]. Another case is the 2HDM where is has been proven that the EW vacuum is stable against CP- or charge-breaking minima [220, 349–351]. In chapter 6, we have shown that this no longer holds when adding another real scalar singlet to obtain the next-to 2HDM (N2HDM). We have analytically categorised the different kinds of vacua that can appear in the N2HDM. We then applied the approach of chapter 3 in a large scan of the phenomenologically viable parameter space of the N2HDM to study the impact of vacuum stability constraints on the relevant regions of parameter space. We have found that vacuum instabilities can appear in a substantial fraction of the otherwise viable parameter space and stress the importance of treating metastable regions as viable.

We furthermore showed that vacuum stability constraints may even directly limit the value of a collider observable — the signal strength of $h_{125} \to \gamma\gamma$ — by constraining the possible values of the coupling between h_{125} and the charged Higgs boson.

Supersymmetric models, such as the minimal supersymmetric extension of the SM (MSSM) have been subject to detailed studies during the last decades. These models are also especially interesting with respect to vacuum stability constraints as they introduce a huge number of new scalars — additional Higgs bosons and scalar superpartners for each SM fermion — that could all obtain vacuum expectation value. In chapter 7 we have used the MSSM to validate our approach to vacuum stability of chapter 3 and derive vacuum stability constraints on recently proposed benchmark scenarios [26]. In comparing our results to the literature, we have found good agreement even when comparing the straight path approximation to more elaborate methods. In particular, we have shown that the reduced numerical complexity of our approach can lead to more reliable results as we can consider tunnelling into all possible deeper minima and are not prone to the danger of misidentifying the most dangerous minimum. The obtained vacuum stability constraints on the benchmark scenarios especially impact scenarios with large trilinear parameters. We have pointed out possible complementarities with experimental searches and show that alignment-without-decoupling scenarios are severely constrained by vacuum stability — even more so when the heavy Higgs boson is identified with h_{125}.

The phenomenological studies presented in this thesis have been carried out to facilitate the experimental investigation of BSM models of EWSB. With the continued analyses of the run II LHC dataset and the upcoming run III, we expect many scenarios of EWSB and models with extended Higgs sectors to be probed in the near future. We hope that these investigations will lead to a better understanding of EWSB — ideally through the discovery of an extended scalar sector.

Acknowledgements

First of all, I would like to thank Georg Weiglein for supervision, advice, and many interesting discussions and explanations. I am grateful to Géraldine Servant for agreeing to co-referee my thesis and to Günter Sigl, Peter Schleper and Kai Schmidt-Hoberg for being on the committee of my disputation. I also thank Christophe Grojean for being my second supervisor, though I never found the time to work on any of your proposed projects. I am grateful to the PIER Helmholtz Graduate School for funding my PhD project at DESY.

I would like to thank all of my collaborators that I had the pleasure to work with during my PhD. I am very grateful to Wolfgang for working with me on my first project at DESY and for feedback on this thesis. Thanks to Tim for countless discussions about way too many projects, for getting me into HiggsBounds, reading parts of my thesis, and always taking the time to discuss whatever questions I stumbled into your office with. I am really grateful to everyone in my former group in Karlsruhe, in particular to Maggie for the awesome visits to Lisbon and for continuing to take care of me. Special thanks to Philipp, for remaining my office-mate remotely, and giving lots of feedback on my thesis. Lots of thanks to Rui and Pedro, for hosting us on our visits to Lisbon, for tons of discussions, for making work incredibly entertaining, and for feedback on my thesis. Also, thanks to Stefan for taking his time to get detailed answers to random questions and to Shruti for accidentally giving very well-timed emotional support.

Thanks a lot to all of my other friends at DESY. To the former and current Whizards — Jürgen, Christian, Bijan, Vincent, and Pascal — for adopting me when I was new and lots of entertaining lunch breaks and evenings with politics and programming. Thanks to all my other office-mates, especially Marco, Frederik, and Ilja, for the debates, jokes, rants and all the Marco stuff. Thanks to Henning for many discussions and for not minding my repeated invasions of your office. I am also really grateful for all the amazing people I got to meet at schools and workshops, a particular shoutout to Tobi, Rupert and Ruud.

Lots of love and thanks to Ines, for everything. In particular, for taking care of me when I was really stressed and helping me get through the writeup without major breakdowns. Thanks to all of my friends and family, who came to visit us in Hamburg. A massive amount of thanks to Jonas and Judith for taking my mind off work on countless evenings and for being awesome friends. Finally, thanks for all the support from my parents, Hannah, my grandparents, and Isolde, all helping me along.

Bibliography

[1] D. Fontes et al., 'The C2HDM revisited', JHEP **02** (2018) 073, 1711.09419.

[2] D. Azevedo et al., 'CP in the dark', JHEP **11** (2018) 091, 1807.10322.

[3] W. G. Hollik, G. Weiglein and J. Wittbrodt, 'Impact of Vacuum Stability Constraints on the Phenomenology of Supersymmetric Models', JHEP **03** (2019) 109, 1812.04644.

[4] P. M. Ferreira et al., 'Vacuum Instabilities in the N2HDM', (2019), 1905.10234.

[5] T. Robens, T. Stefaniak and J. Wittbrodt, 'Two-real-scalar-singlet extension of the SM: LHC phenomenology and benchmark scenarios', (2019), 1908.08554.

[6] P. Basler et al., 'Strong First Order Electroweak Phase Transition in the CP-Conserving 2HDM Revisited', JHEP **02** (2017) 121, 1612.04086.

[7] M. Mühlleitner et al., 'The N2HDM under Theoretical and Experimental Scrutiny', JHEP **03** (2017) 094, 1612.01309.

[8] P. Basler, M. Mühlleitner and J. Wittbrodt, 'The CP-Violating 2HDM in Light of a Strong First Order Electroweak Phase Transition and Implications for Higgs Pair Production', JHEP **03** (2018) 061, 1711.04097.

[9] M. Mühlleitner et al., 'Phenomenological Comparison of Models with Extended Higgs Sectors', JHEP **08** (2017) 132, 1703.07750.

[10] P. M. Ferreira, S. Liebler and J. Wittbrodt, '$pp \to A \to Zh$ and the wrong-sign limit of the two-Higgs-doublet model', Phys. Rev. **D97** (2018) 055008, 1711.00024.

[11] I. Engeln, M. Mühlleitner and J. Wittbrodt, 'N2HDECAY: Higgs Boson Decays in the Different Phases of the N2HDM', Comput. Phys. Commun. **234** (2018) 256, 1805.00966.

[12] D. Azevedo et al., 'Models with Extended Higgs Sectors at Future e^+e^- Colliders', Phys. Rev. **D99** (2019) 055013, 1808.00755.

[13] J. de Blas et al., 'The CLIC Potential for New Physics', (2018), 1812.02093.

[14] ATLAS, 'Observation of a new particle in the search for the Standard Model Higgs boson with the ATLAS detector at the LHC', Phys. Lett. **B716** (2012) 1, 1207.7214.

[15] CMS, 'Observation of a new boson at a mass of 125 GeV with the CMS experiment at the LHC', Phys. Lett. **B716** (2012) 30, 1207.7235.

[16] F. Englert and R. Brout, 'Broken Symmetry and the Mass of Gauge Vector Mesons', Phys. Rev. Lett. **13** (1964) 321.

[17] P. W. Higgs, 'Broken Symmetries and the Masses of Gauge Bosons', Phys. Rev. Lett. **13** (1964) 508.

[18] G. S. Guralnik, C. R. Hagen and T. W. B. Kibble, 'Global Conservation Laws and Massless Particles', Phys. Rev. Lett. **13** (1964) 585.

[19] ATLAS, CMS, 'Measurements of the Higgs boson production and decay rates and constraints on its couplings from a combined ATLAS and CMS analysis of the LHC pp collision data at $\sqrt{s}$=7 and 8 TeV', JHEP **08** (2016) 045, 1606.02266.

[20] S. R. Coleman, 'The Fate of the False Vacuum. 1. Semiclassical Theory', Phys. Rev. **D15** (1977) 2929.

[21] C. G. Callan Jr. and S. R. Coleman, 'The Fate of the False Vacuum. 2. First Quantum Corrections', Phys. Rev. **D16** (1977) 1762.

[22] HL/HE WG2 group, 'Higgs Physics at the HL-LHC and HE-LHC', (2019), 1902.00134.

[23] ATLAS, 'Evidence for the spin-0 nature of the Higgs boson using ATLAS data', Phys. Lett. **B726** (2013) 120, 1307.1432.

[24] CMS, 'Constraints on the spin-parity and anomalous HVV couplings of the Higgs boson in proton collisions at 7 and 8 TeV', Phys. Rev. **D92** (2015) 012004, 1411.3441.

[25] D. Fontes, J. C. Romão and J. P. Silva, '$h \to Z\gamma$ in the complex two Higgs doublet model', JHEP **12** (2014) 043, 1408.2534.

[26] E. Bagnaschi et al., 'MSSM Higgs Boson Searches at the LHC: Benchmark Scenarios for Run 2 and Beyond', Eur. Phys. J. **C79** (2019) 617, 1808.07542.

[27] A. Salam and J. C. Ward, 'Weak and electromagnetic interactions', Nuovo Cim. **11** (1959) 568.

[28] S. L. Glashow, 'The renormalizability of vector meson interactions', Nucl. Phys. **10** (1959) 107.

[29] S. L. Glashow, 'Partial Symmetries of Weak Interactions', Nucl. Phys. **22** (1961) 579.

[30] S. Weinberg, 'A Model of Leptons', Phys. Rev. Lett. **19** (1967) 1264.

[31] S. L. Glashow, J. Iliopoulos and L. Maiani, 'Weak Interactions with Lepton-Hadron Symmetry', Phys. Rev. **D2** (1970) 1285.

[32] Y. Ne'eman, 'Derivation of strong interactions from a gauge invariance', Nucl. Phys. **26** (1961) 222.

[33] M. Gell-Mann, 'Symmetries of baryons and mesons', Phys. Rev. **125** (1962) 1067.

[34] M. Gell-Mann, 'A Schematic Model of Baryons and Mesons', Phys. Lett. **8** (1964) 214.

[35] G. Zweig, 'An SU(3) model for strong interaction symmetry and its breaking', in: *Developments in the Quark Theory of Hadrons*, ed. by D. B. Lichtenberg and S. P. Rosen, vol. 1, 1964 22.

[36] H. Fritzsch, M. Gell-Mann and H. Leutwyler, 'Advantages of the Color Octet Gluon Picture', Phys. Lett. **47B** (1973) 365.

[37] M. E. Peskin and D. V. Schroeder, *An Introduction to quantum field theory*, Addison-Wesley, 1995, ISBN: 9780201503975.

[38] H. E. Logan, 'TASI 2013 lectures on Higgs physics within and beyond the Standard Model', (2014), 1406.1786.

[39] Particle Data Group, 'Review of Particle Physics', Phys. Rev. **D98** (2018) 030001.

[40] Y. Nambu, 'Quasiparticles and Gauge Invariance in the Theory of Superconductivity', Phys. Rev. **117** (1960) 648.

[41] J. Goldstone, 'Field Theories with Superconductor Solutions', Nuovo Cim. **19** (1961) 154.

[42] J. Goldstone, A. Salam and S. Weinberg, 'Broken Symmetries', Phys. Rev. **127** (1962) 965.

[43] F. Zwicky, 'Die Rotverschiebung von extragalaktischen Nebeln', Helv. Phys. Acta **6** (1933) 110.

[44] F. Zwicky, 'On the Masses of Nebulae and of Clusters of Nebulae', Astrophys. J. **86** (1937) 217.

[45] V. C. Rubin and W. K. Ford Jr., 'Rotation of the Andromeda Nebula from a Spectroscopic Survey of Emission Regions', Astrophys. J. **159** (1970) 379.

[46] K. G. Begeman, A. H. Broeils and R. H. Sanders, 'Extended rotation curves of spiral galaxies: Dark haloes and modified dynamics', Mon. Not. Roy. Astron. Soc. **249** (1991) 523.

[47] D. Clowe et al., 'A direct empirical proof of the existence of dark matter', Astrophys. J. **648** (2006) 109, astro-ph/0608407.

[48] Planck, 'Planck 2018 results. VI. Cosmological parameters', (2018), 1807.06209.

[49] J. L. Feng, 'Dark Matter Candidates from Particle Physics and Methods of Detection', Ann. Rev. Astron. Astrophys. **48** (2010) 495, 1003.0904.

[50] XENON, 'Dark Matter Search Results from a One Ton-Year Exposure of XENON1T', Phys. Rev. Lett. **121** (2018) 111302, 1805.12562.

[51] G. Belanger et al., 'MicrOMEGAs 2.0: A Program to calculate the relic density of dark matter in a generic model', Comput. Phys. Commun. **176** (2007) 367, hep-ph/0607059.

[52] G. Belanger et al., 'Dark matter direct detection rate in a generic model with micrOMEGAs 2.2', Comput. Phys. Commun. **180** (2009) 747, 0803.2360.

[53] G. Belanger et al., 'Indirect search for dark matter with micrOMEGAs2.4', Comput. Phys. Commun. **182** (2011) 842, 1004.1092.

[54] G. Belanger et al., 'micrOMEGAs 3: A program for calculating dark matter observables', Comput. Phys. Commun. **185** (2014) 960, 1305.0237.

[55] G. Bélanger et al., 'micrOMEGAs4.1: two dark matter candidates', Comput. Phys. Commun. **192** (2015) 322, 1407.6129.

[56] G. Bélanger et al., 'micrOMEGAs5.0 : Freeze-in', Comput. Phys. Commun. **231** (2018) 173, 1801.03509.

[57] D. Barducci et al., 'Collider limits on new physics within micrOMEGAs 4.3', Comput. Phys. Commun. **222** (2018) 327, 1606.03834.

[58] A. D. Sakharov, 'Violation of CP Invariance, C asymmetry, and baryon asymmetry of the universe', Pisma Zh. Eksp. Teor. Fiz. **5** (1967) 32.

[59] M. Fukugita and T. Yanagida, 'Baryogenesis Without Grand Unification', Phys. Lett. **B174** (1986) 45.

[60] W. Buchmuller, P. Di Bari and M. Plumacher, 'Leptogenesis for pedestrians', Annals Phys. **315** (2005) 305, hep-ph/0401240.

[61] V. A. Kuzmin, V. A. Rubakov and M. E. Shaposhnikov, 'On the Anomalous Electroweak Baryon Number Nonconservation in the Early Universe', Phys. Lett. **155B** (1985) 36.

[62] M. E. Shaposhnikov, 'Possible Appearance of the Baryon Asymmetry of the Universe in an Electroweak Theory', JETP Lett. **44** (1986) 465.

[63] M. Trodden, 'Electroweak baryogenesis', Rev. Mod. Phys. **71** (1999) 1463, hep-ph/9803479.

[64] D. E. Morrissey and M. J. Ramsey-Musolf, 'Electroweak baryogenesis', New J. Phys. **14** (2012) 125003, 1206.2942.

[65] M. E. Shaposhnikov, 'Baryon Asymmetry of the Universe in Standard Electroweak Theory', Nucl. Phys. **B287** (1987) 757.

[66] K. Kajantie et al., 'Is there a hot electroweak phase transition at m(H) larger or equal to m(W)?', Phys. Rev. Lett. **77** (1996) 2887, hep-ph/9605288.

[67] L. Fromme, S. J. Huber and M. Seniuch, 'Baryogenesis in the two-Higgs doublet model', JHEP **11** (2006) 038, hep-ph/0605242.

[68] G. C. Dorsch et al., 'A Second Higgs Doublet in the Early Universe: Baryogenesis and Gravitational Waves', JCAP **1705** (2017) 052, 1611.05874.

[69] G. C. Dorsch et al., 'The Higgs Vacuum Uplifted: Revisiting the Electroweak Phase Transition with a Second Higgs Doublet', JHEP **12** (2017) 086, 1705.09186.

[70] N. S. Manton, 'Topology in the Weinberg-Salam Theory', Phys. Rev. **D28** (1983) 2019.

[71] F. R. Klinkhamer and N. S. Manton, 'A Saddle Point Solution in the Weinberg-Salam Theory', Phys. Rev. **D30** (1984) 2212.

[72] L. Fromme and S. J. Huber, 'Top transport in electroweak baryogenesis', JHEP **03** (2007) 049, hep-ph/0604159.

[73] T. Konstandin, 'Quantum Transport and Electroweak Baryogenesis', Phys. Usp. **56** (2013) 747, 1302.6713.

[74] M. Sher, 'Electroweak Higgs Potentials and Vacuum Stability', Phys. Rept. **179** (1989) 273.

[75] J. A. Casas, J. R. Espinosa and M. Quiros, 'Improved Higgs mass stability bound in the standard model and implications for supersymmetry', Phys. Lett. **B342** (1995) 171, hep-ph/9409458.

[76] J. R. Espinosa and M. Quiros, 'Improved metastability bounds on the standard model Higgs mass', Phys. Lett. **B353** (1995) 257, hep-ph/9504241.

[77] G. Isidori, G. Ridolfi and A. Strumia, 'On the metastability of the standard model vacuum', Nucl. Phys. **B609** (2001) 387, hep-ph/0104016.

[78] J. R. Espinosa, G. F. Giudice and A. Riotto, 'Cosmological implications of the Higgs mass measurement', JCAP **0805** (2008) 002, 0710.2484.

[79] J. Ellis et al., 'The Probable Fate of the Standard Model', Phys. Lett. **B679** (2009) 369, 0906.0954.

[80] G. Degrassi et al., 'Higgs mass and vacuum stability in the Standard Model at NNLO', JHEP **08** (2012) 098, 1205.6497.

[81] F. Bezrukov et al., 'Higgs Boson Mass and New Physics', JHEP **10** (2012) 140, 1205.2893.

[82] K. G. Chetyrkin and M. F. Zoller, 'β-function for the Higgs self-interaction in the Standard Model at three-loop level', JHEP **04** (2013) 091, 1303.2890.

[83] D. Buttazzo et al., 'Investigating the near-criticality of the Higgs boson', JHEP **12** (2013) 089, 1307.3536.

[84] A. Andreassen, W. Frost and M. D. Schwartz, 'Consistent Use of the Standard Model Effective Potential', Phys. Rev. Lett. **113** (2014) 241801, 1408.0292.

[85] Z. Lalak, M. Lewicki and P. Olszewski, 'Higher-order scalar interactions and SM vacuum stability', JHEP **05** (2014) 119, 1402.3826.

[86] M. F. Zoller, 'Standard Model beta-functions to three-loop order and vacuum stability', in: *17th International Moscow School of Physics and 42nd ITEP Winter School of Physics Moscow, Russia, February 11-18, 2014*, 2014, 1411.2843.

[87] A. V. Bednyakov et al., 'Stability of the Electroweak Vacuum: Gauge Independence and Advanced Precision', Phys. Rev. Lett. **115** (2015) 201802, 1507.08833.

[88] V. Branchina, E. Messina and M. Sher, 'Lifetime of the electroweak vacuum and sensitivity to Planck scale physics', Phys. Rev. **D91** (2015) 013003, 1408.5302.

[89] G. Iacobellis and I. Masina, 'Stationary configurations of the Standard Model Higgs potential: electroweak stability and rising inflection point', Phys. Rev. **D94** (2016) 073005, 1604.06046.

[90] A. Andreassen, W. Frost and M. D. Schwartz, 'Scale Invariant Instantons and the Complete Lifetime of the Standard Model', Phys. Rev. **D97** (2018) 056006, 1707.08124.

[91] S. Chigusa, T. Moroi and Y. Shoji, 'State-of-the-Art Calculation of the Decay Rate of Electroweak Vacuum in the Standard Model', Phys. Rev. Lett. **119** (2017) 211801, 1707.09301.

[92] S. Chigusa, T. Moroi and Y. Shoji, 'Decay Rate of Electroweak Vacuum in the Standard Model and Beyond', Phys. Rev. **D97** (2018) 116012, 1803.03902.

[93] A. Andreassen et al., 'Precision decay rate calculations in quantum field theory', Phys. Rev. **D95** (2017) 085011, 1604.06090.

[94] I. P. Ivanov, 'Building and testing models with extended Higgs sectors', Prog. Part. Nucl. Phys. **95** (2017) 160, 1702.03776.

[95] B. Grzadkowski et al., 'Dimension-Six Terms in the Standard Model Lagrangian', JHEP **10** (2010) 085, 1008.4884.

[96] K. Symanzik, 'Renormalization of Models with Broken Symmetries', in: *Fundamental Interactions at High Energy II*, ed. by A. Perlmutter, G. J. Iverson and R. M. Williams, Coral Gables Conference on Fundamental Interactions at High Energy, Gordon & Breach, 1970 369.

[97] H. Georgi and S. L. Glashow, 'Unity of All Elementary Particle Forces', Phys. Rev. Lett. **32** (1974) 438.

[98] H. Georgi, H. R. Quinn and S. Weinberg, 'Hierarchy of Interactions in Unified Gauge Theories', Phys. Rev. Lett. **33** (1974) 451.

[99] A. J. Buras et al., 'Aspects of the Grand Unification of Strong, Weak and Electromagnetic Interactions', Nucl. Phys. **B135** (1978) 66.

[100] D. A. Ross and M. J. G. Veltman, 'Neutral Currents in Neutrino Experiments', Nucl. Phys. **B95** (1975) 135.

[101] M. J. G. Veltman, 'Limit on Mass Differences in the Weinberg Model', Nucl. Phys. **B123** (1977) 89.

[102] J. Hisano and K. Tsumura, 'Higgs boson mixes with an SU(2) septet representation', Phys. Rev. **D87** (2013) 053004, 1301.6455.

[103] S. Kanemura, M. Kikuchi and K. Yagyu, 'Probing exotic Higgs sectors from the precise measurement of Higgs boson couplings', Phys. Rev. **D88** (2013) 015020, 1301.7303.

[104] T. Hambye et al., 'Scalar Multiplet Dark Matter', JHEP **07** (2009) 090, 0903.4010.

[105] H. Georgi and M. Machacek, 'DOUBLY CHARGED HIGGS BOSONS', Nucl. Phys. **B262** (1985) 463.

[106] J. C. Pati and A. Salam, 'Lepton Number as the Fourth Color', Phys. Rev. **D10** (1974) 275.

[107] R. N. Mohapatra and J. C. Pati, 'A Natural Left-Right Symmetry', Phys. Rev. **D11** (1975) 2558.

[108] G. Senjanovic and R. N. Mohapatra, 'Exact Left-Right Symmetry and Spontaneous Violation of Parity', Phys. Rev. **D12** (1975) 1502.

[109] A. J. Buras et al., 'Higgs-mediated FCNCs: Natural Flavour Conservation vs. Minimal Flavour Violation', JHEP **10** (2010) 009, 1005.5310.

[110] G. C. Branco et al., 'Theory and phenomenology of two-Higgs-doublet models', Phys. Rept. **516** (2012) 1, 1106.0034.

[111] V. Barger et al., 'Complex Singlet Extension of the Standard Model', Phys. Rev. **D79** (2009) 015018, 0811.0393.

[112] S. P. Martin, 'A Supersymmetry primer', (1997) 1, hep-ph/9709356.

[113] U. Ellwanger, C. Hugonie and A. M. Teixeira, 'The Next-to-Minimal Supersymmetric Standard Model', Phys. Rept. **496** (2010) 1, 0910.1785.

[114] M. Maniatis, 'The Next-to-Minimal Supersymmetric extension of the Standard Model reviewed', Int. J. Mod. Phys. **A25** (2010) 3505, 0906.0777.

[115] M. Gell-Mann et al., 'Amelioration of divergence difficulties in the theory of weak interactions', Phys. Rev. **179** (1969) 1518.

[116] S. Weinberg, 'Physical Processes in a Convergent Theory of the Weak and Electromagnetic Interactions', Phys. Rev. Lett. **27** (1971) 1688.

[117] J. M. Cornwall, D. N. Levin and G. Tiktopoulos, 'Uniqueness of spontaneously broken gauge theories', Phys. Rev. Lett. **30** (1973) 1268.

[118] S. D. Joglekar, 'S matrix derivation of the Weinberg model', Annals Phys. **83** (1974) 427.

[119] J. M. Cornwall, D. N. Levin and G. Tiktopoulos, 'Derivation of Gauge Invariance from High-Energy Unitarity Bounds on the s Matrix', Phys. Rev. **D10** (1974) 1145.

[120] B. W. Lee, C. Quigg and H. B. Thacker, 'Weak Interactions at Very High-Energies: The Role of the Higgs Boson Mass', Phys. Rev. **D16** (1977) 1519.

[121] J. Horejsi, *Introduction to electroweak unification: Standard model from tree unitarity*, 1993.

[122] S. Kanemura, T. Kubota and E. Takasugi, 'Lee-Quigg-Thacker bounds for Higgs boson masses in a two doublet model', Phys. Lett. **B313** (1993) 155, hep-ph/9303263.

[123] J. Horejsi and M. Kladiva, 'Tree-unitarity bounds for THDM Higgs masses revisited', Eur. Phys. J. **C46** (2006) 81, hep-ph/0510154.

[124] I. F. Ginzburg and I. P. Ivanov, 'Tree-level unitarity constraints in the most general 2HDM', Phys. Rev. **D72** (2005) 115010, hep-ph/0508020.

[125] R. Coimbra, M. O. P. Sampaio and R. Santos, 'ScannerS: Constraining the phase diagram of a complex scalar singlet at the LHC', Eur. Phys. J. **C73** (2013) 2428, 1301.2599.

[126] T. Appelquist and M. S. Chanowitz, 'Unitarity Bound on the Scale of Fermion Mass Generation', Phys. Rev. Lett. **59** (1987) 2405.

[127] M. Golden, 'Unitarity and fermion mass generation', Phys. Lett. **B338** (1994) 295, hep-ph/9408272.

[128] K. Whisnant, B.-L. Young and X. Zhang, 'Unitarity and anomalous top quark Yukawa couplings', Phys. Rev. **D52** (1995) 3115, hep-ph/9410369.

[129] W. J. Marciano, G. Valencia and S. Willenbrock, 'Renormalization Group Improved Unitarity Bounds on the Higgs Boson and Top Quark Masses', Phys. Rev. **D40** (1989) 1725.

[130] P. Basler et al., 'High scale impact in alignment and decoupling in two-Higgs doublet models', Phys. Rev. **D97** (2018) 095024, 1710.10410.

[131] M. D. Goodsell and F. Staub, 'Unitarity constraints on general scalar couplings with SARAH', Eur. Phys. J. **C78** (2018) 649, 1805.07306.

[132] M. D. Goodsell and F. Staub, 'Improved unitarity constraints in Two-Higgs-Doublet-Models', Phys. Lett. **B788** (2019) 206, 1805.07310.

[133] M. E. Krauss and F. Staub, 'Unitarity constraints in triplet extensions beyond the large s limit', Phys. Rev. **D98** (2018) 015041, 1805.07309.

[134] M. E. Peskin and T. Takeuchi, 'Estimation of oblique electroweak corrections', Phys. Rev. **D46** (1992) 381.

[135] J. Haller et al., 'Update of the global electroweak fit and constraints on two-Higgs-doublet models', Eur. Phys. J. **C78** (2018) 675, 1803.01853.

[136] M. Baak et al., 'The global electroweak fit at NNLO and prospects for the LHC and ILC', Eur. Phys. J. **C74** (2014) 3046, 1407.3792.

[137] W. Grimus et al., 'A Precision constraint on multi-Higgs-doublet models', J. Phys. **G35** (2008) 075001, 0711.4022.

[138] W. Grimus et al., 'The Oblique parameters in multi-Higgs-doublet models', Nucl. Phys. **B801** (2008) 81, 0802.4353.

[139] I. Maksymyk, C. P. Burgess and D. London, 'Beyond S, T and U', Phys. Rev. **D50** (1994) 529, hep-ph/9306267.

[140] A. Cherchiglia, D. Stöckinger and H. Stöckinger-Kim, 'Muon g-2 in the 2HDM: maximum results and detailed phenomenology', Phys. Rev. **D98** (2018) 035001, 1711.11567.

[141] E. Bagnaschi et al., 'Likelihood Analysis of the pMSSM11 in Light of LHC 13-TeV Data', Eur. Phys. J. **C78** (2018) 256, 1710.11091.

[142] HFLAV, 'Averages of b-hadron, c-hadron, and τ-lepton properties as of summer 2016', Eur. Phys. J. **C77** (2017) 895, 1612.07233.

[143] M. Misiak et al., 'Updated NNLO QCD predictions for the weak radiative B-meson decays', Phys. Rev. Lett. **114** (2015) 221801, 1503.01789.

[144] M. Misiak and M. Steinhauser, 'Weak radiative decays of the B meson and bounds on $M_{H^\pm}$ in the Two-Higgs-Doublet Model', Eur. Phys. J. **C77** (2017) 201, 1702.04571.

[145] CMS, LHCb, 'Observation of the rare $B_s^0 \to \mu^+\mu^-$ decay from the combined analysis of CMS and LHCb data', Nature **522** (2015) 68, 1411.4413.

[146] LHCb, 'Measurement of the $B_s^0 \to \mu^+\mu^-$ branching fraction and effective lifetime and search for $B^0 \to \mu^+\mu^-$ decays', Phys. Rev. Lett. **118** (2017) 191801, 1703.05747.

[147] X.-Q. Li, J. Lu and A. Pich, '$B_{s,d}^0 \to \ell^+\ell^-$ Decays in the Aligned Two-Higgs-Doublet Model', JHEP **06** (2014) 022, 1404.5865.

[148] C. Bobeth et al., '$B_{s,d} \to l^+l^-$ in the Standard Model with Reduced Theoretical Uncertainty', Phys. Rev. Lett. **112** (2014) 101801, 1311.0903.

[149] X.-D. Cheng, Y.-D. Yang and X.-B. Yuan, 'Revisiting $B_s \to \mu^+\mu^-$ in the two-Higgs doublet models with Z_2 symmetry', Eur. Phys. J. **C76** (2016) 151, 1511.01829.

[150] ATLAS, CMS, LHCb, 'Flavour anomalies: a review', J. Phys. Conf. Ser. **1137** (2019) 012025, 1807.11373.

[151] M. E. Pospelov and I. B. Khriplovich, 'Electric dipole moment of the W boson and the electron in the Kobayashi-Maskawa model', Sov. J. Nucl. Phys. **53** (1991) 638.

[152] M. Pospelov and A. Ritz, 'Electric dipole moments as probes of new physics', Annals Phys. **318** (2005) 119, hep-ph/0504231.

[153] R. D. Peccei and H. R. Quinn, 'CP Conservation in the Presence of Instantons', Phys. Rev. Lett. **38** (1977) 1440.

[154] F. Wilczek, 'Problem of Strong P and T Invariance in the Presence of Instantons', Phys. Rev. Lett. **40** (1978) 279.

[155] S. Weinberg, 'A New Light Boson?', Phys. Rev. Lett. **40** (1978) 223.

[156] ACME, 'Improved limit on the electric dipole moment of the electron', Nature **562** (2018) 355.

[157] T. Abe et al., 'Gauge invariant Barr-Zee type contributions to fermionic EDMs in the two-Higgs doublet models', JHEP **01** (2014) 106, 1311.4704.

[158] J. M. Pendlebury et al., 'Revised experimental upper limit on the electric dipole moment of the neutron', Phys. Rev. **D92** (2015) 092003, 1509.04411.

[159] J. R. Ellis, J. S. Lee and A. Pilaftsis, 'Electric Dipole Moments in the MSSM Reloaded', JHEP **10** (2008) 049, 0808.1819.

[160] K. Cheung et al., 'Higgs Mediated EDMs in the Next-to-MSSM: An Application to Electroweak Baryogenesis', Phys. Rev. **D84** (2011) 015002, 1102.5679.

[161] M. Jung and A. Pich, 'Electric Dipole Moments in Two-Higgs-Doublet Models', JHEP **04** (2014) 076, 1308.6283.

[162] S. Inoue, M. J. Ramsey-Musolf and Y. Zhang, 'CP-violating phenomenology of flavor conserving two Higgs doublet models', Phys. Rev. **D89** (2014) 115023, 1403.4257.

[163] P. Bechtle et al., 'HiggsBounds: Confronting Arbitrary Higgs Sectors with Exclusion Bounds from LEP and the Tevatron', Comput. Phys. Commun. **181** (2010) 138, 0811.4169.

[164] P. Bechtle et al., 'HiggsBounds 2.0.0: Confronting Neutral and Charged Higgs Sector Predictions with Exclusion Bounds from LEP and the Tevatron', Comput. Phys. Commun. **182** (2011) 2605, 1102.1898.

[165] P. Bechtle et al., 'Recent Developments in HiggsBounds and a Preview of HiggsSignals', PoS **CHARGED2012** (2012) 024, 1301.2345.

[166] P. Bechtle et al., 'HiggsBounds-4: Improved Tests of Extended Higgs Sectors against Exclusion Bounds from LEP, the Tevatron and the LHC', Eur. Phys. J. **C74** (2014) 2693, 1311.0055.

[167] P. Bechtle et al., 'Applying Exclusion Likelihoods from LHC Searches to Extended Higgs Sectors', Eur. Phys. J. **C75** (2015) 421, 1507.06706.

[168] P. Bechtle et al., *HiggsBounds*, URL: gitlab.com/higgsbounds/higgsbounds.

[169] ATLAS, 'Search for additional heavy neutral Higgs and gauge bosons in the ditau final state produced in 36 fb^{-1} of pp collisions at $\sqrt{s} = 13$ TeV with the ATLAS detector', JHEP **01** (2018) 055, 1709.07242.

[170] O. Stål and T. Stefaniak, 'Constraining extended Higgs sectors with HiggsSignals', PoS **EPS-HEP2013** (2013) 314, 1310.4039.

[171] P. Bechtle et al., 'HiggsSignals: Confronting arbitrary Higgs sectors with measurements at the Tevatron and the LHC', Eur. Phys. J. **C74** (2014) 2711, 1305.1933.

[172] P. Bechtle et al., 'Probing the Standard Model with Higgs signal rates from the Tevatron, the LHC and a future ILC', JHEP **11** (2014) 039, 1403.1582.

[173] P. Bechtle et al., *HiggsSignals*, URL: gitlab.com/higgsbounds/higgssignals.

[174] ATLAS, CMS, 'Combined Measurement of the Higgs Boson Mass in *pp* Collisions at $\sqrt{s} = 7$ and 8 TeV with the ATLAS and CMS Experiments', Phys. Rev. Lett. **114** (2015) 191803, 1503.07589.

[175] LHC Higgs Cross Section Working Group, 'Handbook of LHC Higgs Cross Sections: 4. Deciphering the Nature of the Higgs Sector', (2016), 1610.07922.

[176] ATLAS, 'Combined measurements of Higgs boson production and decay using up to 80 fb^{-1} of proton–proton collision data at $\sqrt{s} = 13$ TeV collected with the ATLAS experiment', (2019).

[177] CMS, 'Measurements of properties of the Higgs boson decaying to a W boson pair in pp collisions at $\sqrt{s} = 13$ TeV', Phys. Lett. **B791** (2019) 96, 1806.05246.

[178] CMS, 'Measurements of properties of the Higgs boson in the four-lepton final state in proton-proton collisions at $\sqrt{s} = 13$ TeV', (2019).

[179] CMS, 'Measurements of Higgs boson production via gluon fusion and vector boson fusion in the diphoton decay channel at $\sqrt{s} = 13$ TeV', (2019).

[180] CMS, 'Search for the Higgs boson decaying to two muons in proton-proton collisions at $\sqrt{s} = 13$ TeV', Phys. Rev. Lett. **122** (2019) 021801, 1807.06325.

[181] CMS, 'Measurement of Higgs boson production and decay to the $\tau\tau$ final state', (2019).

[182] CMS, 'Evidence for the Higgs boson decay to a bottom quark–antiquark pair', Phys. Lett. **B780** (2018) 501, 1709.07497.

[183] CMS, 'Inclusive search for a highly boosted Higgs boson decaying to a bottom quark-antiquark pair', Phys. Rev. Lett. **120** (2018) 071802, 1709.05543.

[184] CMS, 'Measurement of $\mathrm{t\bar{t}H}$ production in the $\mathrm{H} \to \mathrm{b\bar{b}}$ decay channel in 41.5 fb^{-1} of proton-proton collision data at $\sqrt{s} = 13$ TeV', (2019).

[185] CMS, 'Evidence for associated production of a Higgs boson with a top quark pair in final states with electrons, muons, and hadronically decaying τ leptons at $\sqrt{s} =$ 13 TeV', JHEP **08** (2018) 066, 1803.05485.

[186] CMS, 'Measurement of the associated production of a Higgs boson with a top quark pair in final states with electrons, muons and hadronically decaying τ leptons in data recorded in 2017 at $\sqrt{s} = 13$ TeV', (2018).

[187] T. D. Lee, 'A Theory of Spontaneous T Violation', Phys. Rev. **D8** (1973) 1226.

[188] H. P. Nilles, 'Supersymmetry, Supergravity and Particle Physics', Phys. Rept. **110** (1984) 1.

[189] H. E. Haber and G. L. Kane, 'The Search for Supersymmetry: Probing Physics Beyond the Standard Model', Phys. Rept. **117** (1985) 75.

[190] J. F. Gunion and H. E. Haber, 'Higgs Bosons in Supersymmetric Models. 1.', Nucl. Phys. **B272** (1986) 1.

[191] LEP Working Group for Higgs boson searches, ALEPH, DELPHI, L3, OPAL, 'Search for the standard model Higgs boson at LEP', Phys. Lett. **B565** (2003) 61, hep-ex/0306033.

[192] P. Draper and H. Rzehak, 'A Review of Higgs Mass Calculations in Supersymmetric Models', Phys. Rept. **619** (2016) 1, 1601.01890.

[193] S. Heinemeyer, O. Stal and G. Weiglein, 'Interpreting the LHC Higgs Search Results in the MSSM', Phys. Lett. **B710** (2012) 201, 1112.3026.

[194] P. Bechtle et al., 'MSSM Interpretations of the LHC Discovery: Light or Heavy Higgs?', Eur. Phys. J. **C73** (2013) 2354, 1211.1955.

[195] P. Bechtle et al., 'The Light and Heavy Higgs Interpretation of the MSSM', Eur. Phys. J. **C77** (2017) 67, 1608.00638.

[196] H. E. Haber, S. Heinemeyer and T. Stefaniak, 'The Impact of Two-Loop Effects on the Scenario of MSSM Higgs Alignment without Decoupling', Eur. Phys. J. **C77** (2017) 742, 1708.04416.

[197] A. D. Linde, 'Decay of the False Vacuum at Finite Temperature', Nucl. Phys. **B216** (1983) 421.

[198] J. E. Camargo-Molina et al., 'Constraining the Natural MSSM through tunneling to color-breaking vacua at zero and non-zero temperature', Phys. Lett. **B737** (2014) 156, 1405.7376.

[199] S. R. Coleman and E. J. Weinberg, 'Radiative Corrections as the Origin of Spontaneous Symmetry Breaking', Phys. Rev. **D7** (1973) 1888.

[200] S. Weinberg, 'The cosmological constant problem', Rev. Mod. Phys. **61** (1989) 1.

[201] S. R. Coleman, V. Glaser and A. Martin, 'Action Minima Among Solutions to a Class of Euclidean Scalar Field Equations', Commun. Math. Phys. **58** (1978) 211.

[202] R. Apreda et al., 'Gravitational waves from electroweak phase transitions', Nucl. Phys. **B631** (2002) 342, gr-qc/0107033.

[203] A. Kusenko, P. Langacker and G. Segre, 'Phase transitions and vacuum tunneling into charge and color breaking minima in the MSSM', Phys. Rev. **D54** (1996) 5824, hep-ph/9602414.

[204] I. Dasgupta, 'Estimating vacuum tunneling rates', Phys. Lett. **B394** (1997) 116, hep-ph/9610403.

[205] J. M. Moreno, M. Quiros and M. Seco, 'Bubbles in the supersymmetric standard model', Nucl. Phys. **B526** (1998) 489, hep-ph/9801272.

[206] J. M. Cline, G. D. Moore and G. Servant, 'Was the electroweak phase transition preceded by a color broken phase?', Phys. Rev. **D60** (1999) 105035, hep-ph/9902220.

[207] P. John, 'Bubble wall profiles with more than one scalar field: A Numerical approach', Phys. Lett. **B452** (1999) 221, hep-ph/9810499.

[208] J. M. Cline et al., 'String mediated electroweak baryogenesis: A Critical analysis', Phys. Rev. **D59** (1999) 065014, hep-ph/9810261.

[209] T. Konstandin and S. J. Huber, 'Numerical approach to multi dimensional phase transitions', JCAP **0606** (2006) 021, hep-ph/0603081.

[210] J.-h. Park, 'Constrained potential method for false vacuum decays', JCAP **1102** (2011) 023, 1011.4936.

[211] C. L. Wainwright, 'CosmoTransitions: Computing Cosmological Phase Transition Temperatures and Bubble Profiles with Multiple Fields', Comput. Phys. Commun. **183** (2012) 2006, 1109.4189.

[212] A. Masoumi, K. D. Olum and B. Shlaer, 'Efficient numerical solution to vacuum decay with many fields', JCAP **1701** (2017) 051, 1610.06594.

[213] P. Athron et al., 'BubbleProfiler: finding the field profile and action for cosmological phase transitions', (2019), 1901.03714.

[214] F. C. Adams, 'General solutions for tunneling of scalar fields with quartic potentials', Phys. Rev. **D48** (1993) 2800, hep-ph/9302321.

[215] J. E. Camargo-Molina et al., ': A Tool For Finding The Global Minima Of One-Loop Effective Potentials With Many Scalars', Eur. Phys. J. **C73** (2013) 2588, 1307.1477.

[216] A. Andreassen, W. Frost and M. D. Schwartz, 'Consistent Use of Effective Potentials', Phys. Rev. **D91** (2015) 016009, 1408.0287.

[217] K.-M. Lee and E. J. Weinberg, 'Tunneling without Barriers', Nucl. Phys. **B267** (1986) 181.

[218] A. Strumia, 'Charge and color breaking minima and constraints on the MSSM parameters', Nucl. Phys. **B482** (1996) 24, hep-ph/9604417.

[219] N. G. Deshpande and E. Ma, 'Pattern of Symmetry Breaking with Two Higgs Doublets', Phys. Rev. **D18** (1978) 2574.

[220] I. P. Ivanov, 'Minkowski space structure of the Higgs potential in 2HDM', Phys. Rev. **D75** (2007) 035001, hep-ph/0609018.

[221] K. G. Klimenko, 'On Necessary and Sufficient Conditions for Some Higgs Potentials to Be Bounded From Below', Theor. Math. Phys. **62** (1985) 58.

[222] K. Kannike, 'Vacuum Stability Conditions From Copositivity Criteria', Eur. Phys. J. **C72** (2012) 2093, 1205.3781.

[223] K. Kannike, 'Vacuum Stability of a General Scalar Potential of a Few Fields', Eur. Phys. J. **C76** (2016) 324, 1603.02680.

[224] P. S. Bhupal Dev et al., 'Vacuum structure of the left-right symmetric model', JHEP **02** (2019) 154, 1811.06869.

[225] I. P. Ivanov, M. Köpke and M. Mühlleitner, 'Algorithmic Boundedness-From-Below Conditions for Generic Scalar Potentials', Eur. Phys. J. **C78** (2018) 413, 1802.07976.

[226] M. Maniatis and D. Mehta, 'Minimizing Higgs Potentials via Numerical Polynomial Homotopy Continuation', Eur. Phys. J. Plus **127** (2012) 91, 1203.0409.

[227] A. Morgan, *Solving polynomial systems using continuation for engineering and scientific problems*, Prentice-Hall, 1987, ISBN: 9780898719031.

[228] V. Branchina, F. Contino and P. M. Ferreira, 'Electroweak vacuum lifetime in two Higgs doublet models', JHEP **2018** (2018), 1807.10802.

[229] A. Masoumi, K. D. Olum and J. M. Wachter, 'Approximating tunneling rates in multi-dimensional field spaces', JCAP **1710** (2017) 022, 1702.00356.

[230] G. C. Branco, L. Lavoura and J. P. Silva, *CP Violation*, vol. 103, Int. Ser. Monogr. Phys., 1999 1.

[231] G. Chalons and F. Domingo, 'Analysis of the Higgs potentials for two doublets and a singlet', Phys. Rev. **D86** (2012) 115024, 1209.6235.

[232] D. Curtin et al., 'Exotic decays of the 125 GeV Higgs boson', Phys. Rev. **D90** (2014) 075004, 1312.4992.

[233] S. Baum and N. R. Shah, 'Two Higgs Doublets and a Complex Singlet: Disentangling the Decay Topologies and Associated Phenomenology', JHEP **12** (2018) 044, 1808.02667.

[234] L. Bento and G. C. Branco, 'Generation of a K-M phase from spontaneous CP breaking at a high-energy scale', Phys. Lett. **B245** (1990) 599.

[235] N. Darvishi, 'Baryogenesis of the Universe in cSMCS Model plus Iso-Doublet Vector Quark', JHEP **11** (2016) 065, 1608.02820.

[236] A. Datta and A. Raychaudhuri, 'Next-to-minimal Higgs: Mass bounds and search prospects', Phys. Rev. **D57** (1998) 2940, hep-ph/9708444.

[237] R. M. Schabinger and J. D. Wells, 'A Minimal spontaneously broken hidden sector and its impact on Higgs boson physics at the large hadron collider', Phys. Rev. **D72** (2005) 093007, hep-ph/0509209.

[238] B. Patt and F. Wilczek, 'Higgs-field portal into hidden sectors', (2006), hep-ph/0605188.

[239] D. O'Connell, M. J. Ramsey-Musolf and M. B. Wise, 'Minimal Extension of the Standard Model Scalar Sector', Phys. Rev. **D75** (2007) 037701, hep-ph/0611014.

[240] V. Barger et al., 'LHC Phenomenology of an Extended Standard Model with a Real Scalar Singlet', Phys. Rev. **D77** (2008) 035005, 0706.4311.

[241] C.-Y. Chen, S. Dawson and I. M. Lewis, 'Exploring resonant di-Higgs boson production in the Higgs singlet model', Phys. Rev. **D91** (2015) 035015, 1410.5488.

[242] T. Robens and T. Stefaniak, 'Status of the Higgs Singlet Extension of the Standard Model after LHC Run 1', Eur. Phys. J. **C75** (2015) 104, 1501.02234.

[243] T. Robens and T. Stefaniak, 'LHC Benchmark Scenarios for the Real Higgs Singlet Extension of the Standard Model', Eur. Phys. J. **C76** (2016) 268, 1601.07880.

[244] I. M. Lewis and M. Sullivan, 'Benchmarks for Double Higgs Production in the Singlet Extended Standard Model at the LHC', Phys. Rev. **D96** (2017) 035037, 1701.08774.

[245] A. Ilnicka, T. Robens and T. Stefaniak, 'Constraining Extended Scalar Sectors at the LHC and beyond', Mod. Phys. Lett. **A33** (2018) 1830007, 1803.03594.

[246] L. Alexander-Nunneley and A. Pilaftsis, 'The Minimal Scale Invariant Extension of the Standard Model', JHEP **09** (2010) 021, 1006.5916.

[247] A. Ahriche, A. Arhrib and S. Nasri, 'Higgs Phenomenology in the Two-Singlet Model', JHEP **02** (2014) 042, 1309.5615.

[248] R. Costa et al., 'Two-loop stability of a complex singlet extended Standard Model', Phys. Rev. **D92** (2015) 025024, 1411.4048.

[249] R. Costa et al., 'Singlet Extensions of the Standard Model at LHC Run 2: Benchmarks and Comparison with the NMSSM', JHEP **06** (2016) 034, 1512.05355.

[250] P. M. Ferreira, 'The vacuum structure of the Higgs complex singlet-doublet model', Phys. Rev. **D94** (2016) 096011, 1607.06101.

[251] S. Dawson and M. Sullivan, 'Enhanced di-Higgs boson production in the complex Higgs singlet model', Phys. Rev. **D97** (2018) 015022, 1711.06683.

[252] R. N. Lerner and J. McDonald, 'Gauge singlet scalar as inflaton and thermal relic dark matter', Phys. Rev. **D80** (2009) 123507, 0909.0520.

[253] V. Barger, M. McCaskey and G. Shaughnessy, 'Complex Scalar Dark Matter vis-à-vis CoGeNT, DAMA/LIBRA and XENON100', Phys. Rev. **D82** (2010) 035019, 1005.3328.

[254] M. Gonderinger, H. Lim and M. J. Ramsey-Musolf, 'Complex Scalar Singlet Dark Matter: Vacuum Stability and Phenomenology', Phys. Rev. **D86** (2012) 043511, 1202.1316.

[255] G. Belanger et al., 'Z_3 Scalar Singlet Dark Matter', JCAP **1301** (2013) 022, 1211.1014.

[256] M. Jiang et al., 'Impact of a complex singlet: Electroweak baryogenesis and dark matter', Phys. Rev. **D93** (2016) 065032, 1502.07574.

[257] GAMBIT, 'Status of the scalar singlet dark matter model', Eur. Phys. J. **C77** (2017) 568, 1705.07931.

[258] C.-W. Chiang, M. J. Ramsey-Musolf and E. Senaha, 'Standard Model with a Complex Scalar Singlet: Cosmological Implications and Theoretical Considerations', Phys. Rev. **D97** (2018) 015005, 1707.09960.

[259] P. Athron et al., 'Impact of vacuum stability, perturbativity and XENON1T on global fits of $\mathbb{Z}_2$ and $\mathbb{Z}_3$ scalar singlet dark matter', Eur. Phys. J. **C78** (2018) 830, 1806.11281.

[260] B. Grzadkowski and D. Huang, 'Spontaneous CP-Violating Electroweak Baryogenesis and Dark Matter from a Complex Singlet Scalar', JHEP **08** (2018) 135, 1807.06987.

[261] D. Curtin, P. Meade and C.-T. Yu, 'Testing Electroweak Baryogenesis with Future Colliders', JHEP **11** (2014) 127, 1409.0005.

[262] A. V. Kotwal et al., 'Singlet-catalyzed electroweak phase transitions in the 100 TeV frontier', Phys. Rev. **D94** (2016) 035022, 1605.06123.

[263] A. Beniwal et al., 'Gravitational wave, collider and dark matter signals from a scalar singlet electroweak baryogenesis', JHEP **08** (2017) 108, 1702.06124.

[264] W. Cheng and L. Bian, 'From inflation to cosmological electroweak phase transition with a complex scalar singlet', Phys. Rev. **D98** (2018) 023524, 1801.00662.

[265] ATLAS, 'Search for pair production of Higgs bosons in the $b\bar{b}b\bar{b}$ final state using proton–proton collisions at $\sqrt{s} = 13$ TeV with the ATLAS detector', Phys. Rev. **D94** (2016) 052002, 1606.04782.

[266] ATLAS, 'Search for Higgs boson pair production in the $WW^{(*)}WW^{(*)}$ decay channel using ATLAS data recorded at $\sqrt{s} = 13$ TeV', JHEP **05** (2019) 124, 1811.11028.

[267] CMS, 'Search for resonant and nonresonant Higgs boson pair production in the $\mathrm{b\bar{b}}\ell\nu\ell\nu$ final state in proton-proton collisions at $\sqrt{s} = 13$ TeV', JHEP **01** (2018) 054, 1708.04188.

[268] CMS, 'Search for Higgs boson pair production in events with two bottom quarks and two tau leptons in proton–proton collisions at $\sqrt{s}$ =13TeV', Phys. Lett. **B778** (2018) 101, 1707.02909.

[269] ATLAS, 'Search for Higgs boson pair production in the $b\bar{b}WW^*$ decay mode at $\sqrt{s} = 13$ TeV with the ATLAS detector', JHEP **04** (2019) 092, 1811.04671.

[270] ATLAS, 'Search for resonant and non-resonant Higgs boson pair production in the $b\bar{b}\tau^+\tau^-$ decay channel in pp collisions at $\sqrt{s} = 13$ TeV with the ATLAS detector', Phys. Rev. Lett. **121** (2018) 191801, 1808.00336.

[271] ATLAS, 'Search for Higgs boson pair production in the $\gamma\gamma WW^*$ channel using pp collision data recorded at $\sqrt{s} = 13$ TeV with the ATLAS detector', Eur. Phys. J. **C78** (2018) 1007, 1807.08567.

[272] ATLAS, 'Search for Higgs boson pair production in the $\gamma\gamma b\bar{b}$ final state with 13 TeV pp collision data collected by the ATLAS experiment', JHEP **11** (2018) 040, 1807.04873.

[273] CMS, 'Combination of searches for Higgs boson pair production in proton-proton collisions at $\sqrt{s} = 13$ TeV', Phys. Rev. Lett. **122** (2019) 121803, 1811.09689.

[274] CMS, 'Search for resonant pair production of Higgs bosons decaying to bottom quark-antiquark pairs in proton-proton collisions at 13 TeV', JHEP **08** (2018) 152, 1806.03548.

[275] CMS, 'Search for Higgs boson pair production in the $\gamma\gamma\mathrm{b\bar{b}}$ final state in pp collisions at $\sqrt{s} = 13$ TeV', Phys. Lett. **B788** (2019) 7, 1806.00408.

[276] ATLAS, 'Combination of searches for Higgs boson pairs in pp collisions at $\sqrt{s}$ =13 TeV with the ATLAS detector', (2019), 1906.02025.

[277] CMS, 'Search for an exotic decay of the Higgs boson to a pair of light pseudoscalars in the final state of two muons and two τ leptons in proton-proton collisions at $\sqrt{s} = 13$ TeV', JHEP **11** (2018) 018, 1805.04865.

[278] CMS, 'Search for an exotic decay of the Higgs boson to a pair of light pseudoscalars in the final state with two b quarks and two τ leptons in proton-proton collisions at $\sqrt{s} = 13$ TeV', Phys. Lett. **B785** (2018) 462, 1805.10191.

[279] ATLAS, 'Search for the Higgs boson produced in association with a vector boson and decaying into two spin-zero particles in the $H \to aa \to 4b$ channel in pp collisions at $\sqrt{s} = 13$ TeV with the ATLAS detector', JHEP **10** (2018) 031, 1806.07355.

[280] ATLAS, 'Search for Higgs boson decays into pairs of light (pseudo)scalar particles in the $\gamma\gamma jj$ final state in pp collisions at $\sqrt{s} = 13$ TeV with the ATLAS detector', Phys. Lett. **B782** (2018) 750, 1803.11145.

[281] CMS, 'Search for an exotic decay of the Higgs boson to a pair of light pseudoscalars in the final state with two muons and two b quarks in pp collisions at 13 TeV', Phys. Lett. **B795** (2019) 398, 1812.06359.

[282] CMS, 'Search for light pseudoscalar boson pairs produced from decays of the 125 GeV Higgs boson in final states with two muons and two nearby tracks in pp collisions at $\sqrt{s} = 13$ TeV', (2019), 1907.07235.

[283] ATLAS, 'Search for Higgs boson decays into a pair of light bosons in the $bb\mu\mu$ final state in pp collision at $\sqrt{s}$ =13 TeV with the ATLAS detector', Phys. Lett. **B790** (2019) 1, 1807.00539.

[284] A. Djouadi, J. Kalinowski and M. Spira, 'HDECAY: A Program for Higgs boson decays in the standard model and its supersymmetric extension', Comput. Phys. Commun. **108** (1998) 56, hep-ph/9704448.

[285] J. M. Butterworth et al., 'THE TOOLS AND MONTE CARLO WORKING GROUP Summary Report from the Les Houches 2009 Workshop on TeV Colliders', in: *Physics at TeV colliders. Proceedings, 6 Workshop, dedicated to Thomas Binoth, Les Houches, France, June 8-26, 2009*, 2010, 1003.1643.

[286] A. Djouadi et al., 'HDECAY: Twenty$_{++}$ Years After', Comput. Phys. Commun. **238** (2019) 214, 1801.09506.

[287] A. Bredenstein et al., 'Precise predictions for the Higgs-boson decay $H \to WW/ZZ \to 4$ leptons', Phys. Rev. **D74** (2006) 013004, hep-ph/0604011.

[288] A. Bredenstein et al., 'Precision calculations for the Higgs decays $H \to ZZ/WW \to$ 4 leptons', Nucl. Phys. Proc. Suppl. **160** (2006) 131, hep-ph/0607060.

[289] A. Bredenstein et al., 'Radiative corrections to the semileptonic and hadronic Higgs-boson decays $H \to WW/ZZ \to 4$ fermions', JHEP **02** (2007) 080, hep-ph/0611234.

[290] P. M. Ferreira et al., 'Wrong sign and symmetric limits and non-decoupling in 2HDMs', JHEP **12** (2014) 067, 1409.6723.

[291] LHC Higgs Cross Section Working Group, 'Handbook of LHC Higgs Cross Sections: 3. Higgs Properties', (2013), ed. by S. Heinemeyer et al., 1307.1347.

[292] C. Anastasiou et al., 'High precision determination of the gluon fusion Higgs boson cross-section at the LHC', JHEP **05** (2016) 058, 1602.00695.

[293] ALEPH, DELPHI, L3, OPAL, 'Search for neutral MSSM Higgs bosons at LEP', Eur. Phys. J. **C47** (2006) 547, hep-ex/0602042.

[294] P. Drechsel, G. Moortgat-Pick and G. Weiglein, 'Sensitivity of the ILC to light Higgs masses', in: *International Workshop on Future Linear Collider (LCWS2017) Strasbourg, France, October 23-27, 2017*, 2018, 1801.09662.

[295] ATLAS, 'Combination of searches for heavy resonances decaying into bosonic and leptonic final states using 36 fb^{-1} of proton-proton collision data at $\sqrt{s} = 13$ TeV with the ATLAS detector', Phys. Rev. **D98** (2018) 052008, 1808.02380.

[296] CMS, 'Search for a new scalar resonance decaying to a pair of Z bosons in proton-proton collisions at $\sqrt{s} = 13$ TeV', JHEP **06** (2018) 127, 1804.01939.

[297] I. F. Ginzburg, M. Krawczyk and P. Osland, 'Two Higgs doublet models with CP violation', in: *Linear colliders, Seogwipo, Korea, August 26-30, 2002*, [,703(2002)], 2002 703, hep-ph/0211371.

[298] K. Cheung et al., 'Confronting Higgcision with Electric Dipole Moments', JHEP **06** (2014) 149, 1403.4775.

[299] D. Fontes et al., 'Large pseudoscalar Yukawa couplings in the complex 2HDM', JHEP **06** (2015) 060, 1502.01720.

[300] C.-Y. Chen, S. Dawson and Y. Zhang, 'Complementarity of LHC and EDMs for Exploring Higgs CP Violation', JHEP **06** (2015) 056, 1503.01114.

[301] F. Boudjema et al., 'Lab-frame observables for probing the top-Higgs interaction', Phys. Rev. **D92** (2015) 015019, 1501.03157.

[302] M. R. Buckley and D. Goncalves, 'Boosting the Direct CP Measurement of the Higgs-Top Coupling', Phys. Rev. Lett. **116** (2016) 091801, 1507.07926.

[303] S. Amor Dos Santos et al., 'Probing the CP nature of the Higgs coupling in $t\bar{t}h$ events at the LHC', Phys. Rev. **D96** (2017) 013004, 1704.03565.

[304] D. Azevedo et al., 'CP tests of Higgs couplings in $t\bar{t}h$ semileptonic events at the LHC', Phys. Rev. **D98** (2018) 033004, 1711.05292.

[305] S. Berge, W. Bernreuther and J. Ziethe, 'Determining the CP parity of Higgs bosons at the LHC in their tau decay channels', Phys. Rev. Lett. **100** (2008) 171605, 0801.2297.

[306] S. Berge and W. Bernreuther, 'Determining the CP parity of Higgs bosons at the LHC in the tau to 1-prong decay channels', Phys. Lett. **B671** (2009) 470, 0812.1910.

[307] S. Berge et al., 'How to pin down the CP quantum numbers of a Higgs boson in its tau decays at the LHC', Phys. Rev. **D84** (2011) 116003, 1108.0670.

[308] S. Berge, W. Bernreuther and S. Kirchner, 'Determination of the Higgs CP-mixing angle in the tau decay channels at the LHC including the Drell–Yan background', Eur. Phys. J. **C74** (2014) 3164, 1408.0798.

[309] S. Berge, W. Bernreuther and S. Kirchner, 'Prospects of constraining the Higgs bosons CP nature in the tau decay channel at the LHC', Phys. Rev. **D92** (2015) 096012, 1510.03850.

[310] A. G. Akeroyd, A. Arhrib and E.-M. Naimi, 'Note on tree level unitarity in the general two Higgs doublet model', Phys. Lett. **B490** (2000) 119, hep-ph/0006035.

[311] I. F. Ginzburg and I. P. Ivanov, 'Tree level unitarity constraints in the 2HDM with CP violation', (2003), hep-ph/0312374.

[312] I. P. Ivanov and J. P. Silva, 'Tree-level metastability bounds for the most general two Higgs doublet model', Phys. Rev. **D92** (2015) 055017, 1507.05100.

[313] ACME, 'Order of Magnitude Smaller Limit on the Electric Dipole Moment of the Electron', Science **343** (2014) 269, 1310.7534.

[314] R. V. Harlander, S. Liebler and H. Mantler, 'SusHi: A program for the calculation of Higgs production in gluon fusion and bottom-quark annihilation in the Standard Model and the MSSM', Comput. Phys. Commun. **184** (2013) 1605, 1212.3249.

[315] R. V. Harlander, S. Liebler and H. Mantler, 'SusHi Bento: Beyond NNLO and the heavy-top limit', Comput. Phys. Commun. **212** (2017) 239, 1605.03190.

[316] P. M. Ferreira et al., 'Probing wrong-sign Yukawa couplings at the LHC and a future linear collider', Phys. Rev. **D89** (2014) 115003, 1403.4736.

[317] J. Brod, U. Haisch and J. Zupan, 'Constraints on CP-violating Higgs couplings to the third generation', JHEP **11** (2013) 180, 1310.1385.

[318] J. Shu and Y. Zhang, 'Impact of a CP Violating Higgs Sector: From LHC to Baryogenesis', Phys. Rev. Lett. **111** (2013) 091801, 1304.0773.

[319] C.-Y. Chen, M. Freid and M. Sher, 'Next-to-minimal two Higgs doublet model', Phys. Rev. **D89** (2014) 075009, 1312.3949.

[320] I. P. Ivanov and J. P. Silva, 'CP-conserving multi-Higgs model with irremovable complex coefficients', Phys. Rev. **D93** (2016) 095014, 1512.09276.

[321] R. Barbieri, L. J. Hall and V. S. Rychkov, 'Improved naturalness with a heavy Higgs: An Alternative road to LHC physics', Phys. Rev. **D74** (2006) 015007, hep-ph/0603188.

[322] L. Lopez Honorez et al., 'The Inert Doublet Model: An Archetype for Dark Matter', JCAP **0702** (2007) 028, hep-ph/0612275.

[323] Q.-H. Cao, E. Ma and G. Rajasekaran, 'Observing the Dark Scalar Doublet and its Impact on the Standard-Model Higgs Boson at Colliders', Phys. Rev. **D76** (2007) 095011, 0708.2939.

[324] A. Belyaev et al., 'Anatomy of the Inert Two Higgs Doublet Model in the light of the LHC and non-LHC Dark Matter Searches', Phys. Rev. **D97** (2018) 035011, 1612.00511.

[325] J. Kalinowski et al., 'Benchmarking the Inert Doublet Model for e^+e^- colliders', JHEP **12** (2018) 081, 1809.07712.

[326] CMS, 'Search for invisible decays of a Higgs boson produced through vector boson fusion in proton-proton collisions at $\sqrt{s} = 13$ TeV', Phys. Lett. **B793** (2019) 520, 1809.05937.

[327] ATLAS, 'Combination of searches for invisible Higgs boson decays with the ATLAS experiment', Phys. Rev. Lett. **122** (2019) 231801, 1904.05105.

[328] B. Świeżewska, 'Yukawa independent constraints for two-Higgs-doublet models with a 125 GeV Higgs boson', Phys. Rev. **D88** (2013) 055027, 1209.5725.

[329] M. Spira, 'QCD effects in Higgs physics', Fortsch. Phys. **46** (1998) 203, hep-ph/9705337.

[330] M. Spira, 'Higgs Boson Production and Decay at Hadron Colliders', Prog. Part. Nucl. Phys. **95** (2017) 98, 1612.07651.

[331] CMS, 'Measurements of Higgs boson properties in the diphoton decay channel in proton-proton collisions at $\sqrt{s} = 13$ TeV', JHEP **11** (2018) 185, 1804.02716.

[332] XENON, 'First Dark Matter Search Results from the XENON1T Experiment', Phys. Rev. Lett. **119** (2017) 181301, 1705.06655.

[333] K. Hagiwara et al., 'Probing the Weak Boson Sector in $e^+e^- \to W^+W^-$', Nucl. Phys. **B282** (1987) 253.

[334] G. J. Gounaris, J. Layssac and F. M. Renard, 'Signatures of the anomalous Z_γ and ZZ production at the lepton and hadron colliders', Phys. Rev. **D61** (2000) 073013, hep-ph/9910395.

[335] G. J. Gounaris, J. Layssac and F. M. Renard, 'Off-shell structure of the anomalous Z and γ selfcouplings', Phys. Rev. **D65** (2002) 017302, hep-ph/0005269.

[336] U. Baur and D. L. Rainwater, 'Probing neutral gauge boson selfinteractions in ZZ production at hadron colliders', Phys. Rev. **D62** (2000) 113011, hep-ph/0008063.

[337] B. Grzadkowski, O. M. Ogreid and P. Osland, 'CP-Violation in the ZZZ and ZWW vertices at e^+e^- colliders in Two-Higgs-Doublet Models', JHEP **05** (2016) 025, 1603.01388.

[338] T. Hahn and M. Perez-Victoria, 'Automatized one loop calculations in four-dimensions and D-dimensions', Comput. Phys. Commun. **118** (1999) 153, hep-ph/9807565.

[339] L. Lavoura and J. P. Silva, 'Fundamental CP violating quantities in a SU(2) x U(1) model with many Higgs doublets', Phys. Rev. **D50** (1994) 4619, hep-ph/9404276.

[340] F. J. Botella and J. P. Silva, 'Jarlskog - like invariants for theories with scalars and fermions', Phys. Rev. **D51** (1995) 3870, hep-ph/9411288.

[341] CMS, 'Measurement of the $pp \to ZZ$ production cross section and constraints on anomalous triple gauge couplings in four-lepton final states at $\sqrt{s}$ =8 TeV', Phys. Lett. **B740** (2015) 250, 1406.0113.

[342] ATLAS, 'Measurement of the ZZ production cross section in proton-proton collisions at $\sqrt{s} = 8$ TeV using the $ZZ \to \ell^-\ell^+\ell'^-\ell'^+$ and $ZZ \to \ell^-\ell^+\nu\bar{\nu}$ channels with the ATLAS detector', JHEP **01** (2017) 099, 1610.07585.

[343] ATLAS, '$ZZ \to \ell^+\ell^-\ell'^+\ell'^-$ cross-section measurements and search for anomalous triple gauge couplings in 13 TeV pp collisions with the ATLAS detector', Phys. Rev. **D97** (2018) 032005, 1709.07703.

[344] CMS, 'Measurements of the pp $\to$ ZZ production cross section and the Z $\to 4\ell$ branching fraction, and constraints on anomalous triple gauge couplings at $\sqrt{s} =$ 13 TeV', Eur. Phys. J. **C78** (2018) 165, 1709.08601.

[345] D. Chang, W.-Y. Keung and P. B. Pal, 'CP violation in the cubic coupling of neutral gauge bosons', Phys. Rev. **D51** (1995) 1326, hep-ph/9407294.

[346] G. C. Branco and M. N. Rebelo, 'The Higgs Mass in a Model With Two Scalar Doublets and Spontaneous CP Violation', Phys. Lett. **160B** (1985) 117.

[347] P. M. Ferreira et al., 'CP properties of symmetry-constrained two-Higgs-doublet models', JHEP **08** (2010) 125, 1004.3207.

[348] A. Drozd et al., 'Extending two-Higgs-doublet models by a singlet scalar field - the Case for Dark Matter', JHEP **11** (2014) 105, 1408.2106.

[349] P. M. Ferreira, R. Santos and A. Barroso, 'Stability of the tree-level vacuum in two Higgs doublet models against charge or CP spontaneous violation', Phys. Lett. **B603** (2004) 219, hep-ph/0406231.

[350] P. M. Ferreira, R. Santos and A. Barroso, 'Charge and CP symmetry breaking in two Higgs doublet models', Phys. Lett. **B632** (2006) 684, hep-ph/0507224.

[351] I. P. Ivanov, 'Minkowski space structure of the Higgs potential in 2HDM. II. Minima, symmetries, and topology', Phys. Rev. **D77** (2008) 015017, 0710.3490.

[352] J. Velhinho, R. Santos and A. Barroso, 'Tree level vacuum stability in two Higgs doublet models', Phys. Lett. **B322** (1994) 213.

[353] C. C. Nishi, 'CP violation conditions in N-Higgs-doublet potentials', Phys. Rev. **D74** (2006) 036003, hep-ph/0605153.

[354] M. Maniatis et al., 'Stability and symmetry breaking in the general two-Higgs-doublet model', Eur. Phys. J. **C48** (2006) 805, hep-ph/0605184.

[355] A. Barroso, P. M. Ferreira and R. Santos, 'Neutral minima in two-Higgs doublet models', Phys. Lett. **B652** (2007) 181, hep-ph/0702098.

[356] C. C. Nishi, 'The Structure of potentials with N Higgs doublets', Phys. Rev. **D76** (2007) 055013, 0706.2685.

[357] M. Maniatis, A. von Manteuffel and O. Nachtmann, 'CP violation in the general two-Higgs-doublet model: A Geometric view', Eur. Phys. J. **C57** (2008) 719, 0707.3344.

[358] M. Maniatis, A. von Manteuffel and O. Nachtmann, 'A New type of CP symmetry, family replication and fermion mass hierarchies', Eur. Phys. J. **C57** (2008) 739, 0711.3760.

[359] C. C. Nishi, 'Physical parameters and basis transformations in the Two-Higgs-Doublet model', Phys. Rev. **D77** (2008) 055009, 0712.4260.

[360] M. Maniatis and O. Nachtmann, 'On the phenomenology of a two-Higgs-doublet model with maximal CP symmetry at the LHC', JHEP **05** (2009) 028, 0901.4341.

[361] A. Barroso et al., 'Evading death by vacuum', Eur. Phys. J. **C73** (2013) 2537, 1211.6119.

[362] A. Barroso et al., 'Metastability bounds on the two Higgs doublet model', JHEP **06** (2013) 045, 1303.5098.

[363] A. Barroso et al., 'Stability of the normal vacuum in multi-Higgs-doublet models', Phys. Rev. **D74** (2006) 085016, hep-ph/0608282.

[364] L. Girardello and M. T. Grisaru, 'Soft Breaking of Supersymmetry', Nucl. Phys. **B194** (1982) 65.

[365] K. G. Chetyrkin, J. H. Kuhn and M. Steinhauser, 'RunDec: A Mathematica package for running and decoupling of the strong coupling and quark masses', Comput. Phys. Commun. **133** (2000) 43, hep-ph/0004189.

[366] B. Schmidt and M. Steinhauser, 'CRunDec: a C++ package for running and decoupling of the strong coupling and quark masses', Comput. Phys. Commun. **183** (2012) 1845, 1201.6149.

[367] F. Herren and M. Steinhauser, 'Version 3 of RunDec and CRunDec', Comput. Phys. Commun. **224** (2018) 333, 1703.03751.

[368] L. J. Hall, R. Rattazzi and U. Sarid, 'The Top quark mass in supersymmetric SO(10) unification', Phys. Rev. **D50** (1994) 7048, hep-ph/9306309.

[369] M. Carena et al., 'Electroweak symmetry breaking and bottom - top Yukawa unification', Nucl. Phys. **B426** (1994) 269, hep-ph/9402253.

[370] D. M. Pierce et al., 'Precision corrections in the minimal supersymmetric standard model', Nucl. Phys. **B491** (1997) 3, hep-ph/9606211.

[371] M. Carena et al., 'Effective Lagrangian for the $\bar{t}bH^+$ interaction in the MSSM and charged Higgs phenomenology', Nucl. Phys. **B577** (2000) 88, hep-ph/9912516.

[372] W. G. Hollik, 'Charge and color breaking constraints in the Minimal Supersymmetric Standard Model associated with the bottom Yukawa coupling', Phys. Lett. **B752** (2016) 7, 1508.07201.

[373] J. Guasch, W. Hollik and S. Penaranda, 'Distinguishing Higgs models in $H \to b\bar{b}$ / $H \to \tau^+\tau^-$', Phys. Lett. **B515** (2001) 367, hep-ph/0106027.

[374] J. M. Frere, D. R. T. Jones and S. Raby, 'Fermion Masses and Induction of the Weak Scale by Supergravity', Nucl. Phys. **B222** (1983) 11.

[375] M. Claudson, L. J. Hall and I. Hinchliffe, 'Low-Energy Supergravity: False Vacua and Vacuous Predictions', Nucl. Phys. **B228** (1983) 501.

[376] M. Drees, M. Gluck and K. Grassie, 'A New Class of False Vacua in Low-energy N=1 Supergravity Theories', Phys. Lett. **157B** (1985) 164.

[377] J. F. Gunion, H. E. Haber and M. Sher, 'Charge / Color Breaking Minima and a-Parameter Bounds in Supersymmetric Models', Nucl. Phys. **B306** (1988) 1.

[378] H. Komatsu, 'New Constraints on Parameters in the Minimal Supersymmetric Model', Phys. Lett. **B215** (1988) 323.

[379] P. Langacker and N. Polonsky, 'Implications of Yukawa unification for the Higgs sector in supersymmetric grand unified models', Phys. Rev. **D50** (1994) 2199, hep-ph/9403306.

[380] J. A. Casas, A. Lleyda and C. Munoz, 'Strong constraints on the parameter space of the MSSM from charge and color breaking minima', Nucl. Phys. **B471** (1996) 3, hep-ph/9507294.

[381] J. A. Casas and S. Dimopoulos, 'Stability bounds on flavor violating trilinear soft terms in the MSSM', Phys. Lett. **B387** (1996) 107, hep-ph/9606237.

[382] C. Le Mouel and G. Moultaka, 'Novel electroweak symmetry breaking conditions from quantum effects in the MSSM', Nucl. Phys. **B518** (1998) 3, hep-ph/9711356.

[383] S. Abel and T. Falk, 'Charge and color breaking in the constrained MSSM', Phys. Lett. **B444** (1998) 427, hep-ph/9810297.

[384] C. Le Mouel, 'Optimal charge and color breaking conditions in the MSSM', Nucl. Phys. **B607** (2001) 38, hep-ph/0101351.

[385] P. M. Ferreira, 'Minimization of a one loop charge breaking effective potential', Phys. Lett. **B512** (2001) 379, hep-ph/0102141.

[386] P. M. Ferreira, 'A Full one loop charge and color breaking effective potential', Phys. Lett. **B509** (2001) 120, hep-ph/0008115.

[387] P. M. Ferreira, 'One-loop charge and colour breaking associated with the top Yukawa coupling', (2004), hep-ph/0406234.

[388] J.-h. Park, 'Metastability bounds on flavour-violating trilinear soft terms in the MSSM', Phys. Rev. **D83** (2011) 055015, 1011.4939.

[389] W. Altmannshofer et al., 'Indirect Probes of the MSSM after the Higgs Discovery', JHEP **01** (2013) 160, 1211.1976.

[390] M. Carena et al., 'Vacuum Stability and Higgs Diphoton Decays in the MSSM', JHEP **02** (2013) 114, 1211.6136.

[391] J. E. Camargo-Molina et al., 'Stability of the CMSSM against sfermion VEVs', JHEP **12** (2013) 103, 1309.7212.

[392] U. Chattopadhyay and A. Dey, 'Exploring MSSM for Charge and Color Breaking and Other Constraints in the Context of Higgs@125 GeV', JHEP **11** (2014) 161, 1409.0611.

[393] D. Chowdhury et al., 'Charge and Color Breaking Constraints in MSSM after the Higgs Discovery at LHC', JHEP **02** (2014) 110, 1310.1932.

[394] N. Blinov and D. E. Morrissey, 'Vacuum Stability and the MSSM Higgs Mass', JHEP **03** (2014) 106, 1310.4174.

[395] M. Bobrowski et al., 'Vacuum stability of the effective Higgs potential in the Minimal Supersymmetric Standard Model', Phys. Rev. **D90** (2014) 035025, 1407.2814.

[396] W. Altmannshofer, C. Frugiuele and R. Harnik, 'Fermion Hierarchy from Sfermion Anarchy', JHEP **12** (2014) 180, 1409.2522.

[397] W. G. Hollik, 'A new view on vacuum stability in the MSSM', JHEP **08** (2016) 126, 1606.08356.

[398] M. E. Krauss, T. Opferkuch and F. Staub, 'Spontaneous Charge Breaking in the NMSSM - Dangerous or not?', Eur. Phys. J. **C77** (2017) 331, 1703.05329.

[399] M. Carena et al., 'Suggestions for improved benchmark scenarios for Higgs boson searches at LEP-2', in: *Workshop on New Theoretical Developments for Higgs Physics at LEP-2 Geneva, Switzerland, October 27, 1999*, 1999, hep-ph/9912223.

[400] M. Carena et al., 'CP violating MSSM Higgs bosons in the light of LEP-2', Phys. Lett. **B495** (2000) 155, hep-ph/0009212.

[401] M. Carena et al., 'Suggestions for benchmark scenarios for MSSM Higgs boson searches at hadron colliders', Eur. Phys. J. **C26** (2003) 601, hep-ph/0202167.

[402] M. Carena et al., 'MSSM Higgs Boson Searches at the LHC: Benchmark Scenarios after the Discovery of a Higgs-like Particle', Eur. Phys. J. **C73** (2013) 2552, 1302.7033.

[403] M. Carena et al., 'CP Violation in Heavy MSSM Higgs Scenarios', JHEP **02** (2016) 123, 1512.00437.

[404] CMS, 'Search for additional neutral MSSM Higgs bosons in the $\tau\tau$ final state in proton-proton collisions at $\sqrt{s} = 13$ TeV', JHEP **09** (2018) 007, 1803.06553.

[405] J. E. Camargo-Molina et al., *Vevacious*, URL: vevacious.hepforge.org.

[406] S. Heinemeyer, W. Hollik and G. Weiglein, 'The Masses of the neutral CP-even Higgs bosons in the MSSM: Accurate analysis at the two loop level', Eur. Phys. J. **C9** (1999) 343, hep-ph/9812472.

[407] S. Heinemeyer, W. Hollik and G. Weiglein, 'FeynHiggs: A Program for the calculation of the masses of the neutral CP-even Higgs bosons in the MSSM', Comput. Phys. Commun. **124** (2000) 76, hep-ph/9812320.

[408] G. Degrassi et al., 'Towards high precision predictions for the MSSM Higgs sector', Eur. Phys. J. **C28** (2003) 133, hep-ph/0212020.

[409] M. Frank et al., 'The Higgs Boson Masses and Mixings of the Complex MSSM in the Feynman-Diagrammatic Approach', JHEP **02** (2007) 047, hep-ph/0611326.

[410] T. Hahn et al., 'High-Precision Predictions for the Light CP -Even Higgs Boson Mass of the Minimal Supersymmetric Standard Model', Phys. Rev. Lett. **112** (2014) 141801, 1312.4937.

[411] H. Bahl and W. Hollik, 'Precise prediction for the light MSSM Higgs boson mass combining effective field theory and fixed-order calculations', Eur. Phys. J. **C76** (2016) 499, 1608.01880.

[412] H. Bahl et al., 'Reconciling EFT and hybrid calculations of the light MSSM Higgs-boson mass', Eur. Phys. J. **C78** (2018) 57, 1706.00346.

[413] J. F. Gunion and H. E. Haber, 'The CP conserving two Higgs doublet model: The Approach to the decoupling limit', Phys. Rev. **D67** (2003) 075019, hep-ph/0207010.

[414] N. Craig, J. Galloway and S. Thomas, 'Searching for Signs of the Second Higgs Doublet', (2013), 1305.2424.

[415] M. Carena et al., 'Impersonating the Standard Model Higgs Boson: Alignment without Decoupling', JHEP **04** (2014) 015, 1310.2248.

[416] P. S. Bhupal Dev and A. Pilaftsis, 'Maximally Symmetric Two Higgs Doublet Model with Natural Standard Model Alignment', JHEP **12** (2014) 024, 1408.3405.

[417] M. Carena et al., 'Complementarity between Nonstandard Higgs Boson Searches and Precision Higgs Boson Measurements in the MSSM', Phys. Rev. **D91** (2015) 035003, 1410.4969.

[418] J. Bernon et al., 'Scrutinizing the alignment limit in two-Higgs-doublet models: $m_h = 125$ GeV', Phys. Rev. **D92** (2015) 075004, 1507.00933.

[419] J. Bernon et al., 'Scrutinizing the alignment limit in two-Higgs-doublet models. II. $m_H = 125$ GeV', Phys. Rev. **D93** (2016) 035027, 1511.03682.

[420] ATLAS, 'Measurements of Higgs boson properties in the diphoton decay channel with 36 fb^{-1} of pp collision data at $\sqrt{s} = 13$ TeV with the ATLAS detector', Phys. Rev. **D98** (2018) 052005, 1802.04146.

Eidesstattliche Erklärung

Hiermit erkläre ich an Eides statt, dass ich die vorliegende Dissertationsschrift selbst verfasst und keine anderen als die angegebenen Quellen und Hilfsmittel benutzt habe.

Hamburg, den 29.10.2019 Jonas Wittbrodt